



Pedro Daniel dos Santos Conceição

Licenciado em Ciências de Engenharia Mecânica

**Numerical simulation of two-degree-of-freedom
vortex induced vibration in a circular cylinder
with OpenFOAM**

Dissertação para a obtenção do Grau de Mestre em
Engenharia mecânica

Orientador: José Manuel Paixão Conde, Prof. Auxiliar,
FCT - UNL

Júri

Presidente: Prof. Dr. José Fernando de Almeida Dias
Vogais: Prof. Dr. Eric Lionel Didier
Prof. Dr. José Manuel Paixão Conde



FACULDADE DE
CIÊNCIAS E TECNOLOGIA
UNIVERSIDADE NOVA DE LISBOA

Setembro, 2016

Numerical simulation of two-degree-of-freedom vortex induced vibration in a circular cylinder with OpenFOAM

Copyright © Pedro Daniel dos Santos Conceição, Faculty of Sciences and Technology, NOVA University of Lisbon.

The Faculty of Sciences and Technology and the NOVA University of Lisbon have the right, perpetual and without geographical boundaries, to file and publish this dissertation through printed copies reproduced on paper or on digital form, or by any other means known or that may be invented, and to disseminate through scientific repositories and admit its copying and distribution for non-commercial, educational or research purposes, as long as credit is given to the author and editor.

ACKNOWLEDGEMENTS

First of all I would like to thank my supervisor, Prof. Dr. José Conde, for the guidance that he provided me along the development of this work.

I would like to express my gratitude to my family for all the comprehension and support.

To all of my friends for the companionship.

Finally, to my girlfriend and best friend, Joana, for encouraging and always believe in me, giving me support to overcome with success this journey.

ABSTRACT

Computational fluid dynamics tools are capable to simulate the influence of a fluid flow passing around an object. The ability to predict the impact of such flows on a specific product performance is time consuming and costly without some form of simulation tool. In fact, across a wide range of engineering areas, virtual development allows the reduction of the number of prototypes and less testing until a product is ready to the market. Therefore, it is important to provide computational fluid dynamics users with easy-to-use, robust, time-efficient and validated processes. Bearing this in mind, the current thesis studies the phenomenon of vortex induced vibrations simulating a flow around an oscillatory cylinder.

A flow passing around a rhombic body originates dynamic forces which, consequently, induce a set of body movements that are well characterized in the literature. To perform the numerical investigation of this phenomenon was used the OpenFOAM, an open-source software which is numerically able to perform a detailed and accurate analysis of this complex phenomena. Given the few scientific studies about the vortex induced vibration phenomenon with two degrees of freedom, this thesis aims to validate the OpenFOAM software for this case study, providing the scientific community the validation of a new numerical tool for studies of this kind. With this goal, it was firstly performed a mesh independence study for a flow around a fixed cylinder where it was studied the influence of the mesh on the fundamental quantities, that is, the Strouhal number, St , the mean drag coefficient, $C_{D,mean}$, and the root mean square of the drag, $C_{D,rms}$, and lift, $C_{L,rms}$, coefficients.

Then, it was carried out the study of the flow around a cylinder with one degree of freedom. It was studied the response of the cylinder for two types of systems, mass-spring system and mass-spring-damper system for a mesh with a $2500D$ domain length. The obtained results were then compared with the data described in the literature for a $50D$ length mesh, allowing to infer which is the impact of the mesh size into the obtained results.

Finally, it was studied the phenomena generated by a flow around a cylinder with two degrees of freedom. In order to validate this analysis, the obtained results for a $8D$ mesh were compared with the data described in the literature for a similar numeric study. The main difference obtained between both studies was the symmetry of the geometry of the

cylinder's oscillatory movement which was obtained by the current study whereas the comparative study showed an asymmetric movement of the cylinder. Given this data, it was hypothesised and proven that this fact was associated with the non-symmetry of the mesh used by the literature paper.

Subsequently, it was studied the influence of the mesh refinement level in the response given by the cylinder with two degrees of freedom. It was also analysed how the size of the mesh domain influences the response given by the cylinder with two degrees of freedom. Particularly, it was compared the geometry of the oscillatory motion and the temporal evolution of the respective lift coefficient between meshes with $8D$, $20D$, $500D$ and $2500D$ size.

RESUMO

As ferramentas de dinâmica dos fluidos computacional têm a capacidade de simular qual a influência que um dado escoamento tem ao interagir com um corpo. De facto, sem uma ferramenta de simulação, predizer qual o impacto que determinado escoamento tem na performance de dado produto é moroso e dispendioso. Este facto faz com que, em diversas áreas da engenharia, a análise virtual permita a redução do número de protótipos e os testes necessários para colocar um produto no mercado. Assim, é importante fornecer aos utilizadores de ferramentas de simulação na área de dinâmica dos fluidos ferramentas fáceis de usar, robustas e com processos validados. Com este objetivo em mente, a presente tese pretende estudar o fenómeno de vibrações induzidas por vórtices através da simulação de um escoamento em torno de um cilindro oscilatório.

Um escoamento ao passar por um corpo rômbico origina forças dinâmicas que provocam um conjunto de movimentos característicos deste fenómeno e que estão bem caracterizados na literatura. Para proceder à análise numérica deste fenómeno foi utilizado o OpenFOAM, este é um *software* de uso livre que se entendeu ser numericamente capaz de realizar uma análise suficientemente detalhada e correta deste fenómeno complexo. Tendo em conta os escassos estudos científicos sobre o fenómeno da vibração induzida por vórtices para um corpo com dois graus de liberdade, esta tese tem como objetivo a validação do *software* OpenFOAM para este caso de estudo, disponibilizando à comunidade científica a validação de uma nova ferramenta numérica para realizar estudos deste género. Para tal ser possível, começou por se estudar a independência da malha para o escoamento em torno de um cilindro fixo analisando qual a influência que a malha tem nas quantidades fundamentais, ou seja, o número de Strouhal, St , a média do coeficiente de arrasto, $C_{D,mean}$, e a raiz do valor quadrático médio dos coeficientes de arrasto, $C_{D,rms}$, e de sustentação, $C_{L,rms}$.

De seguida, foi efetuado o estudo do escoamento em torno de um cilindro com um grau de liberdade. Foi analisada a resposta dada pelo cilindro para dois tipos de sistemas, sistema massa-mola e sistema massa-mola-amortecedor para uma malha de domínio $2500D$. Os resultados obtidos foram posteriormente comparados com dados descritos na literatura para uma malha de domínio $50D$, possibilitando averiguar qual o impacto do tamanho da malha nos resultados obtidos.

Por fim, foi estudado o escoamento em torno do cilindro com dois graus de liberdade.

De modo a validar esta análise, os resultados obtidos para uma malha de domínio $8D$ foram comparados com os dados descritos na literatura para um estudo semelhante. A maior diferença entre os resultados de ambos os estudos foi a simetria do movimento oscilatório do cilindro que foi obtida para o presente estudo enquanto que o estudo comparativo apresentou um movimento assimétrico do cilindro. Com isto, foi proposto e demonstrado que este facto está associado com a não-simetria da malha utilizada pelo artigo da literatura.

Posteriormente, foi estudada a influência do nível de refinamento da malha na resposta dada pelo cilindro com dois graus de liberdade. Foi também analisado como a dimensão do domínio da malha influencia a resposta dada pelo cilindro com dois graus de liberdade. Em particular, foi comparada a geometria do movimento oscilatório e a respetiva evolução temporal do coeficiente de sustentação entre as malhas com dimensão $8D$, $20D$, $500D$ e $2500D$.

CONTENTS

List of Figures	xv
List of Tables	xix
Acronyms	xxi
Nomenclature	xxiii
1 Introduction	1
1.1 Context and motivation	1
1.2 Problem formulation	2
1.3 Original contributions	3
1.4 Thesis layout	3
2 Theoretical contextualization	5
2.1 Fundamentals of a flow around a circular cylinder	5
2.1.1 Disturbed regions in a circular cylinder	6
2.1.2 Transition in disturbed regions	6
2.1.3 Types of the flow states	7
2.1.3.1 Laminar state of flow, L	7
2.1.3.1.1 "Creeping" flow, $L1$	8
2.1.3.1.2 Steady separation regime, $L2$	10
2.1.3.1.3 Periodic laminar regime, $L3$	11
2.1.3.2 Transition-in-wake state, TrW	14
2.1.4 Vortex shedding and vortex patterns	17
2.1.5 Response modes for a cylinder with one-degree-of-freedom in transverse motion, Y-only	20
2.1.6 Response modes for a cylinder with two-degrees-of-freedom in XY-motion	23
2.2 Fundamentals of Vibration	27
2.2.1 Two-Degree-of-Freedom Systems	29
2.2.2 Equations of XY-motion and existence of a critical mass	32

2.3	Computational Fluid Dynamics: mathematical equations modelling the fluid flow	34
2.3.1	Finite Volume Method	35
2.3.2	Conservation of Mass	36
2.3.3	Conservation of Linear Momentum	36
2.3.4	Conservation of Energy	36
2.3.5	Newtonian Fluids	37
2.3.6	The Navier-Stokes Equation	37
3	Numerical modelling methodology	39
3.1	Mesh generation using Gmsh	40
3.1.1	Important mesh parameters	40
3.1.2	Mesh geometry	42
3.1.3	State-of-the-art: mesh generation tools	42
3.2	Computational fluid dynamics analysis using OpenFOAM	43
3.2.1	Finite volume mesh	45
3.2.2	The PIMPLE Algorithm	46
3.2.3	Case study setup - OpenFOAM File System overview	46
3.2.3.1	CaseStudy/0 folder - initial conditions	46
3.2.3.2	CaseStudy/constant folder - initial conditions	48
3.2.3.3	CaseStudy/system folder - system parameters	48
3.2.4	State-of-the-art: computacional fluids dynamics tools	48
3.3	Numerical Stability	49
3.4	Simulations preformance	50
4	Flow around a fixed cylinder	51
4.1	Independence mesh study	51
4.1.1	Analysis of the fundamental quantities convergence with the 2500D mesh discretisation	51
4.1.2	Analysis of the fundamental quantities convergence with the time step for a mesh with 2500D domain length	56
4.1.3	Analysis of the fundamental quantities convergence with the domain length	57
4.1.4	Analysis of the fundamental quantities convergence with the 8D mesh discretisation	59
4.2	Flow around a non-oscillatory cylinder	59
5	Flow around a Y-only motion cylinder	63
5.1	Comparative study between a 50D and a 2500D domain length mesh . .	63
5.1.1	Mass-Spring system	67
5.1.2	Mass-Spring-Damping system	78

6	Flow around a two degrees-of-freedom cylinder	89
6.1	Two degrees-of-freedom cylinder with a $8D$ mesh size	89
6.1.1	Asymmetric 8-motion	97
6.2	Distinct oscillation cylinder geometries for different levels of mesh refinement	103
6.2.1	$8D$ for second level of refinement	103
6.2.2	$8D$ for third level of refinement	108
6.3	Distinct oscillation cylinder geometries for different mesh dimensions . .	112
6.3.1	Mesh with $20D$	113
6.3.2	Mesh with $500D$	118
6.3.3	Mesh with $2500D$	124
6.3.4	Comparison of the cylinder displacement amplitude between the $8D$, $20D$, $500D$ and $2500D$ meshes	130
7	Conclusions	133
7.1	Future Work	136
	Bibliography	137
A	Results obtained by T. Li and Zhu (2009) for a cylinder with XY-motion	143

LIST OF FIGURES

2.1	Disturbed flow regions, Zdravkovich (1997).	6
2.2	Transitions in disturbed regions: (a) TrW , (b) $TrSL$, (c), (d) $TrBL$ (BL=boundary layer, L=laminar, T=turbulent, Tr=transition, S=separation), Zdravkovich (1997).	7
2.3	Creeping flow for $Re = 1$, Camichel and Escande (1938).	9
2.4	Flow field around a stationary circular cylinder at $Re = 3.5$, Wieselsberger (1921).	9
2.5	Steady closed near-wake at $Re = 23$, Thom (1933).	10
2.6	Metamorphose of near wake with Re between 20 and 40, Camichel et al. (1927).	11
2.7	Begin of oscillating wake for $Re = 54$, Homann (1936).	11
2.8	Development of near-wake oscillation with the increase of Re from 30 to 60, Camichel et al. (1927).	12
2.9	$St-Re$ relationship non-linear in the laminar periodic regime, $L3$, Zdravkovich (1985).	13
2.10	Roshko's number variation in terms of Re , Zdravkovich (1997)	14
2.11	Effect of number of end cells on St , Williamson (1988, 1989).	15
2.12	Consecutive formation of fingers, $Re = 180$, Gerrard (1978).	16
2.13	Variation of St in terms of Re , Roshko (1954c).	16
2.14	(a) Laminar periodic wake at $Re = 140$; (b) transitional periodic wake at $Re = 300$, Freymuth (1985).	17
2.15	Variation of St in terms of Re . Insert: frequency spectra at $Re = 172$, Zdravkovich (1997).	18
2.16	Representation of one third of one cycle of vortex shedding of the oscillation sequence of pressure field in $Re = 1.12 \times 10^5$, Blevins (1977).	19
2.17	Vortex formation near to the cylinder, Mayes et al. (2003).	19
2.18	Diagram of the vortex shedding patterns described in figure 2.19. P corresponds to a vortex pair and S to a single vortex, being each pattern defined by the number of pairs and single vortices formed per cycle. The dashed lines encircle the vortices shed in one complete cycle. Williamson and Roshko (1988).	21
2.19	Map of vortex synchronization regions in the wavelength-amplitude (λ/D , A/D) plane, Williamson and Roshko (1988).	22

2.20	Map of vortex synchronization regions in the wavelength-amplitude (λ/D , A/D) plane, Williamson and Roshko (1988).	23
2.21	Transverse and streamwise amplitudes (A_Y^* and A_X^*) and frequency (f_Y^*) response in function of the reduced velocity (U^*) for moderate mass ratios, $m^* = 7.0$. Solid symbols correspond to Y-only data and open symbols to XY data. $Re = 2000 - 11000$. Jauvtis and Williamson (2003).	24
2.22	<i>Griffin</i> plot of the transverse amplitude peak variation (A_{Ymax}^*) with the combined mass-damping parameter ($m^* + C_A$) ζ , for moderate mass ratios, $m^* = 6 - 25$. Jauvtis and Williamson (2003).	25
2.23	Transverse and streamwise amplitudes (A_Y^* and A_X^*) and frequency (f_Y^*) response in function of the reduced velocity (U^*) for low mass ratios, $m^* = 2.6$. Solid symbols correspond to Y-only data and open symbols to XY data. $Re = 2000 - 11000$. Jauvtis and Williamson (2003).	26
2.24	Transverse and streamwise amplitudes (A_Y^* and A_X^*) and frequency (f_Y^*) response in function of the reduced velocity (U^*) for low mass ratios, $m^* = 2.6$. Solid symbols correspond to Y-only data and open symbols to XY data. $Re = 2000 - 11000$. Jauvtis and Williamson (2003).	27
2.25	<i>Griffin</i> plot of the transverse amplitude peak variation (A_{Ymax}^*) with the combined mass-damping parameter ($m^* + C_A$) ζ for low mass ratios, $m^* = 2.5 - 4$. Jauvtis and Williamson (2003).	28
2.26	Schematic diagram of XY-motion in a spring-mass-damping system.	30
3.1	Representation of the developed mesh with $2500D$, full domain.	42
3.2	Representation of the mesh with $2500D$, near to the cylinder wall.	43
3.3	OpenFOAM structure extracted from OpenFOAM User Guide Guide (2011).	45
3.4	OpenFOAM File System overview.	47
4.1	Drag, $C_{D,mean}$, and lift, $C_{L,rms}$, coefficients for the set of meshes shown in table 4.1.	56
4.2	(a) Evolution of the St with the time step; (b) Relation between the $C_{D,mean}$ convergence with the time step; (c) Relation between the $C_{D,rms}$ convergence with the time step; (d) Relation between the $C_{L,rms}$ convergence with the time step. Values for the mesh 1 with $2500D$ domain length and $Re = 200$	57
4.3	(a) Evolution of the St with the domain length variation for $Re = 200$; (b) Relation between the $C_{D,mean}$ convergence with the domain length variation for $Re = 200$; (c) Relation between the $C_{L,rms}$ convergence with the domain length variation for $Re = 200$	58
4.4	(a) Spectral analysis of the fixed cylinder; (b) Drag and lift coefficients, C_D and C_L , time series for Mesh 1.	60

4.5	(a) Velocity field near to the cylinder for $time = 140(s)$; (b) Pressure field near to the cylinder for $time = 140(s)$; (c) Vorticity for $time = 140(s)$; (d) Streamlines near to the cylinder for $time = 140(s)$	61
5.1	Mass-spring system schematic diagram.	67
5.2	Displacement, lift and drag coefficients curves of an Y-motion cylinder for a certain frequency ratio.	72
5.3	Relation between the cylinder displacement and the simulated velocity ratios for the current study (squares in red) and the analysis performed by Conde and Lopes (2015) (circles in black). The dashed lines represent the value of the parameter for the fixed cylinder in both studies in comparison.	78
5.4	Mass-spring-damping system schematic diagram.	79
5.5	Displacement, lift and drag coefficients curves of an Y-motion cylinder for a certain frequency ratio.	83
5.6	Relation between the cylinder displacement and the simulated velocity ratios for the current study (squares in red) and the analysis performed by Conde and Lopes (2015) (circles in black). The dashed lines represent the value of the parameter for the fixed cylinder in both studies in comparison.	87
6.1	XY-motion plot of an elastic cylinder for a set of frequency ratio whit an $8D$ mesh.	97
6.2	Representation of the asymmetric mesh with $8D$, near to the cylinder wall. .	98
6.3	XY-motion plot of an elastic cylinder for a set of frequency ratios with an asymmetric $8D$ mesh.	102
6.4	XY-motion plot of an elastic cylinder for a set of frequency ratios for an $8D$ mesh for the second level of refinement studied.	108
6.5	XY-motion plot of an elastic cylinder for a set of frequency ratios for an $8D$ mesh for the third level of refinement studied	112
6.6	XY-motion plot of an elastic cylinder for a set of frequency ratios for the $20D$ mesh.	118
6.7	XY-motion plot of an elastic cylinder for a set of frequency ratios for the $500D$ mesh.	124
6.8	XY-motion plot of an elastic cylinder for a set of frequency ratios for the $2500D$ mesh.	130
6.9	Y maximum cylinder displacement after the cylinder displacement stabilization for the $8D$, $20D$, $500D$ and $2500D$ meshes	131
6.10	X maximum cylinder displacement after the cylinder displacement stabilization for the $8D$, $20D$, $500D$ and $2500D$ meshes	132
6.11	X maximum cylinder initial displacement between the $8D$, $20D$, $500D$ and $2500D$ meshes.	132

A.1	Obtained results by T. Li and Zhu (2009) for XY-motion of an elastic cylinder for a set of frequency ratio and respective displacement and lift coefficient curves.	146
-----	---	-----

LIST OF TABLES

2.1	Disturbance-free flow regimes around a circular cylinder, Zdravkovich (1997). L_w = length of near-wake (only for $L2$ regime), L_f = length of eddy formation region (from $L3$ to $T2$ regimes), C_D Drag coefficient. Abbreviations: \nearrow in- crease, \searrow decrease, \downarrow rapid decrease, (?) unknown.	8
2.2	Separation Reynolds number, Re_s	10
2.3	Re_{osc} according to various authors.	13
2.4	Principal non-dimentional parameters for the analysis of the flow cylinder displacement, Blevins (1977); Khalak and Williamson (1999).	32
3.1	Gmsh commands used in the meshes generation.	41
3.2	Gmsh alternative software to perform mesh generation.	44
3.3	OpenFOAM alternative softwares to perform numerical fluid simulation. . .	49
3.4	Specifications of the machine used to performed the Computational Fluid Dynamics (CFD) simulations.	50
4.1	Relation between the fundamental quantities convergence with the discretiza- tion variation for meshes with $2500D$ domain length and $Re = 200$	53
4.2	Relation between the fundamental quantities convergence with the time step variation for the mesh 1 with $2500D$ domain length and $Re = 200$	56
4.3	Relation between the flow fundamental quantities convergence with the do- main length, L_b , and $Re = 200$	58
4.4	Relation between the fundamental quantities convergence with the discreti- sation variation for meshes with $8D$ domain length and $Re = 200$	59
4.5	Comparison of fundamental quantities obtained in this thesis with the data described in the literature for a flow around a fixed cylinder, $Re = 200$	60
5.1	Cylinder properties.	64
5.2	Flow properties.	64
5.3	Simulation parameters for the mass-spring and mass-spring-damping systems to the cylinder with Y-only motion.	64
5.4	Obtained results to mass-spring system to cylinder with Y-only motion. . . .	67
5.5	Obtained results for the mass-spring system for the cylinder with Y-only mo- tion.	75

5.6	Obtained results to mass-spring-damping system to cylinder with Y-only motion.	85
6.1	Simulation parameters for the cylinder with XY-motion.	91
6.2	Geometric parameters of the $8D$ mesh.	91
6.3	Geometric parameters of the asymmetric $8D$ mesh.	98
6.4	Geometric parameters for second level of refinement in the $8D$ mesh.	103
6.5	Fundamental quantities and 8-motion last cycle of the $8D$ mesh.	104
6.6	Geometric parameters for third level of refinement in the $8D$ mesh.	108
6.7	Fundamental quantities and 8-motion last cycle of the $20D$ mesh.	113
6.8	Geometric parameters of the $20D$ mesh.	114
6.9	Fundamental quantities and 8-motion last cycle of the $500D$ mesh.	119
6.10	Geometric parameters of the $500D$ mesh.	120
6.11	Fundamental quantities and 8-motion last cycle of the $2500D$ mesh.	125
6.12	Geometric parameters of the mesh $2500D$	126

ACRONYMS

CFD Computational Fluid Dynamics.

DOF Degree Of Freedom.

FFT Fast Fourier transform.

FVM Finite Volume Method.

PIMPLE Pressure-Implicit Method for Pressure-Linked Equations.

PISO Pressure Implicit Splitting of Operators.

SIMPLE Semi-Implicit Method for Pressure-Linked Equations.

VIV Vortex Induced Vibration.

NOMENCLATURE

δt	Time-step
δx	Mesh cell size in the direction of the velocity
$\frac{A}{D}$	Adimensional amplitude
$\frac{D}{B}$	Wall blockage parameter
$\frac{e}{D}$	Thickness of the first element along the cylinder wall
ν	Kinematic viscosity
ρ	Density
ζ	Damping coefficient
A	Oscillation amplitude
a_1	Length of the mesh cell first node
B	Distance between two parallel walls of the domain
C_A	Ideal added mass coefficient
$C_{D,mean}$	Drag coefficient mean
$C_{D,rms}$	Drag coefficient root mean square
C_D	Drag coefficient
$C_{L,rms}$	Lift coefficient root mean square
C_L	Lift coefficient
Co	Courant number
D	Cylinder diameter
f	Frequency of vortex shedding
f_n	Natural frequency

NOMENCLATURE

f_{st}	Strouhal frequency
k	Stiffness
L_f	Length of eddy formation region
L_w	Length of near-wake
m	Mass
m^*	Mass ratio
n	Number of radial nodes
N_{ang}	Number of elements around the cylinder
N_{rad}	Number of elements in the radial direction
p	Local pressure
p_∞	Free stream static pressure
r	Progression value of the mesh cells
Re	Reynolds number
Ro	Roshko number
S_n	Mesh radial distributed nodes length
St	Strouhal number
t	Time
T_e	Cylinder oscillation period
U	Velocity magnitude
U^*	Reduced velocity
U_∞	Free stream velocity

INTRODUCTION

1.1 Context and motivation

Engineering had a decisive role in the development of mankind, contributing to a number of innovations that had enabled the twenty-first century way of life. Constantly struggling with new challenges, engineering is in a permanent search of innovative approaches to address those challenges. Particularly, in terms of mechanical structures, the materials have been stretched more frequently for its mechanical limits. With greater exigency levels, new materials with higher levels of flexibility, strength and lightness have been emerging to meet the demands of increasingly ambitious projects. Similarly, in recent times, many investigations have been motivated by the engineering applications of vibration, such as the design of machines, foundations, structures, engines, turbines, and control systems. The development of these novel technologies is closely related with the understanding of the physical phenomenon that they will be subjected to.

In CFD one of the most studied phenomenon is the flow around a circular cylinder. This phenomenon became a subject of special interest in this area after it was understood that it was not as trivial as thought to the date. In fact, it was realized that involved complex physical aspects and was related with some interesting and particular details, like the development of vortex shedding in unsteady flow, Williamson and Govardhan (2004).

The flow around a circular cylinder is usually studied in the Vortex Induced Vibration (VIV) context. There are a wide number of scientific studies where is performed the numerical simulation of VIV around a circular cylinder with no degrees of freedom. There are also some work for one Degree Of Freedom (DOF), particularly, for a flow which direction is orthogonal to the cylinder displacement. Regarding the study of a flow around a cylinder with two DOF, problem which is intended to validate in this thesis,

there are a scarce number of articles focusing the numerical simulation of this kind of problem.

These studies are important to better understand how aerodynamic and hydrodynamic environments influence structures fatigue damage and stability. An example of how crucial these studies are, was the collapse of Tacoma Bridge, built in 1940 in the United States of America, Billah and Scanlan (1991). This bridge caved in only two months after its inauguration due to vortex induced vibrations. More specifically, vortex shedding induced the development of vortices on the back side of the bridge. As the wind increased in speed, vortices were formed on alternate sides of the downwind side which, eventually, broke loose and flew downstream exerting fluctuating vertical forces on the bridge even though the wind was blowing across it in a transverse, horizontal direction. The oscillating forces induced by the vortex shedding were increasingly higher with each cycle because the wind energy was higher than the flexing of the structure was able to dissipate and, finally, drove to the bridge failure due to excessive deflection and stress.

Thus, examples of structures subjected to vortex induced vibrations phenomenon are bridges, high-rise buildings, high voltage towers, industrial chimneys, wind turbines, underwater structures, offshore platforms, ship hulls, drilling and production risers in petroleum exploration, pipelines networks such as pipelines or structures involving different types of cables like electric networks or suspended structures.

Whenever the natural frequency of vibration of a machine or structure coincides with the frequency of the external excitation, there occurs a phenomenon known as resonance, which leads to excessive deflections and failure, as the one that occurred in Tacoma bridge. Therefore, due to the devastating effects that vibrations can have on machines and structures, vibration testing has become a standard procedure in the design and development of most engineering systems. With this interest comes the need for numerical tools with the power to perform a detailed analysis of this kind of phenomena and, at the same time, affordable enough to perform an efficient study.

In this context, the development of this work aims to validate the numerical code of the OpenFOAM *software*. This is an open source tool, which is understood to be strong enough for the numerical simulation of a flow around a cylindrical section with two DOF.

1.2 Problem formulation

The main goal of this thesis is to perform a numerical study of a flow around a cylindrical section with two DOF. With this purpose, it was firstly performed an OpenFOAM analysis for a flow around a stationary cylinder, this is, in a zero DOF conformation. The obtained results were compared with the data described in the literature so the used methodology as well as the obtained results could be validated. At this point, it was also studied how the mesh configuration could influence the obtained numerical results. To perform this analysis, meshes with domain O-type were developed and for each domain type were created three levels of refinement with quadrilateral elements. It was, then,

performed a comparison study between the developed meshes. Comparing its dimensionless parameters values, the simulation performance, and the obtained results with the literature data it was possible to conclude which one of these meshes configurations was the best fit to proceed the analysis of the flow around a cylinder with one and two DOF.

Subsequently, it was studied the VIV phenomena in a circular body with one DOF for a Y axis motion. For this scenario, it was evaluated the cylinder perpendicular displacement towards the flow direction.

Finally, it was studied the VIV for a circular cylinder with two DOF.

For the three cases enumerated above, the results validation was performed by comparing the obtained results with the data described in the literature.

1.3 Original contributions

This thesis validates the use of OpenFOAM for the numerical study of a flow around a cylindrical section in the two DOF scenario. The validation of this tool becomes important in the development of the computational fluid dynamics area, as it validates an alternative tool to the traditional, expensive and inaccessible *software*. Demonstrating that this alternative tool has similar potential but, being open-source, can be easily available to anyone interested in performing this kind of study. Contributing, therefore, for the knowledge to increase in this area which has so many fascinating unexplored subjects.

1.4 Thesis layout

Apart from this introduction, this thesis is structured in six chapters. In chapter 2 are introduced the main theoretical topics related with the phenomena of a flow around a circular cylinder. Furthermore, in section 2.3 are detailed the mathematical equations modelling the flow displacement in CFD.

Chapter 3 describes the numerical modelling methodology used to simulate an unsteady flow around a circular cylinder. Namely, it is described the mesh generation process in section 3.1 and specified how the CFD analysis was set using OpenFOAM in section 3.2.

Then, in chapter 4 the CFD study of a flow around a non-oscillatory cylinder. Particularly, in section 4.1 is done a mesh independence study.

Afterwards, in chapter 5 it is studied a flow around a cylinder with one DOF. Particularly, it was performed an analysis for the mass-spring system in subsection 5.1.1 and for the mass-spring-damping system in subsection 5.1.2.

Lastly, in chapter 6 is described the numerical study of the flow around a circular cylinder for two DOF. The obtained result were compared with the ones described in literature in section 6.1. In section 6.2 is analysed the influence of the mesh refinement in the obtained results. Finally, in section 6.3 it was evaluated the influence of the domain size on the obtained results.

THEORETICAL CONTEXTUALIZATION

2.1 Fundamentals of a flow around a circular cylinder

A fluid flow around a stationary body or, similarly, a movement of a body in a fluid at rest originates a region of disturbed flow at the body boundaries. The extension of the affected region is largely influenced by the body shape, orientation and size and by the fluid velocity and viscosity. This relation is translated by the Reynolds number, Re , which is a dimensionless parameter that depends on the fluid density, ρ , velocity, U_∞ , cylinder external diameter which corresponds to the body characteristic length, D , and dynamic viscosity, μ .

$$Re = \frac{\rho U_\infty D}{\mu} \quad (2.1)$$

Bodies subjected to a fluid flow are classified as being streamlined or bluff, depending on their overall shape. Particularly, in this thesis context, we are interested in the interaction between a bluff structure and a subsonic flow. Bluff bodies are characterized by flow separation along a large section of the structure's surface, Bearman (1984). The primary purpose of these structures is to bear loads, contain flow or provide heat transfer structure and, since these structures are not designed to minimize drag, aerodynamic optimization is not usually a concern. Consequently, flow induced vibrations are generally considered as a secondary design parameter, at least until a failure occurs.

The flow structure around bluff bodies are characterized by a region of disturbed flow behind the body designated by the wake. Within the near-wake zone various forms of flow instabilities may be triggered and amplified. These instabilities are manifested by the generation of unsteady flow structures and eventually turbulence as the Reynolds number is progressively increased. The most well-known instability is that leading to the periodic development of vortices which produces a wake pattern named after von

Kármán street. Circular cross-section bodies such as cylinders are classified as bluff bodies since, as a result of its shape, generate particularly large and typically unsteady flow separation structures.

2.1.1 Disturbed regions in a circular cylinder

The flow disturbed regions are defined by the variation of its velocity magnitude, direction and time. In each region the disturbed flow is characterized by a greater, equal or minor velocity than the free stream velocity, Zdravkovich (1997). Figure 2.1 illustrates the flow different disturbed regions:

- i. narrow region of retarded flow;
- ii. boundary layers attached to the surface of the cylinder;
- iii. sidewise regions of displaced and accelerated flow;
- iv. wide downstream region of separated flow designated by the wake.

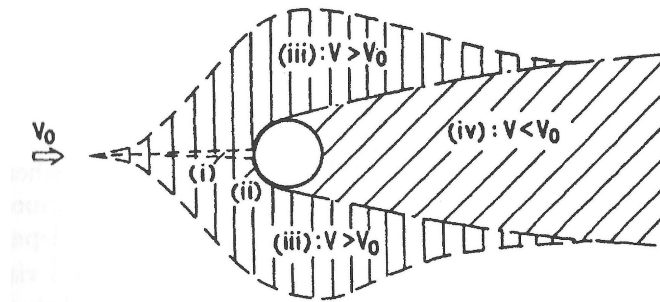


Figure 2.1: Disturbed flow regions, Zdravkovich (1997).

2.1.2 Transition in disturbed regions

The flow transition from laminar to turbulent state is given by the Reynolds number, Re , which represents the ratio between inertial and viscous forces defined by equation 2.1.

Laminar flow occurs for low Reynolds numbers, where viscous forces are dominant, and is characterized by smooth, constant fluid motion. Oppositely, turbulent flow occurs for high Reynolds numbers and is dominated by inertial forces, which tend to produce flow instabilities such as vortices.

For bluff bodies, the transition between laminar and fully turbulent flow states is characterized by a succession of changes in the various regions of the disturbed flow. Figure 2.2 shows the development of these transitions with Re in three disturbed regions: wake (TrW), shear layers ($TrSL$) and boundary layers ($TrBL$), Zdravkovich (1997).

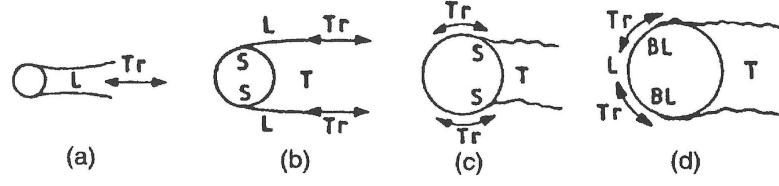


Figure 2.2: Transitions in disturbed regions: (a) TrW , (b) $TrSL$, (c), (d) $TrBL$ (BL=boundary layer, L=laminar, T=turbulent, Tr=transition, S=separation), Zdravkovich (1997).

The first disturbed region, designated by TrW , occurs in the wake and gradually spreads along it while the free shear layers bordering the near-wake remain laminar. The second transition, represented by $TrSL$, occurs in the free shear layers. This transition is characterized by the increasing of the Reynolds number along the free shear layers towards the separation and impacts the length and weight of the near-wake. For the third transition, $TrBL$, the flow is turbulent in the free-shear-layers and the remaining flow is in a transition state. The third transition is considered to be completed when all the regions of disturbed flow are fully turbulent. At this point, the stagnation point, where the fluid local velocity is zero, and the separation point, where the wall shear stress is equal to zero, are coincident.

2.1.3 Types of the flow states

The flow around a circular cylinder is an extremely complex phenomenon. Nevertheless, flow patterns are expected to be confined within a fixed range of Re for genuinely disturbance free flows, Zdravkovich (1997).

The flow states can be fully laminar, L , one of the three transitions TrW , $TrSL$ or $TrBL$, or fully turbulent, T . Each flow state can be described in a flow regime context depending on the Reynolds number. Table 2.1 enumerates the flow regimes for a flow around a circular cylinder.

The Reynolds number considered for the simulations developed in this work corresponds to $Re = 200$. For this reason, in the next subsections will be discussed the L and TrW flow regimes, the existent regimes until $Re = 200$. The remaining flow states and flow regimes will not be discussed in detail in this work, since they are not relevant in this thesis context.

2.1.3.1 Laminar state of flow, L

The laminar state of flow can be divided into three basic flow regimes:

$L1$: "Creeping" flow or non-separation regime; $0 < Re < 4$ to 5

$L2$: Steady separation or closed near-wake regime; 4 to $5 < Re < 30$ to 48

$L3$: Periodic laminar regime; 30 to $48 < Re < 180$ to 200

Table 2.1: Disturbance-free flow regimes around a circular cylinder, Zdravkovich (1997). L_w = length of near-wake (only for $L2$ regime), L_f = length of eddy formation region (from $L3$ to $T2$ regimes), C_D Drag coefficient. Abbreviations: ↗ increase, ↘ decrease, ↓ rapid decrease, (?) unknown.

State		Regime		Re Ranges	$\frac{L_w}{L_f}$	C_D
L	Laminar	1	No-separation	0 to 4-5	None	↘
		2	Closed wake	4-5 to 30-48	↗	↘
		3	Periodic wake	30-48 to 180-200	↘	↗
TrW	Transition in wake	1	Far-wake	180-200 to 220-250	↘	↗
		2	Near-wake	220-250 to 350-400	↗	↘
$TrSL$	Transition in shear layers	1	Lower	350-400 to 1k-2k	↗	↘
		2	Intermediate	1k-2k to 20k-40k	↘	↗
		3	Upper	20k-40k to 100k-200k	↘	↗
$TrBL$	Transition in boundary layers	0	Pre-critical	100k-200k to 300k-340k	↗	↘
		1	Single bubble	300k-340k to 380k-400k	(?)	↓
		2	Two-bubble	380k-400k to 500k-1M	(?)	↓
		3	Supercritical	500k-1M to 3.5M-6M	None	↗
		4	Post-critical	3.5M-6M to (?)	(?)	↗
T	Fully turbulent	1	Invariable	(?) to ∞	(?)	↗
		2	Ultimate	(?) to ∞	(?)	(?)

2.1.3.1.1 "Creeping" flow, $L1$

The "creeping" flow regime occurs for low Reynolds values and is dominated by viscous forces to such an extent that all disturbed regions remain laminar, as figure 2.3 shows. The creeping flow, $L1$, past a cylinder persists without separation up to $Re \approx 5$, Camichel and Escande (1938).

Figure 2.4 shows the streamlines and three velocity profiles superimposed at stations $-8D$, 0 , and $8D$. The retarded region of flow is very large, being almost $20D$ wide at the upstream station $-8D$. The thick shear layers displaced by the cylinder are not surrounded by the accelerated region as illustrated in figure 2.1. The sidewise divergence of all streamlines in figure 2.4 prevents the increase of velocity throughout the visible flow field. The velocity deficit at $8D$ downstream at the wake axis is around 50%. The cylinder is "pushing" and "dragging" a $20D$ wide trail by the action of large viscous forces.

The considerable divergence of streamlines downstream in figure 2.4 can be strongly influenced by the vicinity of side walls. White (1946) discovered that a cylinder confined in a $500D$ wide container was still affected by the side walls at low Reynolds.

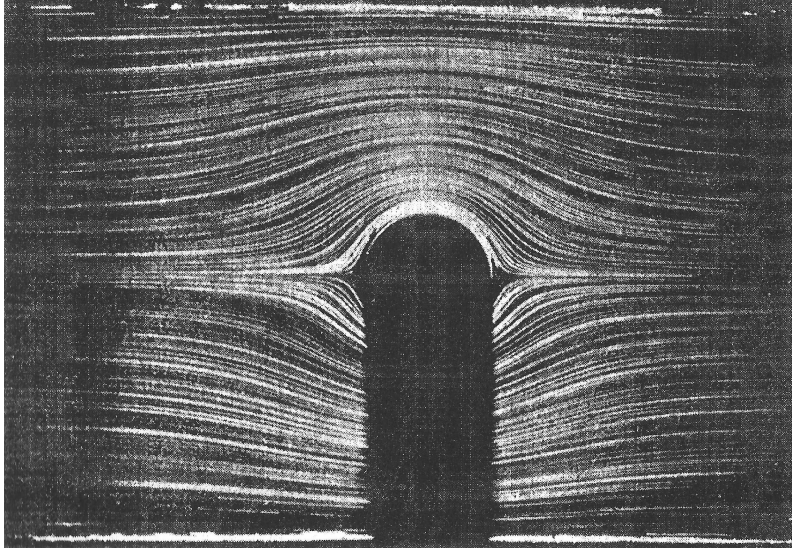


Figure 2.3: Creeping flow for $Re = 1$, Camichel and Escande (1938).

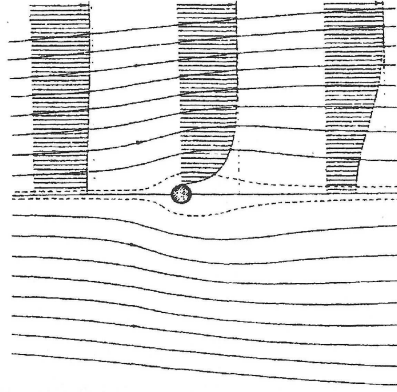


Figure 2.4: Flow field around a stationary circular cylinder at $Re = 3.5$, Wieselsberger (1921).

The velocity field around a circular cylinder at low Re is associated with the characteristic pressure distribution around the cylinder. The measured pressure is expressed in a non-dimensional parameter designed by pressure coefficient:

$$C_p = \frac{p - p_\infty}{\frac{1}{2}\rho V^2} \quad (2.2)$$

where p is the local pressure on surface, p_∞ is the free stream static pressure and $\frac{1}{2}\rho U^2$ is the free stream dynamic pressure. The circumferential angle is usually measured from the stagnation point, where $\theta = 0^\circ$ up to 180° .

A favourable pressure gradient extends until $\theta = 115^\circ$ at $Re = 3.5$ followed by a very small adverse pressure gradient that is insufficient to induce separation.

The viscous forces magnitude decreases with the Re increasing until the separation of the boundary layers occurs. When the separation of the boundary layers occurs the Reynolds value is designed by Re_s . The determination of the Re_s value is not trivial

because the size of the near-wake is small and the separation occurs in a region where the velocity is also very small. Nisi and Porter (1923) observed this separation by using smoke visualization and noted the strong effect of the blockage on Re_s . In table 2.2 are enumerated some estimated Re_s values and the respective wall blockage parameter, $\frac{D}{B}$, where D corresponds to the cylinder diameter and B to the distance between two parallel walls of the domain.

Table 2.2: Separation Reynolds number, Re_s .

Authors	$\frac{D}{B}$	Re_s
Nisi and Porter (1923)		4.3
Homann (1936)	0.067	6.0
Taneda (1956)	0.01	5-6
Coutanceau and Bouard (1977)	0.12	9.6
	0.07	7.2
	0.00	4.4

2.1.3.1.2 Steady separation regime, $L2$

For $Re > 4 - 5$, starts a new laminar flow regime. This flow regime occurs until $Re < 30 - 48$ and is characterized by the development of a steady region confined in a closed and symmetric near-wake, marked by a noticeable change in pressure distribution. As it is possible to conclude from figure 2.5, the separation of the shear layers merge the wake and make a symmetric, steady and closed near-wake.

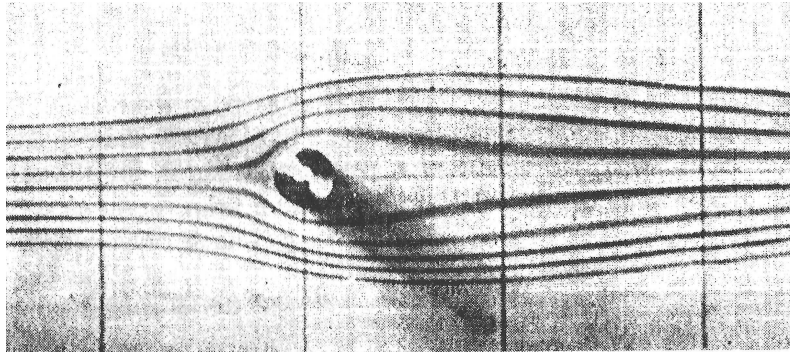


Figure 2.5: Steady closed near-wake at $Re = 23$, Thom (1933).

Camichel et al. (1927) demonstrated in figure 2.6 a remarkable metamorphose of the near-wake when Re is increased from 20 to 40, where image 1 illustrates the answer for the lowest Re value of 20. Images 1, 2 and 3 from figure 2.6 illustrate the elongation and images 4 and 5 the obliteration of the initially closed near-wake. The development

of a new near-wake is accomplished by a secondary separation of the free shear layers from the near-wake, phenomena illustrated in images 4, 5 and 6. In image 9 is shown the approximation and, finally, the merge of the separated shear layers. The last image, image 10, shows the steady near-wake at $Re = 40$.

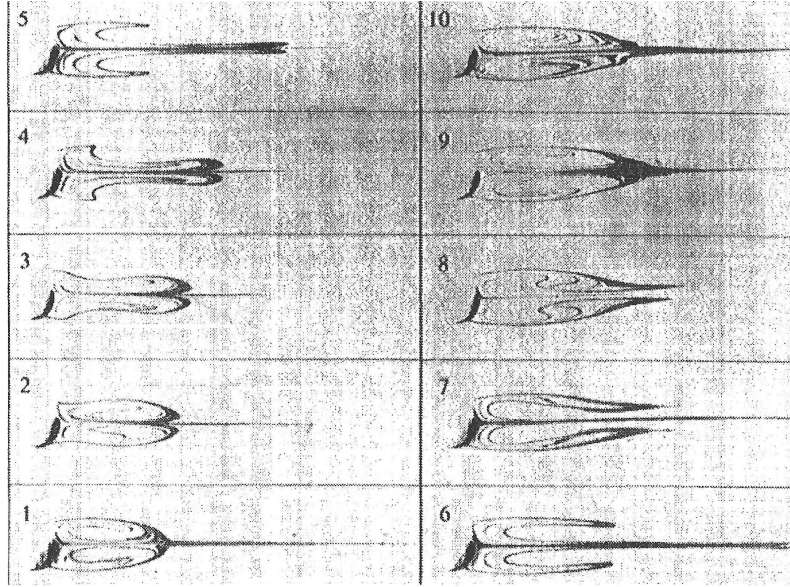


Figure 2.6: Metamorphose of near wake with Re between 20 and 40, Camichel et al. (1927).

2.1.3.1.3 Periodic laminar regime, $L3$

The steady, elongated and closed near-wake becomes unstable when $Re > Re_{osc}$, which occurs for $Re > 30 - 48$. The transverse oscillation begins at the end of the near-wake and initiates a wave along the trail as shown in figure 2.7, Homann (1936). The maximum adverse gradient also occurs around the confluence point at the near-wake end, where the instability starts. The coincidence between the location of the instability and the adverse pressure gradient suggests their correlation.

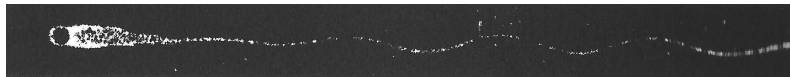


Figure 2.7: Begin of oscillating wake for $Re = 54$, Homann (1936).

Camichel et al. (1927) were the first to observe the initiation of the near-wake instability when Re increases from 30 to 60, phenomena illustrated in figure 2.8. The initiation of the near-wake instability is characterized by the development of "secondary separations" of the free shear layers from the near-wake boundary accompanied by the transverse oscillation of the trail. These secondary separations prevent the free shear layers from meeting at the confluence point as they do behind the steady and closed near-wake.

Taneda (1956) called the spiky ends in figure 2.8 by "gathers". He stated that "the gathers first appear for $Re > 35$ near the downstream end of the near-wake border-line, move towards the rear end of the near-wake, tremble there for a while and die away". Also, he referred that the trail began to oscillate sinusoidally before the gathers were formed, meaning that the former induced the latter. Contrary to that, Gerrard (1978) observed that the periodic appearance of gathers resulted in a wavy trail.

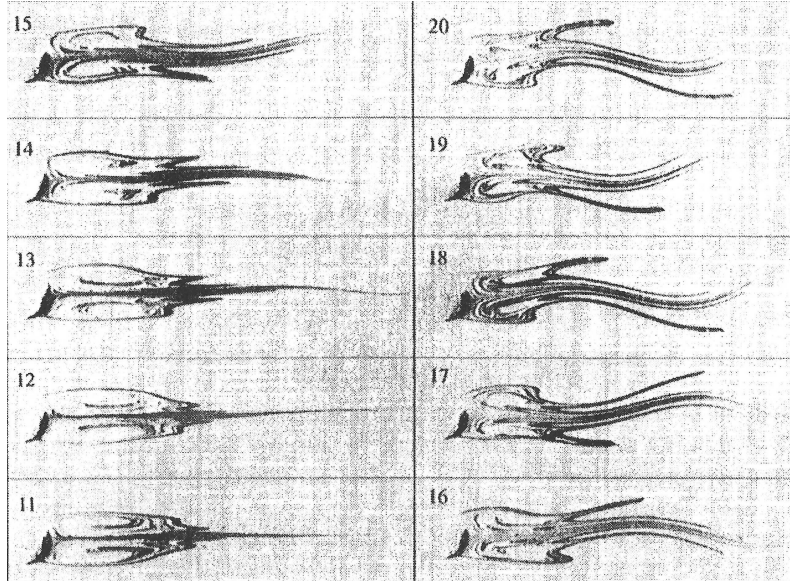


Figure 2.8: Development of near-wake oscillation with the increase of Re from 30 to 60, Camichel et al. (1927).

Figure 2.8 illustrates the near-wake oscillation with the increase of Re from 30 to 60 from image 11 to 20, respectively. Analysing figure 2.8, is visible a gradual reduction in length of the closed near-wake from $\frac{L_w}{D} = 3.5$ to 2 and a continuous increase in amplitude of oscillation at the end of the near-wake from 0 to $\frac{1}{2}D$, where L_w represents the wake length and D the cylinder diameter. Nishioka and Sato (1978) found a gradual and continuous reduction of $\frac{L_w}{D}$ for $40 < Re < 120$ while Gerrard (1978) reported a sudden shrink between $60 < Re < 70$.

There is a wide range of reported Re_{osc} values at which the near-wake instability initiates even when the blockage is negligible. The flow visualisation data tend to be on the lower side and hot-wire anemometry measurements on the higher side as shown in table 2.3. The latter may be due to insensitivity of a single hot wire to a periodic change in velocity direction. Furthermore, Kovasznay (1949) reported that Re_{osc} did not show a hysteresis effect, this means that the same value was found when increasing or decreasing the velocity magnitude.

The instability of the near-wake begins when $Re > Re_{osc}$. Also, when the blockage effect is negligible, some disparity is observed in the obtained results for the Re_{osc} values between some authors, as it can be observed in table 2.3.

The frequency of eddy shedding was investigated by Strouhal (1878), who created a

2.1. FUNDAMENTALS OF A FLOW AROUND A CIRCULAR CYLINDER

Table 2.3: Re_{osc} according to various authors.

Method	Author(s)	Re_{osc}
Flow visualization	Taneda (1956)	30
	Coutanceau and Bouard (1977)	34
	Gerrard (1966)	33
Hot-wire anemometry	Kovaszny (1949)	40
	Roshko (1954a)	40
	Nishioka and Sato (1978)	48

dimensionless parameter which describes oscillating flow mechanisms. This parameter was later designed by the Strouhal number:

$$St = \frac{fD}{U} \quad (2.3)$$

where f is the frequency of vortex shedding, D is the characteristic length of the cylinder and U is the free stream velocity.

Zdravkovich (1985) adapted from Strouhal the measured variation of St in terms of Re , fact illustrated in figure 2.9.

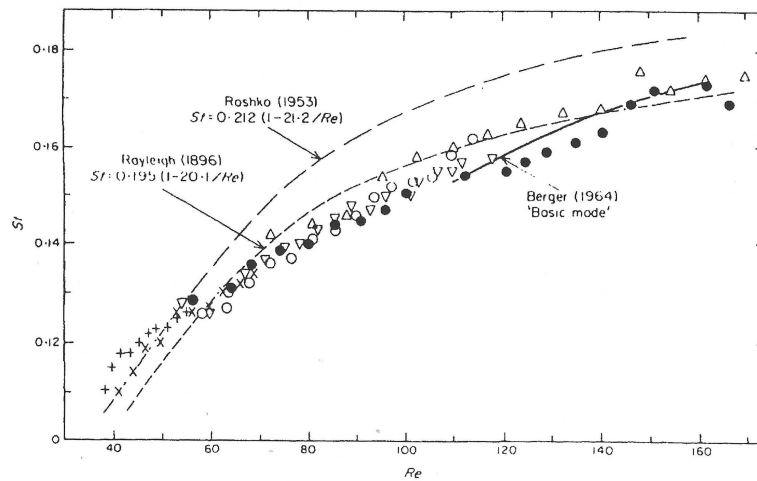


Figure 2.9: $St-Re$ relationship non-linear in the laminar periodic regime, L3, Zdravkovich (1985).

Roshko (1954b) suggested a new dimensionless parameter, where ν corresponds to the kinematic viscosity:

$$Ro = \frac{fD^2}{\nu} \quad (2.4)$$

that makes the following linear relationship $Ro - Re$:

$$Ro = 0.212.Re - 21.2 \quad (2.5)$$

this linear relation between the eddy frequency and the velocity is illustrated in figure 2.10 and can be used to measure very low velocity values.

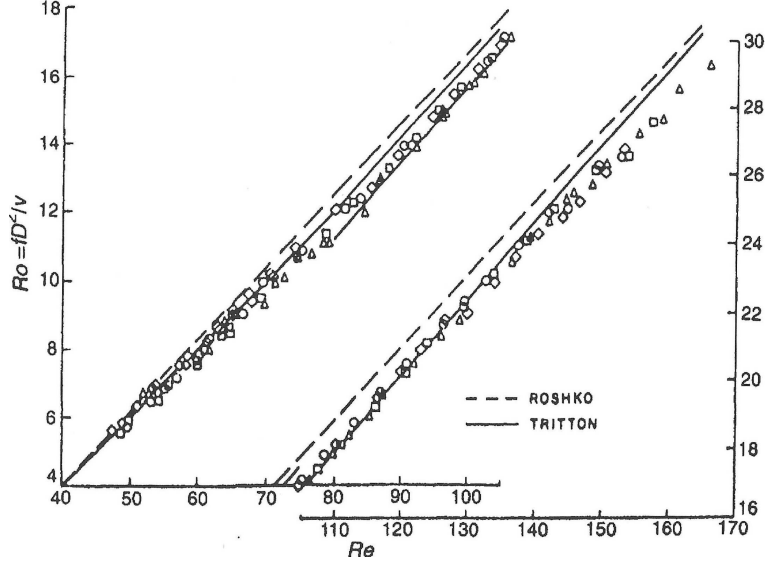


Figure 2.10: Roshko's number variation in terms of Re , Zdravkovich (1997)

Tritton (1959) discovered that for $Re = 80$ existed a discontinuous drop in shedding frequency using Roshko's relationship. Nevertheless, surprisingly he also discovered that the drag coefficient was not affected by this discontinuity. Williamson (1988, 1989) resolved this enigma when he proved that the discontinuity was caused by the transition from one slanted shedding mode to another slanted mode. Figure 2.11 shows the simultaneous measurements of the angle of the slanted eddy filament, β , and the Strouhal number, St , in terms of Re .

Williamson (1989) proved that the parallel shedding mode is the universal one. Any slanted eddy shedding, St , could be transformed into the universal mode St_u , by the trigonometric relation given by equation 2.6.

$$St_u = St \cos(\beta). \quad (2.6)$$

2.1.3.2 Transition-in-wake state, TrW

All laminar flows eventually become unstable above a certain Re and undergo transition to turbulent. The flow in a wake does not become fully turbulent as soon as it ceases to follow the laws of laminar flow. This transformation occurs in a finite transition region characterized by the random initiation and growth of irregularities. Furthermore, the viscous diffusion and mutual interaction of laminar eddies add a greater complexity to the periodic laminar wakes transition.

The transition-in-wake, TrW , state of flow may be divided into two flow regimes as is shown in table 2.1:

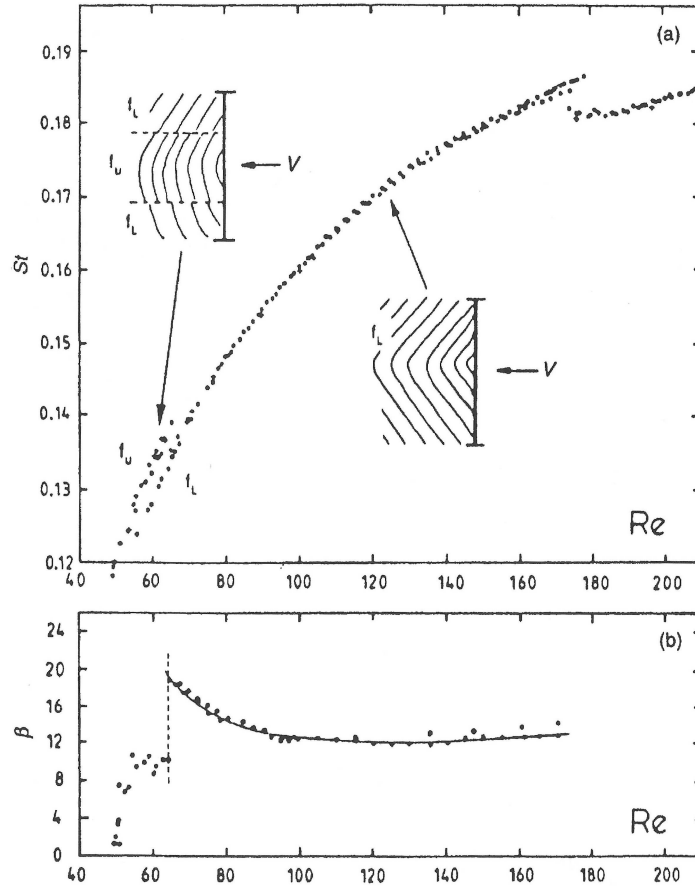


Figure 2.11: Effect of number of end cells on St , Williamson (1988, 1989).

TrW1 Lower transition regime, where the eddies are formed laminar and regular but become irregular and transitional downstream.

TrW2 Upper transition regime, where the eddies are formed laminar and irregular but become partly turbulent before they are shed and carried downstream.

Peculiar distortions of the laminar filaments adjacent to the cylinder are shown in figure 2.12. The development of these structures occurs when a flow in laminar state is close to the transition state. This phenomenon is related with distortions that are typically formed in the laminar eddy filaments at this point. These distortions were designated by fingers by Gerrard (1978) because they pointed towards the cylinder. Illustrated in figure 2.12 are two types of fingers, a finger of type A at $Re = 180$ and a second finger of type B at $Re = 230$.

Gerrard attempted to quantify the occurrence frequency of fingers of type A and B in terms of Re . At the lower end of *TrW1* and at the upper end of *TrW2* fingers A are predominant while at the boundary between *TrW1* and *TrW2* fingers B are more frequently formed. They appear in the range $150 < Re < 160$ and disappear in the range $300 < Re < 400$. The range of their appearance coincides with the transition between two

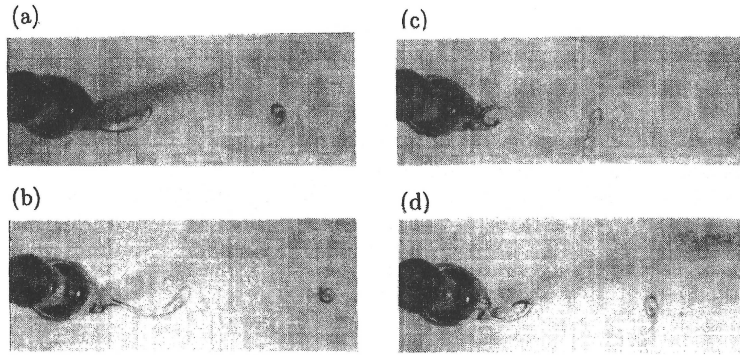


Figure 2.12: Consecutive formation of fingers, $Re = 180$, Gerrard (1978).

modes of eddy shedding. Roshko (1954c) repeated measurements of shedding frequency in a large low-turbulence wind tunnel and proposed the following ranges:

- i. Stable range, $40 < Re < 150$, regular velocity fluctuations and rising St .
- ii. Unstable range, $150 < Re < 300$, irregular bursts in velocity fluctuations, St unstable.
- iii. Irregular range, $Re > 300$, irregular and periodic, St is constant.

The figure 2.13 shows a particularly large scatter of experimental points in the TrW regime. The boundary between $TrW1$ and $TrW2$ is marked by a jump in St at $Re \approx 250$ which separates rising St from $St = constant$.

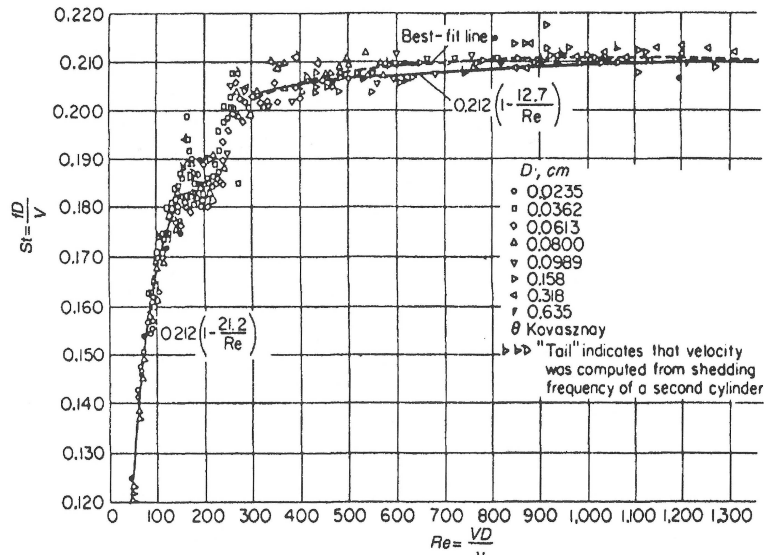


Figure 2.13: Variation of St in terms of Re , Roshko (1954c).

Roshko suggested two empirical relations:

$$\begin{aligned}
 St &= 0.212\left(1 - \frac{21.2}{Re}\right) \text{ for } Re < 180 \\
 St &= 0.212\left(1 - \frac{12.7}{Re}\right) \text{ for } Re > 300
 \end{aligned} \tag{2.7}$$

The two different St curves correspond to two different modes of eddy shedding.

Kovasznay (1949) noted that laminar eddies are not shed from the cylinder but rather formed gradually as they are carried downstream. He attributed this low-speed mode to the instability of the laminar wake. As an example of the low-speed mode, figure 2.14(a) shows the laminar periodic wake at $Re = 140$, which illustrates that all eddies are mutually connected by the trail streak-line originated in the near-wake. Figure 2.14(b) exhibits the salient features of high-speed mode at $Re = 300$ in $TrW2$ regime. In this figure the trail streamline is not seen and that means that the eddies are not mutually connected.

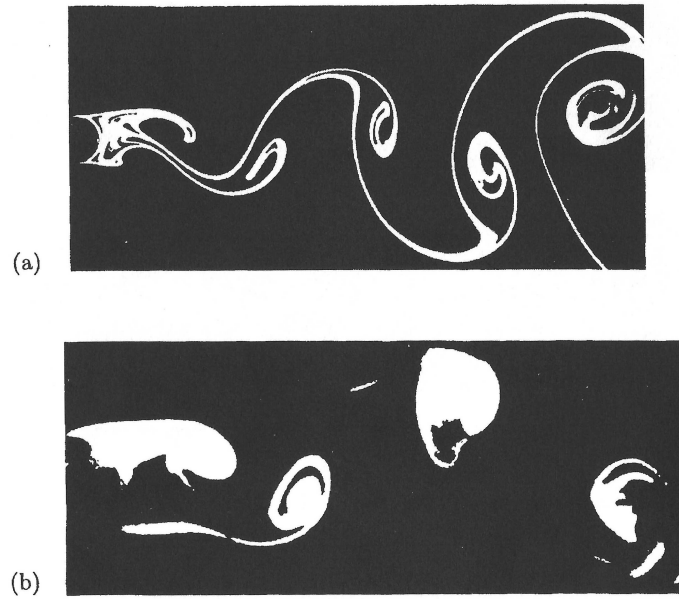


Figure 2.14: (a) Laminar periodic wake at $Re = 140$; (b) transitional periodic wake at $Re = 300$, Freymuth (1985).

In Zdravkovich (1997) it was referred the existence of two discontinuities in the $St-Re$ relationship. Figure 2.15 shows a rising St up to the first discontinuity at $Re = 170$. A narrow frequency peak is showed in figure 2.15 when Re increases and a wide frequency peak at a slightly lower value of St when Re decreases. A possible explanation for the lower value of St when Re decreases, is the occurrence of the hysteresis effect in the fingers formation. The second discontinuity in St occurs between, $225 < Re < 270$. Two suggestions were made to explain this. The first was provided by Williamson (1989) who proposed that they do not coexist simultaneously. The other suggestion was presented by Zdravkovich (1992) who affirmed that the two peaks represent the overlapping of two modes of eddy shedding, and both may exist simultaneously.

2.1.4 Vortex shedding and vortex patterns

Periodic forces in the cylinder generate alternated vortices, which are released successively from each cylinder side. The oscillatory pressure field is responsible for the

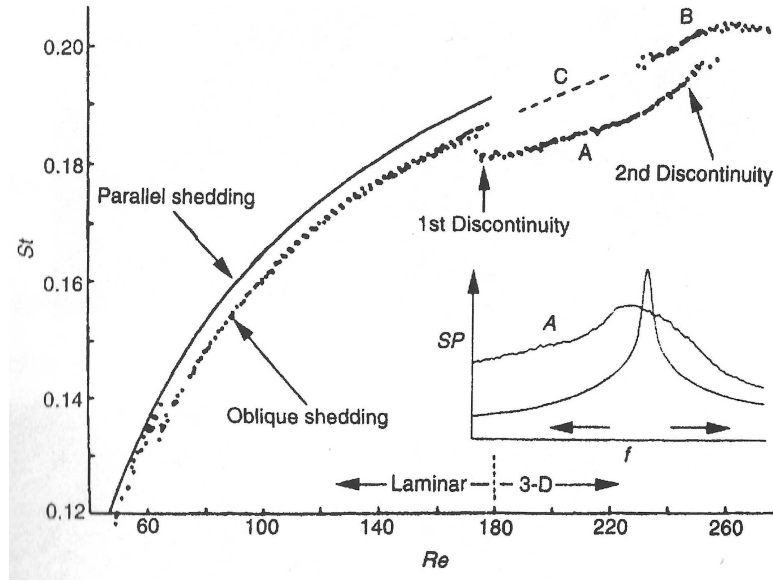


Figure 2.15: Variation of St in terms of Re . Insert: frequency spectra at $Re = 172$, Zdravkovich (1997).

alternated vortex shedding release, as shown in figure 2.16. When the pressure field is maximum in the cylinder top, the flow is accumulated in the bottom side. As the bottom side of this flow accumulation has a higher flow velocity, because it is in contact with the flow free stream, and the top side of the flow accumulated is in cylinder aft and has a lower velocity flow, the flow tends to whirl developing, this way, a vortex. The detachment of the vortex is triggered by the pressure field displacement to the bottom side of the cylinder. When the pressure field arrives the bottom side, pushes the vortex, slitting the connection between the vortex and the cylinder. When the vortex is released, moves in the wake, being gradually elongated and expanded. The vortex is finally dissipated when its pressure evens the free stream velocity. This process is repeated while the fluid flows around the circular cylinder corresponding each vortex released to a cycle in the alternated vortex shedding, Blevins (1977). The detail of the vortex development in the cylinder boundary wall is shown in figure 2.17.

The development of the vortex shedding phenomenon induces the creation of several forces which promote the cylinder oscillation. These forces are designated by lift force and drag force. Particularly, the lift force is the force caused by the interaction between the fluid and the structure, in the problem studied in this thesis corresponds to the force applied in the cylinder in the transversal direction towards the flow displacement direction. As the name indicates, corresponds to the force which is able to sustain the body by the flow displacement, overcoming the gravity force that the body is also subjected too. In the other hand, the drag force is the force generated by the interaction between the body and the fluid in the parallel direction to the fluid motion direction. It represents the force that the body needs to overcome to be able to move through the fluid.

Normally, for studies within the fluid mechanics' context it is usual to represent to

2.1. FUNDAMENTALS OF A FLOW AROUND A CIRCULAR CYLINDER

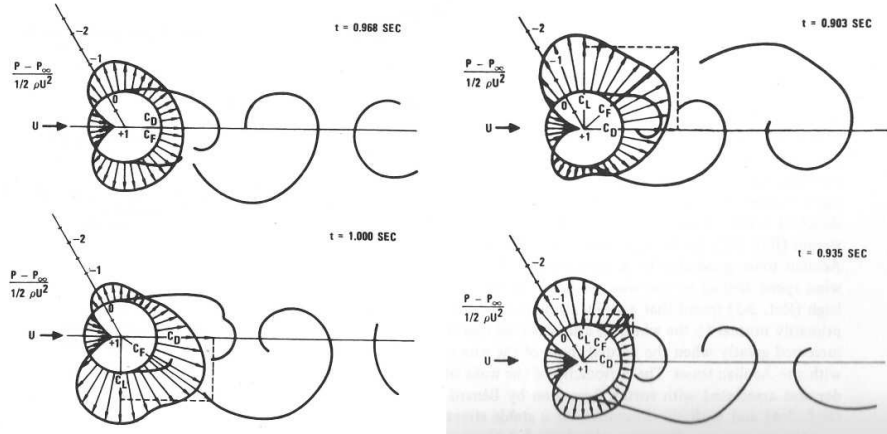


Figure 2.16: Representation of one third of one cycle of vortex shedding of the oscillation sequence of pressure field in $Re = 1.12 \times 10^5$, Blevins (1977).

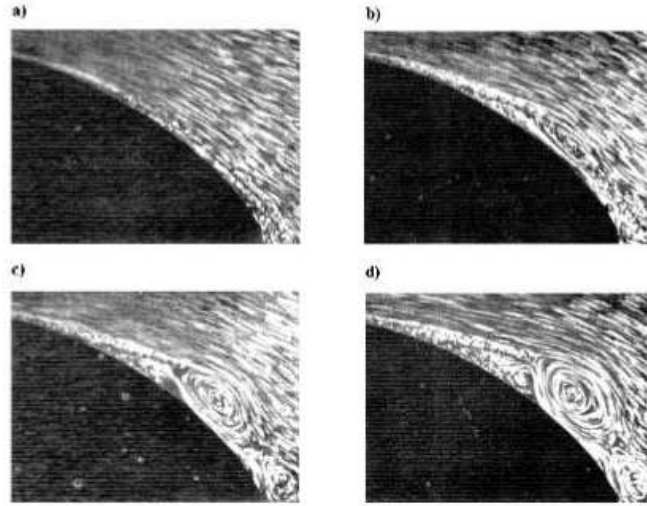


Figure 2.17: Vortex formation near to the cylinder, Mayes et al. (2003).

lift and drag by their one-dimensional quantities, lift coefficient and drag coefficient. Equations 2.8 and 2.9 represent the lift and drag coefficient, respectively. Regarding the lift coefficient, C_L , F_L represents the lift force and for the drag coefficient, C_D , F_D represents the drag force. Common to both coefficients, ρ represents the density, D is the body diameter and U_∞ is the value of the free stream velocity.

$$C_L = \frac{F_L}{\frac{1}{2} \rho D U_\infty^2} \quad (2.8)$$

$$C_D = \frac{F_D}{\frac{1}{2} \rho D U_\infty^2} \quad (2.9)$$

2.1.5 Response modes for a cylinder with one-degree-of-freedom in transverse motion, Y-only

A high attention has been given to studying the flow around the oscillating cylinder with one DOF, in Y-only motion (transverse to the flow motion). An example of that is the work developed by Bearman (1984) and Sarpkaya (1979). A flow around a circular cylinder creates a fluctuating lift force, transverse to the flow direction caused by the alternating vortex shedding, inducing the vibration of the structure. One of the main characteristics of flow-induced vibration is the ability of the vibration originated by the vortex shedding to be synchronized with the natural frequency, (f_n) , of the structure. The occurrence of this phenomenon during a long period of time can lead to the structure collapse.

In the case of a cylinder oscillating transversely to the free stream, the relevant dimensionless parameters in addition to the Reynolds Number, which was already presented in section 2.1.1, is the oscillation amplitude, A and the frequency, f_e (or the period T_e). However, it is common to use the wavelength which corresponds to the sinusoidal path along which the body travels relative to the fluid. Therefore, the relevant parameters are:

$$\text{Amplitude ratio} = \frac{A}{D} \quad (2.10)$$

$$\text{Wavelength ratio} = \frac{UT_e}{D} = \frac{\lambda}{D} \quad (2.11)$$

where U is the velocity in the x -direction, and T_e is the cylinder oscillation period in the transverse direction. The normalized wavelength is equivalent to what is usually referred to as reduced velocity.

Williamson and Roshko (1988) studied the vortex wake patterns for a cylinder, translating in a sinusoidal trajectory, over a wide range of amplitudes and wavelengths. They defined a whole set of different regimes for vortex wake modes, using controlled vibrations, in the plane of $(\lambda/D, A/D)$. With this, Williamson and Roshko created a map which standardized the vortex shedding with the oscillation of the cylinder with Y-only motion in the plane $(\lambda/D, A/D)$. These authors also defined nomenclatures for each vortex wake mode. The terminology P was assigned when a vortex pair was released in each peak of the cylinder oscillation and the terminology S was attributed when a unique vortex was released in each peak of the cylinder oscillation. In figure 2.18 are represented the different types of vortex pattern shedding for each cycle defined by these authors.

Figure 2.19 displays the map created by Williamson and Roshko. Analysing this figure, it is possible to observe the map with the different zones corresponding to the vortex pattern shedding into the cylinder transversely to the flow in function of the oscillation amplitude and wavelength.

The most important patterns of vortex shedding are represented by $2S$, $2P$ and $P + S$. The designation $2S$ means that it is released a single vortex every half cycle, $2P$

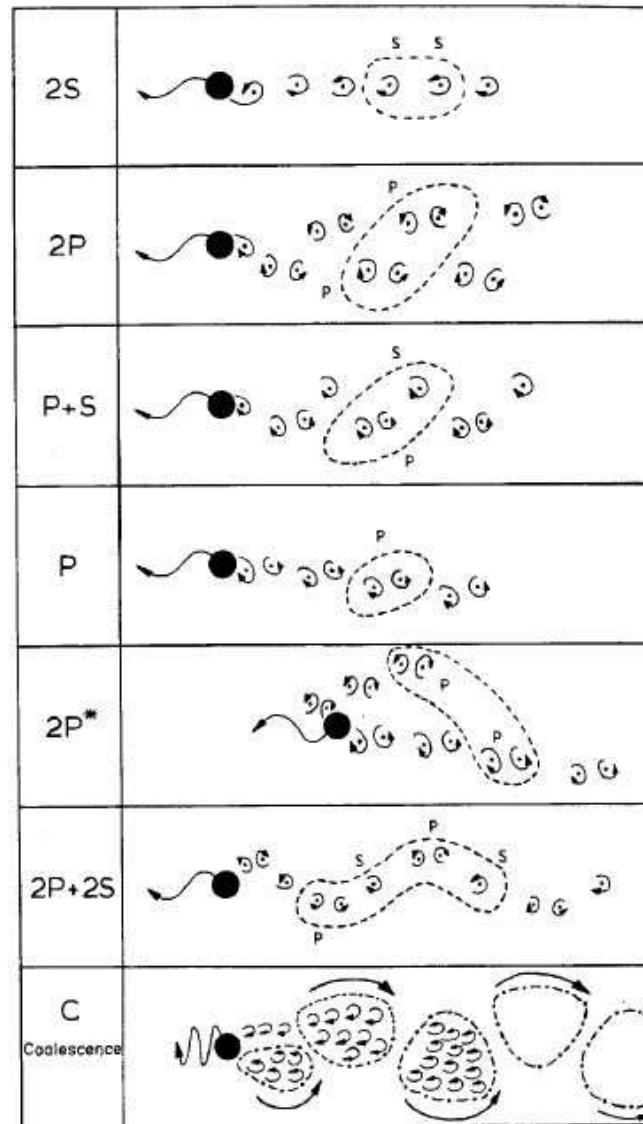


Figure 2.18: Diagram of the vortex shedding patterns described in figure 2.19. P corresponds to a vortex pair and S to a single vortex, being each pattern defined by the number of pairs and single vortices formed per cycle. The dashed lines encircle the vortices shed in one complete cycle. Williamson and Roshko (1988).

designation means it is released a vortex pair for each peak in the amplitude of the cylinder oscillation, and the designation $P + S$ means that is released a vortex pair in the oscillation peak with another single vortex released in the symmetric peak, forming a vortex pattern shedding according to asymmetric vortex swing by the cylinder axis of symmetry. Other patterns are denoted by $C(2S)$ and $C(P + S)$, which means that close to the cylinder are formed $2S$ and $P + S$ vortex pattern shedding but these vortex are small and are joined immediately behind the cylinder. The regions denoted by P and $2P^*$ are referred to as the "single pair" and "double pair" by Williamson Williamson (1985). Finally, the vortex pattern defined by $2P + 2S$ compress two vortex pairs formed during one oscillation cycle in the two cylinder peaks but with the release of a vortex cylinder each time through the movement of the axis of symmetry. The part of the $(\lambda/D, A/D)$ plane in figure 2.19 which has no nomenclature associated corresponds to regions where no periodic synchronized mode of vortex formation was observed by Williamson and Roshko.

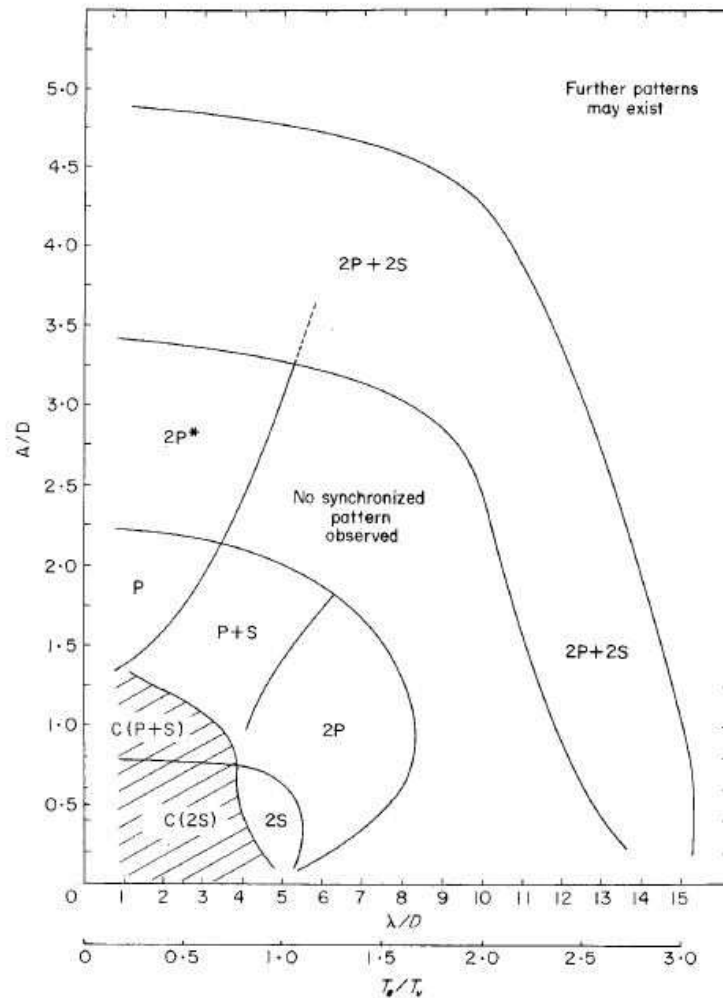


Figure 2.19: Map of vortex synchronization regions in the wavelength-amplitude $(\lambda/D, A/D)$ plane, Williamson and Roshko (1988).

2.1.6 Response modes for a cylinder with two-degrees-of-freedom in XY-motion

The cylinder 8-motion is characterized by the relation between the lift and drag forces. Throughout the development of the phenomenon, i.e., the oscillation of the pressure field and the variation of the lift and drag forces causing the release of vortices in the cylinder back, the intensity of drag and lift forces vary, causing the cylinder movement along the X and Y axis, respectively. The existence and interaction of both these forces are the reason why a cylinder with two DOF describes a movement in an eight conformation. There are several types of 8-motion which are influenced by the phase in which the lift and drag forces are. Figure 2.20 illustrates the movement's dependence on the phase in which the drag and lift forces are, showing a set of possible 8-motions.

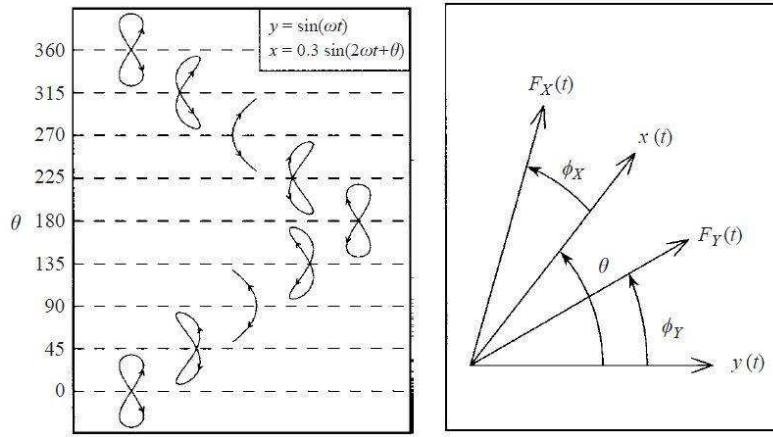


Figure 2.20: Map of vortex synchronization regions in the wavelength-amplitude (λ/D , A/D) plane, Williamson and Roshko (1988).

Contrarily to the high attention given to the study of the flow around an oscillating cylinder with one DOF, transverse to the flow direction, there are seldom studies published about the oscillating cylinder with two DOF. Thus, one of the most interesting subject between these two movement types, the Y -only motion and XY -motion, that still holds is:

What differences exist between a flow around a cylinder with one DOF transversely to the flow and a flow around a cylinder with two DOF?

Furthermore, Jauvtis and Williamson (2003) also asked a key question,

To what extent are these transverse response modes and amplitudes influenced by the body's freedom to respond in the streamwise direction?

Some differences were found by Jauvtis and Williamson (2003) in the standard development of vortex shedding and response between the cylinder with the Y -only motion and XY -motion for moderate mass ratios, $m^* < 6$, parameter which is defined in table 2.4.

They feature comparison of the cylinder amplitudes, for movements in X and Y , and the frequency, f_Y , in relation to the reduced speed, U^* which is similarly defined in table 2.4. These values are illustrated in figure 2.21.

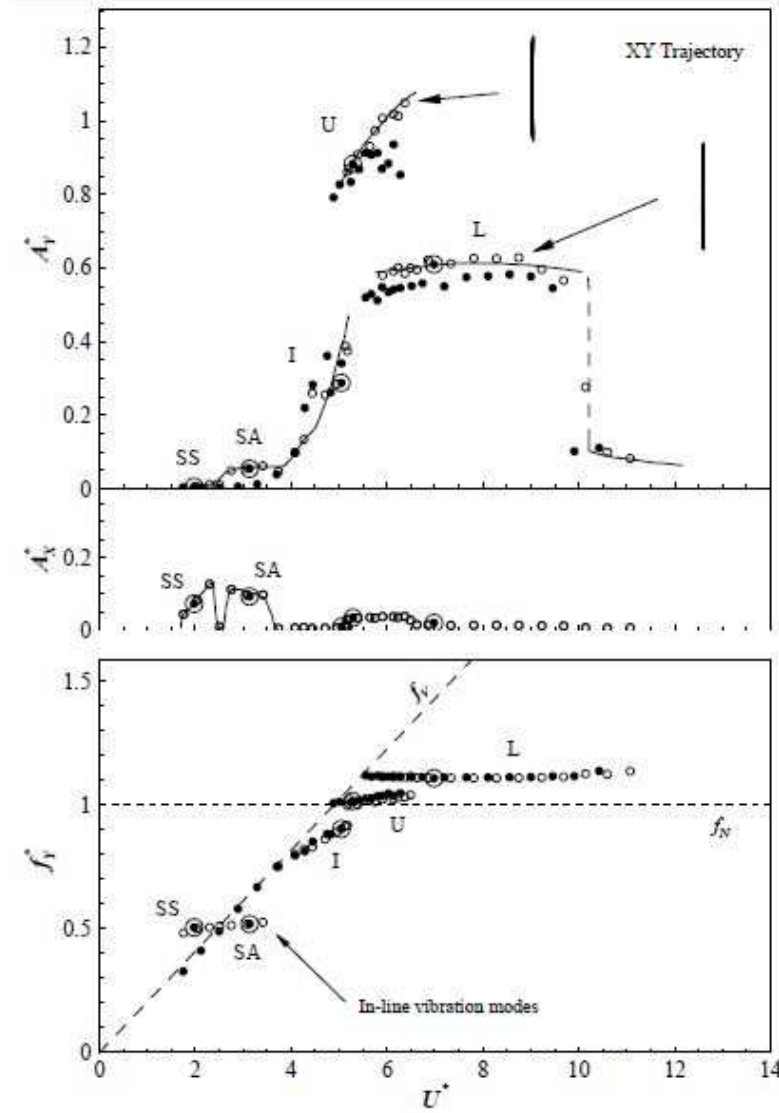


Figure 2.21: Transverse and streamwise amplitudes (A_Y^* and A_X^*) and frequency (f_Y^*) response in function of the reduced velocity (U^*) for moderate mass ratios, $m^* = 7.0$. Solid symbols correspond to Y -only data and open symbols to XY data. $Re = 2000 - 11000$. Jauvtis and Williamson (2003).

Interestingly, as shown in figure 2.21, the response differences between a cylinder in a one DOF and in a two DOF conformation are not very significant even for low mass value ratio, $m^* = 6.9$, and low mass damping $(m^* + C_A)\zeta = 0.0115$, where C_A is the ideal added mass coefficient = 1.0 and ζ is the structural damping coefficient. The response branches are designated (I) for initial, by (U) for upper and by (L) for lower branches in figure 2.21. Jauvtis and Williamson (2003) found a small increase of about 10% of the cylinder amplitude peak response in the upper branch when comparing the XY -motion with the Y -only motion.

A set of amplitude peaks of the upper and lower branches, were also measured by Jauvtis and Williamson (2003) as illustrated in figure 2.22, depending on the mass damping parameter $(m^* + C_A)\zeta$. The only change noted in the response amplitude between the two movements was between the range of values of the mass damping $(m^* + C_A)\zeta = 0.01 - 0.1$ and between the range of values of the mass ratio $m^* = 5.0 - 25.0$. The figure 2.22 shows the transverse amplitude with the mass-damping parameter.

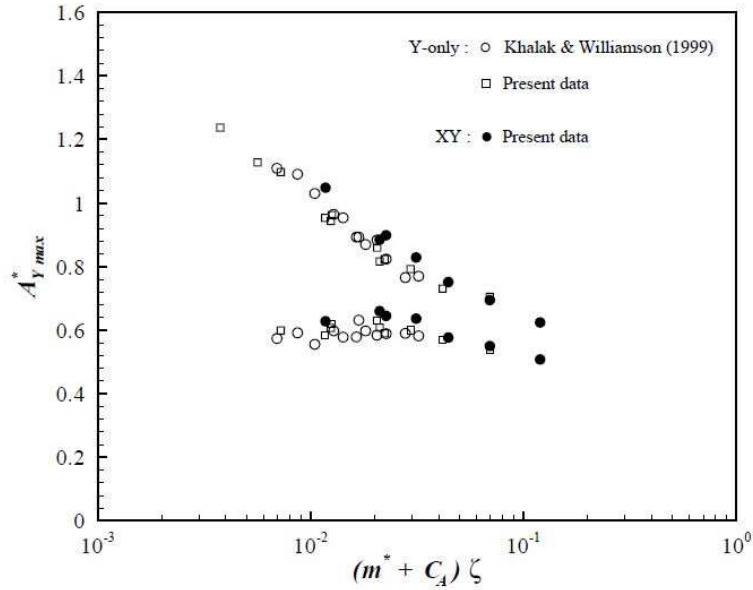


Figure 2.22: Griffin plot of the transverse amplitude peak variation ($A_{Y max}^*$) with the combined mass-damping parameter $(m^* + C_A)\zeta$, for moderate mass ratios, $m^* = 6 - 25$. Jauvtis and Williamson (2003).

Jauvtis and Williamson (2003) shows that for lower mass ratios, $m^* < 6$, exists a remarkable jump that increases the amplitude of cylinder response, corresponding to a new mode of cylinder response, which is quite distinct from the response phenomena in Y-only motion.

The first evident difference regarding the amplitude response is the remarkably high amplitude, about $A_Y^* = 1.5$. For this high amplitude of the cylinder response with 2 DOF, Jauvtis and Williamson (2003) define this as the "super-upper" branch of response, different from the "upper" branch observed in the Y-only motion.

The figure 2.23 shows the cylinder response with two DOF for reduced velocity values between $U^* = 2 - 13.5$ observed in Jauvtis and Williamson (2003). Also, in Jauvtis and Williamson (2003) it are described the several branches of the cylinder response.

Following the results shown in figure 2.23, in figure 2.24 it is possible to observe the 8-motion types detected by Jauvtis and Williamson (2003) as the reduced velocity increases for lower values of reduced mass.

In figure 2.24 shows the peak amplitude levels for super-upper branch and for lower branch, for small mass ratios between $m^* = 2.5 - 3.2$ and for Reynolds number between

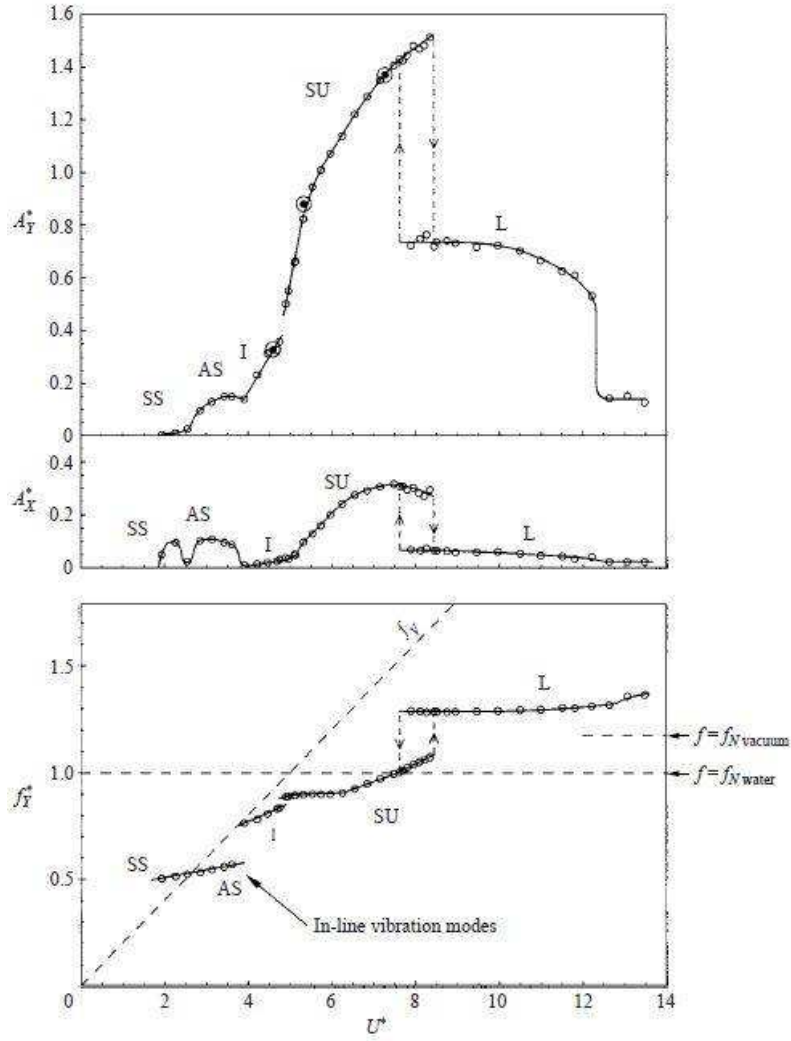


Figure 2.23: Transverse and streamwise amplitudes (A_Y^* and A_X^*) and frequency (f_Y^*) response in function of the reduced velocity (U^*) for low mass ratios, $m^* = 2.6$. Solid symbols correspond to Y-only data and open symbols to XY data. $Re = 2000 - 11000$. Jauvtis and Williamson (2003).

$Re = 330 - 15300$. About the super-upper and lower branch levels of peak response Jauvtis and Williamson (2003) said apparently are independent of the Reynolds number for this range investigated by Jauvtis and Williamson (2003).

Interestingly, Jauvtis and Williamson (2003) observed that when the mass ratio is gradually reduced at a fixed mass-damping, the peak of the transverse amplitude is not affected and remains at the value of the upper branch. This occurs until the mass ratio of $m^* = 6$, from which the streamwise amplitude starts to increase, as m^* is further reduced. It is only when the amplitude reaches the super-upper branch, for a mass ratio $m^* = 4$, that the vibrations reach a stable periodic solution.

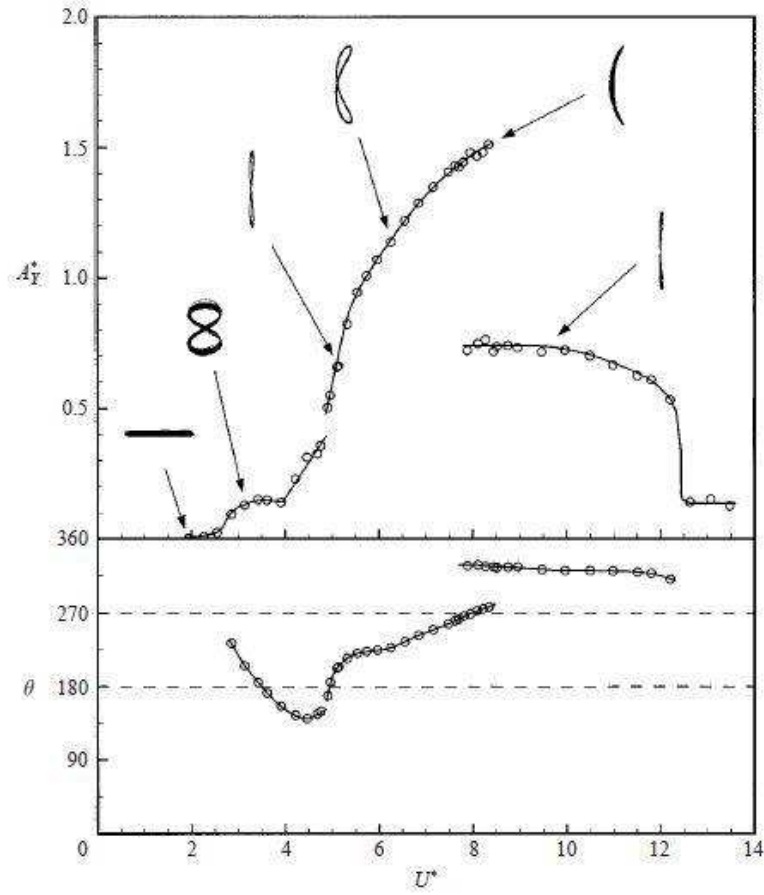


Figure 2.24: Transverse and streamwise amplitudes (A_Y^* and A_X^*) and frequency (f_Y^*) response in function of the reduced velocity (U^*) for low mass ratios, $m^* = 2.6$. Solid symbols correspond to Y-only data and open symbols to XY data. $Re = 2000 - 11000$. Jauvtis and Williamson (2003).

2.2 Fundamentals of Vibration

Any motion that repeats itself after an interval of time is called vibration or oscillation. The theory of vibration deals with the study of oscillatory motions of bodies and the forces associated with them. A vibratory system, in general, includes the means for storing potential energy (spring or elasticity), the means for storing kinetic energy (mass or inertia), and the means by which energy is gradually lost (damper).

The vibration of a system involves the transfer of its potential energy to kinetic energy and of kinetic energy to potential energy, alternately. If the system is damped, some energy is dissipated in each cycle of vibration and must be replaced by an external source if a state of steady vibration is to be maintained. However, in practice, the magnitude of oscillation (u) gradually decreases and the pendulum ultimately stops due to the resistance (damping) offered by the surrounding medium (for instance air). This means that some energy is dissipated in each cycle of vibration due to damping by the air.

The vibration mode can be classified as Rao and Fah (2011) described:

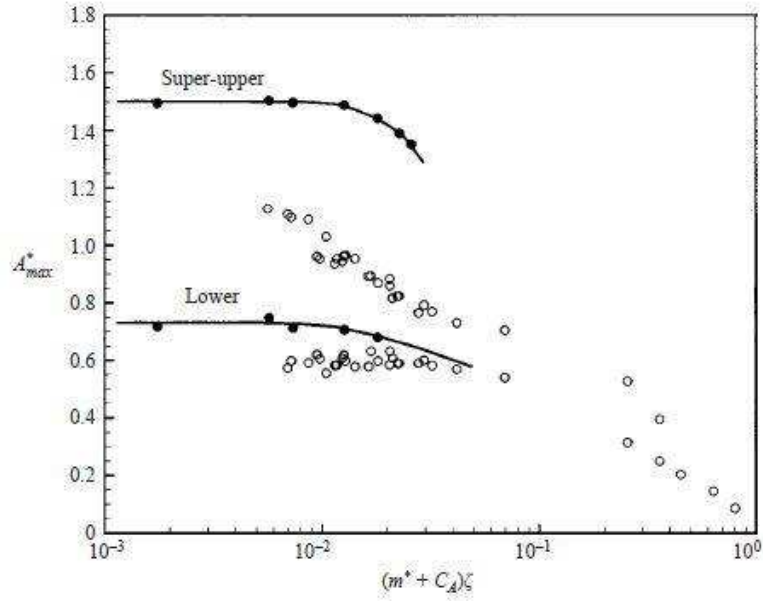


Figure 2.25: Griffin plot of the transverse amplitude peak variation ($A_{Y\max}^*$) with the combined mass-damping parameter $(m^* + C_A)\zeta$ for low mass ratios, $m^* = 2.5 - 4$. Jauvtis and Williamson (2003).

- **Free Vibration:** if a system, after an initial disturbance, is left to vibrate on its own, the ensuing vibration is known as free vibration. No external force acts on the system. The oscillation of a simple pendulum is an example of free vibration.
- **Forced Vibration:** if a system is subjected to an external force (often, a repeating type of force), the resulting vibration is known as forced vibration. The oscillation that arises in machines such as diesel engines is an example of forced vibration. If the frequency of the external force coincides with one of the natural frequencies of the system, a condition known as resonance occurs, and the system undergoes dangerously large oscillations. Failures of such structures as buildings, bridges, turbines, and airplane wings have been associated with the occurrence of resonance.
- **Undamped vibration:** if no energy is lost or dissipated in friction or other resistance during oscillation, the vibration is known as undamped.
- **Damped vibration:** if some energy is lost in friction or other resistance during oscillation, the vibration is called damped vibration. In many physical systems, the amount of damping is so small that it can be disregarded. However, consideration of damping becomes extremely important in analysing vibratory systems near resonance.

If all the basic components of a vibratory system - the spring, the mass, and the damper - behave linearly, the resulting vibration is known as linear vibration. If, however, any of the basic components behave non-linearly, the vibration is called non-linear

vibration. The differential equations that govern the behaviour of linear and non-linear vibratory systems are linear and non-linear, respectively. If the vibration is linear, the principle of superposition holds, and the mathematical techniques of analysis are well developed. For non-linear vibration, the superposition principle is not valid, and techniques of analysis are less well known. Since all vibratory systems tend to behave non-linearly with increasing amplitude of oscillation, a knowledge of non-linear vibration is desirable in dealing with practical vibratory systems.

If the value or magnitude of the excitation (force or motion) acting on a vibratory system is known at any given time, the excitation is called deterministic. The resulting vibration is known as deterministic vibration. In some cases, the excitation is non-deterministic or random and, for these situations, the value of the excitation at a given time cannot be predicted. In these cases, a large collection of records of the excitation may exhibit some statistical regularity. It is possible to estimate averages such as the mean and mean square values of the excitation. Examples of random excitations are wind velocity, road roughness, and ground motion during earthquakes. If the excitation is random, the resulting vibration is called random vibration. In this case the vibratory response of the system is also random and it can only be described in terms of statistical quantities.

Regarding the damping elements, viscous damping is the most commonly used damping mechanism in vibration analysis. When mechanical systems vibrate in a fluid medium such as air, gas, water, or oil, the resistance offered by the fluid to the moving body causes energy to be dissipated. In this case, the amount of dissipated energy depends on many factors, such as the size and shape of the vibrating body, the viscosity of the fluid, the frequency of vibration, and the velocity of the vibrating body. In viscous damping, the damping force is proportional to the velocity of the vibrating body.

2.2.1 Two-Degree-of-Freedom Systems

Usually, the mass, spring and damper do not appear as separate components but as an inherent and integral part of the system. For example, in an airplane wing, the mass of the wing is distributed throughout the wing. Also, due to its elasticity, the wing undergoes noticeable deformation during flight so that it can be modelled as a spring. In addition, the deflection of the wing introduces damping due to relative motion between components such as joints, connections and support as well as internal friction due to micro-structural defects in the material.

Assuming that the motion of the instrument is confined to the XY -plane, the system can be modelled as a mass m supported by springs in the X and Y directions, as figure 2.26 illustrates. Thus the system has one-point mass m and two degrees of freedom, because the mass has two possible types of motion: translations along the X and Y directions.

Thus, the general rule for the computation of the number of degrees of freedom can be stated as the multiplication between the number of masses in the system and the number of possible motion types for each mass.

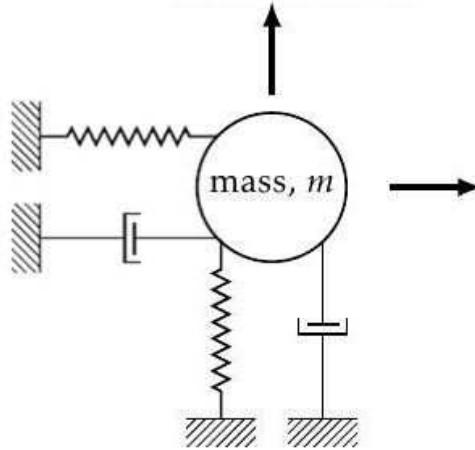


Figure 2.26: Schematic diagram of XY-motion in a spring-mass-damping system.

There are two equations of motion for a two DOF system, one for each degree of freedom. They are, generally, in the form of coupled differential equations and each equation involves all the coordinates. If a harmonic solution is assumed for each coordinate, the equations of motion lead to a frequency equation that gives two natural frequencies for the system. With the appropriate initial excitation, the system vibrates at one of these natural frequencies. During free vibration at one of the natural frequencies, the amplitudes of the two degrees of freedom are related in a specific manner and the configuration is called a normal mode, principal mode, or natural mode of vibration. Thus, a two DOF system has two normal modes of vibration corresponding to the system two natural frequencies. If we give an arbitrary initial excitation to the system, the resulting free vibration will be a superposition of the two normal modes of vibration. Nevertheless, if the system vibrates under the action of an external harmonic force, the resulting forced harmonic vibration occurs at the frequency of the applied force. Furthermore, under harmonic excitation the amplitudes of the two coordinates will be maximum when the forcing frequency is equal to one of the natural frequencies of the system. This phenomenon is designated by resonance.

The configuration of a system can be specified by a set of independent coordinates such as length, angle, or some other physical parameters. Any such set of coordinates is called generalized coordinates. Although the equations of motion of a two DOF system are generally coupled so that each equation involves all the coordinates, it is always possible to find a particular set of coordinates such that each equation of motion contains only one coordinate. The equations of motion are then uncoupled and can be solved independently of each other. Such a set of coordinates, which leads to an uncoupled system of equations, is termed principal coordinates.

Considering the viscously damped two DOF spring-mass-damping system shown in figure 2.26. The motion of the system is completely described by the coordinates

$x(t)$ and $y(t)$, which define the position of the mass m at any time t from the respective equilibrium positions. The external forces $F_x(t)$ and $F_y(t)$ act on the mass m , in the x and y axis direction, respectively.

The free body diagram of the mass m , is shown in figure 2.26. The application of the Newton's second law of motion to each mass move in axes direction gives the linear equation that represents the XY -motion of the cylinder with two DOF:

$$m\ddot{x} + c\dot{x} + kx = F_X(t) \quad (2.12)$$

$$m\ddot{y} + c\dot{y} + ky = F_Y(t) \quad (2.13)$$

The equations 2.12 and 2.13 can be written in matrix form as:

$$[m]\ddot{x} + [c]\dot{x} + [k]x = F(t) \quad (2.14)$$

where $[m]$, $[c]$ and $[k]$ are called the mass, damping and stiffness matrices, respectively. For the cylinder with two DOF case these matrices are given by equations 2.15, 2.16 and 2.17 correspondingly.

$$[m] = \begin{bmatrix} m & 0 \\ 0 & m \end{bmatrix} \quad (2.15)$$

$$[c] = \begin{bmatrix} c_X & 0 \\ 0 & c_Y \end{bmatrix} \quad (2.16)$$

$$[k] = \begin{bmatrix} k_X & 0 \\ 0 & k_Y \end{bmatrix} \quad (2.17)$$

The vector $\vec{A}(t)$ is the displacement vector and is given by equation 2.18 while the respective representation of the displacements are represented by equations 2.19 and 2.20.

$$\vec{A}(t) = \begin{bmatrix} x(t) \\ y(t) \end{bmatrix} \quad (2.18)$$

$$x(t) = A_X \sin(2\omega t + \theta) \quad (2.19)$$

$$y(t) = A_Y \sin(\omega t) \quad (2.20)$$

The vector $\vec{f}(t)$ corresponds to the force vector which is given by equation 2.21. A representation of the fluid forces on the cylinder can be written by equations 2.22 and 2.23.

$$\vec{f}(t) = \begin{bmatrix} F_X(t) \\ F_Y(t) \end{bmatrix} \quad (2.21)$$

$$F_X(t) = F_{X0} \sin(2\omega t + [\phi_X + \theta]) \quad (2.22)$$

$$F_Y(t) = F_{Y0} \sin(\omega t + \phi_Y) \quad (2.23)$$

Khalak and Williamson (1996) proved that by adding weights it is possible to adjust the mass of the system and by changing the springs it is possible to adjust the stiffness of the system. Moreover, changing the cylinder diameters also impacts the fluid mass displacement. The variation of these parameters allow to change independently m^* within limits. Khalak and Williamson (1996) also conclude that changing the system springs do not change significantly the system damping, but it does significantly change the critical damping. By varying these system components, the authors could operate the experimental system in a range of reduced damping.

2.2.2 Equations of XY-motion and existence of a critical mass

Table 2.4: Principal non-dimentional parameters for the analysis of the flow cylinder displacement, Blevins (1977); Khalak and Williamson (1999).

Parameter	Symbol	Equation
Mass ratio	m^*	$\frac{m}{\pi \rho D^2 \frac{L}{4}}$
Damping ratio	ζ	$\frac{c}{2\sqrt{k(m+m_A)}}$
Velocity ratio or reduced velocity	U^*	$\frac{U}{f_N D}$
Amplitude ratios	A_Y^*, A_X^*	$\frac{A_Y}{D}, \frac{A_X}{D}$
Frequency ratios	f_Y^*, f_X^*	$\frac{f_Y}{f_N}, \frac{f_X}{f_N}$
Force coefficients	C_Y, C_X	$\frac{F_Y}{\frac{1}{2}\rho U^2 DL}, \frac{F_X}{\frac{1}{2}\rho U^2 DL}$

Table 2.4 enumerates the most relevant parameters in the evaluation of a flow around a circular body. In particular, the mass ratio, m^* , represents the susceptibility of the structure to flow-induced vibrations. The damping ratio, ζ , corresponds to the energy dissipated by the structure as it vibrates. The velocity ratio, U^* , is the ratio between the length of the vibration path per cycle (U/f) and the model width (D), meaning that a small velocity ratio corresponds to a strong interaction between the model and the periodic

components of the near wake. The amplitude ratio, A^* , translates the body displacement towards its diameter. The frequency ratio, f^* , represents the proportion between the oscillation frequency of the fixed and the DOF body. Lastly, the force coefficient, C , translates the forces induced by the flow displacement in the body.

The parameter m_A corresponds to the added mass which is equal to $C_A m_d$, where C_A is the added mass coefficient and m_d is the displaced fluid mass. f_n is the system natural frequency, D is the cylinder diameter, L is the cylinder length, ρ is the fluid density, U is the free-stream velocity and ν is the fluid viscosity

An important relation deduced to characterize the XY -motion was formulated by Williamson and Jauvtis (2004). This relation states that, for periodic vibrations, the stream-wise oscillation frequency (f_X) is twice the frequency for the transverse direction (f_Y), which is given by equation 2.24.

$$f_X = 2f_Y \quad (2.24)$$

The X -frequency is twice the Y -frequency because when the cylinder describes an 8-motion, obviously per each cycle performed in Y direction, two cycles are describes in the X -direction.

Khalak and Williamson (1999) defined the following set of equations:

$$A_X^* = \frac{C_X \sin \phi_X}{4\pi^3(m^* + C_A)\zeta} \left(\frac{U^*}{2f_Y^*}\right)^2 2f_Y^* \quad (2.25)$$

$$A_Y^* = \frac{C_Y \sin \phi_Y}{4\pi^3(m^* + C_A)\zeta} \left(\frac{U^*}{f_Y^*}\right)^2 f_Y^* \quad (2.26)$$

These equations relate the cylinder oscillation amplitudes to the excitation of the body in X and Y directions, corresponding to the cylinder displacement transverse and in-line to the flow. The form of the equations are identical except for the frequencies relation, that are

$$f_X^* = 2f_Y^* \quad (2.27)$$

in accordance to the equation 2.24.

The frequencies are determined by

$$f_X^* = \sqrt{\frac{m^* + C_A}{m^* + C_{EAX}}} \quad (2.28)$$

$$f_Y^* = \sqrt{\frac{m^* + C_A}{m^* + C_{EAY}}} \quad (2.29)$$

where the coefficient C_{EA} represents the force due to the vortex dynamics that is in phase with the body acceleration, not being a true "added mass". These coefficients are given by

$$C_{EAX} = \frac{C_X \cos \phi_X}{2\pi^3 A_X^*} \left(\frac{U^*}{2f_Y^*}\right)^2 \quad (2.30)$$

$$C_{EAY} = \frac{C_Y \cos \phi_Y}{2\pi^3 A_Y^*} \left(\frac{U^*}{f_Y^*} \right)^2 \quad (2.31)$$

where A^* and f^* equations, are respectively

$$\left(\frac{A_X^*}{A_Y^*} \right) = \frac{1}{2} \left(\frac{C_X \sin \phi_X}{C_Y \sin \phi_Y} \right) \quad (2.32)$$

$$C_{EAX} = \frac{1}{4} C_{EAY} - \frac{3}{4} m^* \quad (2.33)$$

Equation 2.33 results from the combination between the frequency equations 2.29 and 2.28, which relates the effective added masses in the X and Y directions, and involves the mass ratio, m^* . This equation is particularly interesting because, if $m^* < m_{crit}^*$ Govardhan and Williamson (2002) proved that the system tends to infinite U^* and infinite f^* , meaning that equation 2.31 can be simplified to

$$C_{EAY} = -m^* \quad (2.34)$$

Replacing equation 2.34 in equation 2.33 the forces due to the vortex dynamics in X-direction and Y-direction take the same value

$$C_{EAY} = C_{EAX} \quad (2.35)$$

The coefficient C_A in the equations 2.26 and 2.25 is the ideal added mass coefficient, and takes the value 1.0 according to Govardhan and Williamson (2002). With a set of experiments these authors found a good ratio for the lower branch, deducing the frequency of the lower response branch

$$f_{Ylower}^* = \sqrt{\frac{m^* + 1}{m^* - 0.54}} \quad (2.36)$$

Equation 2.36 shows that for vortex-induced vibration of this X and Y system the critical mass is evaluated as

$$m_{crit}^* = 0.52 \quad (2.37)$$

which is close to the value for Y-only motion as Govardhan and Williamson (2002) show that exists a critical mass, below which the large-amplitude vibrations will persist, up to infinitely high normalized velocities, U^* .

2.3 Computational Fluid Dynamics: mathematical equations modelling the fluid flow

CFD is a field of computational theory which attempts to model and analyse fluid mechanic problems through the application of numerical methods and algorithms within

a discretized computational domain. The advent of CFD practice can be tracked back to the first use of the general-purpose digital computer in the early 1950s, and the field has expanded over the subsequent years in proportionally to the development of computing power, Wendt et al. (1996). CFD has become an important tool in product development allowing the decrease of prototype testing required for a given product. Nevertheless, CFD employment is limited by the complexity of the problem being considered given that it is restricted to the available computational power. In fact, a case which is too large may take too long to solve, eliminating CFD as a useful analysis tool.

The application of CFD potential requires first understanding of the physical laws that govern the fluid displacement. These equations are presented in this section. Fluid theory states that these equations measure the conservation of mass, momentum and energy, and are referred to, respectively, as the continuity, momentum and energy equations. In CFD context, these equations are used to discretize the solution across the individual mesh cells which together constitute the computational domain of the case in study.

2.3.1 Finite Volume Method

The Finite Volume Method (FVM) is a numerical technique that transforms the partial differential equations representing conservation laws into discrete algebraic equations over finite volumes, Ferziger and Peric (2001), Versteeg and Malalasekera (2007), Moukalled et al. (2015). This method is an extension of the finite difference method and, therefore, the first step in the solution process is the discretisation of the geometric domain, which, in the FVM, is discretised into non-overlapping elements or finite volumes. The partial differential equations are then transformed into algebraic equations by integrating them over each discrete element. The system of algebraic equations is then solved to compute the values of the dependent variable for each of the elements.

In this process the partial differential equations are integrated and transformed into balance equations over an element. The result is a set of semi-discretised equations. In the second step, interpolation profiles are chosen to approximate the variation of the variables within the element and relate the surface values of the variables to their cell values and thus transform the algebraic relations into algebraic equations.

In other words, the FVM turns the conservation equation into face fluxes and evaluates the gradient at the centroids of finite control volume meshes. Because the flux entering a given volume is identical to that leaving the adjacent volume, the FVM is strictly conservative. This inherent conservation property of the FVM makes it the preferred method in CFD. Another important attribute of the FVM is that it can be formulated in the physical space on unstructured polygonal meshes. Finally, in the FVM it is quite easy to implement a variety of boundary conditions in a non-invasive manner, since the unknown variables are evaluated at the centroids of the volume elements, not at their boundary faces. These characteristics have made the FVM quite suitable for the numerical simulation of a variety of applications involving fluid flow and heat and mass transfer, and developments in

the method have been closely entwined with advances in CFD. From a limited potential at inception confined to solving simple physics and geometry over structured grids, the FVM is now capable of dealing with all kinds of complex physics and applications.

2.3.2 Conservation of Mass

The principle of conservation of mass states that a "mass can neither be created nor destroyed", Wendt et al. (1996); Moukalled et al. (2015). The continuity equation can be described by equation 2.38.

$$\frac{\partial \rho}{\partial t} + \nabla \cdot (\rho U) = 0 \quad (2.38)$$

where the ∇ is the nabla operator and corresponds to the gradient of ρU given by equation 2.39, which mathematically translates the variation of the value of ρU in both magnitude and direction with position.

$$\nabla = \frac{\partial}{\partial x}i + \frac{\partial}{\partial y}j + \frac{\partial}{\partial z}k \quad (2.39)$$

where i , j and k are the unit vectors in the x , y and z direction in the Cartesian coordinate system, respectively.

2.3.3 Conservation of Linear Momentum

The principle of conservation of linear momentum indicates that in the absence of any external force acting on a body, the body retains its total momentum, Wendt et al. (1996); Moukalled et al. (2015).

Relating equations 2.40, 2.41 and 2.42 translate the component of the momentum equation for the x , y and z directions, respectively.

$$\rho f_x - \frac{\partial p}{\partial x} + \frac{\partial \tau_{xx}}{\partial x} + \frac{\partial \tau_{yx}}{\partial y} + \frac{\partial \tau_{zx}}{\partial z} = \frac{\partial(\rho u)}{\partial t} + \nabla \cdot (\rho u U) \quad (2.40)$$

$$\rho f_y - \frac{\partial p}{\partial y} + \frac{\partial \tau_{xy}}{\partial x} + \frac{\partial \tau_{yy}}{\partial y} + \frac{\partial \tau_{zy}}{\partial z} = \frac{\partial(\rho v)}{\partial t} + \nabla \cdot (\rho v U) \quad (2.41)$$

$$\rho f_z - \frac{\partial p}{\partial z} + \frac{\partial \tau_{xz}}{\partial x} + \frac{\partial \tau_{yz}}{\partial y} + \frac{\partial \tau_{zz}}{\partial z} = \frac{\partial(\rho w)}{\partial t} + \nabla \cdot (\rho w U) \quad (2.42)$$

2.3.4 Conservation of Energy

The conservation of energy is governed by the first law of thermodynamics which states that energy can be neither created nor destroyed during a process, it can only change from one form into another. Consequently, in this thesis context, the energy equation mathematically stipulates that the energy net flux into a given control volume must be equal to the rate of energy change inside that element. Nevertheless, since both

isothermality and incompressibility apply to all the situations simulated in thesis, there is no need to solve the energy equation.

2.3.5 Newtonian Fluids

A Newtonian fluid is characterized by a linear relation between the fluid's shear stress and the velocity gradients. The Stokes equations for Newtonian stresses are stated in the following equations, Wendt et al. (1996):

$$\tau_{xx} = \lambda(\nabla \cdot U) + 2\mu \frac{\partial u}{\partial x} \quad (2.43)$$

$$\tau_{yy} = \lambda(\nabla \cdot U) + 2\mu \frac{\partial v}{\partial y} \quad (2.44)$$

$$\tau_{zz} = \lambda(\nabla \cdot U) + 2\mu \frac{\partial w}{\partial z} \quad (2.45)$$

$$\tau_{xy} = \tau_{yx} = \mu \left(\frac{\partial v}{\partial x} + \frac{\partial u}{\partial y} \right) \quad (2.46)$$

$$\tau_{xz} = \tau_{zx} = \mu \left(\frac{\partial u}{\partial z} + \frac{\partial w}{\partial x} \right) \quad (2.47)$$

$$\tau_{yz} = \tau_{zy} = \mu \left(\frac{\partial w}{\partial y} + \frac{\partial v}{\partial z} \right) \quad (2.48)$$

where μ is the molecular viscosity and λ is the second viscosity coefficient. In the current thesis the simulated fluids are incompressible and isotropic and, thereby, Newtonian fluids. In this conditions the equation of mass 2.38 assume the following form

$$\nabla \cdot U = 0 \quad (2.49)$$

2.3.6 The Navier-Stokes Equation

Substituting equations 2.43 to 2.43 in equations 2.40 to 2.42 and considering equation 2.49 which implies that the velocity must be non-divergent the equations which translate x , y and z components of the isotropic Newtonian fluid are substantially simplified.

$$\frac{\partial(\rho u)}{\partial t} + \nabla \cdot (\rho u U) = \frac{\partial}{\partial y} \left(\mu \left[\frac{\partial v}{\partial x} + \frac{\partial u}{\partial y} \right] + \frac{\partial}{\partial z} \left(\mu \left[\frac{\partial u}{\partial z} + \frac{\partial w}{\partial x} \right] + \right) + \rho f_x \quad (2.50)$$

$$\frac{\partial(\rho v)}{\partial t} + \nabla \cdot (\rho v U) = \frac{\partial}{\partial x} \left(\mu \left[\frac{\partial v}{\partial x} + \frac{\partial u}{\partial y} \right] + \frac{\partial}{\partial z} \left(\mu \left[\frac{\partial w}{\partial y} + \frac{\partial v}{\partial z} \right] + \right) + \rho f_y \quad (2.51)$$

$$\frac{\partial(\rho w)}{\partial t} + \nabla \cdot (\rho w U) = \frac{\partial}{\partial x} \left(\mu \left[\frac{\partial u}{\partial z} + \frac{\partial w}{\partial x} \right] + \frac{\partial}{\partial y} \left(\mu \left[\frac{\partial w}{\partial y} + \frac{\partial v}{\partial z} \right] + \right) + \rho f_z \quad (2.52)$$

After this simplification, equations 2.50 to 2.51 can be converted into a conservative equation which corresponds to the Navier-Stokes equation for incompressible and Newtonian fluids:

$$\frac{\partial(\rho U)}{\partial t} + \nabla \cdot (\rho U U) = -\nabla p + \mu \nabla^2 U \quad (2.53)$$

NUMERICAL MODELLING METHODOLOGY

This chapter aims to explain the numerical modelling methodology used to simulate an unsteady flow around a circular cylinder. The steps that will be explained in the next sub-chapters intend to model the features of this phenomena as accurately as possible. The simulation of reality leads to large numerical models, requiring considerable computational power. To achieve that it was, firstly, formulated the problem to simulate. Next, it was developed the respective mesh using, for that, the Gmsh software, Geuzaine and Remacle (2009). The defined mesh was then used as an input to proceed analysis with OpenFOAM, Weller et al. (1998). This software has a huge potential, providing a wide range of tools that can be used in the majority of the engineering and scientific areas. Furthermore, it is covered by the GNU general public license (GPL), which guarantees end users the freedom to run, study, and modify the software without any costs associated. Generally, it is used in UNIX operating systems, being compatible with some Linux distributions such as Ubuntu. Finally, the results obtained with OpenFOAM were analysed by studying the variation of the drag and lift coefficients along the time, analysing the mean and the standard deviation of the drag and lift coefficients which, at a higher level, allowed to conclude about the influence of a fluid flowing through a circular cylinder. Examples of the examined parameters are: the cylinder oscillation frequency, the time-step at which the vortex release stabilizes or the comparison between the simulation vortex shedding with the vortex shedding patterns described in the literature.

Studies in CFD are characterized by three main phases: a pre-processor, a solver and a post-processor, Versteeg and Malalasekera (2007). More precisely, the pre-processing phase consists on the input of a flow problem into a CFD program such as the definition of the computational domain, the mesh generation, the selection of the system of equations, the definition of the fluid properties and the specification of the boundary conditions. The solver phase is defined by the numerical solution of the simulated problem. And,

lastly, in the post-processing is performed the analysis of the obtained results by the means of plots which may include animation for dynamic result display.

3.1 Mesh generation using Gmsh

The mesh generation was done using the Gmsh software, Geuzaine and Remacle (2009). This an open source three-dimensional finite element grid generator software which has a graphical user interface. Nevertheless, for more complex meshes, this software allows to change directly the input file that defines the mesh. In the current work context, it was used the later functionality. Thus, the first step of the meshes definition was to establish the domain center point, the cylinder and the domain boundary points which where, subsequently, joined with a circular arc. After having the cylinder and the domain boundary lines set, it was settled the domain area between the cylinder and the domain. At the lines level, it was defined the number of points as well as the connections between the mesh boundary lines, definition that will determine the mesh number of elements. Next, it is critical to define a progression for the line's points in order to allow a greater detail of the mesh near the cylinder boundary, allowing the analysis of the physical phenomenon in this area. Finally, it was defined the mesh type of elements, triangular or quadrangular. At this point, the mesh is fully described at a two-dimensional level. Since OpenFOAM is only able to process three-dimensional meshes, it was done an extrude with a unitary value to transpose the mesh for a three-dimensional domain. Thenceforth, were defined the domain physical areas namely, the inlet, the outlet and the cylinder zones. After having all these properties defined at the mesh it was done a mirror parallel to the flow displacement direction. This is an important step since this configuration is crucial for the movement of the cylinder calculated in the simulation. The symmetry between the upper and the lower zone of the cylinder guarantees that the vortex shedding induces an equal force in the cylinder higher and inferior area which will influence the cylinder displacement into an 8-motion movement, data that will be discussed in greater detail in chapter 6.

The Gmsh is organized in three different modules: geometry, mesh and solver. The commands used in each one of the available modules are enumerated in table 3.1.

3.1.1 Important mesh parameters

The solution of a flow problem is defined at the mesh nodes inside each cell. The accuracy of a CFD solution is determined by the number of cells in the mesh. Generally, the increase of the number of cells implies the improvement of the solution accuracy. Both the accuracy of a solution and its cost in terms of necessary computer hardware and calculation time are dependent and calculation time are dependent on the fineness of the mesh. Optimal meshes are non-uniform, in other words, finer in areas where large variations occur and coarser in regions with relatively little changes from point to point.

Table 3.1: Gmsh commands used in the meshes generation.

Command name	Description
Add Point	Creates an elementary point.
Add Straight line	Creates a straight line segment between two points.
Add Circle arc	Creates a circle arc (strictly) smaller than Pi.
Line loop	Creates an oriented line loop.
Add Ruled surface	Creates a ruled surface, i.e., a surface that can be interpolated using transfinite interpolation.
Transfinite Line	Selects the lines in expression-list to be meshed with the 1D transfinite algorithm.
Transfinite Surface	Selects surfaces to be meshed with the 2D transfinite algorithm.
Transfinite Volume	Selects five- or six-face volumes to be meshed with the 3D transfinite algorithm.
Recombine surface	Recombines the triangular meshes of the surfaces listed in expression-list into mixed triangular/quadrangular meshes.
Extrude surface	Extrudes all elementary entities (points, lines or surfaces) in extrude-list using a translation.
Physical Surface	Creates a physical surface.

In the mesh development process is crucial to validate the mesh quality. The most important parameters are the aspect-ratio, the skewness and the non-orthogonality of the mesh cells. The OpenFOAM has a utility that allows to check the quality of the mesh parameters. This functionality can be used by typing the command `checkMesh` in the Ubuntu terminal. This utility has an important role in the analysis development by allowing the evaluation of important mesh parameters informing, for instance, about the mesh total number of cells or the total number of cells for each mesh element type. It is also possible to evaluate the mesh maximum and minimum aspect-ratio, skewness and non-orthogonality values.

Particularly, the mesh skewness value can vary between zero and one. The best case scenario is having a mesh with zero skewness, meaning that the mesh cells have no distortion and, hence, are equilateral. In opposition, when this property has values approximate of one it indicates that the mesh cells are completely degenerated and might compromise the accuracy of the interpolated regions.

The non-orthogonality and aspect-ratio values can be equal or superior to 1. For the higher quality cells both these parameters have the value 1, meaning that the cells have the square form with 90 degrees angles for each double crossed line. In other words, when non-orthogonality and aspect-ratio are equal to 1, it means that all the cell's angles have the same proportionality between them and, similarly, all the cell's lines have the

same proportionality between them.

3.1.2 Mesh geometry

Different types of meshes can be used in different types of numerical studies, affecting the obtained results. Particularly, in this work, were used O-type meshes.

The O-type mesh has circular exterior domain with the cylinder positioned in the mesh center. Hence, the mesh is generated between the cylinder and the external boundary. The dimension of the O-type mesh is shown in figure 3.1. The detail of the elements near the cylinder wall is illustrated in figure 3.2. The domain with $2500D$ was chosen to minimize the blockage effect in the studies performed in this thesis. Besides, the domain dimension was also chosen to enable the mesh independence study, by performing a comparison study between the obtained results and the results described by Didier (2012), work that will be presented in greater detail in the section 4.1.

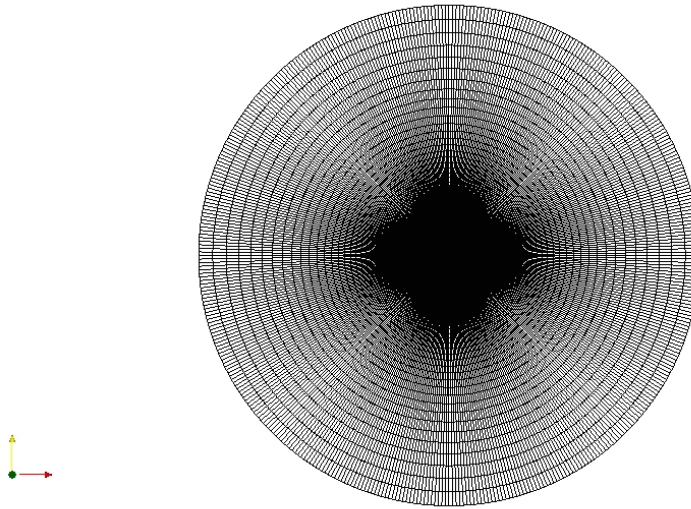


Figure 3.1: Representation of the developed mesh with $2500D$, full domain.

3.1.3 State-of-the-art: mesh generation tools

The Gmsh software was chosen to generate the meshes throughout this work. Nevertheless, it is important to refer that there are available several alternative tools to perform this task. Examples of alternative software are shown in table 3.2. All these enumerated programs provide the tools to generate meshes, using each one a specific methodology. However, Gmsh has significant added value for its clearness and simplicity combined with the display of all important information. Furthermore, features the possible to edit easily in the graphical user interface the mesh geometry and properties allowing, this way, to build, mesh, and assign zone types to a model in a simple and intuitive way. This

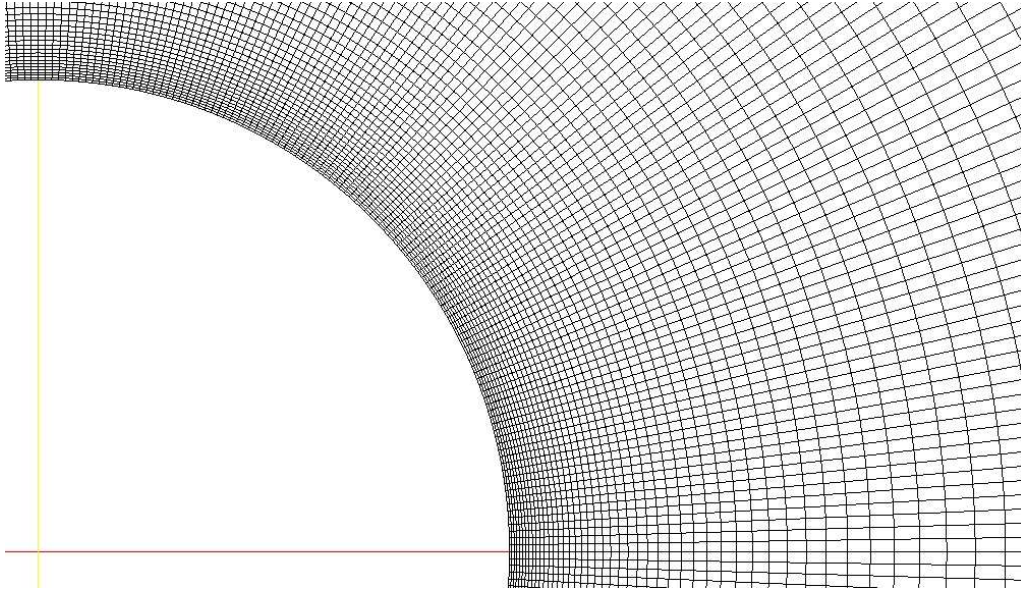


Figure 3.2: Representation of the mesh with $2500D$, near to the cylinder wall.

is an advantage over, for instance, the `blockMesh` which do not allow the instant visualization of the developed mesh. A mesh built with `blockMesh` can be visualized by using an additional software like the Paraview. Another alternative is GAMBIT, which is a tool integrated in Ansys and, thus, has the disadvantage of not being open-source.

3.2 Computational fluid dynamics analysis using OpenFOAM

CFD tools are able to simulate a fluid passing through or around an object. The ability to predict the impact of such flows on a specific product performance is time consuming and costly without some form of simulation tool. Therefore, engineers across a wide range of industries can benefit from CFD, such as automotive, aeronautic, life science, environmental and machinery. Indeed, almost every design encounters fluid dynamics at some point, whether heat or liquids, internal or external. In all the previously described areas the virtual development allows a reduced number of prototypes and less testing. Therefore, it is important to provide CFD users with easy-to-use, robust, time-efficient and validated processes. In this thesis the CFD analysis was done using the OpenFOAM software.

The OpenFOAM (Open source Field Operation And Manipulation) - OpenFoam (2009); Weller et al. (1998) - software is a C++ object-oriented framework composed by solvers and utilities. The solvers are designed to solve a specific problem in continuum mechanics and the utilities help the user with data manipulation. One of the great advantages of this software towards others programs is the power that gives to its users allowing the development of self-adjusted solvers and utilities. The OpenFOAM structure is illustrated in figure 3.3. Specifically, the pre-processing phase is where the user chooses which OpenFOAM solver best suits the simulated problem. OpenFoam contains several

Table 3.2: Gmsh alternative software to perform mesh generation.

Software	Description
blockMesh, OpenFoam (2009)	Mesh generation utility supplied with OpenFOAM. The principle behind blockMesh is to decompose the domain geometry into a set three dimensional blocks. The edges of the blocks can be straight lines, arcs or splines. The mesh is characterized by the number of cells in each direction of the block, information that is processed by the blockMesh utility to generate the mesh data.
NETGEN, Schöberl et al.	Automatic two and three-dimensional tetrahedral mesh generator which generates essentially unstructured triangular/tetrahedral meshes. Input can be provided by simple ASCII files, or imported from CAD programs via IGES, Step, or STL files.
enGrid, enGits GmbH	Features surface mesher, prism layer extrusion of individual surfaces, boundary and solver setup and export of ready-to-run case directories for OpenFOAM.
SMESH, CASCADE	Module integrated in the SALOME platform which allows to create meshes on the basis of geometrical models created or imported into GEOM. Features the possibility to add a new mesher by using the existing plug-in mechanism.
GAMBIT, ANSYS	Mesh building toolkit integrated in Ansys.

pre-processing utilities. Examples are blockMesh, tool that can be used in the mesh generation as referred in section 3.1, or mirrorMesh, utility which allows to mirror a mesh around a given plane specified in the dictionary `system/mirrorMeshDict` ensuring the symmetry between the mesh nodes.

In the solving section, OpenFOAM has available some standard solvers adapted to case studies that were already solved and validated. To the user is given the flexibility to use one of the pre-defined solvers, change a pre-defined solver adapting it to a particular case in study adding, for example, parts of other solvers which take into account characteristics of the problem being solved or even create new solvers. Lastly, for the post-processing step OpenFOAM installation package includes a complementary software, the ParaView. The ParaView is also an open-source application developed to analyse extremely large datasets using distributed memory computing resources. Provides, therefore, the tools to visualize and analyse the simulated data using qualitative and quantitative techniques, in a three dimensional graphic user interface.

Having in mind the CFD analysis steps referred in this chapter introduction, the OpenFOAM corresponds to the solver element in the CFD methodology developed in this thesis. The numerical algorithm used by this software begins by the integration of the governing equations of fluid flow over all the finite control volumes of the domain, followed by the conversion of the resulting integral equations into a system of algebraic

equations - processing designated by discretisation - and ends by solving the algebraic equations using an iterative method.

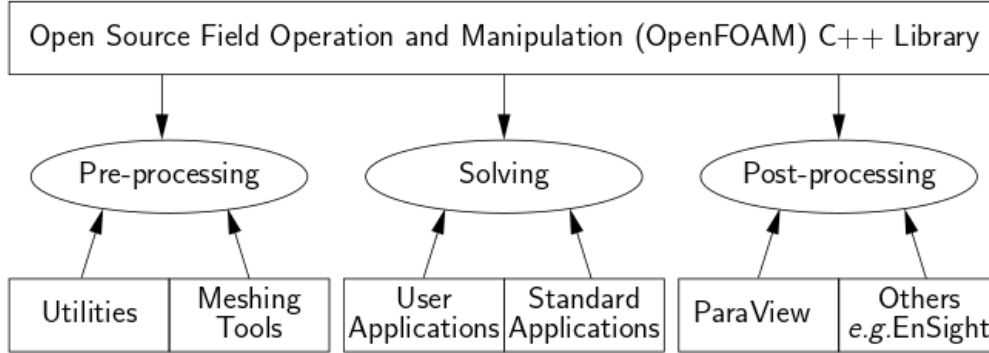


Figure 3.3: OpenFOAM structure extracted from OpenFOAM User Guide Guide (2011).

3.2.1 Finite volume mesh

The first step of the FVM is setting up the geometrical support framework for the problem in analysis. The finite volume mesh is defined by the mesh characteristics formed by a contiguous set of non-overlapping elements delimited by a set of faces, by the definition of the physical boundaries through the marking of the faces boundary and by the manner how they are related and located one with respect to the other.

Bearing in mind the considerations about the FVM in subsection 2.3.1, OpenFOAM has implemented a finite volume cell-centred discretisation of the domain - Moukalled et al. (2015). The data for points, faces, and elements are stored in a number of lists (arrays). The list of points contains the three dimensional spatial coordinates, defined as vectors, which correspond to the vertices of the actual mesh. Moreover, each vertex has a label defined by the position in the list. The faces are defined by a list of labels referring to points in which the ordering is such that each two adjacent points are connected by an edge. The face list is organized in a way that all internal faces appear first in the list followed by faces related to the first boundary, then faces related to the second boundary, and so on. Lists of boundary faces are also named patches. It is important to remember that internal faces belong to two cells while boundary faces belong to one cell only. Finally, the element or cell list is defined by a list of indices, where the position in that list is the cell index, the first index at any position is the number of faces for that element, and the face indices at a given position represent the faces for that cell.

In OpenFOAM the mesh is named `polyMesh` and has to be defined with a set of proper files. These files are placed in the directory `constant/polyMesh`. Based on the previous description the names of the files whose contents are self-explanatory are given by `points`, `faces`, `owner`, `neighbour` and `boundary`. Particularly, for the analysis performed in this thesis, it was used the Gmsh to assemble the several meshes, as mentioned

in section 3.1. To convert the .msh file written by Gmsh to OpenFOAM it was used the gmshToFoam tool provided by the OpenFOAM.

3.2.2 The PIMPLE Algorithm

The Pressure-Implicit Method for Pressure-Linked Equations (PIMPLE) - OpenFoam (a) - algorithm is used to solve the Navier-Stokes equations described in section 2.3.6. This algorithm combines the Pressure Implicit Splitting of Operators (PISO) algorithm with the iterative Semi-Implicit Method for Pressure-Linked Equations (SIMPLE) algorithm.

The PISO - OpenFoam (b) - algorithm is one of the most well-accepted algorithms found in the OpenFOAM framework. This algorithm can determine the velocity and pressure combination found between the continuity and Navier-Stokes equations by isolating the pressure and velocity solving procedures in an iterative fashion. Succinctly, after solving one field, the calculated result is plugged into the equation set as a constant in the calculation of the other field. This process is then repeated until an acceptable error tolerance is reached. This algorithm is suitable for transient simulations where it is necessary to fully solve the velocity-pressure coupling for each time step. The non-linear effects of the velocity are reduced setting small time steps characterized by Courant numbers below one.

The SIMPLE - OpenFoam (c) - algorithm is the algorithm generally used in steady-state problems, where the treatment of the non-linear effects of the velocity during the resolution is more important than the precise determination of the pressure field. Each iteration of this algorithm corresponds to a pseudo time step and, consequently, the solved values are under-relaxed in order to stabilize and converge the results.

The PIMPLE algorithm associates the SIMPLE loop with the solving technique implemented in the PISO algorithm. The equations inside the SIMPLE loop are solved as many times as required to reach convergence for each time-step or until the maximum number of outer iterations is reached, value fixed by the user - Moukalled et al. (2015).

3.2.3 Case study setup - OpenFOAM File System overview

The OpenFOAM file system is constituted by three distinct folders: system, constant, and 0, as illustrated in figure 3.4.

3.2.3.1 CaseStudy/0 folder - initial conditions

The CaseStudy/0 folder files contain the information about the simulation initial values and boundary conditions. OpenFOAM will add to this directory several folders which names are based on the simulated time at which the data is written. Having this in mind and taking into account that the performed simulations start at time $t = 0$, it is only logic that the problem initial conditions are stored in a directory named 0: the velocity field U and pressure field p are initialised from files 0/ U and 0/ p , respectively.

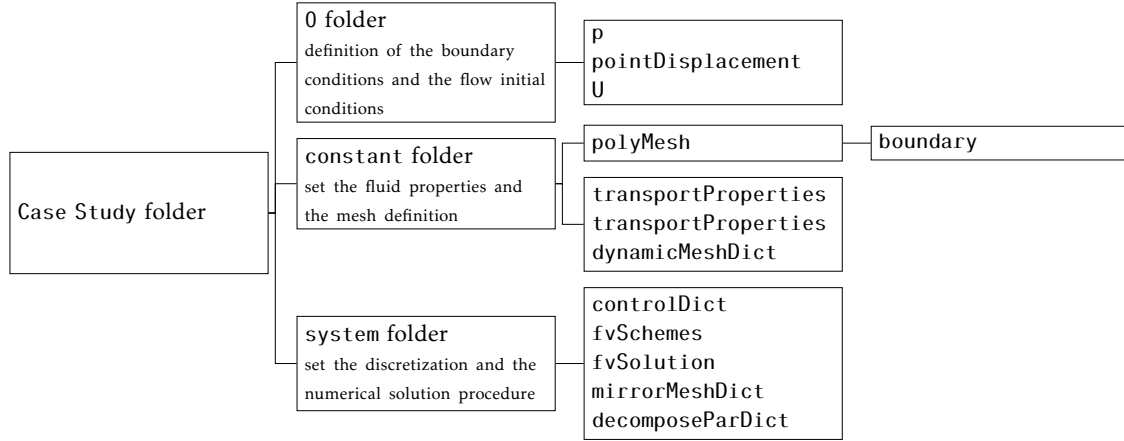


Figure 3.4: OpenFOAM File System overview.

In OpenFOAM physical properties need to be specified with their associated dimensions. According to SI unit system, the parameter dimensions stands for the following physical dimensions: $[kg\ m\ s\ K\ mol\ A\ cd]$. For instance, the definition of the kinematic pressure, which corresponds to the ratio between the pressure ($Pa = kg.m^{-1}.s^{-2}$) and the mass density ($kg.m^3$), which SI unit is $m^2.s^{-2}$ is represented by the $[0\ 2\ -2\ 0\ 0\ 0\ 0]$ dimensions vector. Similarly, in the U file the dimensions are defined as $[0\ 1\ -1\ 0\ 0\ 0\ 0]$.

Following that, it is needed to define the `internalField`. This parameter defines the values along the mesh cell volumes and might assume two distinct values: `uniform`, for which a single value is assigned to all elements within the domain, and `nonuniform`, for which different values can be assigned to each cell according to its ids. For the cases simulated in this thesis, it was used the atmosphere pressure as starting point and, therefore, the `internalField` property assumes the value `uniform 0` in the `p` file. For the velocity, this parameter was set to $1m.s^{-1}$ and points in the direction of the coordinate x axis which in the `U` file is translated to the value `uniform (1 0 0)`. This format is easy to understand since the velocity is a vector that has three different components ($U_x\ U_y\ U_z$).

Finally, the `boundaryField` defines the mesh boundary conditions. This parameter is a dictionary containing a set of entries whose names correspond to each of the names of the boundary patches listed in the boundary file in the `polyMesh` directory. Each patch entry is itself a dictionary containing a list of keyword entries. The `pair` entry and `type` describe the patch field condition specified for the field. The remaining entries correspond to the type of patch field condition selected and can typically include field data specifying initial conditions on patch faces.

The files `p` and `U` were configured for the several simulations performed in this thesis. The `zeroGradient`, also called homogeneous Neumann boundary condition, means that the quantity gradient is zero perpendicularly to the domain boundary. When the boundary condition is defined as `empty` this means that there is no flow in the direction perpendicular to the boundary. The `fixedValue` patch type, also named the Dirichlet

boundary condition, means there is a fixed value for the correspondent boundary condition along all the simulation. The `movingWallVelocity` parameter set in `U` file for the cylinder boundary defines that the velocity is associated with the cylinder under consideration.

In addition to the `p` and `U` files, we have the `pointDisplacement` file. In this file are defined the cylinder characteristics, the problem degrees of freedom which restrict the body movement and constraints related with the mass-spring-damper system in the desired directions.

3.2.3.2 CaseStudy/constant folder - initial conditions

The constant directory contains in the `polyMesh` folder the files that fully describe the case mesh. In this directory root are defined the boundary file which specifies the simulation boundary properties and the `dynamicMeshDict`, `transportProperties` and `turbulenceProperties` files which specify the physical properties of the simulation fluid.

3.2.3.3 CaseStudy/system folder - system parameters

The `CaseStudy/system` directory files set the parameters associated with the solution procedure itself. In this thesis context it was defined the `controlDict` file, where several run control parameters were defined including start/end time, time-step and parameters for data output. In greater detail, `controlDict` has defined a wide range of parameters that determine the simulation output. For instance, the value of the `startFrom` was set to `latestTime` in order to allow to restart the simulation from the most recent time step from the set of time directories. This directory contains also the `fvSchemes` file where are defined the finite volume discretisation schemes used in the simulation and the `fvSolution` file which sets the equation solvers and tolerances.

The OpenFOAM requires at least the definition of the previously three referred files. Nevertheless, in this thesis context it were used two additional files: the `decomposeParDict` which allows to perform the simulation with parallel computing, in which the geometry and associated fields are broken into pieces and allocated to separate processors for solution; and the `mirrorMeshDict` file which mirrors the mesh around a given plane.

3.2.4 State-of-the-art: computational fluids dynamics tools

Despite the great potential of OpenFOAM, there is available alternative tools to perform numerical simulation the CFD field. Examples such as Ansys Fluent or Autodesk CFD, which have a strong implementation in the market being used in several businesses areas. Nevertheless, these tools have the disadvantage of not being open-source nor having the flexibility to change the source code recombining allowing the implementation of algorithms fitted for the case in analysis. Table 3.3 provides a brief description of the possible alternatives tools within the computational fluid mechanics area.

Table 3.3: OpenFOAM alternative softwares to perform numerical fluid simulation.

Software	Description
ANSYS Fluent (ANSYS)	Used in much of the industry and scientific world, this software is the best known and trusted in the context of computational fluid mechanics. An extensive track record makes Ansys Fluent an excellent tool that can serve as a reference for comparisons between numerical studies.
Autodesk CFD (Autodesk)	With the advantage of being a software implemented by the company that developed the well-known software to handle CAD projects, the AutoCAD, this software has the advantage of being able to numerically process CFD projects in CAD.
SU2 (SU2)	Similar to OpenFOAM, this software is open-source and enables code customization enabling, this way, greater flexibility when compared to traditional commercial software.
STAR-CCM+ (cd adapco)	Developed by SIEMENS, this software possesses a strong component in the industry optical, constituting a strong alternative in the context of computational fluid mechanics in the industrial sector.
SALOME (CASCADE)	SALOME is an open-source software that provides a generic platform for pre and post processing in CFD numerical simulation. It is based on an open and flexible architecture made of reusable components.

3.3 Numerical Stability

The analysis of the numerical scheme stability is crucial in a CFD study. A numerical method is referred to as being stable when the iterative process converges and as being unstable when it diverges. As mentioned in chapter 2, a common methodology used in CFD codes for steady problems is to solve the unsteady equations and march in time until the solution converges to a steady state. Therefore, numerical stability studies are performed in the context of time-marching, in which are evaluated the asymptotic behaviour of a given problem at large times. So, ideally, we would like to take as large a time-step δt as possible to reach the steady state in the least number of time-steps. Usually the value of δt has a maximum allowable time-step δt_{max} beyond which the numerical scheme is unstable. If $\delta t > \delta t_{max}$, the numerical errors will grow exponentially in time causing the solution to diverge from the steady-state result. The δt_{max} value is related with the numerical discretisation scheme and with the problem complexity.

The Courant number, Co , is a dimensionless parameter given by equation 3.1 which translates the best temporal accuracy and numerical stability during the simulation.

$$Co = \frac{\delta t |U|}{\delta x} \quad (3.1)$$

where δt is the time step, $|U|$ is the magnitude of the velocity through that cell and δx is the cell size in the direction of the velocity.

The Courant number, Co , depends on the flow velocity, cell-size and time-step and is typically calculated for each cell. The Courant number will change accordingly with the velocity for a static mesh and a constant time-step. When the mesh is static and the velocity field is nearly fully developed, changing the time step is a good way of controlling the Courant number.

The Courant number is an important parameter because informs about how fluid is moving through the computational cells. A particular problem has an acceptable stability when the Courant number is ≤ 1 . If the Courant number is ≤ 1 this means that the fluid particles are moving from one cell to another within one time-step at most. If it is > 1 the fluid particles are moving through more than one cell at each time-step and this can affect convergence negatively. Robust systems and good solvers can deal with large Courant numbers, but it is always important to check this parameter to confirm that there are no convergence problems, affecting the accuracy of a transient simulation.

3.4 Simulations preformance

In this section are shown in table 3.4 the specifications of the machine used to perform the studies described in this thesis.

Table 3.4: Specifications of the machine used to performed the CFD simulations.

	Processor	Graphics	OS type
Computer	Intel® Core i7 5820K CPU @ 3.30GHz × 12	Quadro K620/PCIe/SSE2	Ubuntu 14.04

The average length of the simulation duration for a $2500D$ mesh with 82404 cells, was 46h12min with the simulation running in parallel mode, using six processors for each simulation.

FLOW AROUND A FIXED CYLINDER

In this chapter it is described the CFD study of a flow around a non-oscillatory cylinder. This analysis was performed in a validation context, so we can have confidence on the results obtained where the study with a cylinder with two DOF is described. Validation is a crucial procedure in a good CFD analysis. Validation certifies if the pre-processing was correctly done, namely, ensures that the numerical code definitions and the mesh specifications are well established for the intended case study. A good definition for a validation in CFD can be described as "solving the right equations and solving the equations right", Versteeg and Malalasekera (2007). In this chapter, it is given special emphasis to the mesh independence study which is essential to validate the meshes used throughout this thesis.

4.1 Independence mesh study

4.1.1 Analysis of the fundamental quantities convergence with the $2500D$ mesh discretisation

The domain chosen for the developed meshes was $2500D$, where D corresponds to the diameter of the cylinder. This size was defined accordingly to the studies that were used to perform a comparison analysis in chapters 5 and 6. This diameter is big enough so it allows the minimization of the blockage effect, which occurs when the cylinder outer walls are excessively near to the domain boundaries. For studies with one and two DOF this configuration enhances the development of multiple vortex shedding patterns along the wake as well as the cylinder displacement.

The first length of the elements near the cylinder wall is determined using the geometric progression 4.1.

$$S_n = \sum_{i=1}^n a_1 r^{i-1} = \frac{a_1(r^n - 1)}{r - 1} \quad (4.1)$$

The S_n is the radial distributed nodes length, r is the progression value, a_1 is the length of the first node and the n is the number of radial nodes.

In order to conclude about the refinement level quality and the time step for which the results converge, a considerable number of simulations were made to determine which mesh best suited the cylinder problem. The studies were conducted with a Reynolds number of $Re = 200$ and, therefore, the flow regime can be considered as laminar, with a non-slip condition applied to the cylinder wall of ($u = v = 0$) and with a velocity at infinity $U_\infty = 1 \text{ m.s}^{-1}$ on the domain boundary.

The table 4.1 compares the results of several key quantities obtained for the different levels of mesh refinement, depending on the number of elements around the cylinder, N_{ang} , the number of elements in the radial direction, N_{rad} , and the thickness of the first element along the cylinder wall, $\frac{\epsilon}{D}$.

It was chosen to vary the elements in the radial and angular directions progressively to prove the mesh independence. For that, the length of the smallest element was defined with two different values: $\frac{\epsilon}{D} = 0.0012$ and $\frac{\epsilon}{D} = 0.0006$, being these elements the ones along the cylinder wall. With this configuration, it was observed how the results were altered with the increase of the number of elements at radial level, angular and both jointly with the decreasing of the size of the elements along the cylinder wall. Tests have also been made using progressions of value 1.06, 1.04, 1.03 and 1.02 having as direction the mesh boundary to the cylinder.

Analysing table 4.1 it is possible to conclude that the results are similar without large fluctuations for the several studied meshes. Furthermore, the obtained results are also congruent with the data described in the literature, subject that will be analysed in greater detail in section 4.2.

With the incrementing of the number of elements in the mesh the simulation time increases drastically. For this reason, it was opted for a mesh that met the "best of both worlds", allowing good results in conjunction with an acceptable and viable simulation time. With this in mind and since all the meshes in table 4.1 are a good approximation of reality, it was chosen to perform the simulations carried out throughout this work with mesh 1. This choice was also influenced by the fact that it is possible to obtain a fast discretisation of the results with this mesh. Figure 4.1.1 sustain this statement, given that the moment when the vortices begin to be released coincides with the start of the graphical oscillation of drag and lift coefficient. Both these phenomena can be related since the oscillation of the pressure field in the cylinder wake will lead to the release of vortices.

The time-point when the flow oscillation begins for the several meshes enumerated in table 4.1 was examined from the respective image in figure 4.1.1. From this analysis it is possible to conclude that the mesh configuration influences the moment when the flow

Table 4.1: Relation between the fundamental quantities convergence with the discretization variation for meshes with $2500D$ domain length and $Re = 200$.

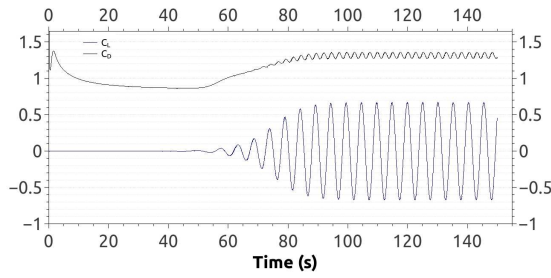
Mesh	$\frac{e}{D}$	N_{rad}	N_{ang}	N_{cells}	r	St	$C_{D,mean}$	$C_{D,rms}$	$C_{L,rms}$
1	0.0012	189	436	82404	1.06	0.1953	1.3187	0.0308	0.4727
2	0.0012	189	596	112644	1.06	0.1957	1.3188	0.0309	0.4722
3	0.0006	201	716	143916	1.06	0.1954	1.3189	0.0310	0.4741
4	0.0006	201	916	184116	1.06	0.1952	1.3184	0.0309	0.4645
5	0.0006	201	1116	224316	1.06	0.1957	1.3177	0.0309	0.4674
6	0.0012	271	476	128996	1.04	0.1952	1.3180	0.0308	0.4721
7	0.0012	271	716	194036	1.04	0.1951	1.3184	0.0309	0.4717
8	0.0006	289	476	137564	1.04	0.2081	1.3177	0.0309	0.4704
9	0.0006	289	716	206924	1.04	0.1952	1.3172	0.0308	0.4694
10	0.0006	289	1116	322524	1.04	0.1951	1.3161	0.0308	0.4633
11	0.0012	349	556	194044	1.03	0.1950	1.3186	0.0308	0.4715
12	0.0012	349	876	305724	1.03	0.1951	1.3161	0.0306	0.4679
13	0.0006	373	956	356588	1.03	0.1951	1.3183	0.0310	0.4648
14	0.0006	373	1236	461028	1.03	0.1958	1.3161	0.0307	0.4571
15	0.0012	501	1116	559116	1.02	0.1953	1.3176	0.0306	0.4629
16	0.0006	539	1116	601524	1.02	0.1961	1.3165	0.0308	0.4536

oscillation begins. The fact that the initiation of vortices release occurs at different times is related with the used numerical diffusion scheme, with the used turbulence model and with the refinement level of the mesh. Applying erroneous numerical diffusivity schemes or steady solvers will lead to incorrect simulation results. Regarding the numerical diffusivity scheme, it was used the same along the performed simulations. Concerning the used solvers, steady solvers are not suitable to solve the problem studied in this thesis since it will induce the fluid to "relax", in order to force the fluid unsteadiness to become steady. This circumstance would influence negatively the numerical study results. Hence, it was used `pimpleFoam`, an unsteady solver which is suitable to simulate unsteady flows, fact that was already discussed in greater detail in section 3.2.2. Finally, it were not used turbulence models since for a $Re = 200$ the fluid has a laminar flow, as can be seen in table 2.1.

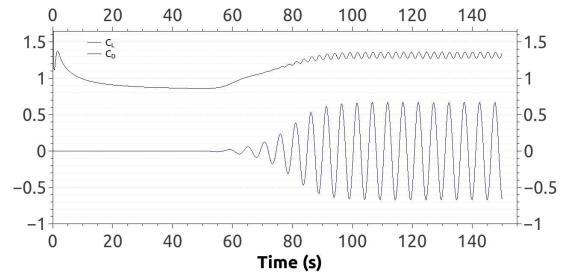
Thus, the only changed parameter was the mesh refinement level by increasing the element's density along the cylinder boundary wall applying a geometric progression in the cylinder radial direction. The refinement level must be greater at the cylinder walls where the development and respective release of vortices occurs at the cylinder

downstream wall. Thereby, and given that this is the area most susceptible to changes by the development of the boundary layer, it is in this domain region where we must have smaller mesh elements so we can study in greater detail the vortices development phenomena.

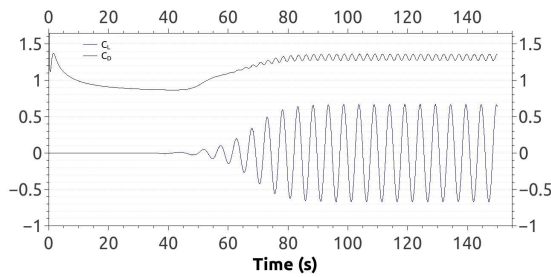
Furthermore, the mesh will also influence the time hiatus until the vortices release occurs at a constant frequency. For mesh 1 this stabilization occurs after 90 seconds, which is a quite acceptable result taking into account the data described by C. Y. Zhou and Lam (1999), Conde and Lopes (2015) and T. Li and Zhu (2009). This mesh is shown in figure 3.1 of chapter 3.



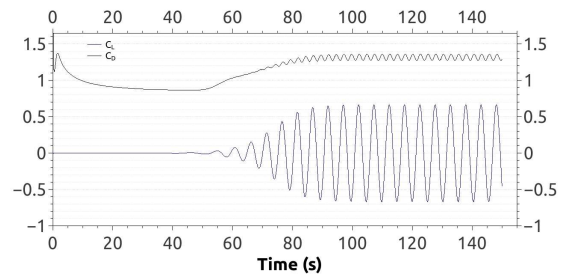
(a) Mesh 1



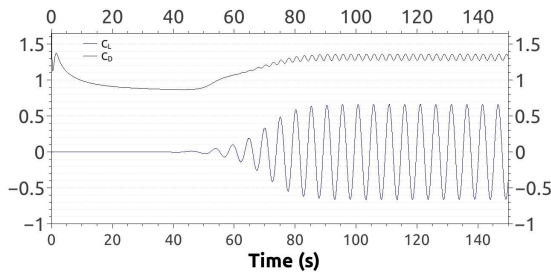
(b) Mesh 2



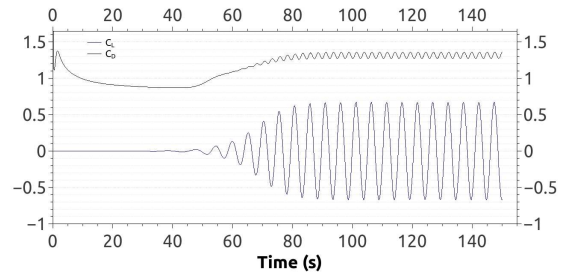
(c) Mesh 3



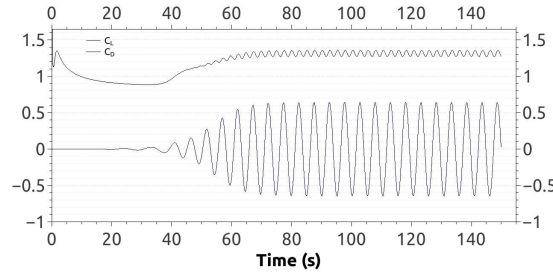
(d) Mesh 4



(e) Mesh 5



(f) Mesh 6



(q) Mesh 16

Figure 4.1: Drag, $C_{D,mean}$, and lift, $C_{L,rms}$, coefficients for the set of meshes shown in table 4.1.

4.1.2 Analysis of the fundamental quantities convergence with the time step for a mesh with $2500D$ domain length

In table 4.2 is shown the relation between flow fundamental quantities with the time step for the mesh 1 whereas figure 4.2 illustrates these results graphically. Analysing this data, it is possible to conclude that from a time step of $\delta t = 0.001s$ the obtained results will not be significantly influenced by this parameter, presenting all the studied time step values good convergence results.

Table 4.2: Relation between the fundamental quantities convergence with the time step variation for the mesh 1 with $2500D$ domain length and $Re = 200$.

Time step (s)	St	$C_{D,mean}$	$C_{D,rms}$	$C_{L,rms}$
0.1	0.1867	1.2280	0.0526	0.3159
0.05	0.1978	1.3126	0.0329	0.4177
0.01	0.1933	1.3172	0.0308	0.4688
0.005	0.1952	1.3184	0.0308	0.4724
0.001	0.1953	1.3187	0.0308	0.4727
0.0005	0.1954	1.3153	0.0316	0.4683

Regarding the mesh independence study, Didier (2012) states that the choice of the mesh to study the flow fundamental quantities convergence must be performed when between meshes these fundamental quantities vary as low as possible with the modification of the mesh refinement level and time step. Evaluating table 4.2, it is possible to conclude that the results variation with the change of the mesh refinement is small and can be negligible. Similarly, it is also possible to infer that the obtained results are approximately stable with the decreasing of the time step and, consequently, not affected by this parameter. Both these facts sustain the validation of mesh 1 to proceed with the study of the flow around a cylinder for one and two DOF, since the impact of the simulation time step and the mesh refinement within the studied range of values are irrelevant in the simulation result.

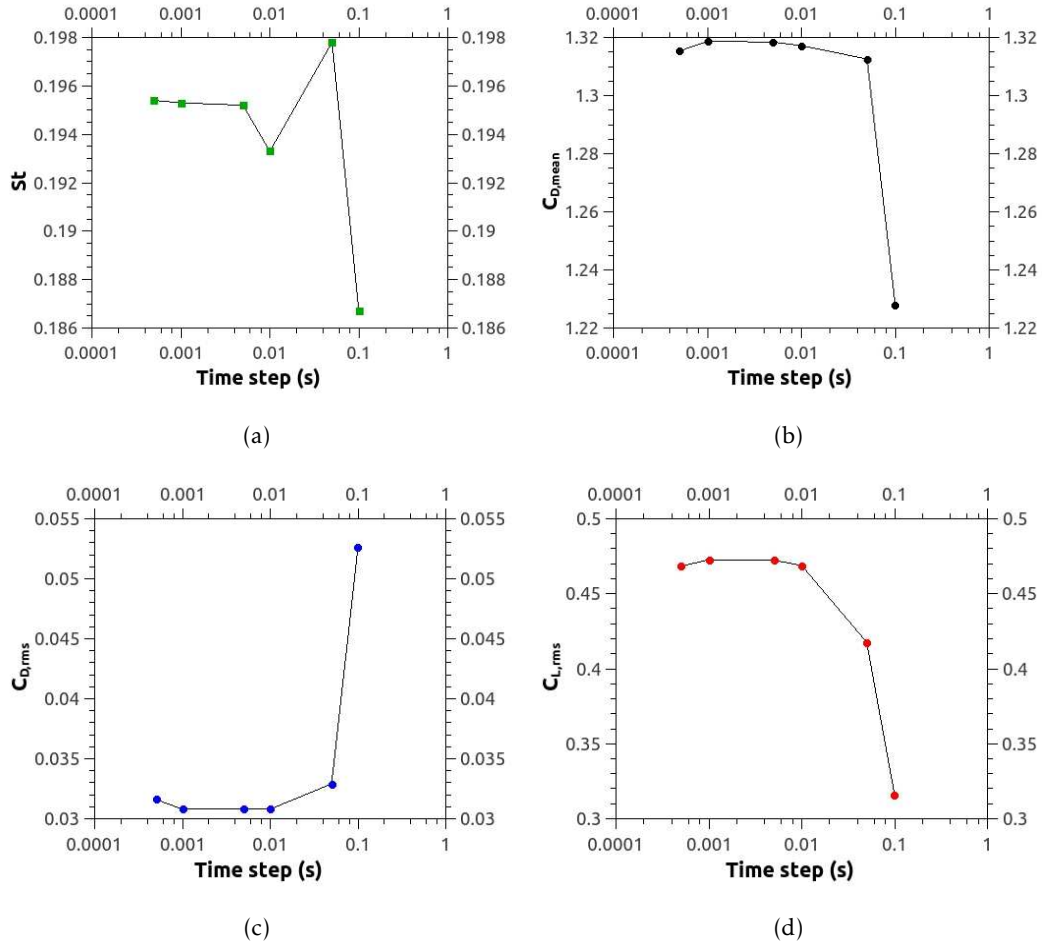


Figure 4.2: (a) Evolution of the St with the time step; (b) Relation between the $C_{D,mean}$ convergence with the time step; (c) Relation between the $C_{D,rms}$ convergence with the time step; (d) Relation between the $C_{L,rms}$ convergence with the time step. Values for the mesh 1 with $2500D$ domain length and $Re = 200$.

4.1.3 Analysis of the fundamental quantities convergence with the domain length

Table 4.3 compares the simulation fundamental quantities between several mesh domains values, $\frac{L_b}{D}$, varying between the values $8D$, $20D$, $500D$ and $2500D$. For all the developed meshes, the smallest element thickness, adjacent to the cylinder boundary, is 0.0012 , the time step, δt , is $0.001s$ and the progression value, r , is 1.06 (equation 4.1). In chapters 5 and 6 will be studied in greater detail how the domain extension impacts the cylinder movement for one, Y-motion, and two DOF.

Table 4.3: Relation between the flow fundamental quantities convergence with the domain length, L_b , and $Re = 200$.

$\frac{L_b}{D}$	$\frac{e}{D}$	N_{rad}	N_{ang}	N_{cells}	r	St	$C_{D,mean}$	$C_{L,rms}$
8	0.0012	89	436	38804	1.06	0.2	1.3951	0.5131
20	0.0012	106	436	46216	1.06	0.2	1.3449	0.4806
500	0.0012	162	436	70632	1.06	0.1955	1.3243	0.4779
2500	0.0012	189	436	82404	1.06	0.1953	1.3187	0.4727

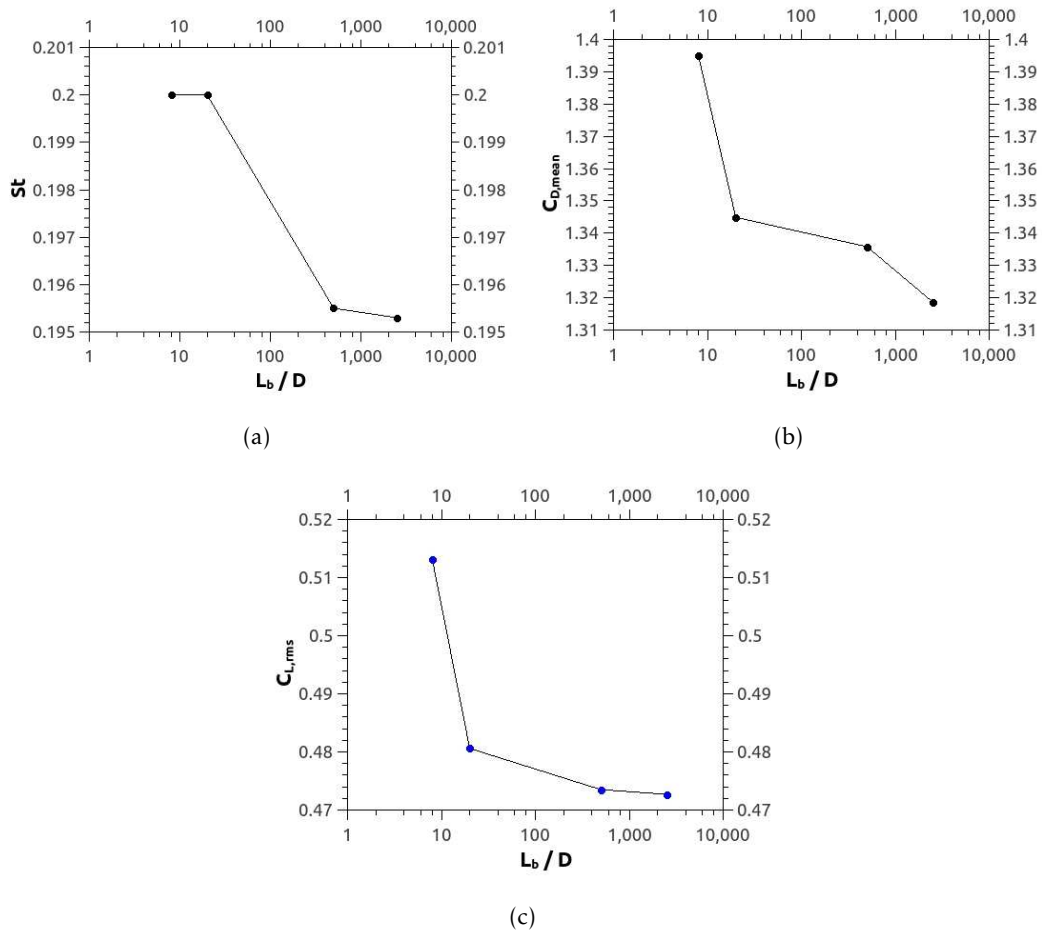


Figure 4.3: (a) Evolution of the St with the domain length variation for $Re = 200$; (b) Relation between the $C_{D,mean}$ convergence with the domain length variation for $Re = 200$; (c) Relation between the $C_{L,rms}$ convergence with the domain length variation for $Re = 200$.

From the results described in the table 4.3 it is possible to conclude about the dependence of the fundamental quantities with the extension of the mesh domain. The obtained results express a clear tendency for the mesh fundamental quantities to decrease with the increasing of the mesh length. This fact is congruent with the results obtained by Posdziech and Grundmann (2007).

4.1.4 Analysis of the fundamental quantities convergence with the 8D mesh discretisation

Table 4.4 correlates the fluid fundamental quantities between the meshes with the 8D domain. Analysing this data, it is possible to reckon that the mean drag coefficient decreases as the level of mesh refinement increases. Regarding the lift coefficient, its standard deviation is not influenced by the mesh refinement since this coefficient remains in the same range of values with the domain higher discretisation.

The current validation sustains that, despite meshes with greater refinement level translate with greater reliability the reality, for the presented discretisation values the increase of the mesh discretisation is not crucial in the attainment of relevant better results. The three levels of discretisation enumerated in table 4.4, will be later used to study in chapter 6 the influence of a flow around a cylinder with 2 DOF.

Table 4.4: Relation between the fundamental quantities convergence with the discretisation variation for meshes with 8D domain length and $Re = 200$.

$\frac{L_b}{D}$	$\frac{e}{D}$	N_{rad}	N_{ang}	N_{cells}	r	St	$C_{D,mean}$	$C_{L,rms}$
8	0.0049	45	136	6120	1.10	0.2430	1.4156	0.5152
8	0.0012	89	436	38804	1.06	0.2	1.3951	0.5131
8	0.0012	89	536	47704	1.06	0.2233	1.3953	0.5152

4.2 Flow around a non-oscillatory cylinder

In the current section is presented the study for the flow around a fixed cylinder. Next, the obtained results are compared with the data described in the literature to validate the methodology described in chapter 3.

Table 4.5 shows the results described in subsection 4.1.1 for mesh 1 in comparison with the results obtained by other authors for the flow around a fixed cylinder with $Re = 200$. The fundamental quantities compared between studies, are the mean drag coefficient, $C_{D,mean}$, the standard deviation of lift coefficient, $C_{L,rms}$, and the Strouhal number, St , calculated using the Fast Fourier transform (FFT) which was determined by the software QtiPlot (2004). In detail, the Strouhal number was determined by using the lift coefficient values, extracting full oscillation periods after the stabilization of the oscillation phenomenon.

The fundamental quantities determined by other authors, presented in table 4.5, were extracted from studies performed with $Re = 200$. By the comparison of the data enumerated in table 4.5 it is possible to conclude that the obtained results for the fixed cylinder are congruent with the results described in the literature. Note that with the increase of the distance between the cylinder boundary wall and the mesh outer border, the greater is the tendency for the flow fundamental quantities values to decrease. Nevertheless, it

is important to refer that to achieve valid fundamental quantities is not only necessary to increase the distance between the outer boundary of the mesh and the cylinder wall, but also the mesh refinement level has relevant influence in the numerical calculation of fundamental quantities. This fact was not relevant in the study performed in subsection 4.1.1 because the discretisation starting values were already good enough to simulate accurately the reality.

Table 4.5: Comparison of fundamental quantities obtained in this thesis with the data described in the literature for a flow around a fixed cylinder, $Re = 200$.

Authors	$\frac{L_b}{D}$	St	$C_{D,mean}$	$C_{L,rms}$
Current thesis	2500	0.1953	1.3187	0.4727
Conde and Lopes (2015)	50	0.1961	1.3326	0.4804
Didier (2012)	2500	0.1941	1.3099	0.4680
Posdziech and Grundmann (2007)	2000	0.1940	1.3090	0.4378
Posdziech and Grundmann (2007)	4000	0.1940	1.3086	0.4374

Figure 4.4(a) illustrates the spectral analysis of the lift coefficient over the FFT and the release of vortices frequency, equivalent to the Strouhal frequency, f_{st} which is mathematically translated by equation 2.3. This frequency corresponds to the amplitude peak in figure 4.4(a) which has a value of $f_{st} = 0.1953$. This value is equal to the number of Strouhal, St , shown in table 4.5 given that it was considered both the cylinder diameter and the flow velocity with an unitary value. Figure 4.4(b) shows the drag and lift coefficients from which it is possible to observe that the periodic regime and the consequent stabilization of the vortices alternating release is obtained around a dimensionless time of 90.

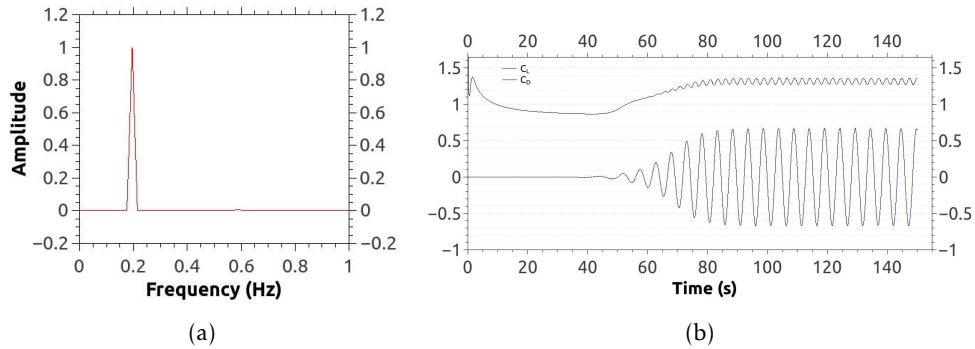


Figure 4.4: (a) Spectral analysis of the fixed cylinder; (b) Drag and lift coefficients, C_D and C_L , time series for Mesh 1.

Figure 4.5(a) shows the flow velocity field for the numerical time of $t = 140s$. It is possible to observe at the cylinder upstream area the stagnation point. The top and bottom areas of the cylinder are where the flow reaches higher speed values due to the

"compression" of the flow induced by the rhombic body presence which causes the flow to split to both these areas. This phenomenon is easily observable in figure 4.5(d), which shows the flow streamlines and where it is clear the streamlines compression in the areas where the flow reaches higher speed values. It is interesting to note that in the zone where the vortex is developed, in this case the top zone as it can be seen in figure 4.5(c), the flow velocity decreases considerably contrasting with the symmetrically opposite area, in this case the bottom zone. While the flow velocity increases when the vortices are released, the pressure is much higher when the vortex is being formed. Consequently, the pressure value is lower on the cylinder bottom zone, where the vortex is being released, in opposition with the cylinder top zone where the vortices are in development.

Moreover, it is also possible to observe that when the vortex is generated, the flow gains rotational speed around a point, the center of the vortex, where the speed is zero and the pressure is maximal. As the vortex moves on the wake, loses intensity, spreading itself, tending its pressure and velocity to homogenize with the field value of pressure and velocity.

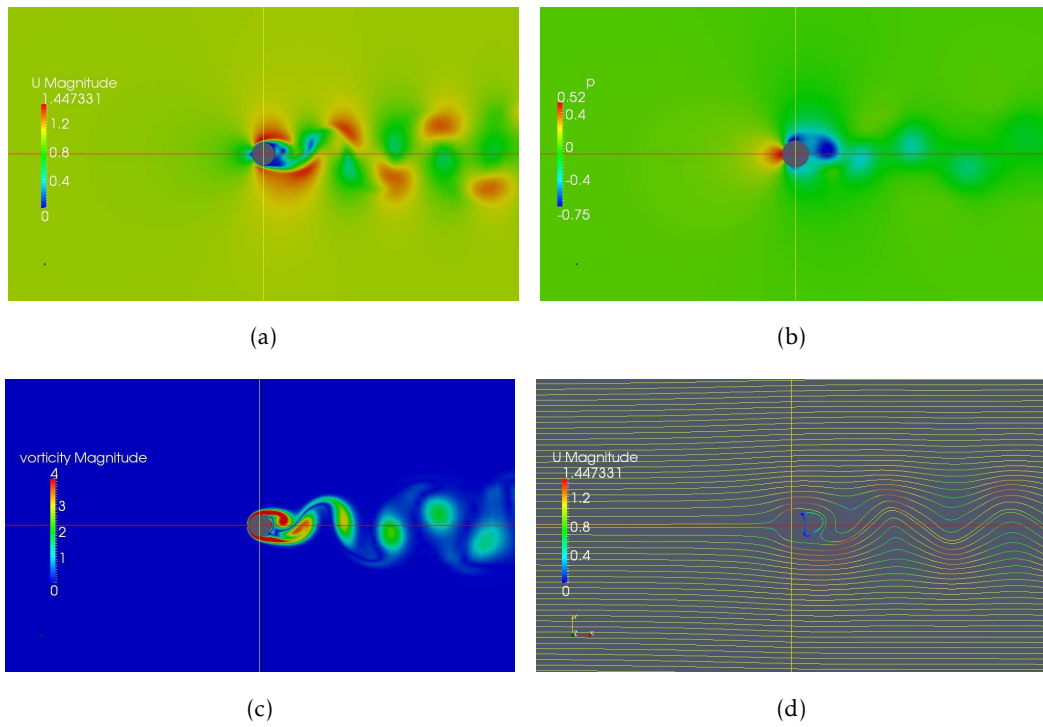


Figure 4.5: (a) Velocity field near to the cylinder for $time = 140(s)$; (b) Pressure field near to the cylinder for $time = 140(s)$; (c) Vorticity for $time = 140(s)$; (d) Streamlines near to the cylinder for $time = 140(s)$.

FLOW AROUND A Y-ONLY MOTION CYLINDER

In this chapter it is studied a flow around a cylinder with one DOF. It will be performed a comparative study with the work developed by Conde and Lopes (2015). More specifically, it will be analysed for the same frequency ratios and flow conditions which is the influence of the domain length increase. The domain used in this thesis has $L_b = 2500D$ while the one used by Conde and Lopes has a $L_b = 50D$ size, having both studies a time-step δt of 0.001. The conclusions about this subject are exposed in section 5.1.

5.1 Comparative study between a 50D and a 2500D domain length mesh

The work developed by Conde and Lopes (2015) considered two distinct physical systems: a mass-spring system, which neglected the existence of damping forces; and a spring-mass-damper system, which simulates the damping caused by the structure, by the fluid and by the material itself.

The goal in this section is to analyse for one DOF how the increase of the mesh's domain influences the obtained result comparing, for that, the obtained results with the ones described by Conde and Lopes for a smaller domain. Thereby, all the other parameters related with the fluid, structure and simulation were kept constant and equal between both studies. In table 5.1 are enumerated the cylinder characteristics used to perform this study. The cylinder under study has a diameter D of 1 meter, mass m equal to 1 kg, cylinder length l of 1 meter and moments of inertia with respect to the x , y and z axes coordinates, defined by I_{xx} , I_{yy} and I_{zz} , respectively.

Similarly, table 5.2 introduces the fluid properties. Namely, this table lists the density defined by ρ , the dynamic viscosity defined by μ , the kinematic viscosity defined by ν

Table 5.1: Cylinder properties.

$D(m)$	$m(kg)$	$l(m)$	$I_{xx}(kg.m^2)$	$I_{yy}(kg.m^2)$	$I_{zz}(kg.m^2)$
1	1	1	0.146	0.146	0.125

and the flow field velocity defined by U_∞ .

Table 5.2: Flow properties.

$\rho(kg/m^3)$	$\mu(kg/m.s)$	$\nu(m/s)$	$U_\infty(m/s)$	$Pressure(Pa)$
1	0.005	0.005	1	Atmospheric

As mentioned in section 4.1.1, it was employed mesh 1 to perform the flow simulations. This is the least refined of the meshes shown in table 4.1 and it was selected among the other tested meshes because presented the best quality and simulation time ratio. In fact, to this mesh corresponds the lowest simulation time without prejudicing relevantly the results quality and allowing, this way, to perform all the proposed simulations within the deadlines establish for this work.

Table 5.3 contains the structural parameters associated with the simulation mass-spring and mass-spring-damping physical systems. For both mass-spring and mass-spring-damper systems the applied parameters were the same. The difference lies in the mass-spring-damper system in which is used a damping coefficient C shown in table 5.3.

Table 5.3: Simulation parameters for the mass-spring and mass-spring-damping systems to the cylinder with Y-only motion.

U^*	$f_n(Hz)$	$k(N/m)$	$C(N_s/m)$	$\frac{f_n}{f_{st}}$
1	1	39.5	0.63	5.1
1.5	0.667	17.6	0.42	3.4
2	0.5	9.87	0.31	2.56
2.5	0.4	6.32	0.25	2.05
3	0.333	4.38	0.21	1.71
3.5	0.286	3.23	0.18	1.46
4	0.25	2.47	0.16	1.28
4.5	0.222	1.95	0.14	1.14

5.1. COMPARATIVE STUDY BETWEEN A 50D AND A 2500D DOMAIN LENGTH
MESH

Table 5.3 - continuation: Simulation parameters for the mass-spring and mass-spring-damping systems to the cylinder with Y-only motion.

U^*	$f_n(Hz)$	$k(N/m)$	$C(N_s/m)$	$\frac{f_n}{f_{st}}$
5	0.2	1.58	0.13	1.02
5.5	0.182	1.31	0.11	0.93
6	0.167	1.1	0.1	0.86
6.5	0.154	0.94	0.097	0.79
7	0.143	0.81	0.09	0.73
7.5	0.133	0.7	0.084	0.68
8	0.125	0.62	0.079	0.64
8.5	0.118	0.55	0.074	0.6
9	0.111	0.49	0.07	0.57
9.5	0.105	0.44	0.066	0.54
10	0.1	0.39	0.062	0.51
10.5	0.095	0.36	0.06	0.49
11	0.091	0.33	0.057	0.47
11.5	0.087	0.3	0.055	0.45
12	0.083	0.27	0.052	0.42
12.5	0.08	0.25	0.05	0.41
13	0.077	0.23	0.048	0.39
13.5	0.074	0.22	0.046	0.38
14	0.071	0.20	0.045	0.36
14.5	0.069	0.19	0.043	0.35
15	0.067	0.18	0.042	0.34
15.5	0.065	0.16	0.041	0.33
16	0.063	0.15	0.040	0.32
16.5	0.061	0.145	0.038	0.31

Table 5.3 - continuation: Simulation parameters for the mass-spring and mass-spring-damping systems to the cylinder with Y-only motion.

U^*	$f_n(\text{Hz})$	$k(\text{N/m})$	$C(\text{Ns/m})$	$\frac{f_n}{f_{st}}$
17	0.059	0.14	0.037	0.30
17.5	0.057	0.13	0.036	0.29
18	0.056	0.12	0.035	0.286

The spring constant and the velocity ratio are intrinsically related by the equation 5.1 and 5.3 through which it is possible to obtain the spring constant value k from the velocity ratio U^* .

$$\omega_n = \sqrt{\frac{k}{m}} \quad (5.1)$$

The system natural frequency ω_n is given by the square root of the ratio between the spring constant k and the system mass m . The value of the system natural frequency can also be resolved by equation 5.2.

$$\omega_n = 2\pi f_n \quad (5.2)$$

The system velocity ratio U^* can be determined by the ratio between the flow velocity U_∞ and the natural frequency f_n times the cylinder diameter D which corresponds to equation 5.3.

$$U^* = \frac{U_\infty}{f_n D} \quad (5.3)$$

It follows from equation 5.3 that the velocity ratio is inversely proportional to the natural frequency of the system. Furthermore, by equation 5.1 it is observable that the spring constant is directly proportional to the natural frequency of the system. This means that springs with higher stiffness have associated higher natural frequency of the system and, consequently, the flow velocity must be increased to induce oscillation in the cylinder and overcome the forces provided by the spring to reach the same oscillation magnitude as for a spring offering less resistance.

Given that the fluid studied by Conde and Lopes has characteristics similar to a gas, the portion of the damping constant corresponding to the fluid damping and to the structural damping could be discarded. Therefore, the total damping factor ζ is described by the material damping value. For this reason, Conde and Lopes chose a common total damping factor of $\zeta = 0.05$, which is usually used in civil structures and is in accordance

5.1. COMPARATIVE STUDY BETWEEN A 50D AND A 2500D DOMAIN LENGTH MESH

with Blevins (1977) considerations. Thus, the damping constant C is calculated using equation 5.4 where C_C is the critical damping coefficient.

$$\zeta = \frac{C}{C_C} \quad (5.4)$$

The data in table 5.4 was extracted directly from the study developed by Conde and Lopes. In this table are defined a set of dimensionless parameters that impact the cylinder oscillation behaviour. These parameters are the mass ratio M^* and m^* , the mass-damping ratio $m^* \zeta$, the stability parameter K_s , and the Skop-Griffin parameter S_G .

Table 5.4: Obtained results to mass-spring system to cylinder with Y-only motion.

M^*	m^*	$m^* \zeta$	K_s	S_G
1	1.27	0.0635	0.628	0.152

5.1.1 Mass-Spring system

In this section it is performed the comparative evaluation between the results obtained in this study and the results obtained by Conde and Lopes for the mass-spring system. Figure 5.1 is a representative diagram of the mass-spring system, where the spring is anchored to the cylinder in its geometric center and fixed at a ground point which distance from the cylinder center is equal to the the spring's length at rest.

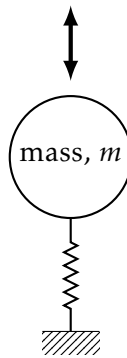
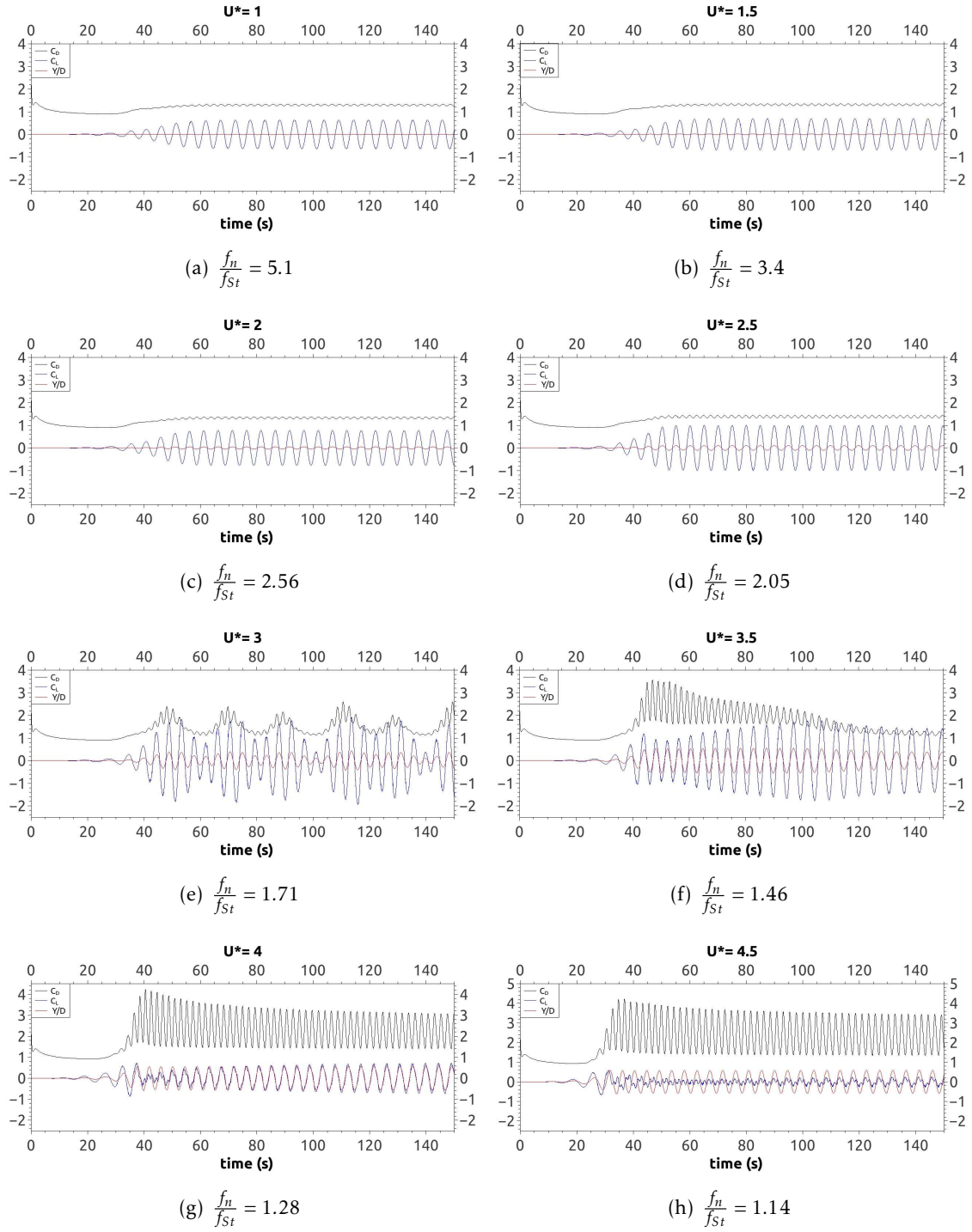
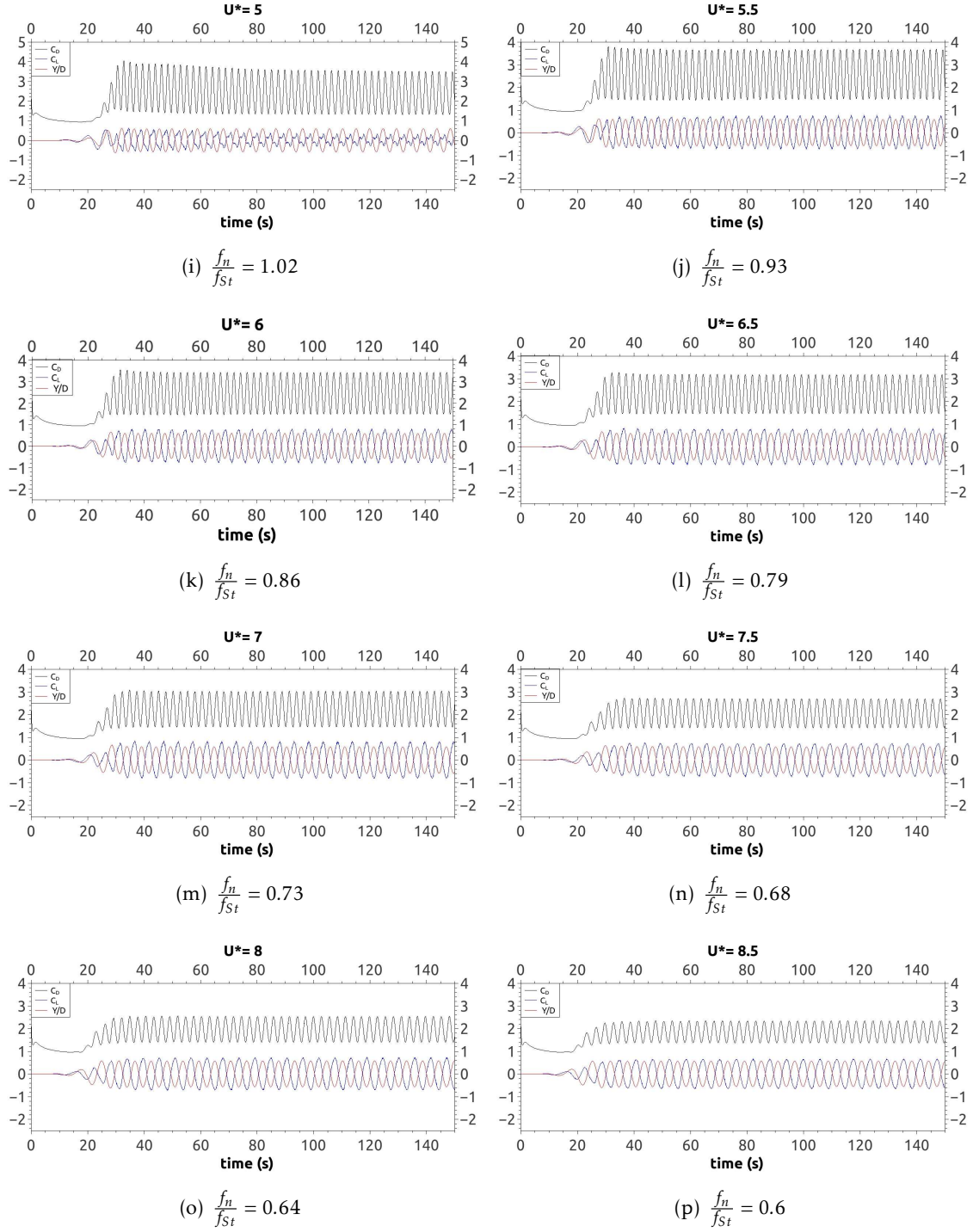


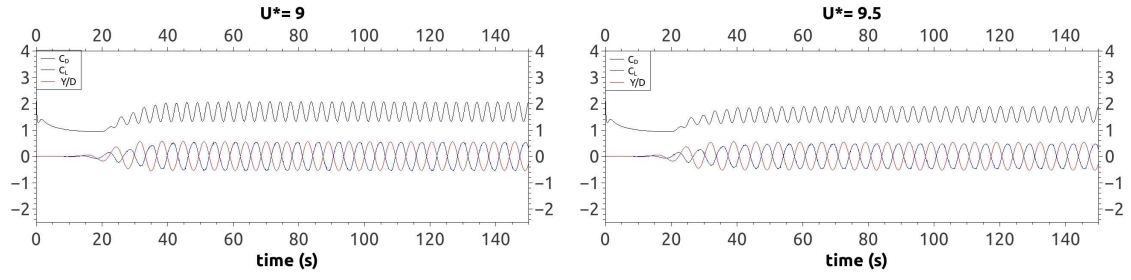
Figure 5.1: Mass-spring system schematic diagram.

In figure 5.2 are represented the drag coefficient in black, the lift coefficient in blue and the cylinder oscillation amplitude in red. These parameters are shown in function of the simulation time, which was defined as 150 seconds, time interval considered enough for the cylinder oscillation to achieve a constant frequency as can be observed by the figure 5.2 plots.



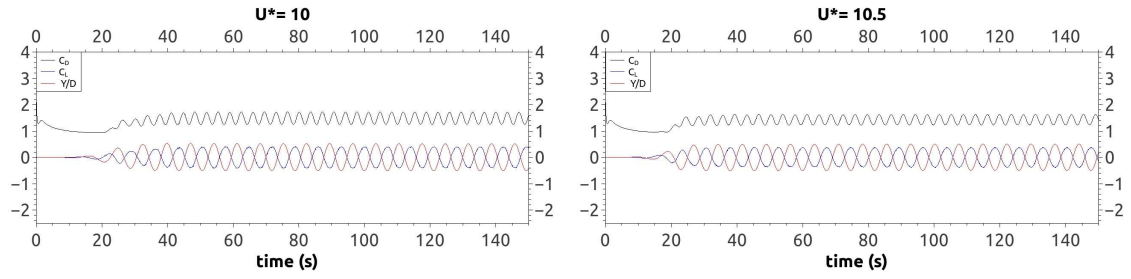
5.1. COMPARATIVE STUDY BETWEEN A 50D AND A 2500D DOMAIN LENGTH MESH





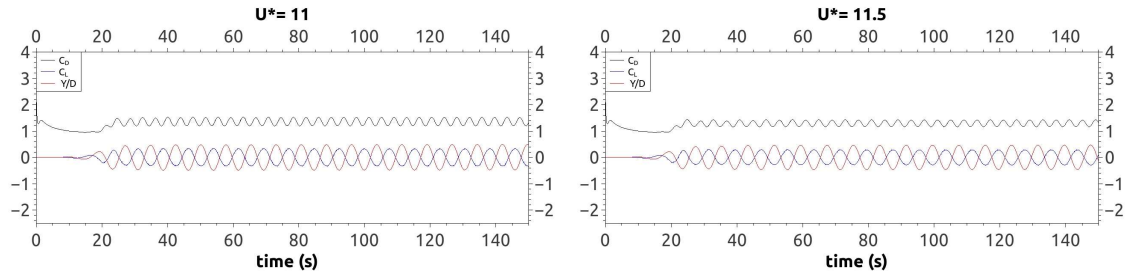
(q) $\frac{f_n}{f_{St}} = 0.57$

(r) $\frac{f_n}{f_{St}} = 0.54$



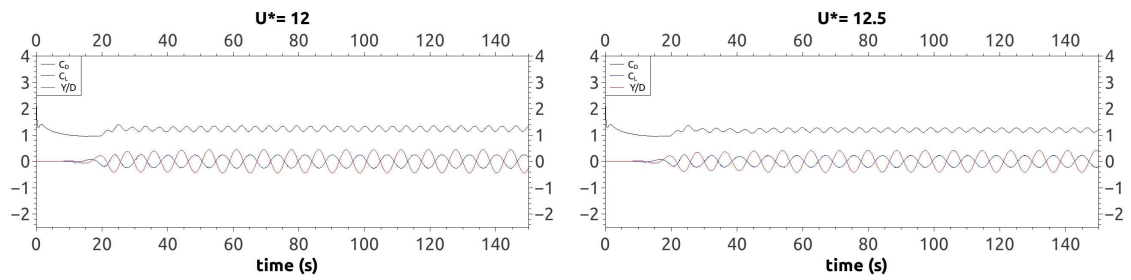
(s) $\frac{f_n}{f_{St}} = 0.51$

(t) $\frac{f_n}{f_{St}} = 0.49$



(u) $\frac{f_n}{f_{St}} = 0.47$

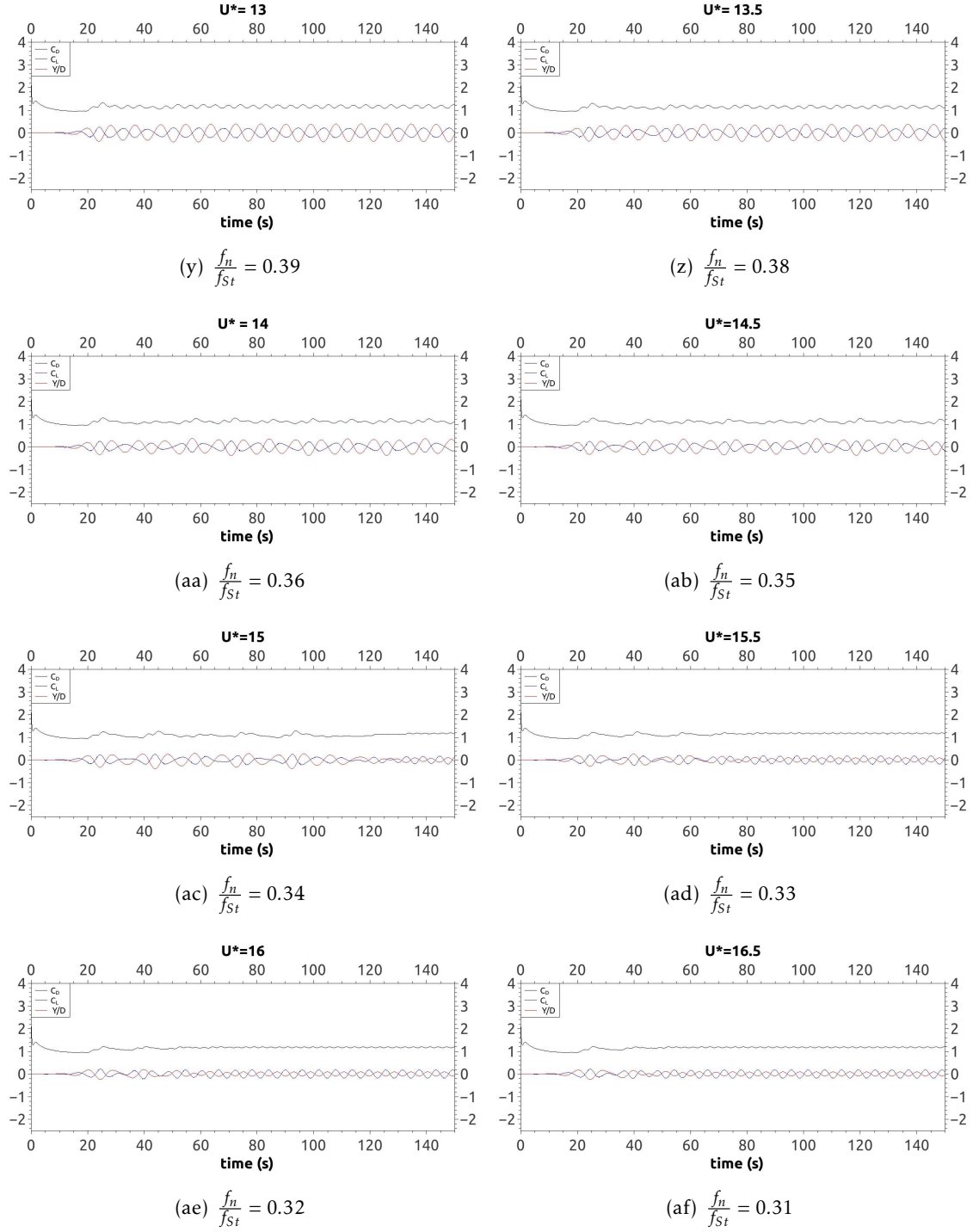
(v) $\frac{f_n}{f_{St}} = 0.45$



(w) $\frac{f_n}{f_{St}} = 0.42$

(x) $\frac{f_n}{f_{St}} = 0.41$

5.1. COMPARATIVE STUDY BETWEEN A 50D AND A 2500D DOMAIN LENGTH MESH



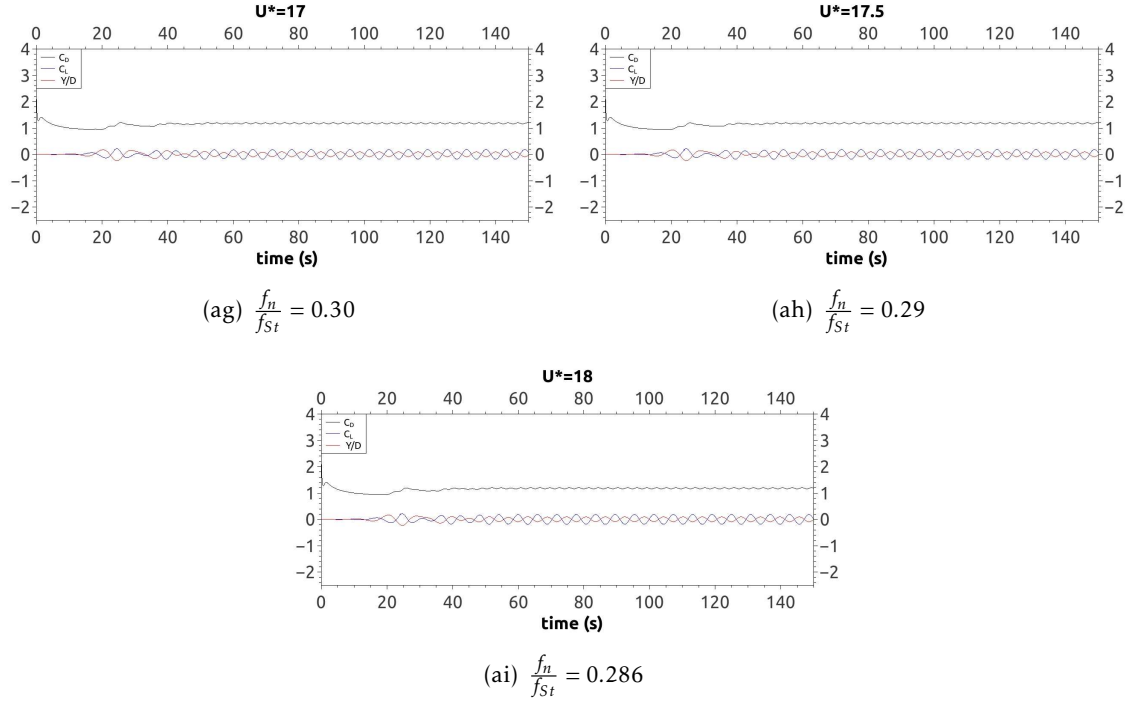


Figure 5.2: Displacement, lift and drag coefficients curves of an Y-motion cylinder for a certain frequency ratio.

Analysing the several plots in figure 5.2 it is possible to conclude that the oscillatory response of the cylinder obtained in the current study is overall in agreement with the data obtained by Conde and Lopes. In fact, with the velocity ratio increase both studies present similar variations. Nevertheless, it is possible to observe differences that lie at the level of the amplitudes of the three fundamental quantities analysed. Considering that the only change made in this study was the implementation of a larger mesh domain with $2500D$, the differences can be related with the blockage effect existing in the analysis performed by Conde and Lopes which used a $50D$ length domain. As referred previously, for $2500D$ the blockage effect is negligible. This fact can be easily confirmed by the streamlines outlined along the cylinder. Since the cylinder size does not change, the current study has a higher rate between the cylinder and the domain size and, consequently, the flow streamlines are less confined when comparing with the study performed by Conde and Lopes. This will also influence the flow velocity along the cylinder boundaries which, for the current study, has a lower value and a respectively higher pressure when correlating with the results obtained by Conde and Lopes.

Furthermore, for all the studied velocity ratios it is visible that, after the beginning of the phenomenon, it occurs for the current study a stabilization zone before the results decrease whereas Conde and Lopes present always decreasing results. This fact influences the time hiatus for the start of the phenomenon stabilization. In the current work this circumstance occurs for higher time values than in Conde and Lopes's study. This matter can be also related with the blockage effect, which is preventing the cylinder to oscillate

freely for median velocity ratios. Indeed, when the blockage effect is negligible for ratio velocities in the range of $U^* = 4$ to $U^* = 6$ it is visible the increase of the oscillation amplitude whereas when the blockage effect occurs for these velocity ranges the amplitude is always decreasing.

In greater detail, and likewise it was observed by Conde and Lopes, the cylinder response for the first four figures 5.5(a), 5.5(b), 5.2(c) and 5.2(d), which correspond to the velocity ratios $U^* = 1$, $U^* = 1.5$, $U^* = 2$ and $U^* = 2.5$, is similar to the response obtained for the fixed cylinder. Additionally, there is a consistent geometry of the plots between both fixed and one DOF studies.

In figure 5.2(e), which corresponds to the velocity ratio of $U^* = 3$, it is visible the beat phenomena as noticed by Conde and Lopes. For the figure 5.2(f), which corresponds to the velocity ratio $U^* = 3.5$, this phenomena is not visible for the mesh with 2500D used in the current study. However, in Conde and Lopes's study this phenomenon is evidenced in this velocity ratio range. Contrastingly, for the mesh with 2500D it is observable after $t = 125s$ the stabilization of the cylinder oscillation amplitude and the lift and drag coefficients. Yet, it is congruent the fact that $U^* = 3.5$ is associated with higher period values than $U^* = 3$.

Regarding the velocity ratio $U^* = 4$, it is noticeable that the lift coefficient and the displacement curves are almost superposed, fact that is also congruent with the considerations made by Conde and Lopes. This means that the cylinder oscillation frequency and vortices release are very close to each other. When this happens the vibratory system, develops the phenomenon of resonance. This can be confirmed by the low yet constant increase, from cycle to cycle, of the lift coefficient and of the cylinder oscillation amplitude. It is also observed that the lift coefficient, which depends on the lifting force increases more rapidly than the cylinder oscillation amplitude. This is explained by the fact that with the increase of the cylinder oscillation amplitude, the applied forces need to be larger (not proportionally) to overcome the resistance caused by the fluid towards the cylinder displacement and, thus, the amplitude oscillation increment requires increasingly greater lifting forces. This effect is more evident for fluids with greater density, because the increase of the oscillation amplitude will induce the displacement of a higher mass of fluid by its movement. Moreover, it is also observed that the maximum of the drag coefficient for the current study is bigger than 4 while the maximum drag coefficient value obtained by Conde and Lopes is not above 3.5. However, for both studies it is discernible that the value of this coefficient tend to 3, after its stabilization.

For the velocity ratio of $U^* = 4.5$, the drag coefficient amplitude peak is similar to the one observed for $U^* = 4$. However, it is evident that for this velocity ratio the value of the drag coefficient tends to an higher value when compared with the one obtained for $U^* = 4$. In addition, this coefficient stabilizes for higher values when compared with the one obtained by Conde and Lopes. In the current study this value tends to approximately 3.5 while in Conde and Lopes's study tends to 3. In this analysis it is still possible to observe that when the vortices release phenomena start the cylinder amplitude oscillation and

the lift coefficient are in counter-phase. This fact is not observable in Conde and Lopes's study. Nonetheless, as the phenomenon develops and tends to a stable value, the cylinder oscillation amplitude and the lift coefficient will tend to be in phase with each other, fact that is well evidenced from $t = 80s$.

With respect to $U^* = 5$, in both studies it is evidenced a phase shift to counter-phase of the lift coefficient and the cylinder oscillation amplitude between $t = 0s$ e $t = 150s$. This means that the frequency of the cylinder displacement and the frequency of the vortex release occurs in opposite directions. Analysing plot 5.2(i) it is evident that when the cylinder displacement assumes negative values, the lift coefficient has positive values. It is interesting to refer that until this velocity ratio this phenomenon occurred precisely in an inverse way: the cylinder oscillation amplitude and the lift coefficient were in phase and, thus, varied in a similar way. However, it is possible to observe that the amplitude of the lift coefficient decreases as the simulation progresses.

It is for a velocity ratio of $U^* = 5.5$ that it is possible to infer that the lift coefficient and the cylinder oscillation amplitude are completely off phase, remaining its amplitudes peaks constant approximately after $t = 30s$. Oppositely to the study conducted by Conde and Lopes, for the current study the lift coefficient amplitude value exceeds the cylinder oscillation amplitude value. Actually, all the parameters have greater magnitude in the current study when compared with Conde and Lopes's analysis. The drag coefficient reaches almost the amplitude value of 3.8 and stabilizes very close to that value ranging between 3.6 and 1.5, while in Conde and Lopes's study this parameter does not exceed 2.8 of amplitude and stabilizes between 2.5 and 1.3. Similarly, the amplitude of the lift coefficient reaches almost 0.74 in the present study whereas in Conde and Lopes's study this parameter only reaches 0.25. Finally, the oscillation amplitude has a maximum value of about 0.62 while the maximum amplitude attained by Conde and Lopes was approximately 0.52.

From the velocity ratio of $U^* = 6$ to $U^* = 8.5$, the phenomenon described for $U^* = 5.5$ are perpetuated. As the velocity ratio increases, the coefficients and cylinder oscillation amplitude tend to decrease. Moreover, between the present and Conde and Lopes's study the parameters maintained the same ratios with its magnitude decrease, with the oscillation amplitude of the studied parameters being always superior in the current study.

With respect to the velocity ratio $U^* = 9$, it is detectable the occurrence of a phenomena that was previously detected for the velocity ratio of $U^* = 4$ but with different characteristics. The amplitudes of the lift coefficient and of the cylinder oscillations are virtually the same, which means that the vortices release frequency and the cylinder oscillation frequency have the same value, however, as figure 5.2(q) illustrates these two frequencies are in counter-phased.

In Conde and Lopes's study the amplitude of the lift coefficient exceeds the cylinder oscillation amplitude value from the velocity ratio $U^* = 9.5$ whereas in the present study

5.1. COMPARATIVE STUDY BETWEEN A 50D AND A 2500D DOMAIN LENGTH MESH

that fact occurs since $U^* = 5.5$. Furthermore, in the current analysis it is observed precisely the inverse from $U^* = 9.5$, with the lift coefficient being lower than the cylinder oscillation amplitude. This observation is congruent until the velocity ratio of $U^* = 18$, the maximum velocity ratio studied.

Within the velocity ratios of $U^* = 9.5$ to $U^* = 18$, there is a continuously decreasing of the magnitude of the lift and drag coefficients and of the cylinder oscillation amplitude.

Table 5.5 contains the results obtained for the current study depending on the simulated velocity ratios, from 1 to 18 with 0.5 gaps. It was calculated the maximum cylinder oscillation amplitude for the Y-motion Y/D , the drag coefficient mean $C_{D,mean}$, the lift coefficient root mean square $C_{L,rms}$ and the frequency ratios $\frac{f}{f_n}$. The values of the drag and lift coefficients were extracted from OpenFOAM for the stipulated time-step for each simulation. After an initial analysis in order to understand the time it takes to stabilize the oscillatory phenomenon, it was calculated, given that time, the mean and the standard mean root of drag and lift coefficients, respectively. To extract the coordinates of the cylinder center position it was adapted a bashscript file called `extractData`, which is provided in the tutorial `mesh/moveDynamicMesh/simpleHarmonicMotion`. By invoking the command line `extractData log`, with the `log` corresponding to the full simulation `log` file, it was possible to extract the position of the cylinder center for each analysed time-step. Then, using the `MAX` function in *libreOffice* it was determined the cylinder maximum oscillation amplitude. The frequency ratio is the ratio between the cylinder oscillation frequency for the given simulation velocity ratio U^* and the natural frequency obtained for the fixed cylinder, analysis performed in chapter 4. The frequency of the cylinder oscillation was determined by the employment of the FFT for each studied case depending on the used velocity.

Table 5.5: Obtained results for the mass-spring system for the cylinder with Y-only motion.

U^*	Y/D	$C_{D,mean}$	$C_{L,rms}$	$\frac{f}{f_n}$
1	0.0084	1.2959	0.4523	0.1908
1.5	0.0216	1.3084	0.4864	0.3223
2	0.0470	1.3259	0.5478	0.3934
2.5	0.1076	1.3793	0.7026	0.5028
3	0.4321	1.4721	1.0134	0.6967
3.5	0.5502	1.5013	1.1243	0.7514
4	0.5683	2.2545	0.4660	0.9612
4.5	0.5862	2.3351	0.1405	0.9676

Table 5.5 - continuation: Obtained results to mass-spring system to cylinder with Y-only motion.

U^*	Y/D	$C_{D,mean}$	$C_{L,rms}$	$\frac{f}{f_n}$
5	0.6072	2.2481	0.1565	1.051
5.5	0.6191	2.5791	0.5059	1.2132
6	0.6601	2.4481	0.5436	1.2639
6.5	0.6630	2.3170	0.5484	1.3078
7	0.6576	2.2372	0.5678	1.5315
7.5	0.6361	2.0503	0.5108	1.3774
8	0.5823	1.9621	0.4980	1.4192
8.5	0.5735	1.8521	0.4629	1.4331
9	0.5772	1.6922	0.3886	1.4270
9.5	0.5605	1.5879	0.3413	1.4333
10	0.5364	1.4821	0.2900	1.656
10.5	0.5090	1.4277	0.2670	1.44
11	0.4902	1.3573	0.2357	1.4330
11.5	0.4662	1.2969	0.2041	1.4989
12	0.4442	1.2401	0.1820	1.7313
12.5	0.4172	1.1924	0.1616	1.7313
13	0.3990	1.1614	0.1477	1.7558
13.5	0.3853	1.1400	0.1370	1.8689
14	0.3722	1.1217	0.1282	1.5169
14.5	0.3646	1.1120	0.1270	1.8768
15	0.2939	1.1192	0.1035	2.8045
15.5	0.2689	1.1771	0.1264	2.9185
16	0.2033	1.1781	0.1278	2.6794
16.5	0.1771	1.1786	0.1293	2.6492

5.1. COMPARATIVE STUDY BETWEEN A 50D AND A 2500D DOMAIN LENGTH MESH

Table 5.5 - continuation: Obtained results to mass-spring system to cylinder with Y-only motion.

U^*	Y/D	$C_{D,mean}$	$C_{L_{rms}}$	$\frac{f}{f_n}$
17	0.1750	1.1790	0.1291	2.8644
17.5	0.1707	1.1797	0.1304	2.8667
18	0.1664	1.1804	0.1316	3.0232

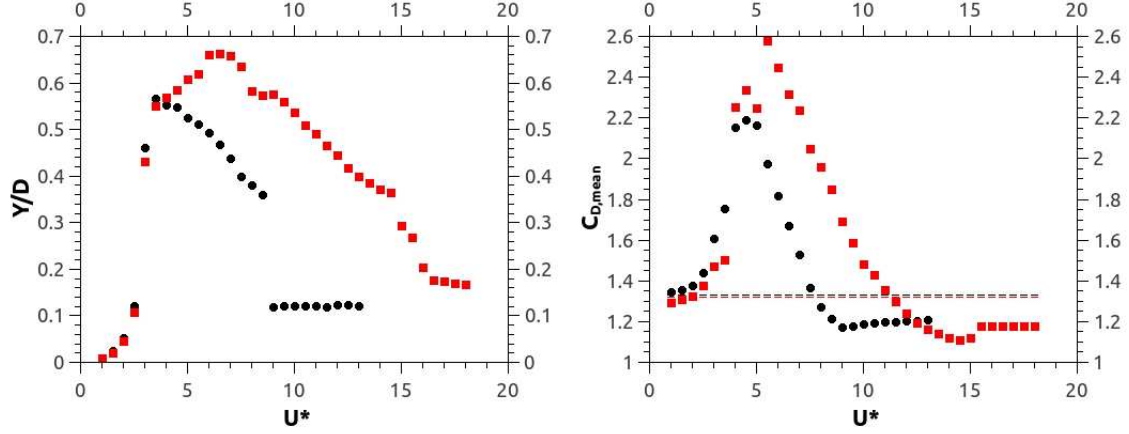
Given the values presented in table 5.5 concerning the cylinder oscillation amplitude Y/D , the drag coefficient mean $C_{D,mean}$, the root square mean of the lift coefficient $C_{L_{rms}}$, and the frequency ratios f/f_n , it were developed the plots illustrated in figure 5.3 in which it is possible to observe the differences obtained between the current study and Conde and Lopes's analysis. Each point in these plots correspond to a given velocity ratio allowing, this way, to compare in a more straightforward way the results obtained for a 2500D and for a 50D mesh domain.

Analysing the plots in figure 5.3 it is visible that the values obtained for a 2500D mesh are lower than the ones obtained by Conde and Lopes until a velocity ratio of $U^* = 4$. From this velocity ratio the amplitude of the fundamental quantities mentioned in this study become higher than the value presented by Conde and Lopes. Additionally, it is noticeable that in Conde and Lopes's study the value of the oscillation amplitude and of the lift coefficient start to decrease for $U^* = 3.5$ and the value of the drag coefficient start similarly to decrease for $U^* = 4.5$ while in the current study this decline only occurs for $U^* = 7$. Yet for $U^* = 3.5$ and $U^* = 4.5$ the lift and drag coefficient begin to decrease, respectively, just like it was observed by Conde and Lopes. This can be explained by the increase of the area of study which, consequently, decreases the proportion between the cylinder and the total domain size. Given that the body existence will force the movement of the fluid around it, the distance between the cylinder and the domain boundary layers will influence the fluid response. Another relevant difference between both studies is the abrupt decrease of the oscillation maximum amplitude obtained by Conde and Lopes whereas for the current analysis this decrease is moderate and constant.

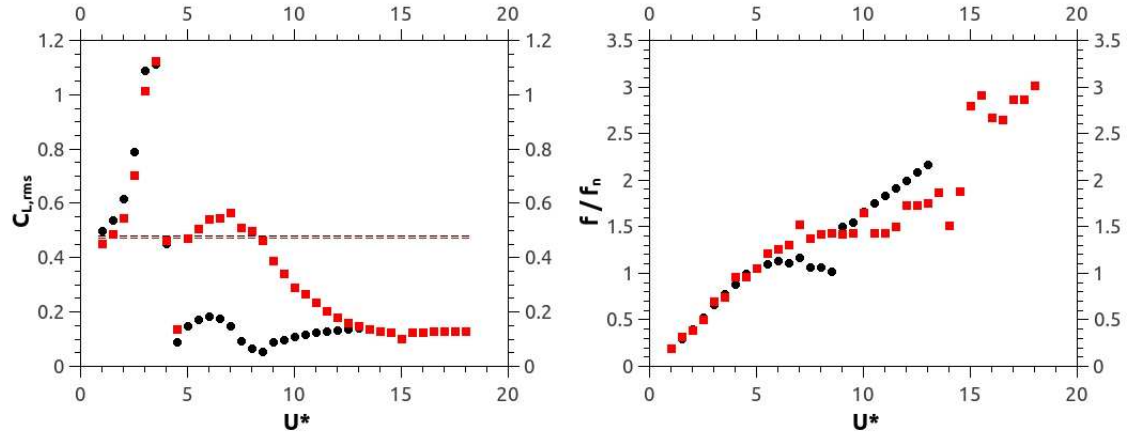
The vortex shedding phenomena occurs in a more "harmonious" mode for the 2500D mesh than for the 50D mesh being captured, for the 2500D mesh, portions of the cylinder oscillation evolution with the increase of the reduced velocity which were omitted for the analysis with a 50D mesh domain. This is verified in the evolution of the oscillation amplitude with the increase of the reduced velocity for the values between 4.5 and 7.5.

In plots 5.3(b) and 5.3(c), which describe the evolution of the lift and drag coefficients, it is verified that the evolution of the cylinder response is slower for the 2500D domain than for the 50D domain. For the 50D domain the response has a more abrupt evolution

whereas for the 2500D domain it is captured with greater detail the answer given by the cylinder with the increase of the reduced velocity.



(a) Relation between the cylinder displacement and (b) Relation between the drag coefficient mean and the simulated velocity ratios.



(c) Relation between the lift coefficient square mean (d) Relation between the frequency ratios and the simulated velocity ratios.

Figure 5.3: Relation between the cylinder displacement and the simulated velocity ratios for the current study (squares in red) and the analysis performed by Conde and Lopes (2015) (circles in black). The dashed lines represent the value of the parameter for the fixed cylinder in both studies in comparison.

5.1.2 Mass-Spring-Damping system

Similarly to the study previously described, in the current subsection it is going to be compared the results obtained for the present thesis with the ones obtained by Conde and Lopes (2015) for the mass-spring-damping system.

Figure 5.4 is a representative diagram of the mass-spring system, where the spring and a damper are anchored to the cylinder in its geometric center and fixed at a point corresponding to the spring's and damping's length at rest.

5.1. COMPARATIVE STUDY BETWEEN A 50D AND A 2500D DOMAIN LENGTH MESH

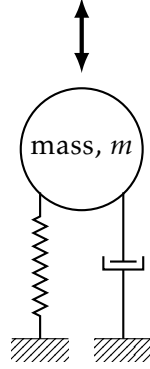
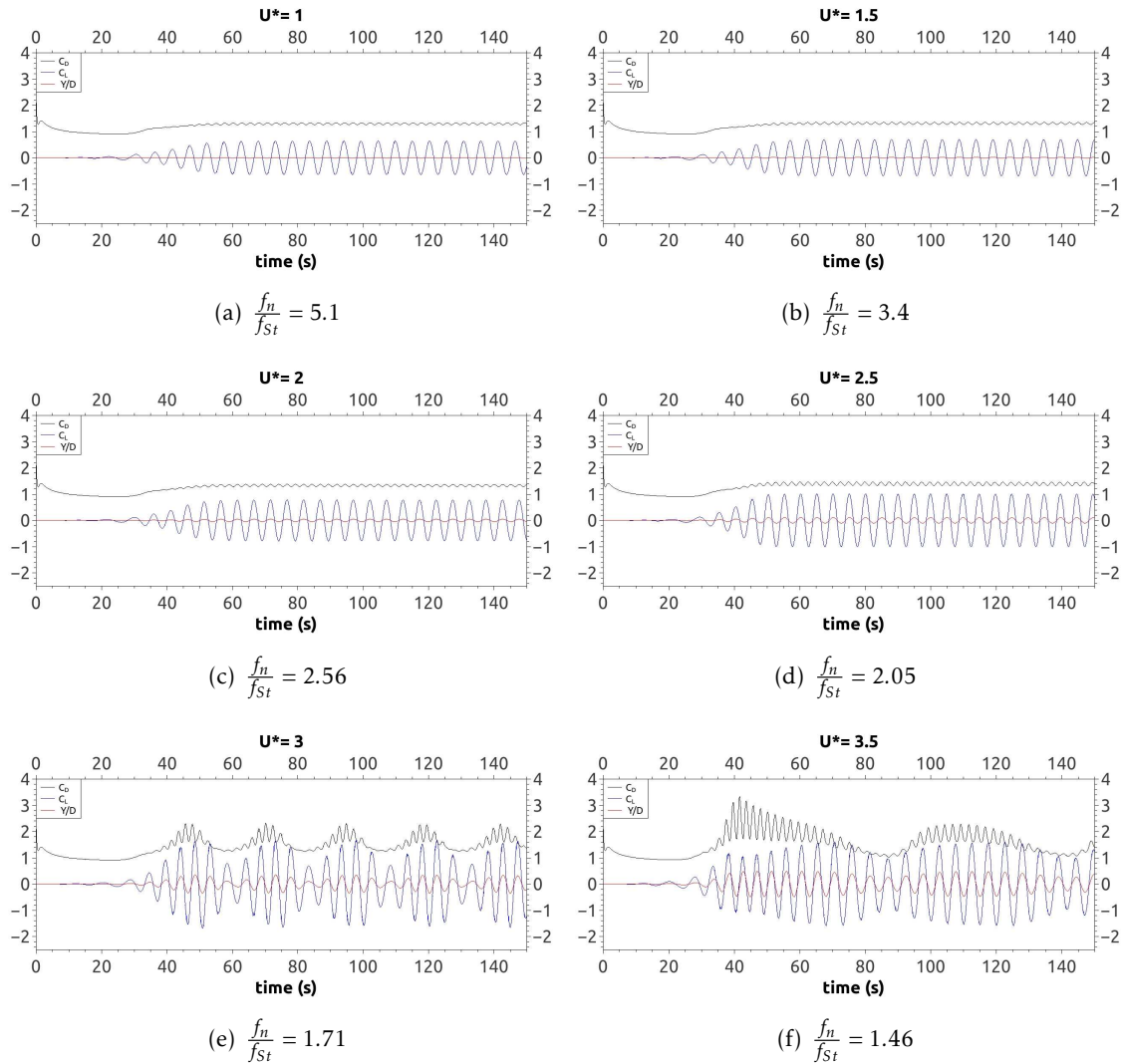
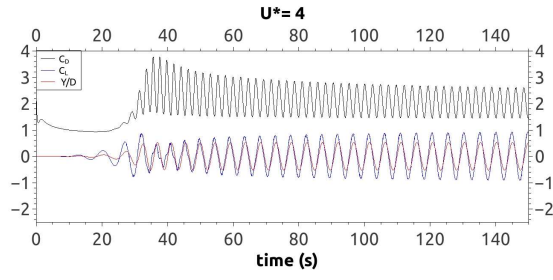


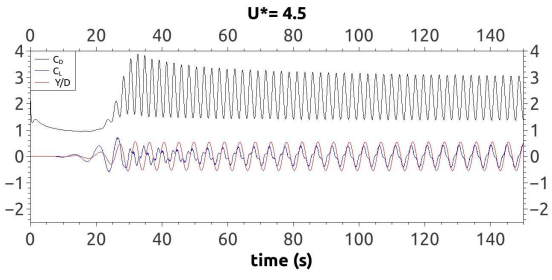
Figure 5.4: Mass-spring-damping system schematic diagram.

In figures 5.5 are represented the drag coefficient in black, the lift coefficient in blue and the cylinder oscillation amplitude in red. These parameters are shown in function of the time being simulated, which was defined as 150 seconds, time interval considered enough for the cylinder oscillation to achieve a constant frequency.

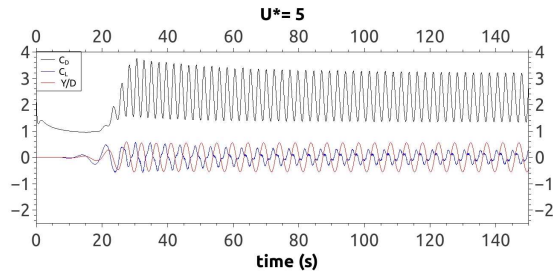




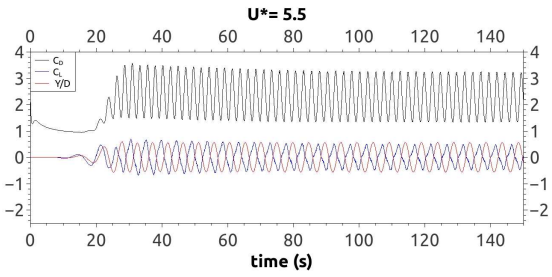
(g) $\frac{f_n}{f_{St}} = 1.28$



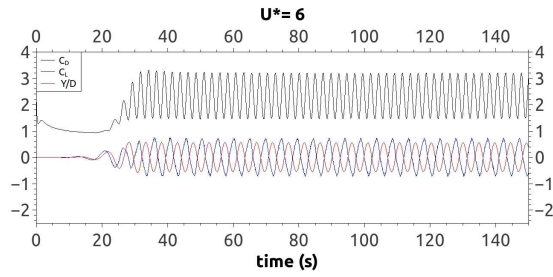
(h) $\frac{f_n}{f_{St}} = 1.14$



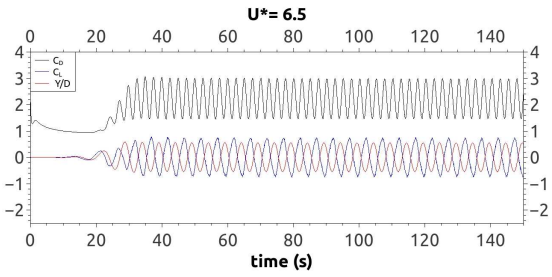
(i) $\frac{f_n}{f_{St}} = 1.02$



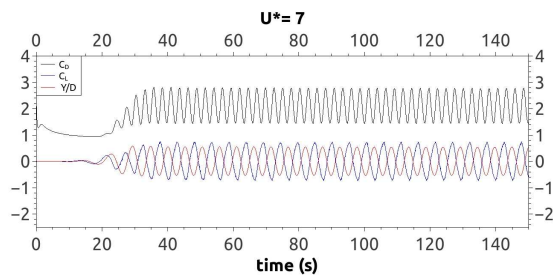
(j) $\frac{f_n}{f_{St}} = 0.93$



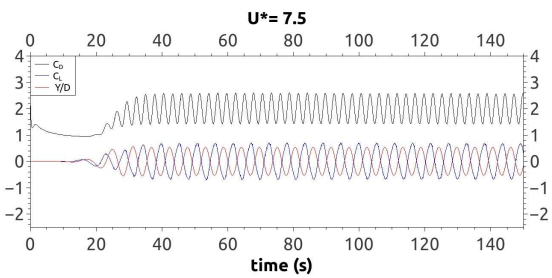
(k) $\frac{f_n}{f_{St}} = 0.86$



(l) $\frac{f_n}{f_{St}} = 0.79$

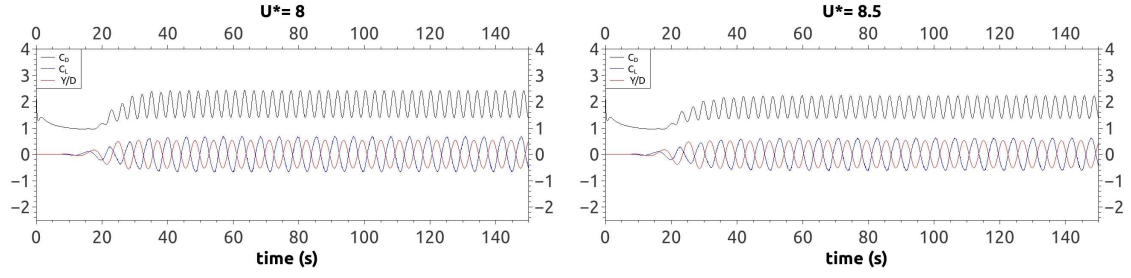


(m) $\frac{f_n}{f_{St}} = 0.73$



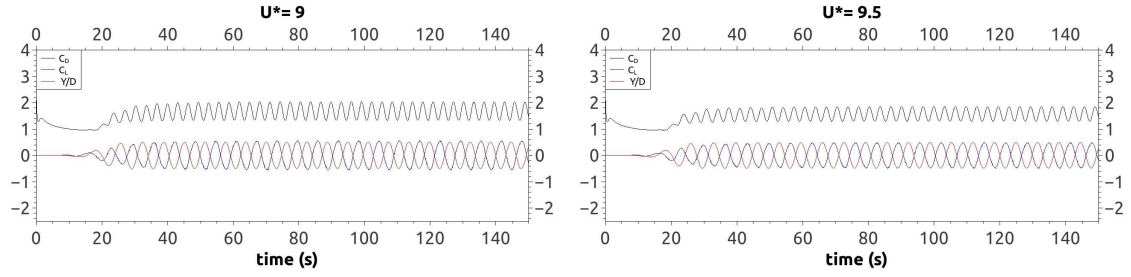
(n) $\frac{f_n}{f_{St}} = 0.68$

5.1. COMPARATIVE STUDY BETWEEN A 50D AND A 2500D DOMAIN LENGTH MESH



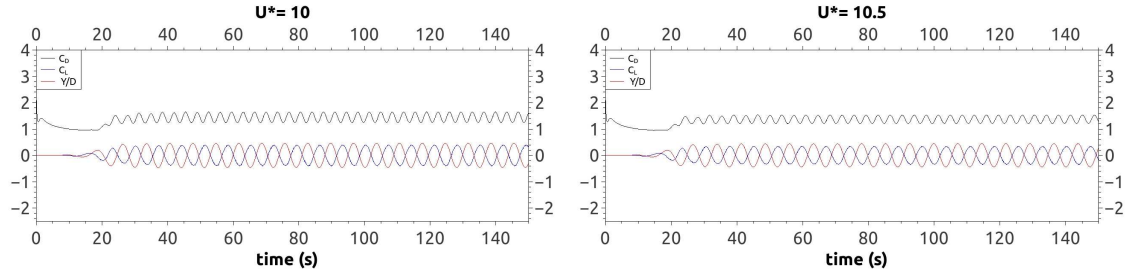
(o) $\frac{f_n}{f_{St}} = 0.64$

(p) $\frac{f_n}{f_{St}} = 0.60$



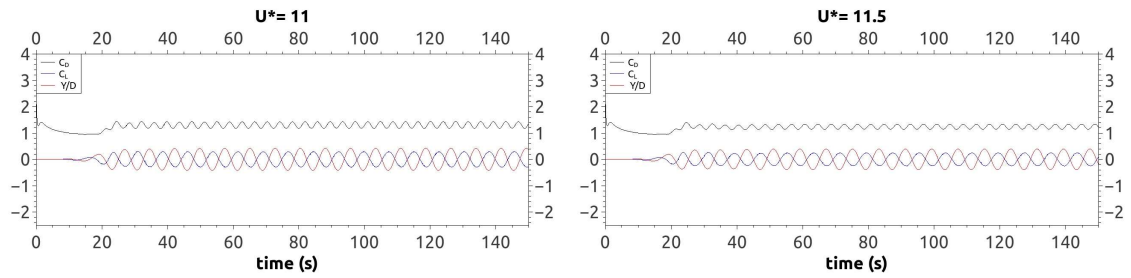
(q) $\frac{f_n}{f_{St}} = 0.57$

(r) $\frac{f_n}{f_{St}} = 0.54$



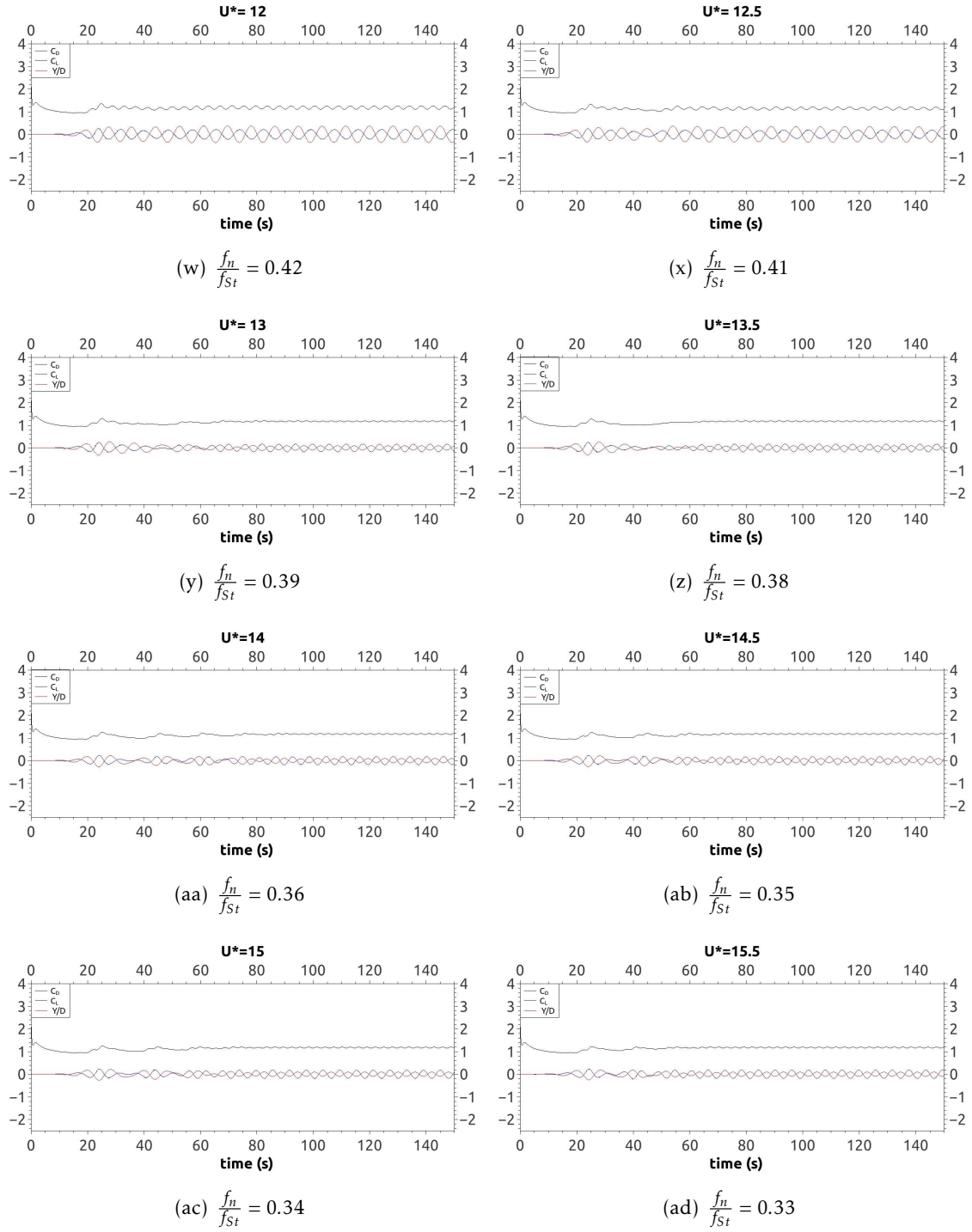
(s) $\frac{f_n}{f_{St}} = 0.51$

(t) $\frac{f_n}{f_{St}} = 0.49$



(u) $\frac{f_n}{f_{St}} = 0.47$

(v) $\frac{f_n}{f_{St}} = 0.45$



5.1. COMPARATIVE STUDY BETWEEN A 50D AND A 2500D DOMAIN LENGTH MESH

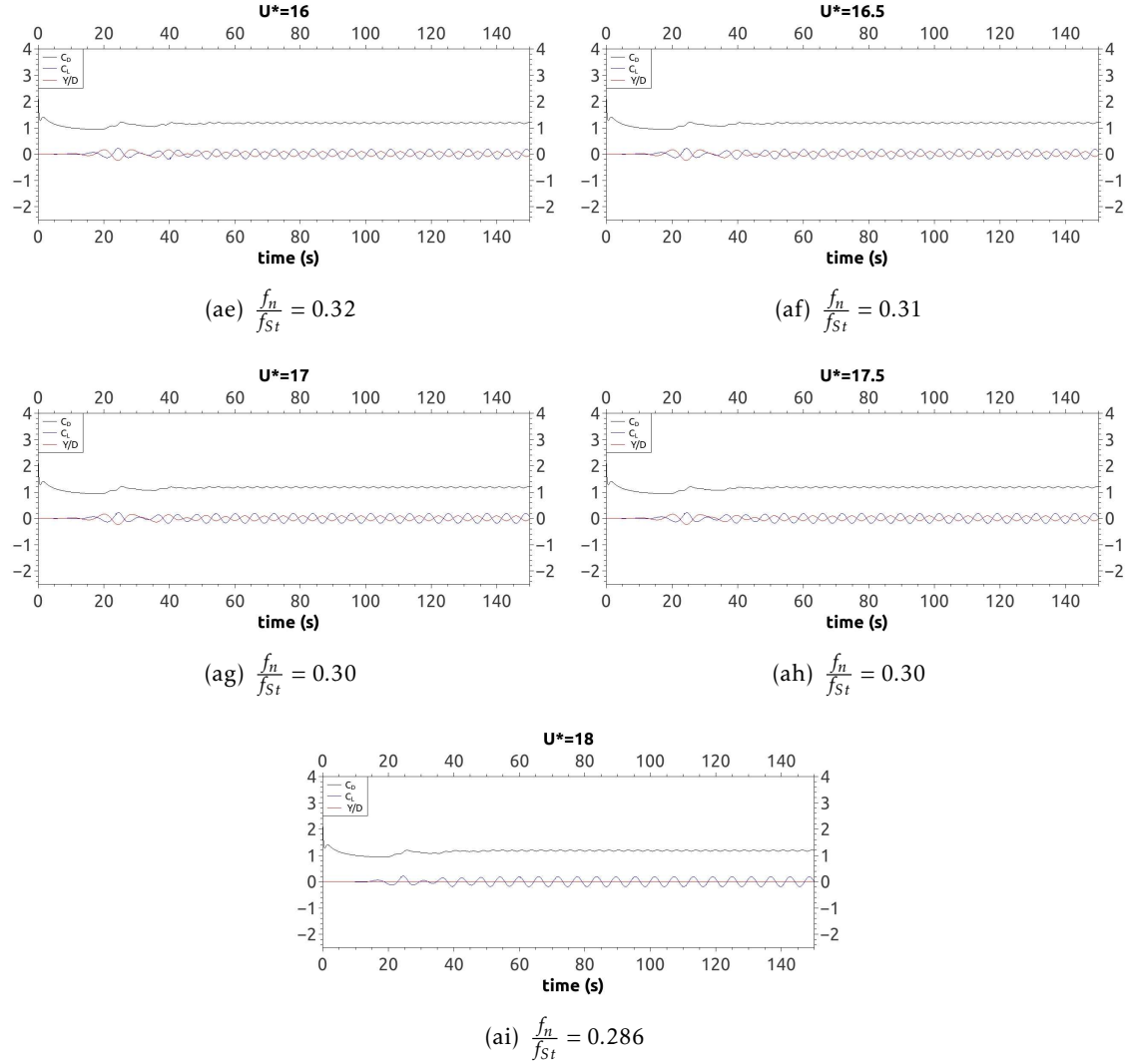


Figure 5.5: Displacement, lift and drag coefficients curves of an Y-motion cylinder for a certain frequency ratio.

As it was referred in section 5.1.1 and congruently to the considerations made by Conde and Lopes for the mass-spring-dumper system, the first four velocity ratios, $U^* = 1$, $U^* = 1.5$, $U^* = 2$ and $U^* = 2.5$ display characteristics similar to the ones obtained for the fixed cylinder. The values for these velocity ratio ranges are identical to the ones achieved by Conde and Lopes.

With the increase of the velocity ratio to $U^* = 3$, it is observed the beat phenomena, which was already detected for the mass-spring system. When comparing the results with the ones obtained by Conde and Lopes, for both studies the drag coefficient has five amplitude peaks. In fact, in Conde and Lopes's study the drag coefficient, the lift coefficient and the cylinder oscillation amplitude tend to a given value. Contrastingly, in the current analysis these parameters keep the initial characteristics presented in the first envelope.

For a velocity ratio of $U^* = 3.5$, it is observed that both studies retain similar characteristics such as a long beat period. However, in the present study is visible the tendency of the parameters to stabilize throughout the phenomena development while for Conde and Lopes's results the phenomena characteristics are maintained between the first and second beat phenomenon of the cycle.

Regarding the velocity ratio of $U^* = 4$, the conclusions are similar to the ones explained for the mass-spring system. At this velocity ratio range occurs the resonance phenomenon with the continuous increase of the lift coefficient and of the cylinder oscillation amplitude. In the present study the amplitudes of the displayed parameters are higher than the ones referred in the study developed by Conde and Lopes. The drag coefficient reaches the value of 3.8 and decreases sharply to stabilize between 1.5 and 2.6 while in Conde and Lopes's analysis the maximum amplitude of the drag coefficient is 3.2, stabilizing very close to the present study values. Concerning the cylinder oscillation amplitude and the lift coefficient, the variation curves are very similar and within the same ranges of values for both studies.

For velocity ratios of $U^* = 4.5$ and $U^* = 5$ the vortices release frequency and the cylinder oscillation frequency are no longer in phase to pass to be in anti-phase. This phenomenon is observable by the lift coefficient and the cylinder oscillation amplitude curves. Likewise Conde and Lopes noted, there is a decrease in the amplitude of the lift coefficient with the increase of the velocity ratio from $U^* = 4.5$ to $U^* = 5$. The maximum of the drag coefficient is reached for $U^* = 4.5$. However, after its stabilization, the drag coefficient amplitude is higher for $U^* = 5$, while in Conde and Lopes's study this fact occurs earlier for $U^* = 4.5$. For the mentioned velocity ratios of $U^* = 4.5$ and $U^* = 5$ the initial peak of maximum amplitude is not visible, ceasing for the velocity ratio of $U^* = 4$. In the present study, this phenomenon is visible even at the velocity ratio of $U^* = 5$, disappearing only for the next value of low speed $U^* = 6$.

It is for this velocity ratio, $U^* = 6$, that is possible to observe the total mismatch between the frequency of the vortices release and the frequency of oscillation given by the cylinder lift coefficient curves and the cylinder oscillation amplitude. Analogously to what was verified for the mass-spring system, the amplitude of the lift coefficient is greater than the cylinder oscillation amplitude. This phenomenon remains evident, with a constant reduction in amplitudes of the three analysed parameters, as the velocity ratio value increases up to the value of $U^* = 6$.

For the mass-spring-damper system is at a velocity ratio of $U^* = 9.5$, while for the mass-spring system is at $U^* = 9$, that it is expressed the phenomena referred for the velocity ratio of $U^* = 4$ in which the amplitude of the lift coefficient and the amplitude of the oscillation cylinder are identical but, for this velocity ratio ranges, are in anti-phase.

From the velocity ratio of $U^* = 10$, the conclusions are similar to the ones already mentioned for the mass-spring system. In the present study, the amplitude of the lift coefficient returns to have values lower than the cylinder oscillation amplitude. This fact is incongruous with the results obtained by Conde and Lopes which from a velocity

5.1. COMPARATIVE STUDY BETWEEN A 50D AND A 2500D DOMAIN LENGTH MESH

ratio of $U^* = 9$ show lift coefficient values higher than the cylinder oscillation amplitude values.

Equivalently to what was done for the mass-spring system, table 5.3 shows the results obtained for this study depending on the simulated velocity ratios, from 1 to 18 with 0.5 gaps. It was calculated the maximum cylinder oscillation amplitude for Y -motion, the drag coefficient mean $C_{D,mean}$, the lift coefficient root mean square $C_{L,rms}$ and the frequencies ratio $\frac{f}{f_n}$.

The values enumerated in table 5.6 were extracted from OpenFOAM and calculated using the same methodology used for the mass-spring system referred in subsection 5.1.1.

Table 5.6: Obtained results to mass-spring-damping system to cylinder with Y -only motion.

U^*	Y/D	$C_{D,mean}$	$C_{L,rms}$	$\frac{f}{f_n}$
1	0.0084	1.2964	0.4523	0.2121
1.5	0.0216	1.3089	0.4871	0.2895
2	0.0472	1.3305	0.5513	0.3942
2.5	0.1080	1.393	0.7111	0.504
3	0.3549	1.5527	0.9044	0.6767
3.5	0.4903	1.2720	0.9926	0.6671
4	0.5293	2.0544	0.6146	0.9108
4.5	0.5540	2.1850	0.2610	0.9243
5	0.5830	2.2338	0.1585	1.018
5.5	0.5907	2.2502	0.2872	1.1170
6	0.5746	2.3246	0.4699	1.2389
6.5	0.5858	2.2199	0.4901	1.2922
7	0.5802	2.1016	0.4861	1.3329
7.5	0.5560	1.9930	0.4746	1.5459
8	0.5405	1.9044	0.4630	1.4104
8.5	0.5289	1.7936	0.4286	1.4305
9	0.5113	1.6771	0.3833	1.4477
9.5	0.4932	1.5693	0.3323	1.5343

Table 5.6 - continuation: Obtained results to mass-spring-damping system to cylinder with Y-only motion.

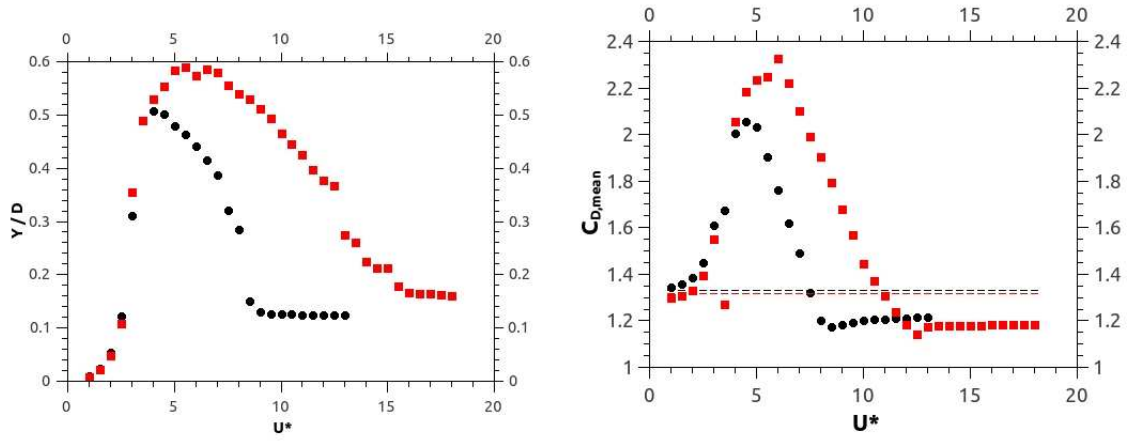
U^*	Y/D	$C_{D,mean}$	$C_{L,rms}$	$\frac{f}{f_n}$
10	0.4655	1.4468	0.2768	1.432
10.5	0.4464	1.3715	0.2393	1.44
11	0.4259	1.3057	0.2079	1.4374
11.5	0.3974	1.2403	0.1771	1.4345
12	0.3770	1.1842	0.1525	1.7241
12.5	0.3674	1.1442	0.1330	1.4363
13	0.2740	1.1764	0.1208	2.1779
13.5	0.2600	1.1770	0.1213	2.5534
14	0.2245	1.1781	0.1246	2.3676
14.5	0.2133	1.1791	0.1258	2.4391
15	0.2133	1.1791	0.1258	2.5119
15.5	0.1786	1.1812	0.1295	2.5969
16	0.1674	1.1820	0.1308	2.6825
16.5	0.1648	1.1822	0.1313	2.7721
17	0.1634	1.1825	0.1318	2.8661
17.5	0.1600	1.1831	0.1332	3.1632
18	0.1565	1.1837	0.1341	3.025

The figure 5.6 demonstrates the differences in the parameters calculated and shown in table 5.6 for the present study and the study performed by Conde and Lopes. Similarly to the mass-spring system behaviour, it is observed in figure 5.6 that this study values have lower amplitude than the values determined by Conde and Lopes until the velocity ratio of $U^* = 4$. From this point, the amplitude of the fundamental quantities in the present study become higher than the values presented by Conde and Lopes. Furthermore, for Conde and Lopes's study the value of the cylinder oscillation maximum amplitude and the lift coefficient variation start to decrease from $U^* = 3.5$ and the drag coefficient root square mean also decreases from $U^* = 4.5$, whereas in the present study the oscillation maximum amplitude only begins to decrease from $U^* = 7$. Conforming with the results

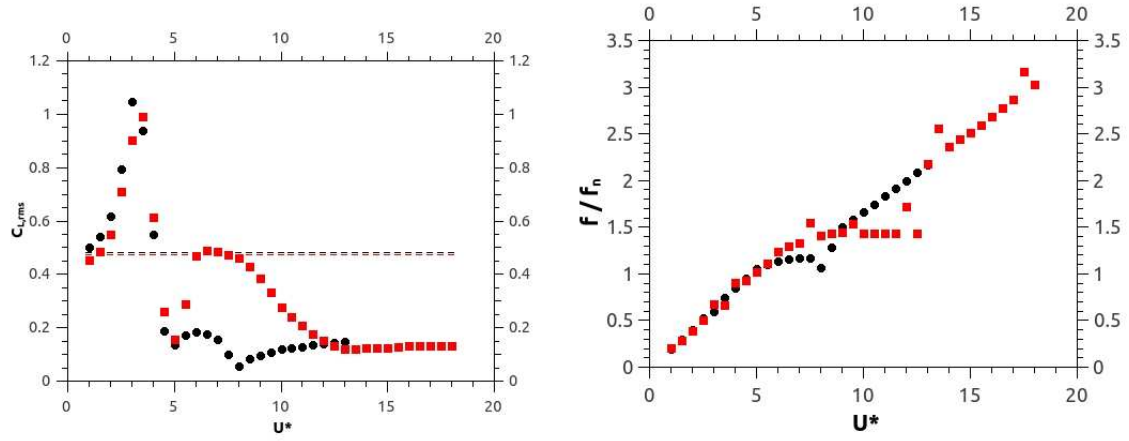
5.1. COMPARATIVE STUDY BETWEEN A 50D AND A 2500D DOMAIN LENGTH MESH

obtained by Conde and Lopes, the lift coefficient and the drag coefficient root mean square decrease for the velocity ratios of $U^* = 3.5$ and $U^* = 4.5$, respectively.

Identically to the mass-spring system, the differences obtained between the Conde and Lopes study and the present study are due to the increase of the mesh domain. The differences caused by the existence of a damp in the system influences the calculated parameters range of values, simulating the effect caused by a structural damping, despising the material and the fluid damping since they present characteristics of a fluid in a gaseous state, contributing in a insignificant way to influence the cylinder response.



(a) Relation between the cylinder displacement and (b) Relation between the drag coefficient mean and the simulated velocity ratios.



(c) Relation between the lift coefficient square mean (d) Relation between the frequency ratios and the simulated velocity ratios.

Figure 5.6: Relation between the cylinder displacement and the simulated velocity ratios for the current study (squares in red) and the analysis performed by Conde and Lopes (2015) (circles in black). The dashed lines represent the value of the parameter for the fixed cylinder in both studies in comparison.

FLOW AROUND A TWO DEGREES-OF-FREEDOM CYLINDER

This chapter exposes the numerical study of a flow around a circular cylinder with two DOF. Firstly, it was performed a comparison analysis of the obtained results with the numerical study performed by T. Li and Zhu (2009) for a mesh with the same domain size, subject described in section 6.1. In section 6.2 is investigated how different refinement levels of the mesh influence the cylinder 8-motion movement, by varying the mesh refinement level maintaining the same circular domain $L_b = 8D$ context. Finally, in section 6.3 three meshes with different domains sizes are used, respectively $20D$, $500D$ and $2500D$, in order to analyse the influence of the domain size on the reliability of the obtained results. The results obtained by T. Li and Zhu (2009) are shown in the Appendix A.

6.1 Two degrees-of-freedom cylinder with a $8D$ mesh size

The study performed by T. Li and Zhu (2009) was made for a constant Reynolds value of $Re = 200$, with an uniform flow velocity $U_\infty = 1 \text{ m.s}^{-1}$, diameter cylinder $D = 1 \text{ m}$ and viscosity $\nu = 5 \times 10^{-3} \text{ kg.(s.m)}^{-1}$. Different frequency ratios are simulated ranging between $\frac{f_n}{f_0} = 0.9$ and $\frac{f_n}{f_0} = 2.5$. f_n is the natural frequency of the system and f_0 is the frequency of the vortex shedding for the fixed cylinder. The frequency ratio $\frac{f_n}{f_0}$ is a quite important parameter since it influences the phenomenon of vortex induced vibration. It is through the frequency ratio parameter that a baseline to perform the comparison between studies is established. Thereby, the same frequency ratio values are used among the studies being compared, as shown in table 6.1. Moreover, it is based on the frequency ratio values and on the Strouhal frequency value that the remaining parameters values shown in table 6.1 are obtained. The Strouhal frequency, as mentioned in chapter 4, corresponds to the

vortex shedding frequency for the given system. This frequency is calculated from the system when the cylinder has no DOF. It is based on this frequency, applied in the ratio between the frequencies, that is obtained the system natural frequency.

The vortex shedding frequency obtained in chapter 4 for a flow around the fixed cylinder with the $8D$ mesh, for the lower refinement level, was used to perform the comparison study with the work developed by T. Li and Zhu. The mesh used by T. Li and Zhu has a lower refinement level, with 64 elements on the cylinder wall, whereas in chapter 4 it was used a mesh with 140 elements around the cylinder wall composed by elements with a good asymmetry and orthogonality values.

The current study presents a vortex shedding frequency with a value of about $f_{St} = 0.2430$ while the same parameter is much lower for the study performed by T. Li and Zhu, being about $f_{St} = 0.1972$. Given that both studies share the same simulation conditions, the same properties and the same fluid cylinder characteristics the differences between them reside in the meshes geometric differences. It is interesting to note, however, that if the two structural systems have similar characteristics but distinct frequency ratios, then we are dealing with systems with different stiffness. In this specific case, is the alternating release of vortices that causes the cylinder oscillation and is the frequency with which these vortices are released that determines the cylinder oscillation frequency. Thus, the structural system implemented by T. Li and Zhu has a greater elasticity than the system of the current study, which has a higher vortex shedding frequency and for that reason can be considered as a more rigid system.

The goal of this section is to simulate the study performed by T. Li and Zhu. For that it were used the same simulation parameters and the same vortex shedding frequency as the ones applied by T. Li and Zhu in order to achieve the same spring elastic constants as the ones used in this paper.

Therefore, using the vortex shedding frequency obtained in the study performed by T. Li and Zhu, $f_{St} = 0.1972$, it was possible to determine the natural frequency f_n . To obtain that value, the natural frequency is converted from Hz to rad through equation 5.2 and applying equation 5.1 to the cylinder with mass $m = 1Kg$ it is possible to obtain the desired elastic constants, in order to use the same spring values as T. Li and Zhu. These values are shown in table 6.1. The damping constant for the study developed by T. Li and Zhu is the same for all the different values of frequency ratios, being $C = 0.00306$. For this reason, it was kept the same damping value for all the simulated frequency ratios.

For each frequency ratio value, it was performed a numerical study with a circular mesh which length from the cylinder wall to the domain boundary was $L_b = 8D$. This configuration was set in order to retain the main dynamical characteristics of the mesh which impact the results of the numerical study allowing, this way, to perform a correct comparison between the study performed by T. Li and Zhu and the current analysis.

Figure 6.1 shows the motion geometry of the cylinder displacement for a flow around a cylinder with the same numerical conditions as the ones used by T. Li and Zhu. To this end, the used mesh was defined with the characteristics enumerated in table 6.2.

Table 6.1: Simulation parameters for the cylinder with XY-motion.

$\frac{f_n}{f_0}$	U^*	f_n	$k(N/m)$	$C(N_s/m)$
0.5	3.1846	0.0986	0.3838	0.00306
0.9	2.3736	0.1775	1.2435	0.00306
1.0	2.2519	0.1972	1.5352	0.00306
1.1	2.1472	0.2169	1.8576	0.00306
1.3	1.9749	0.2565	2.5945	0.00306
1.4	1.9031	0.2761	3.0091	0.00306
1.5	1.8387	0.2958	3.4544	0.00306
1.6	1.7803	0.3155	3.9302	0.00306
2.5	1.4242	0.4930	9.5951	0.00306

Table 6.2: Geometric parameters of the 8D mesh.

Mesh	$\frac{e}{D}$	N_{rad}	N_{ang}	N_{cells}	r
Present study	0.0049	45	136	6120	1.10

The simulations performed in the current study are congruent with the results obtained by T. Li and Zhu, as it is possible to ascertain from the plots in figure 6.1. The same range of values was obtained nearly for all the several frequency ratios analysed. It is important to highlight the almost perfect symmetry of the cylinder 8-motion, fact that is in accordance with the expected, since the mesh and the simulation conditions are symmetrical along the X-axis, which divides the mesh and the cylinder in two semi-circles with symmetrical domains. Divergently, the cylinder motion obtained by T. Li and Zhu is not symmetrical and hence the 8-motion obtained in both studies are different.

The initial position of the cylinder geometric center is constant along the performed studies, located at coordinates $x = 0$ and $y = 0$. Evaluating the plots in figure 6.1, which graphically demonstrate the response of the cylinder with two DOF, it is possible to observe that the cylinder has an initial motion only in the parallel direction to the flow displacement. This movement is in line with the direction of the flow displacement, from the left to the right. This displacement of the cylinder to the area where it starts to oscillate cyclically is directly related with the value of the spring constant. It is possible to infer that with the increase of the frequency ratio values and, consequently, with the increase of the spring constant the zone of the cylinder oscillation stabilization is increasingly closer to its original position, that is, the coordinate point $x = 0$ and $y = 0$. The zone of cyclical oscillation corresponds to the area when the cylinder displacement stabilizes and reaches the continuing vortex shedding. This phenomenon is observable in the figure's 6.1 plots which illustrate the variation of the lift coefficient, of the cylinder oscillation

amplitude parallel to the flow displacement direction x , and of the cylinder oscillation amplitude orthogonal to the flow displacement direction y .

The movement performed by the cylinder for the frequency ratio value of $\frac{f_n}{f_0} = 0.5$ is shown in figure 6.1(a). The obtained motion is similar to the one attained by T. Li and Zhu. Furthermore, as it can be seen by figure 6.1(b), the amplitudes achieved in the current study are also consistent with the ones obtained by T. Li and Zhu, establishing after the stabilization of the phenomenon with a magnitude of 1.6 in the parallel direction of the flow and with a fluctuation in the orthogonal direction of flow varying between -0.25 and 0.25 . In the plot 6.1(b) it is possible to observe that the oscillation phenomenon is present from about the time $t = 120s$. The starting point of the oscillation phenomenon is constant among the several frequency ratio simulated for the $8D$ mesh. Comparing with the results obtained by T. Li and Zhu, the oscillation phenomenon occurs later for the current study. Nevertheless, this fact does not influence the quality of results, only translating a later development of the vortex shedding phenomena. In section 6.2 will be discussed in greater detail how the mesh refinement level influences the initiation of the vortex shedding phenomenon.

For the lift coefficient curve and the displacement curves along the x and the y axis the data shows a tendency to stabilize but at the final simulation time-point the phenomena is not yet fully stabilized. Regarding the cylinder x displacement, there is no cyclic continuation, being its development somewhat random. The lift coefficient curve shows a greater tendency to stabilize than the x displacement curve. However, its stabilization it is not fully evident presenting along the simulation time instabilities and a slightly fuzzy scatter. Contrasting, the curve of the y -direction displacement stabilizes and shows a cyclic movement which is repeated after a certain period of time.

The current frequency ratio of $\frac{f_n}{f_0} = 0.5$ is the lowest of the studied frequency ratios and, hence, the lowest elastic constant studied of about $k = 0.3838 \text{ N/m}$. To the lowest elasticity value corresponds, consequently, the longest displacement of the cylinder in the parallel direction to the fluid achieving the value of $x = 1.6$. On the other hand, as the spring does not have sufficient elasticity to simulate the oscillatory movement the oscillatory amplitude is very small.

The figure 6.1(c) demonstrates the oscillatory movement of the cylinder for the frequency ratio of $\frac{f_n}{f_0} = 0.9$. For this frequency ratio, the obtained movement has the form of an eight, named as 8-motion, with a slight tilt to the right. Moreover, the motion along the x axis for this frequency ratio is fully symmetrical. In fact, this is the main difference between the current study and the study developed by T. Li and Zhu, in which the asymmetry is quite evident. Regarding the oscillation amplitudes, the obtained values are similar to the ones described by T. Li and Zhu. In detail, for the current study the values range between -0.6 and 0.6 for the direction orthogonal to the flow displacement with the cylinder center near the position 0.8 for the x axis. Concerning the amplitude achieved in the parallel direction to the flow motion, it has a maximum amplitude of 0.1 and varies between 0.75 and 0.85 in the description of the 8-motion.

Plot 6.1(d) illustrates the temporal variation of the lift coefficient and the cylinder oscillation amplitudes in the x and y axis. From this plot it is possible to conclude that the cylinder oscillation starts at $t = 110s$ and stabilizes, approximately, at $t = 145s$.

Figure 6.1(e) shows the cylinder movement for a frequency ratio of $\frac{f_n}{f_0} = 1.0$. Comparing this figure with the one obtained by T. Li and Zhu, the oscillation amplitudes are very similar ranging between -0.6 and 0.6 orthogonally to the flow displacement and the oscillation geometric center corresponds to $x = 0.7$. The horizontal oscillation amplitude is 0.1 and varies between 0.65 and 0.75 . Furthermore, the tilt of the cylinder 8-motion is greater for this frequency ratio than the verified for the previous frequency ratios. The obtained results are in concordance with the results shown by T. Li and Zhu, except the fact that for the current study the cylinder motion is perfectly symmetric, while for the later study this motion is asymmetrical.

With the increase of the frequency ratio, the cylinder oscillation center approaches the referential origin which coincides with the initial geometric center of the cylinder at $t = 0s$. This fact is visible for the frequency ratio of $\frac{f_n}{f_0} = 1.1$ which has an oscillation center in the coordinates $x = 0.625$ and $y = 0$ describing, as observed for the previous frequency ratios, a truly symmetric motion. The amplitude of oscillation orthogonal to the flow ranges from -0.65 to 0.65 . The amplitude of oscillation parallel to the flow varies between 0.57 and 0.68 . The amplitude values between the present study and the study developed by T. Li and Zhu are in excellent compliance. Highlighting the excellent symmetry achieved in the current study compared to the asymmetry demonstrated by T. Li and Zhu.

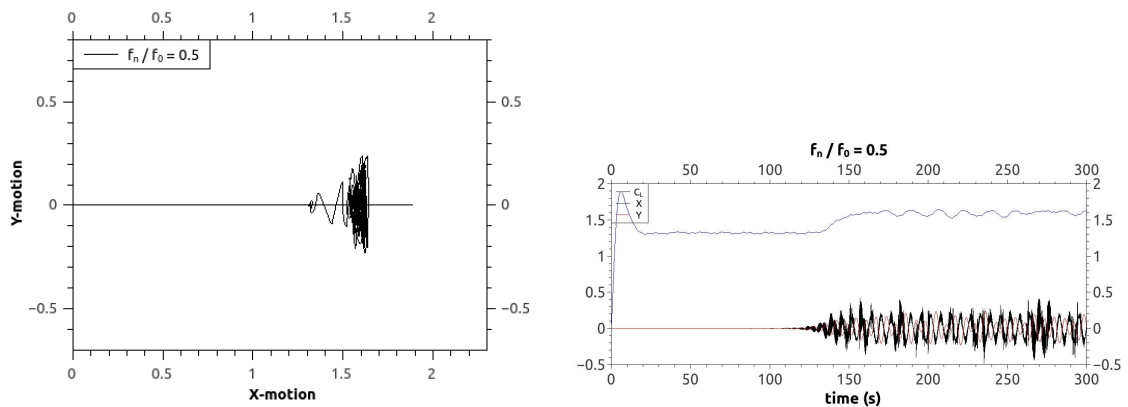
As the spring constant increases, the 8-motion described by the cylinder is increasingly tilted to the right at the upper and lower movement extremities. Similarly, the oscillation amplitude in the parallel direction towards the fluid displacement is also increased as can be seen in figure 6.1(i). This figure shows several 8-motions described from right to left by the cylinder until the stabilization of the movement in the geometric center at $x = 0.44$. It is possible to identify the stabilization zone since the plot line seems to be in bold in that area. In fact, this occurs because the cylinder does numerous passages in that area. The oscillation amplitude for this frequency ratio is, in the orthogonal direction to the flow displacement, between -0.7 and 0.7 . The amplitude of oscillation parallel to the flow direction ranges between 0.4 and 0.56 .

Figure 6.1(m) illustrates the cylinder motion for a frequency ratio of $\frac{f_n}{f_0} = 1.5$. The cylinder response is given with two distinct motion frequencies, fact that is easily distinguishable by the analysis of the respective temporal relation which is illustrated in figure 6.1(n). The motion which corresponds to the higher frequency value occurs when the cylinder has a longer displacement in the x axis, ranging between 0.3 and 0.4 , and in the y axis, varying between -0.6 and 0.6 . This frequency originates, clearly, the cylinder motion which is darker and more to the right of the figure's 6.1(m) plot, thus forming a semi-circle. The drastic drop of the lift coefficient and of the respective amplitude of the movement visible in the figure 6.1(n) is related with the changing of the cylinder

frequency oscillation. This fact is also noticeable in figure 6.1(m) which shows distinct oscillation motions. The cylinder has several random paths which constitute the link between the two different frequencies of the cylinder motion. When the cylinder moves from the semi-circular movement, in the right zone of the plot, to the leftmost motion the oscillation amplitudes decrease sharply to a range of 0.24 to 0.16 on the x axis, parallel to the motion of the flow, and between -0.15 and 0.15 on the y axis, orthogonal to the motion of the flow.

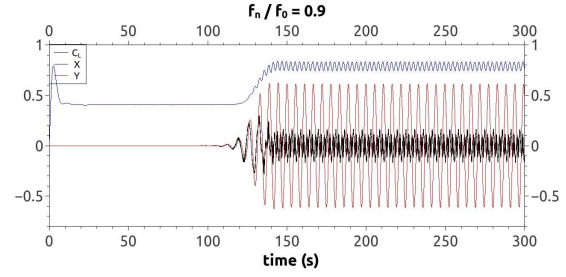
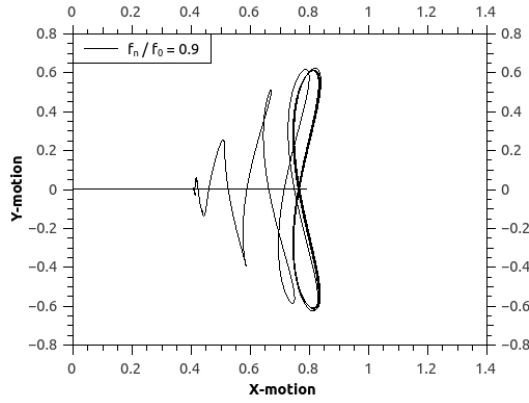
The lift coefficient reaches its peak for the frequency ratio value of $\frac{f_n}{f_0} = 1.5$. For the frequency ratio value of $\frac{f_n}{f_0} = 1.6$ is attained the lowest peak value of the lift coefficient. It is also observable the increase of the temporal bandwidth in which one cycle is observable. However, for this frequency ratio, the oscillation cycle is divided in half with a drastic decrease of the lift coefficient value. This fact splits the cycle stability which was observed for the frequency ratio of $\frac{f_n}{f_0} = 1.4$ until $\frac{f_n}{f_0} = 1.6$, having a duration of about $t = 80$ s. Taking this into account, figure 6.1(o) shows a scarcer motion for the several oscillation frequencies, describing three distinct frequencies: the first occurs in the right zone of figure's 6.1(o) plot and has a greater oscillation amplitude; this gives rise to a lower oscillation amplitude which occurs in the leftmost area of the plot; and this is followed by a drastic reduction in the amplitude of the lift coefficient. This movement is repeated twice every described cycle.

It is for the frequency ratio value of $\frac{f_n}{f_0} = 2.5$ that the 8-motion cylinder motion is almost perfect, with amplitudes between 0.06 and 0.09 in the parallel direction of the flow movement and the amplitude ranges between -0.055 and 0.055 in the orthogonal direction of the flow movement. It is also for this frequency ratio value that, in congruence with the studied performed by T. Li and Zhu, the answer given by the cylinder describes the closest 8-motion format. It is observed once more an excellent symmetry achieved in the current study which is similarly observed by T. Li and Zhu for this frequency ratio, not being visible the asymmetry detected for lower frequency values for the results obtained by T. Li and Zhu.

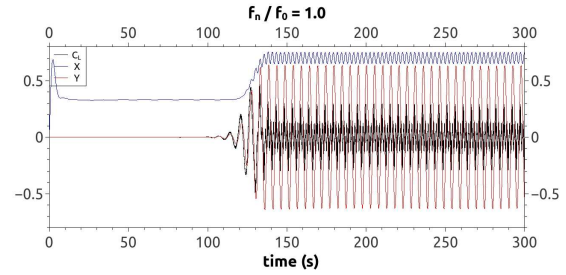
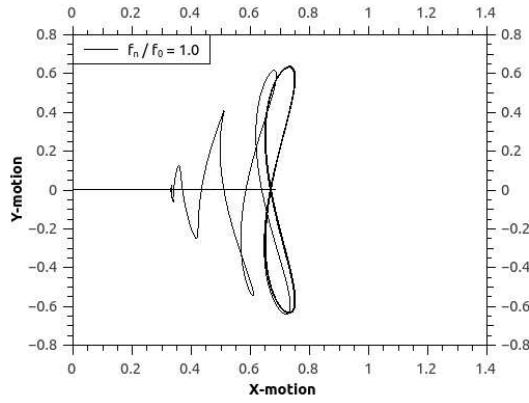


(a) XY-motion plot of an elastic cylinder for $\frac{f_n}{f_0} = 0.5$ (b) Displacement and lift coefficient curves of an elastic cylinder for $\frac{f_n}{f_0} = 0.5$.

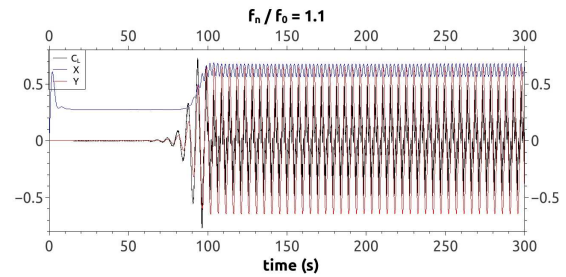
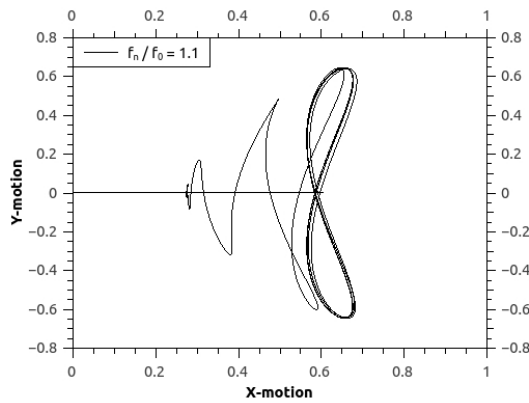
6.1. TWO DEGREES-OF-FREEDOM CYLINDER WITH A 8D MESH SIZE



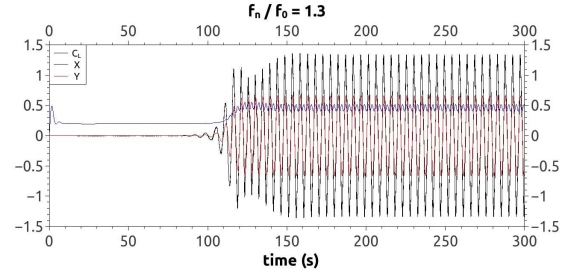
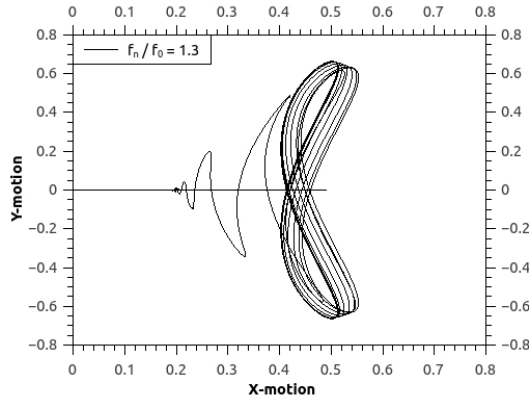
(c) XY-motion plot of an elastic cylinder for $f_n/f_0 = 0.9$ (d) Displacement and lift coefficient curves of an elastic cylinder for $f_n/f_0 = 0.9$.



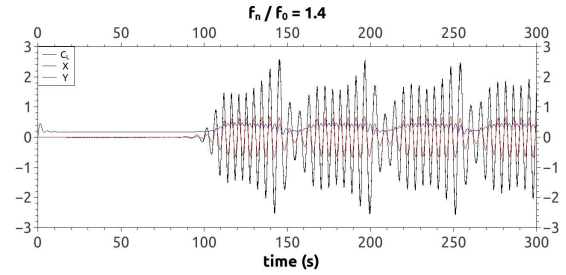
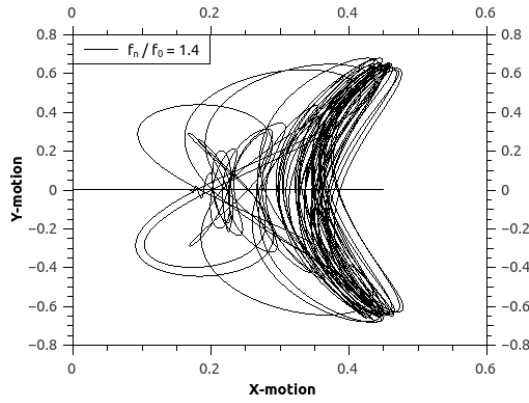
(e) XY-motion plot of an elastic cylinder for $f_n/f_0 = 1.0$ (f) Displacement and lift coefficient curves of an elastic cylinder for $f_n/f_0 = 1.0$.



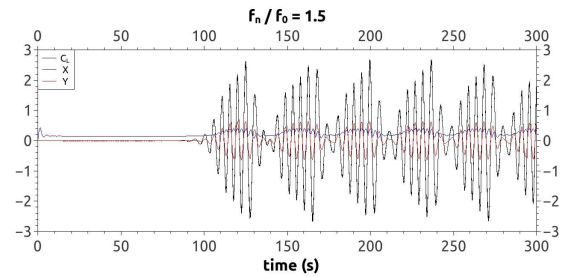
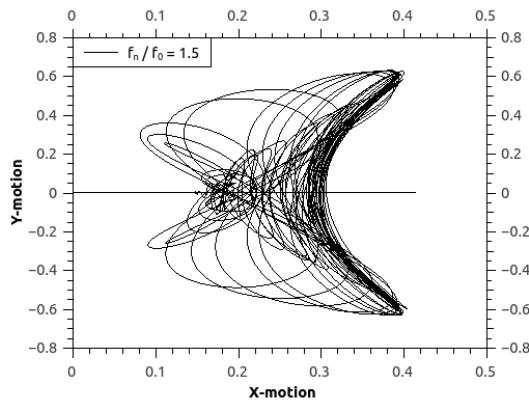
(g) XY-motion plot of an elastic cylinder for $f_n/f_0 = 1.1$ (h) Displacement and lift coefficient curves of an elastic cylinder for $f_n/f_0 = 1.1$.



(i) XY-motion plot of an elastic cylinder for $\frac{f_n}{f_0} = 1.3$ (j) Displacement and lift coefficient curves of an elastic cylinder for $\frac{f_n}{f_0} = 1.3$.



(k) XY-motion plot of an elastic cylinder for $\frac{f_n}{f_0} = 1.4$ (l) Displacement and lift coefficient curves of an elastic cylinder for $\frac{f_n}{f_0} = 1.4$.



(m) XY-motion plot of an elastic cylinder for $\frac{f_n}{f_0} = 1.5$ (n) Displacement and lift coefficient curves of an elastic cylinder for $\frac{f_n}{f_0} = 1.5$.

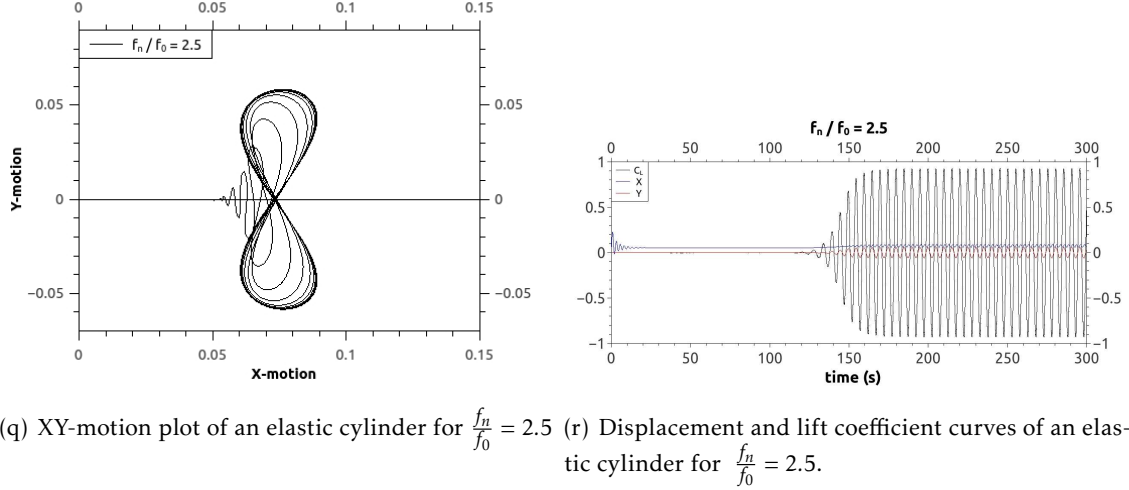
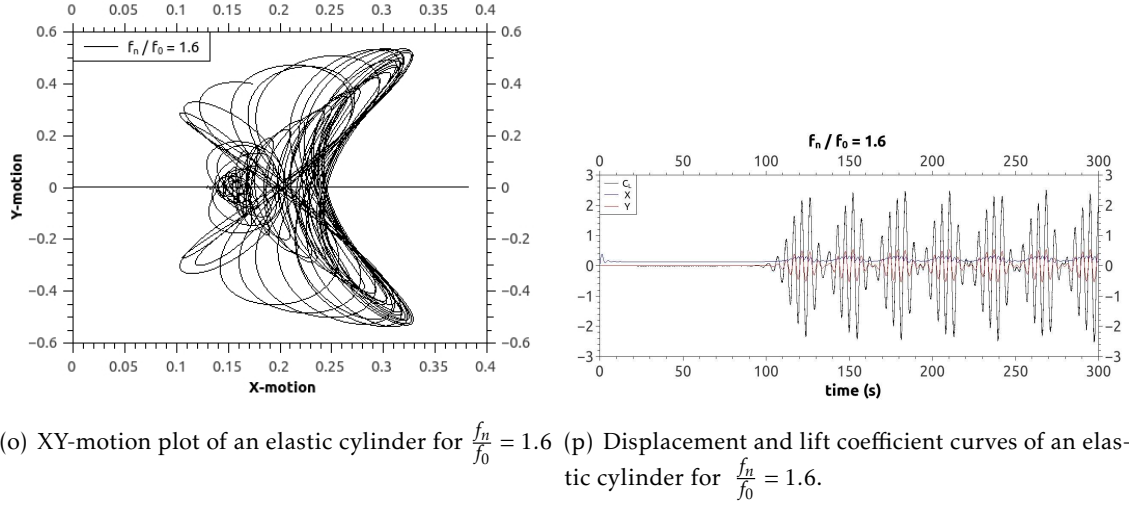


Figure 6.1: XY-motion plot of an elastic cylinder for a set of frequency ratio whit an 8D mesh.

6.1.1 Asymmetric 8-motion

One of the reasons which may cause the asymmetry of the oscillating movement of the cylinder is a bad design of the mesh, not being completely symmetric in the same zone where the flow is also symmetrical. A non-symmetric mesh can be originated by diverse causes, which include the not properly use of mesh blocks that allow for a larger control in mesh generation software, such as Gmsh. Usually this kind of software performs this generation automatically, requiring to handle the mesh generation controllably in each mesh block. This means that each mesh block does not influence the positioning of the nodes of the mesh elements of neighbouring blocks.

Since the studies previously described are using an O-type mesh, it is important to make at least the split of the mesh using two distinct mesh blocks, an upper and a lower block. This configuration allows the nodes of the mesh generated in the upper block to

not influence the generation of the mesh's lower block. However, the use of mesh blocks properly positioned is not enough to ensure the symmetry of a mesh. It is required that the elements have of the same geometry and, moreover, that the progressions used for the different mesh blocks are correctly symmetrical. Still, with the software automatic mesh generation the perfect symmetry is not guaranteed. It is, therefore, desirable that to study a high sensitivity problem, as it is the case of the cylinder movement induced by the flow displacement with two DOF, to use a utility tool which is able to perform a mesh mirror. Such tool is available in OpenFOAM, designated by `mirrorMesh`. This tool insures, hence, that all mesh nodes are symmetrically positioned.

Therefore, it was decided to reconfigure the mesh used in the previous study and described in the table 6.2, to have asymmetrical properties. To perform that it were defined four distinct mesh units and delineated the flow asymmetry line between both upper and lower mesh blocks. This allows to manipulate independently the elements of both blocks. Next, it was defined triangular elements in all four blocks. Finally, it was changed the progression which defines the increase of the number of elements in the cylinder direction distinctly for both mesh blocks. In detail, for the upper blocks it was defined the progression value of 1 whereas for the lower blocks it was configured the progression value of 1.1, becoming thereby a perfectly asymmetric mesh. The mesh characteristics are described in table 6.3.

Table 6.3: Geometric parameters of the asymmetric 8D mesh.

Mesh	$\frac{e}{D}_{above}$	$\frac{e}{D}_{below}$	N_{rad}	N_{ang}	N_{cells}	r_{above}	r_{below}
Current study	0.2	0.0012	45	136	6120	1	1.06

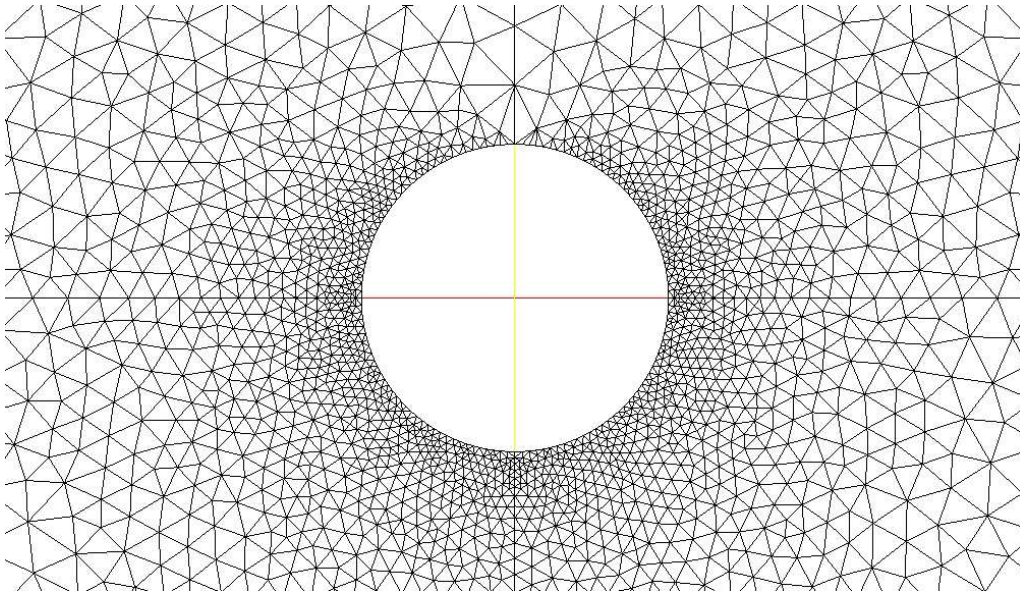
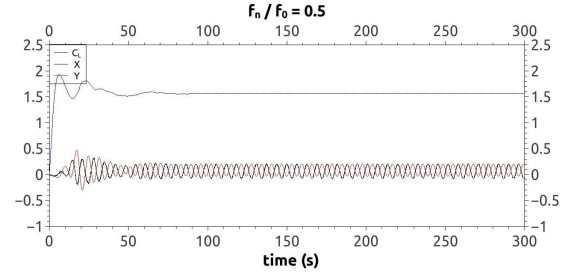
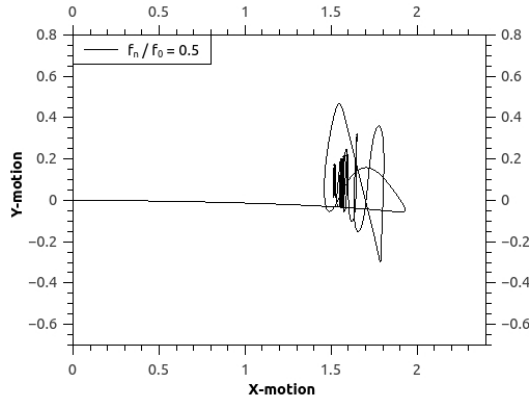


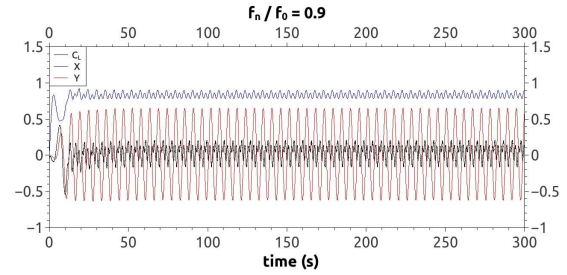
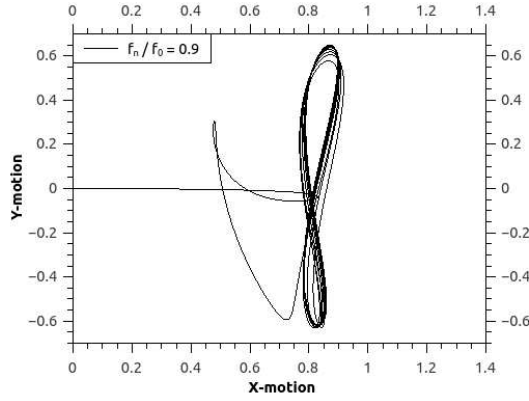
Figure 6.2: Representation of the asymmetric mesh with 8D, near to the cylinder wall.

Figure's 6.3 plots illustrate the response of the cylinder with the use of the previously described asymmetric mesh. For the frequency ratio values, it is visible a clear asymmetry between the upper and the lower part of the described movement. Congruently with the results presented by T. Li and Zhu, the lower part of the movement has greater amplitude and lower circular movement when compared to the circle described at the upper zone of the plots. Several tests were made with different progression values between the upper and the lower zone of the mesh. From these tests it was concluded that the distinct motions are directly related with the size of the mesh elements. That is, by decreasing the value of the progression in the upper part of the mesh to the value of $r = 1$, the spacing between elements is equal and there is no increase or decrease of the distance between nodes near the cylinder wall. This implies that the element width, that is, the distance between the cylinder wall to the second element of mesh in a radial direction is much larger than the element in the lower part of the mesh where it is used progression of $r = 1.1$ from the mesh domain boundary to the cylinder boundary wall. In table 6.3 it is possible to see the size of the element along the cylinder wall at the top of the cylinder $\frac{e}{D}_{above} = 0.2$ and the mesh element size at the bottom the cylinder with the cylinder wall of $\frac{e}{D}_{below} = 0.0012$. This difference in the element size causes that the cylinder displacement motion is much greater, since the mesh embracing area is much greater at the domain top given that the elements are larger and take up a significantly larger area when compared with the mesh embracing area in the mesh inferior zone. The reverse was also tested, using for that the progression value of $r = 1.1$ in the upper part and $r = 1$ in the lower part. The obtained cylinder motion was congruent with what was expected, with the inverse response of the previously described one. This means that to the inverse configuration the upward movement on the circle is tighter and reduced when compared with the bottom movement.

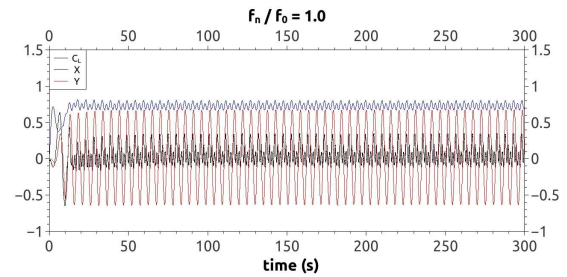
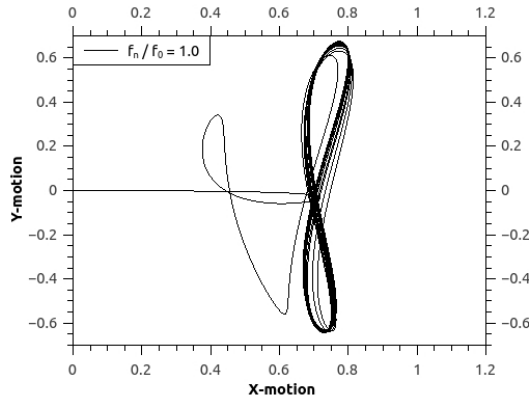
The plots in figure 6.3 describe the movement obtained for the asymmetric mesh for different frequency ratios. One can observe an excellent similarity to the cylinder motion geometry demonstrated by T. Li and Zhu. Equivalently, it is possible to observe a good approximation between both studies in terms of the oscillation amplitudes, according to the parallel and the orthogonal motions to the direction of the flow displacement. The same can be concluded for the distance between the geometric center of oscillation and the referential origin. Nevertheless, both studies have differences in the path made by the cylinder to stabilize its oscillatory movement.



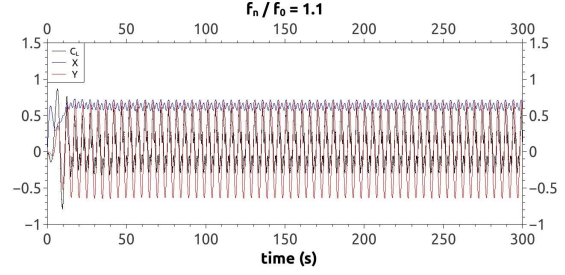
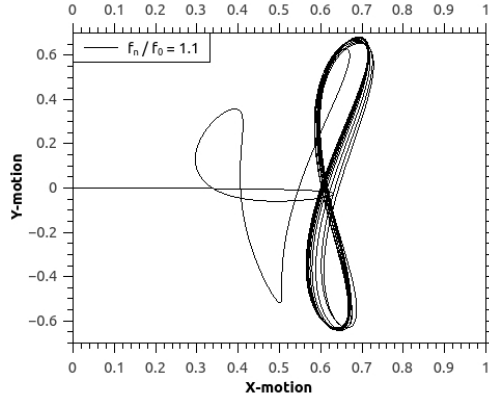
(a) XY-motion plot of an elastic cylinder for $\frac{f_n}{f_0} = 0.5$ (b) Displacement and lift coefficient curves of an elastic cylinder for $\frac{f_n}{f_0} = 0.5$.



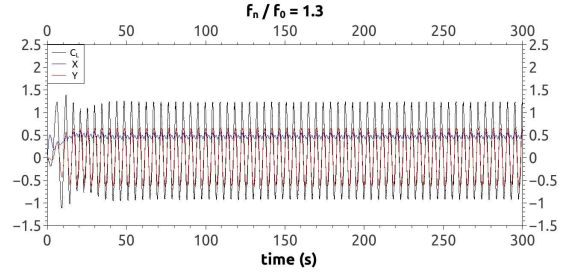
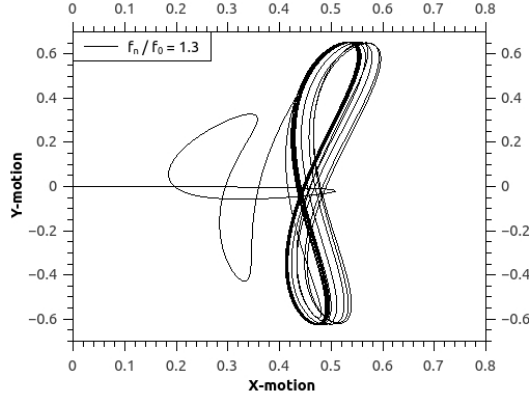
(c) XY-motion plot of an elastic cylinder for $\frac{f_n}{f_0} = 0.9$ (d) Displacement and lift coefficient curves of an elastic cylinder for $\frac{f_n}{f_0} = 0.9$.



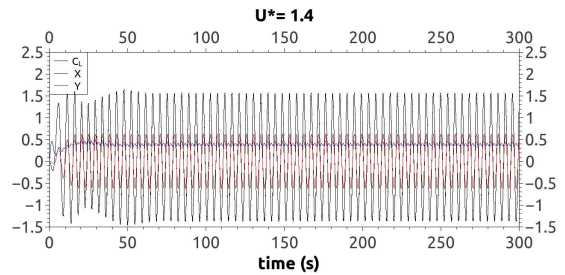
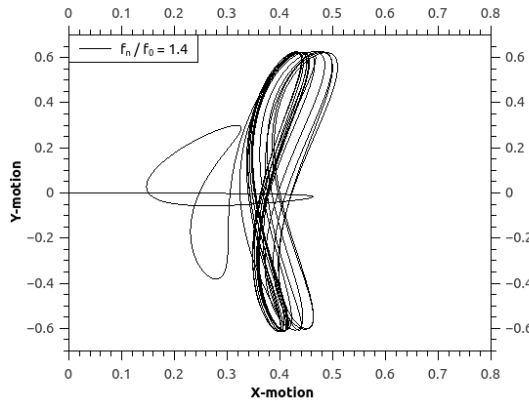
(e) XY-motion plot of an elastic cylinder for $\frac{f_n}{f_0} = 1.0$ (f) Displacement and lift coefficient curves of an elastic cylinder for $\frac{f_n}{f_0} = 1.0$.



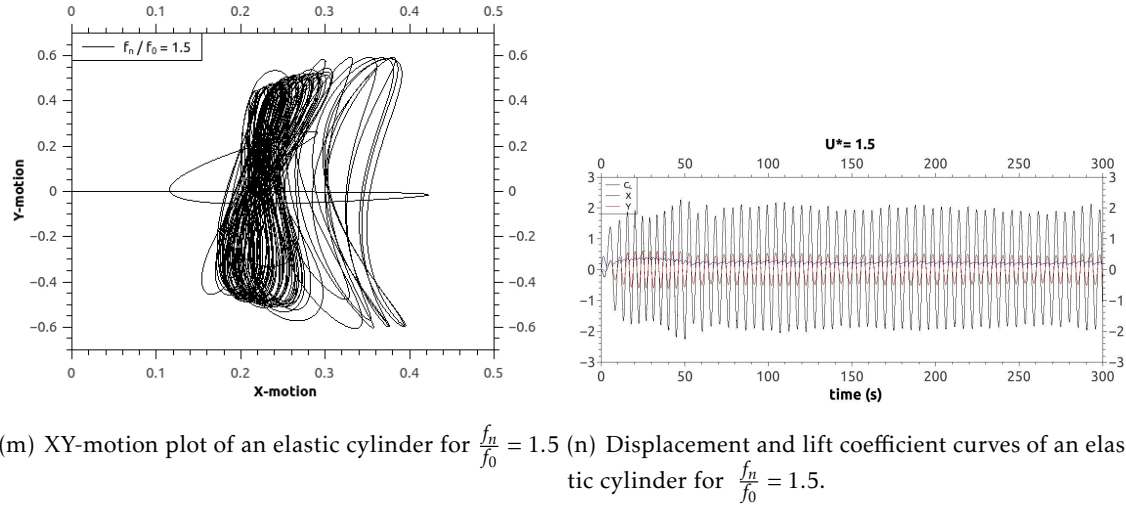
(g) XY-motion plot of an elastic cylinder for $\frac{f_n}{f_0} = 1.1$ (h) Displacement and lift coefficient curves of an elastic cylinder for $\frac{f_n}{f_0} = 1.1$.



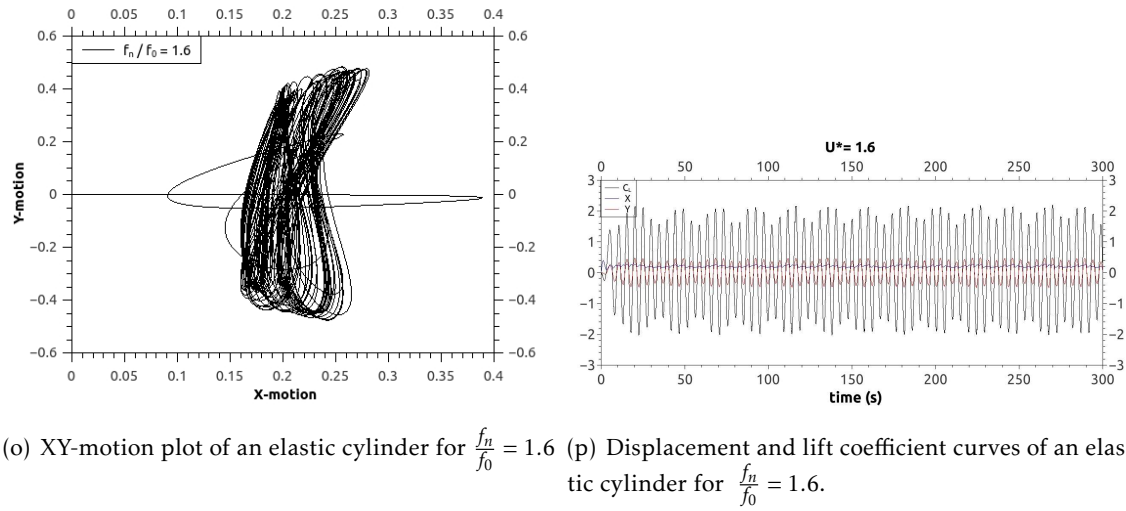
(i) XY-motion plot of an elastic cylinder for $\frac{f_n}{f_0} = 1.3$ (j) Displacement and lift coefficient curves of an elastic cylinder for $\frac{f_n}{f_0} = 1.3$.



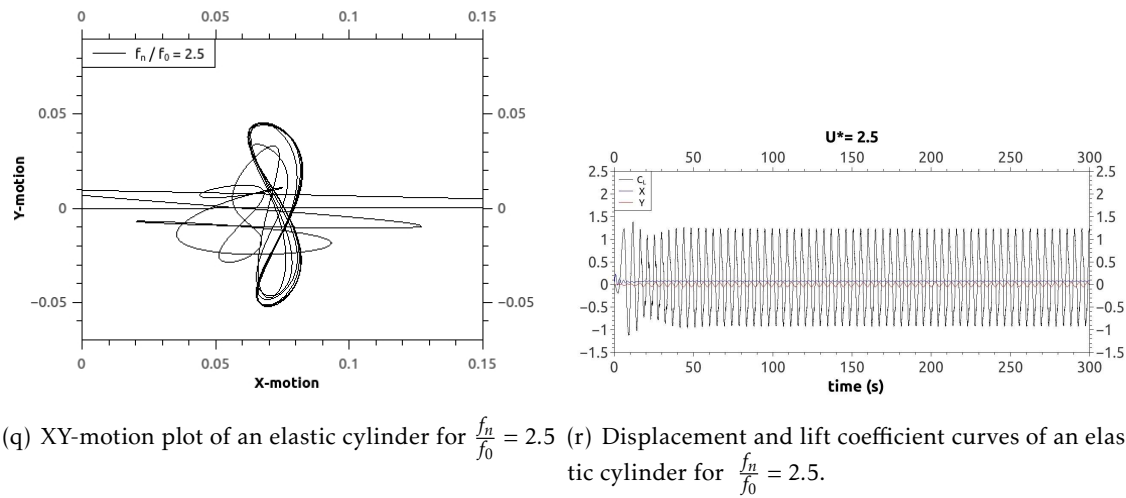
(k) XY-motion plot of an elastic cylinder for $\frac{f_n}{f_0} = 1.4$ (l) Displacement and lift coefficient curves of an elastic cylinder for $\frac{f_n}{f_0} = 1.4$.



(m) XY-motion plot of an elastic cylinder for $f_n/f_0 = 1.5$ (n) Displacement and lift coefficient curves of an elastic cylinder for $f_n/f_0 = 1.5$.



(o) XY-motion plot of an elastic cylinder for $f_n/f_0 = 1.6$ (p) Displacement and lift coefficient curves of an elastic cylinder for $f_n/f_0 = 1.6$.



(q) XY-motion plot of an elastic cylinder for $f_n/f_0 = 2.5$ (r) Displacement and lift coefficient curves of an elastic cylinder for $f_n/f_0 = 2.5$.

Figure 6.3: XY-motion plot of an elastic cylinder for a set of frequency ratios with an asymmetric 8D mesh.

6.2 Distinct oscillation cylinder geometries for different levels of mesh refinement

Along with the study done in section 6.1 for the 8D mesh, it was investigated how the increase of the 8D mesh refinement influences the obtained results and, later, these results were compared with the results described by T. Li and Zhu.

6.2.1 8D for second level of refinement

The characteristics of the second mesh refinement are displayed in table 6.4. The value of the elements progression in the radial direction towards the the cylinder wall was the only maintained characteristic, with $r = 1.06$. The reason why it was used in this study a mesh with characteristics so disparate, with an element size much greater than the used for this refinement, was to mimic the mesh used by T. Li and Zhu. Therefore, this fact was used to evaluate how the decrease of the elements size along the cylinder boundary influences the obtained results for a first refinement level. Thus, it was decided to scale the size of the element neighbouring the cylinder wall to $\frac{e}{D} = 0.0012$, according to the criteria that has been used and chosen throughout this thesis. The number of elements in the radial direction was modified to 440 and in the angular direction to 89.

Table 6.4: Geometric parameters for second level of refinement in the 8D mesh.



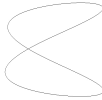
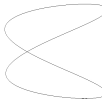




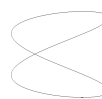
Mesh	$\frac{e}{D}$	N_{rad}	N_{ang}	N_{cells}	r
Current study	0.0012	89	436	38804	1.06

It is possible to observe distinct cylinder responses for this refinement level of the 8D mesh, both in terms of amplitudes demonstrated by the cylinder movement as well as in terms of the cylinder movement geometry. Additionally, the cylinder response for the current refinement level is similar to one obtained when using a 20D mesh, subject that will be discussed in section 6.3.1.

Table 6.5 shows the in-line and the transversal cylinder oscillation amplitude relatively to flow direction and the x maximum initial cylinder displacement. In this table is also illustrated the cylinder 8-motion respective to the last cycle for each frequency ratio.

For the first studied frequency ratio with this mesh refinement level, $\frac{f_n}{f_0} = 0.5$, the variables amplitudes are amplified when compared with cylinder response demonstrated in section 6.1 for the original 8D mesh. The geometric center of oscillation remains similar to the one obtained for the 8D mesh demonstrated in section 6.1, corresponding to $x = 1.6$. The differences between both analysis are related with the cylinder horizontal oscillation, namely, the oscillatory movement of the cylinder and the oscillation amplitudes orthogonal to the flow movement, which are between -0.4 and 0.4 for this refinement level, are not so focused as previously obtained.

Table 6.5: Fundamental quantities and 8-motion last cycle of the 8D mesh.

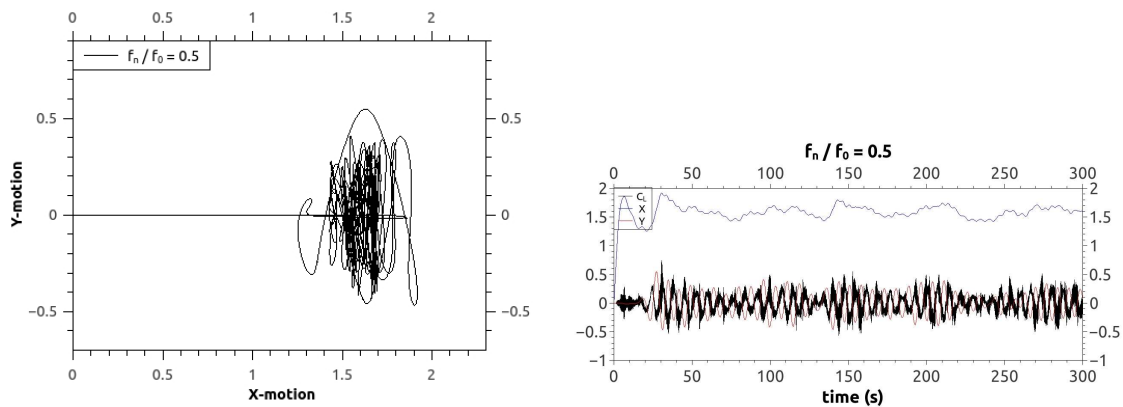
$\frac{f_n}{f_0}$	$Y_{max,osc}$	$X_{max,osc}$	X_{max}	8-motion
0.5	0.5474	0.3189	1.9177	
0.9	0.6941	0.1571	0.9873	
1.0	0.6831	0.1340	0.8459	
1.1	0.6988	0.1388	0.7691	
1.3	0.7324	0.5362	0.6405	
1.4	0.6662	0.4235	0.5060	
1.5	0.6042	0.2231	0.4300	
1.6	0.4961	0.2366	0.3569	
2.5	0.0626	0.0350	0.2055	

6.2. DISTINCT OSCILLATION CYLINDER GEOMETRIES FOR DIFFERENT LEVELS OF MESH REFINEMENT

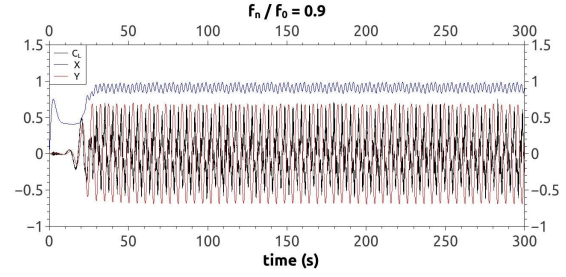
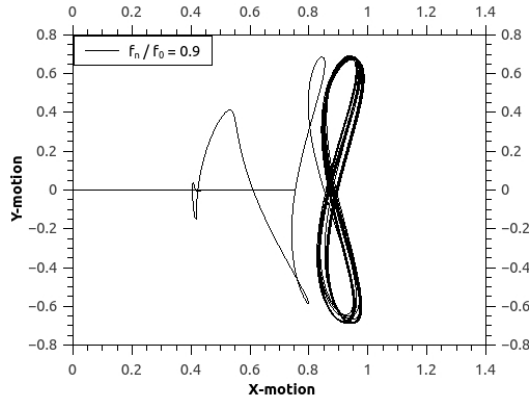
Regarding the frequency ratio of $\frac{f_n}{f_0} = 0.9$ the cylinder oscillation displayed an oscillatory movement very similar to the original analysis, having the cylinder moved around the geometric oscillation center located lightly more to the left in about 0.9 to the right of the referential origin. Only the orthogonal amplitudes to the flow movement increased moderately, with the cylinder oscillating between -0.7 and 0.7 .

Concerning the frequency ratio of $\frac{f_n}{f_0} = 1.0$ illustrated in figure 6.4(e) it is visible a similar geometry to the one achieved for the $8D$ mesh in section 6.1. However, the oscillatory geometric center is located slightly to the right, with a coordinate of about $x = 0.78$, keeping the values of the amplitudes obtained very similar to the first study. The same is true for figure 6.4(g) which shows the cylinder's response for the frequency ratio of $\frac{f_n}{f_0} = 1.1$.

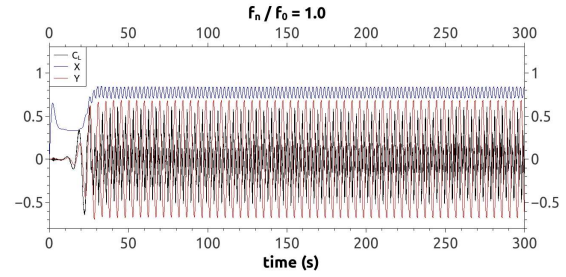
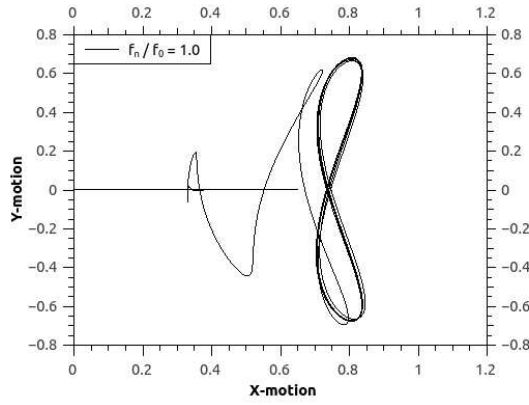
Contrasting to the results obtained for the frequency ratio of $\frac{f_n}{f_0} = 1.3$ with the $8D$ mesh in section 6.1 the obtained response in figure 6.4(i) has similarities with figure 6.6(i) which exhibits the cylinder movement for the mesh with $20D$ length. Furthermore, this fact is verified for the remaining frequency ratios, $\frac{f_n}{f_0} = 1.3$, $\frac{f_n}{f_0} = 1.4$, $\frac{f_n}{f_0} = 1.5$, $\frac{f_n}{f_0} = 1.6$ and $\frac{f_n}{f_0} = 2.5$ presented for the given mesh refinement level with the $8D$ mesh showing, hence, greater similarities with the results obtained for the $20D$ mesh.



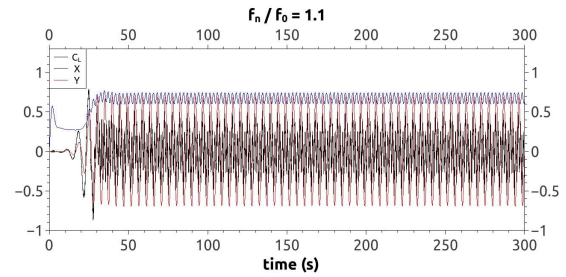
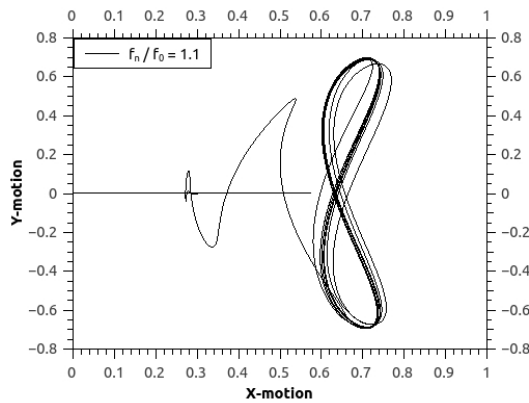
(a) XY-motion plot of an elastic cylinder for $\frac{f_n}{f_0} = 0.5$ (b) Displacement and lift coefficient curves of an elastic cylinder for $\frac{f_n}{f_0} = 0.5$.



(c) XY-motion plot of an elastic cylinder for $\frac{f_n}{f_0} = 0.9$ (d) Displacement and lift coefficient curves of an elastic cylinder for $\frac{f_n}{f_0} = 0.9$.

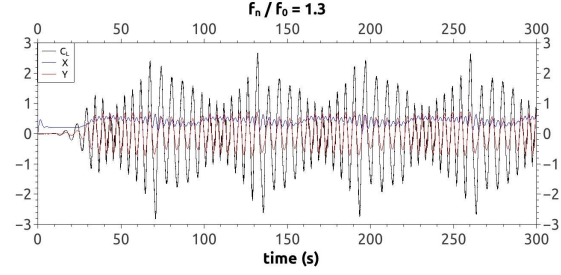
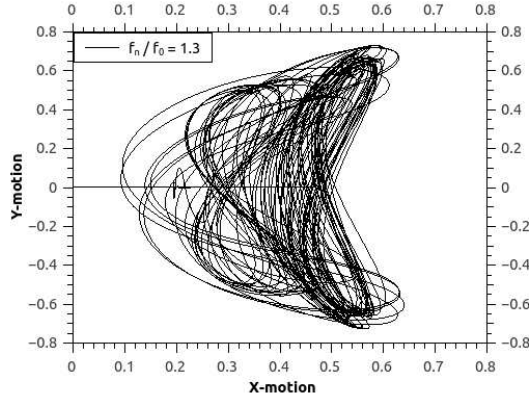


(e) XY-motion plot of an elastic cylinder for $\frac{f_n}{f_0} = 1.0$ (f) Displacement and lift coefficient curves of an elastic cylinder for $\frac{f_n}{f_0} = 1.0$.

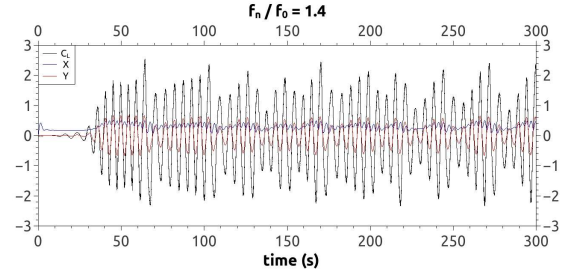
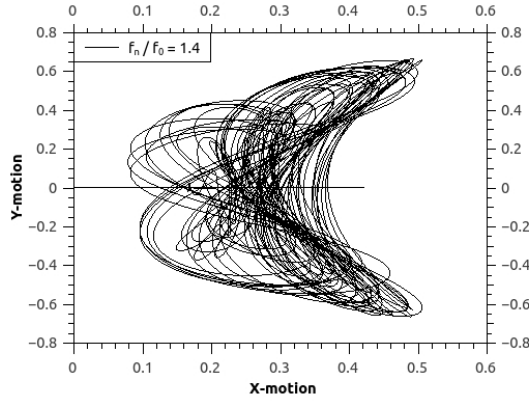


(g) XY-motion plot of an elastic cylinder for $\frac{f_n}{f_0} = 1.1$ (h) Displacement and lift coefficient curves of an elastic cylinder for $\frac{f_n}{f_0} = 1.1$.

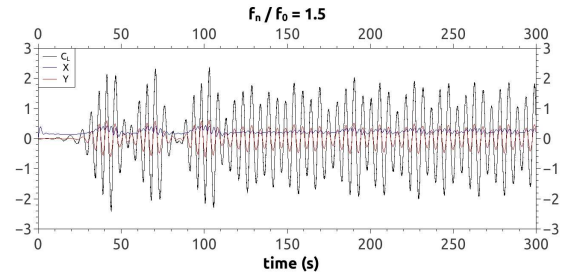
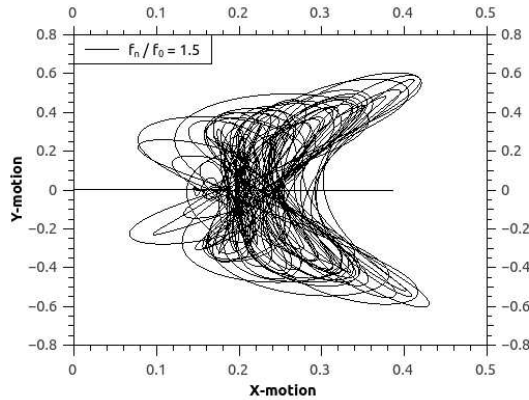
6.2. DISTINCT OSCILLATION CYLINDER GEOMETRIES FOR DIFFERENT LEVELS OF MESH REFINEMENT



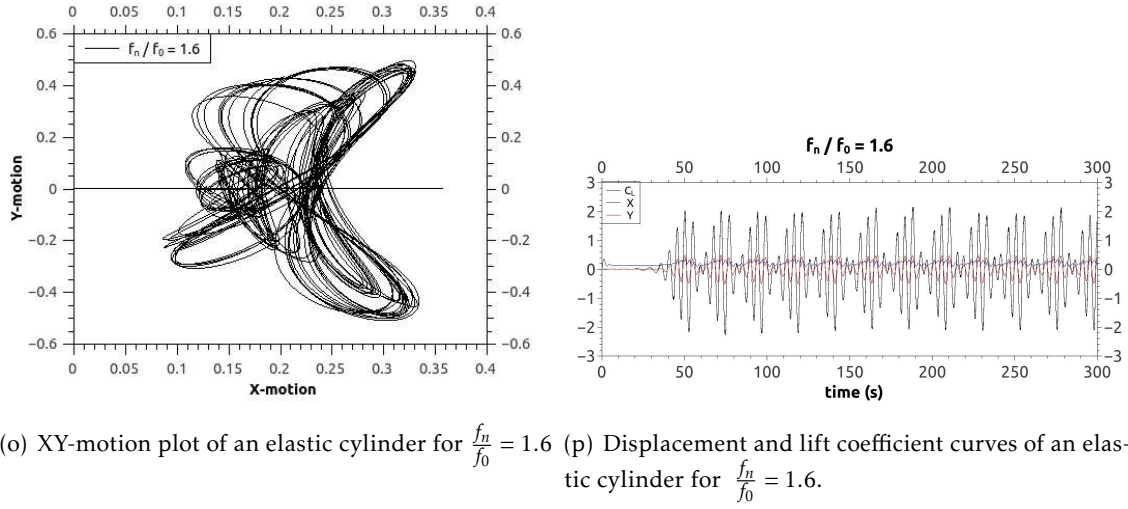
(i) XY-motion plot of an elastic cylinder for $\frac{f_n}{f_0} = 1.3$ (j) Displacement and lift coefficient curves of an elastic cylinder for $\frac{f_n}{f_0} = 1.3$.



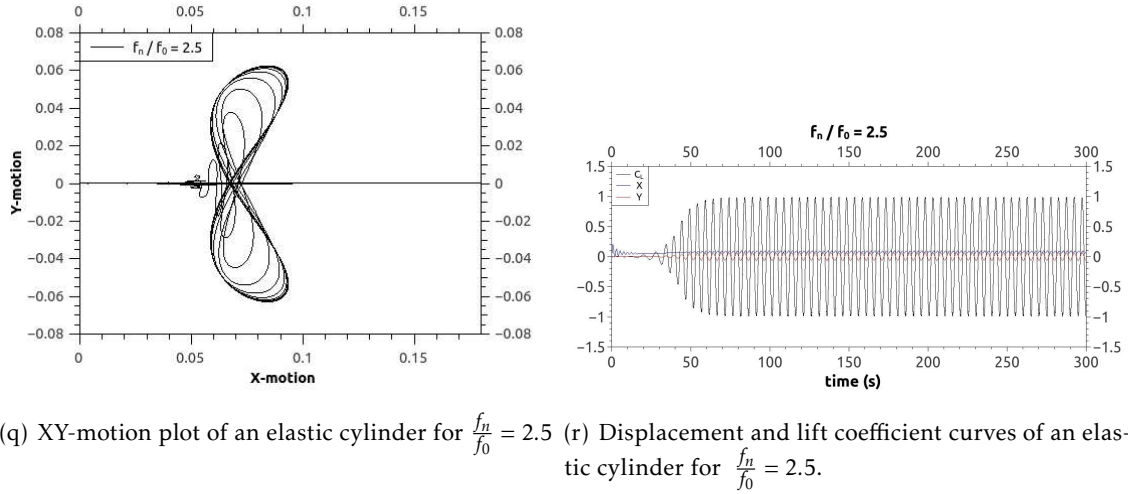
(k) XY-motion plot of an elastic cylinder for $\frac{f_n}{f_0} = 1.4$ (l) Displacement and lift coefficient curves of an elastic cylinder for $\frac{f_n}{f_0} = 1.4$.



(m) XY-motion plot of an elastic cylinder for $\frac{f_n}{f_0} = 1.5$ (n) Displacement and lift coefficient curves of an elastic cylinder for $\frac{f_n}{f_0} = 1.5$.



(o) XY-motion plot of an elastic cylinder for $\frac{f_n}{f_0} = 1.6$ (p) Displacement and lift coefficient curves of an elastic cylinder for $\frac{f_n}{f_0} = 1.6$.



(q) XY-motion plot of an elastic cylinder for $\frac{f_n}{f_0} = 2.5$ (r) Displacement and lift coefficient curves of an elastic cylinder for $\frac{f_n}{f_0} = 2.5$.

Figure 6.4: XY-motion plot of an elastic cylinder for a set of frequency ratios for an 8D mesh for the second level of refinement studied.

6.2.2 8D for third level of refinement

The current section exposes the results for a third level of refinement of the mesh in order to verify, as was made in section 6.2.1, the influence of the mesh refinement level in the elastic cylinder motion. Table 6.6 enumerates the characteristics of the mesh used in this study.

Table 6.6: Geometric parameters for third level of refinement in the 8D mesh.

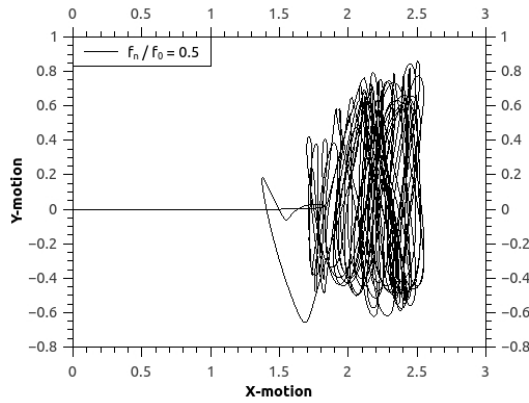
Mesh	$\frac{\epsilon}{D}$	N_{rad}	N_{ang}	N_{cells}	r
Current study	0.0012	89	536	47704	1.06

Some differences are observed in the amplitudes reached to this level of refinement,

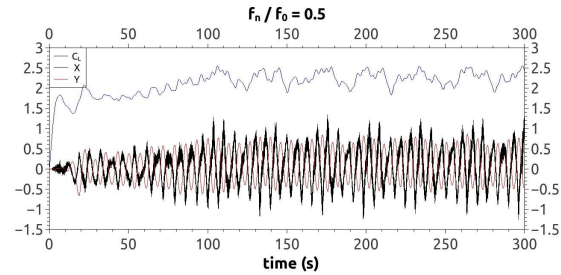
6.2. DISTINCT OSCILLATION CYLINDER GEOMETRIES FOR DIFFERENT LEVELS OF MESH REFINEMENT

as it can be observed by the plots in figure 6.2.2. The main difference occurs for the frequency ratio of $\frac{f_n}{f_0} = 0.5$ to which corresponds a much greater oscillation amplitude for the in the parallel and orthogonal directions to the flow displacement when compared with the previous refinement level.

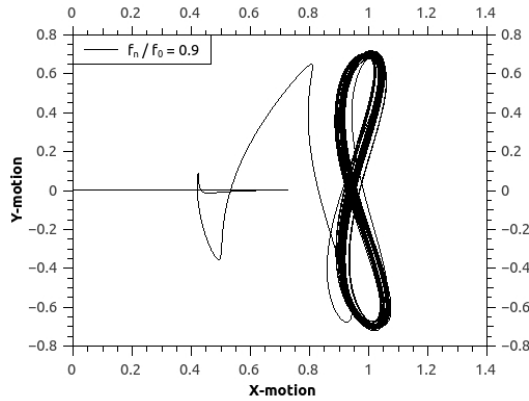
For other frequency ratios a small difference is observed in the amplitude achieved in the transverse direction and, in the same way, a small difference is noted for in-line cylinder movement. It is noticeable, however, that the oscillation center is slightly farther from the referential origin than for the second level of refinement. This observation is common to all frequency ratios, with this small difference obtained between the two levels of refinement. The exception is the frequency ratio of $\frac{f_n}{f_0} = 1.6$ for which the trajectory of the cylinder oscillatory movement changes slightly between the two levels of refinement.



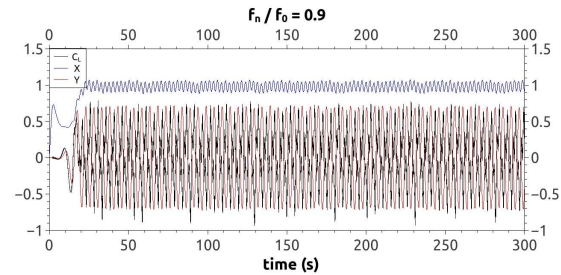
(a) XY-motion plot of an elastic cylinder for a second level of refinement for $\frac{f_n}{f_0} = 0.5$.



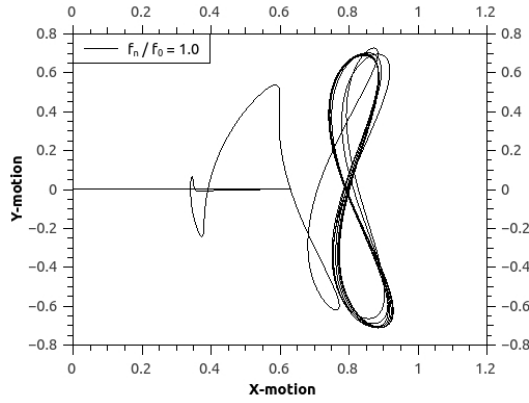
(b) Displacement and lift coefficient curves of an elastic cylinder for a second level of refinement for $\frac{f_n}{f_0} = 0.5$.



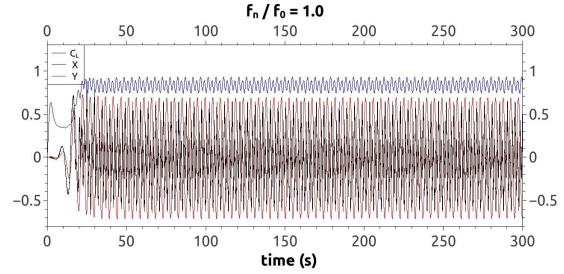
(c) XY-motion plot of an elastic cylinder for a second level of refinement for $\frac{f_n}{f_0} = 0.9$.



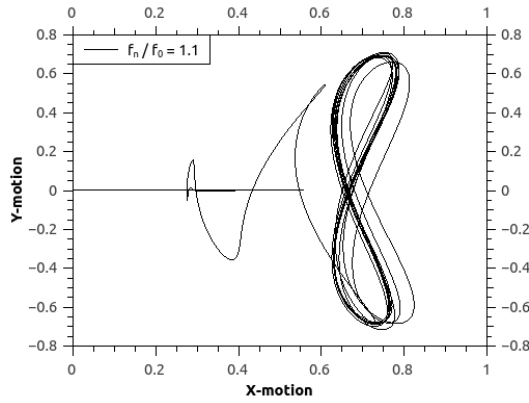
(d) Displacement and lift coefficient curves of an elastic cylinder for a second level of refinement for $\frac{f_n}{f_0} = 0.9$.



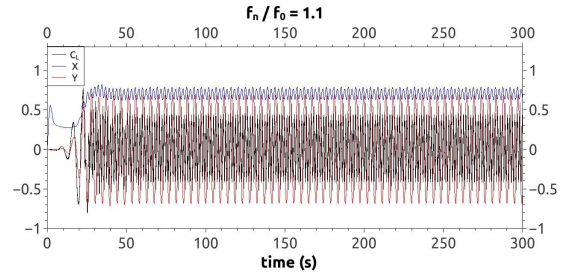
(e) XY-motion plot of an elastic cylinder for a second level of refinement for $\frac{f_n}{f_0} = 1.0$.



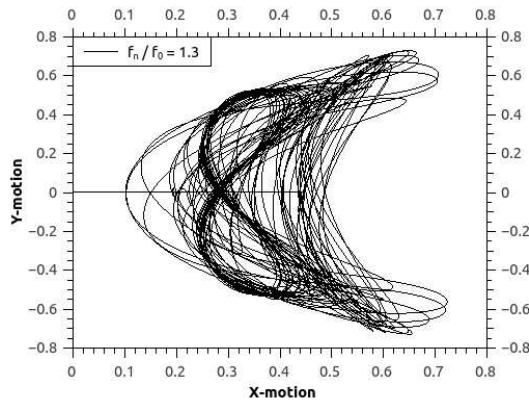
(f) Displacement and lift coefficient curves of an elastic cylinder for a second level of refinement for $\frac{f_n}{f_0} = 1.0$.



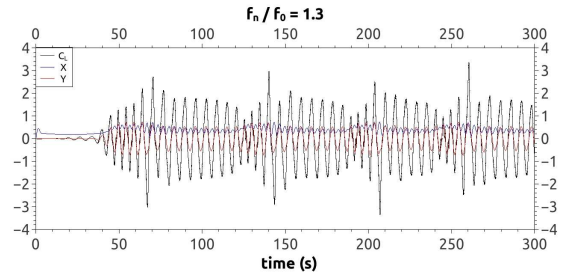
(g) XY-motion plot of an elastic cylinder for a second level of refinement for $\frac{f_n}{f_0} = 1.1$.



(h) Displacement and lift coefficient curves of an elastic cylinder for a second level of refinement for $\frac{f_n}{f_0} = 1.1$.

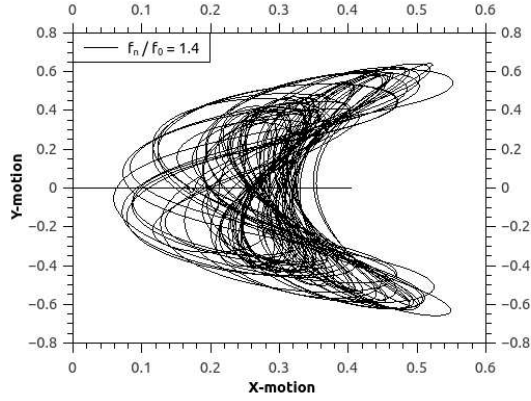


(i) XY-motion plot of an elastic cylinder for a second level of refinement for $\frac{f_n}{f_0} = 1.3$.

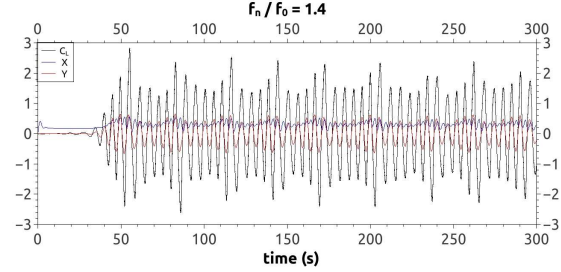


(j) Displacement and lift coefficient curves of an elastic cylinder for a second level of refinement for $\frac{f_n}{f_0} = 1.3$.

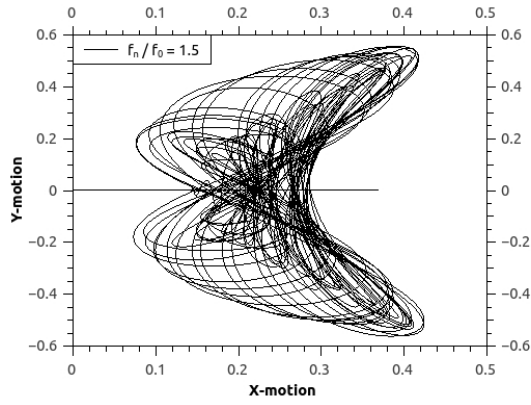
6.2. DISTINCT OSCILLATION CYLINDER GEOMETRIES FOR DIFFERENT LEVELS OF MESH REFINEMENT



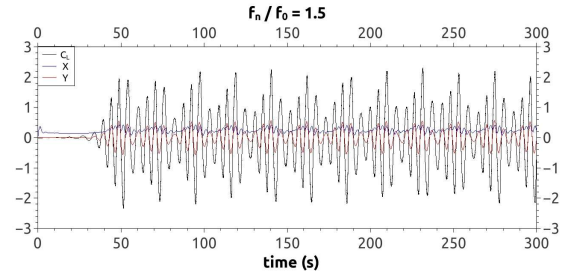
(k) XY-motion plot of an elastic cylinder for a second level of refinement for $\frac{f_n}{f_0} = 1.4$.



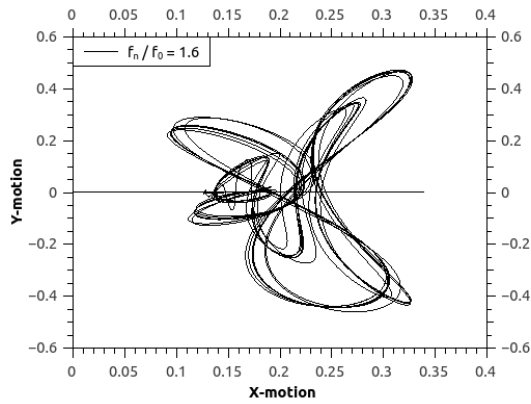
(l) Displacement and lift coefficient curves of an elastic cylinder for a second level of refinement for $\frac{f_n}{f_0} = 1.4$.



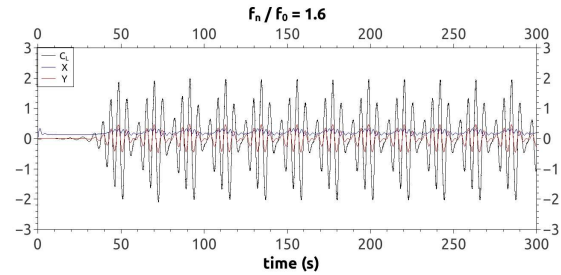
(m) XY-motion plot of an elastic cylinder for a second level of refinement for $\frac{f_n}{f_0} = 1.5$.



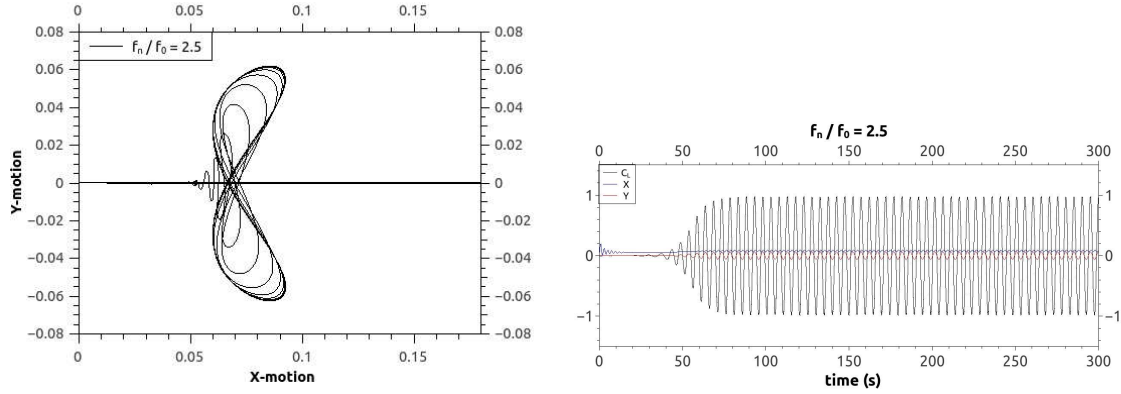
(n) Displacement and lift coefficient curves of an elastic cylinder for a second level of refinement for $\frac{f_n}{f_0} = 1.5$.



(o) XY-motion plot of an elastic cylinder for a second level of refinement for $\frac{f_n}{f_0} = 1.6$.



(p) Displacement and lift coefficient curves of an elastic cylinder for a second level of refinement for $\frac{f_n}{f_0} = 1.6$.



(q) XY-motion plot of an elastic cylinder for a second level of refinement for $\frac{f_n}{f_0} = 2.5$. (r) Displacement and lift coefficient curves of an elastic cylinder for a second level of refinement for $\frac{f_n}{f_0} = 2.5$.

Figure 6.5: XY-motion plot of an elastic cylinder for a set of frequency ratios for an 8D mesh for the third level of refinement studied

6.3 Distinct oscillation cylinder geometries for different mesh dimensions









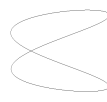
The blockage effect is influenced by the distance between the cylinder and the respective boundaries parallel to the direction of the flow. The boundary walls induce the flow confinement by increasing the flow rate and decreasing the respective value of the pressure field which subsequently influences the cylinder movement. It was conducted a study about the influence that the distance of the boundary walls to the cylinder have in its respective movement for two DOF in a mesh with domain size of $8D$, $20D$, $500D$ and $2500D$. Having already been presented the study of the flow around the cylinder for two DOF for the $8D$ mesh in section 6.2, in the current section is presented the study of the remaining meshes and the respective comparison between these various domains.

Something that was taken into account for the four different meshes developed was the size of the element along the cylinder wall, while maintaining the same size, $\frac{e}{D} = 0.0012$, regardless of the size of the mesh. It is also important to note that there was the concern to maintain the progression of equal value for all four scenarios, presenting a progression value of $r = 1.06$. Finally, the number of elements along the cylinder wall was also maintained, with the value of $N_{rad} = 440$. The goal of fixing these parameters was to exclude the possibility of changes in the cylinder response related with the change in mesh elements near the cylinder wall and in the area where the vortex shedding phenomenon is developed. Hence, to keep these fixed parameters, the response of the cylinder to these four different meshes, can only be determined by the change in the domain length. Thus, it is possible to conclude about how the mesh size influences and alters the response of the cylinder with two DOF for a flow around it with the characteristics presented in chapter 3.

6.3.1 Mesh with 20D

Table 6.7 shows the in-line and the transversal cylinder oscillation amplitude relatively to flow direction and the x maximum initial cylinder displacement for the 20D mesh. In this table is also illustrated the cylinder 8-motion respective to the last cycle for each frequency ratio.

Table 6.7: Fundamental quantities and 8-motion last cycle of the 20D mesh.

$\frac{f_n}{f_0}$	$Y_{max,osc}$	$X_{max,osc}$	X_{max}	8-motion
0.5	0.5636	0.1490	1.8829	
0.9	0.7561	0.1734	1.1108	
1.0	0.7440	0.1774	0.9853	
1.1	0.7260	0.1872	0.8643	
1.3	0.7229	0.5419	0.6184	
1.4	0.6456	0.4449	0.5172	
1.5	0.5334	0.1528	0.3872	
1.6	0.4632	0.2125	0.3464	
2.5	0.0589	0.0309	0.1972	

With the increase of the domain length, from $8D$ to $20D$, some variations in the cylinder response are evident, proving that only the change of the mesh domain size influences greatly the cylinder response.

The fact that the cylinder is not in an area so confined, allows the movement to "release", expanding its movement so that its response is less influenced by the domain size. Thus, the cylinder movement shall be due more to the interaction between the flow and the cylinder for this mesh, $20D$, than what was observed for the mesh $8D$.

In the table 6.8 are described the $20D$ mesh characteristics. As mentioned above, the parameters related to the size of the element along the cylinder wall, the number of elements in the cylinder wall and the progression of the value of the mesh elements were remained constant, being the size of the mesh from $8D$ to $20D$ the only changed parameter and, consequently, the number of radial elements due to the increase of the mesh size.

Table 6.8: Geometric parameters of the $20D$ mesh.

Mesh	$\frac{e}{D}$	N_{rad}	N_{ang}	N_{cells}	r
Current study	0.0012	106	436	46216	1.06

Thus, by observing the response of the cylinder to the frequency ratio of $\frac{f_n}{f_0} = 0.5$ in figure 6.6(a) the motion geometry is preserved, showing the increase of the amplitudes orthogonal to the cylinder movement for more than double, varying from -0.6 to 0.6 , along with the deviation of the oscillation geometric center in relation to the referential origin, corresponding to 1.75 .

For the frequency ratio of $\frac{f_n}{f_0} = 0.9$ the amplitudes increase towards the same frequency ratio for the $8D$ mesh. No difference is noted in the geometry of the cylinder oscillatory movement, describing a very similar motion with respect to the $8D$ mesh. The oscillation in the direction orthogonal to the flow, registers values ranging between -0.7 and 0.7 , and the oscillation center geometry changes to the position 1 .

Concerning the frequency ratio of $\frac{f_n}{f_0} = 1.0$ the cylinder begins to describe the movement before stabilizing, describing a cyclically movement of an eight. This fact decreases the oscillation geometric center to the area where the movement is stable. The amplitude range also increases when compared to the same case analysed for the $8D$ mesh, having in the direction orthogonal to the flow a variation of -0.75 to 0.75 with an oscillation geometric center of 0.8 .

Figure 6.6(g) illustrates the cylinder response for the frequency ratio of $\frac{f_n}{f_0} = 1.1$. The displayed amplitudes are closer to the ones obtained for the $8D$ mesh study. The amplitudes recorded for the frequency ratio vary in the orthogonal direction to the fluid between -0.75 and 0.75 with an oscillating geometric center of 0.65 .

One of the major differences in the comparison between the $8D$ and the $20D$ meshes study lies in the response of the cylinder to the frequency ratio of $\frac{f_n}{f_0} = 1.3$. For the

6.3. DISTINCT OSCILLATION CYLINDER GEOMETRIES FOR DIFFERENT MESH DIMENSIONS

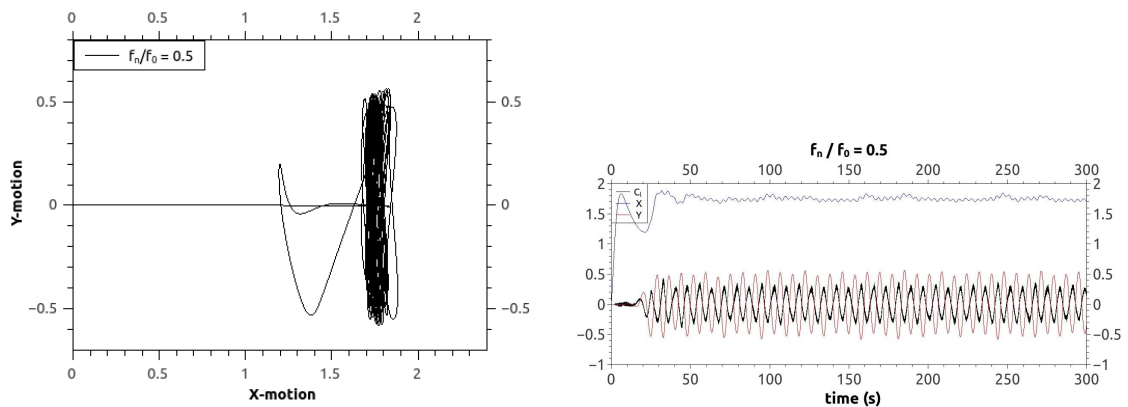
8D mesh the cylinder response is characterized by a stable movement with amplitudes and lift coefficient varying between the same values at each oscillation and describing a movement of a perfectly noticeable eight. While the cylinder motion for the 20D mesh shows two overlapping frequencies which can be observable in figure 6.6(i).

It is for the frequency ratio of $\frac{f_n}{f_0} = 1.4$ that both the 8D and the 20D meshes show the superposition of two different frequencies, causing the effect demonstrated in figure 6.6(l). Among the oscillatory movement caused by the cylinder and demonstrated by both figures 6.4(k) and 6.6(l) for the 8D and 20D meshes, respectively, it is visible the difference between both studies.

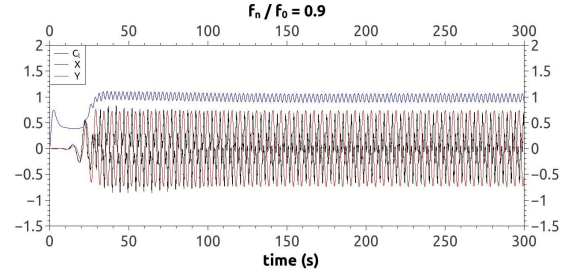
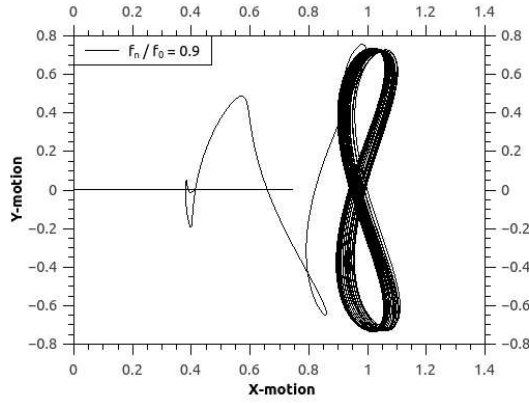
For figure 6.6(m) it is illustrated the cylinder behaviour for the 20D mesh and for the frequency ratio of $\frac{f_n}{f_0} = 1.5$. In this figure are noticeable the similarities with the motion obtained for the 8D mesh. The large upper circle that ranges, approximately, from 0.15 to 0.35, reaches the same flow orthogonal amplitude for $y = 0.5$.

The frequency ratio of $\frac{f_n}{f_0} = 1.6$ is the one that has the greatest similarities with the cylinder response obtained for the 8D mesh, among the frequency ratios that have two frequencies superposition, $\frac{f_n}{f_0} = 1.3$ 1.6. The resemblance between the two frequency responses are a consequence of a symmetrical effect in the x -axis, giving two figures with a geometry which resembles the geometry of a butterfly.

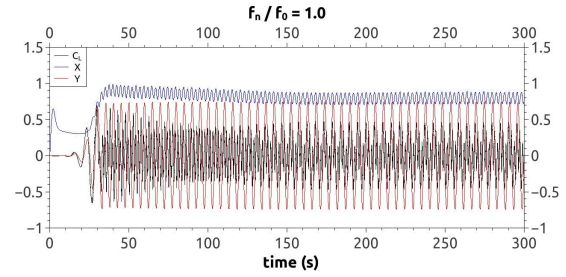
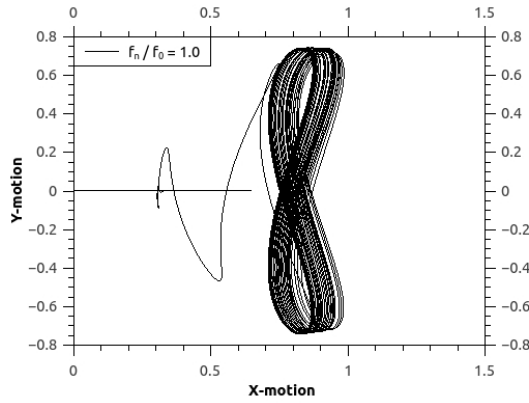
The figure 6.6(q) shows the geometry achieved by the oscillating movement of the cylinder for the frequency ratio of $\frac{f_n}{f_0} = 2.5$. Amplitudes between the responses given by the cylinder with different meshes, 8D and 20D, are practically the same varying between -0.06 and 0.06 for the orthogonal movement to the flow and with a geometric center of 0.07 to the right of the referential origin. The difference lies in the geometry of the cylinder motion. For the 20D mesh, the geometry of the movement both at the top and at the bottom is characterized by an elongation to the right direction in each half of the eight movement. While for the 8D mesh the cylinder describes a symmetrically motion in the x -axis which resembles the perfect geometry of a tear.



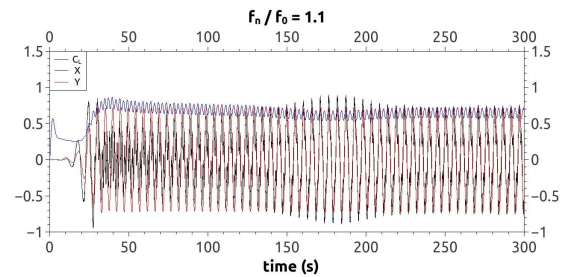
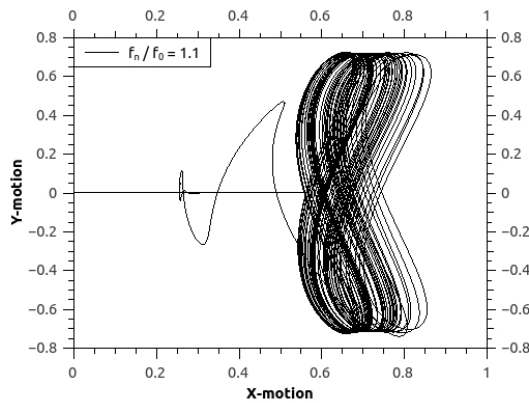
(a) XY-motion plot of an elastic cylinder for $\frac{f_n}{f_0} = 0.5$ (b) Displacement and lift coefficient curves of an elastic cylinder for $\frac{f_n}{f_0} = 0.5$.



(c) XY-motion plot of an elastic cylinder for $\frac{f_n}{f_0} = 0.9$ (d) Displacement and lift coefficient curves of an elastic cylinder for $\frac{f_n}{f_0} = 0.9$.

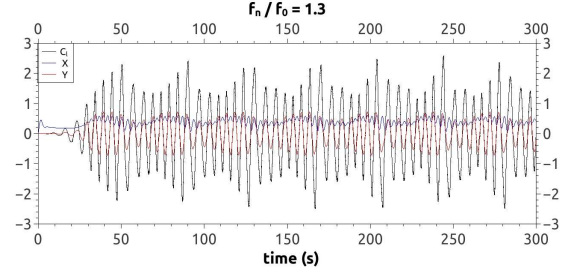
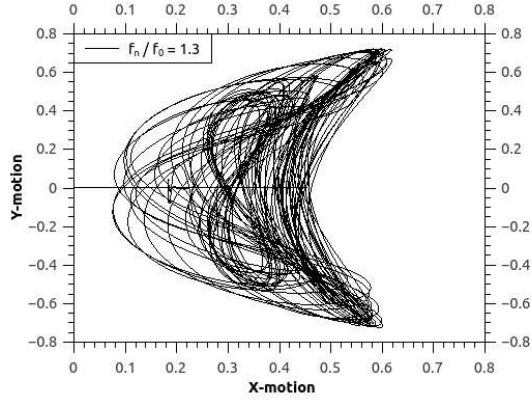


(e) XY-motion plot of an elastic cylinder for $\frac{f_n}{f_0} = 1.0$ (f) Displacement and lift coefficient curves of an elastic cylinder for $\frac{f_n}{f_0} = 1.0$.

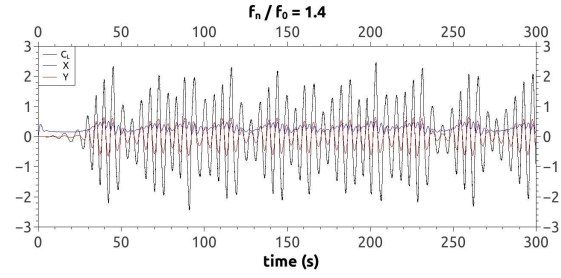
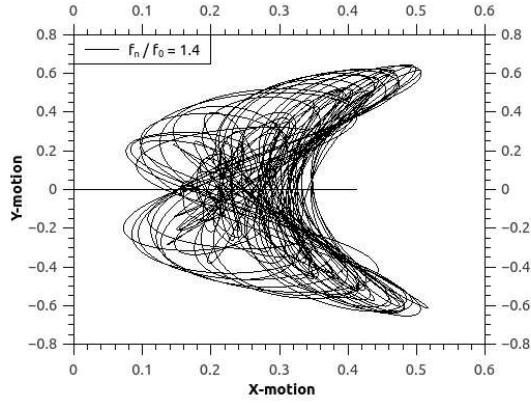


(g) XY-motion plot of an elastic cylinder for $\frac{f_n}{f_0} = 1.1$ (h) Displacement and lift coefficient curves of an elastic cylinder for $\frac{f_n}{f_0} = 1.1$.

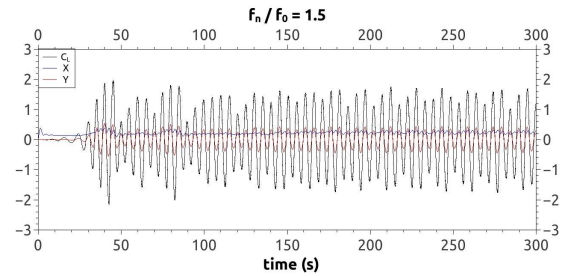
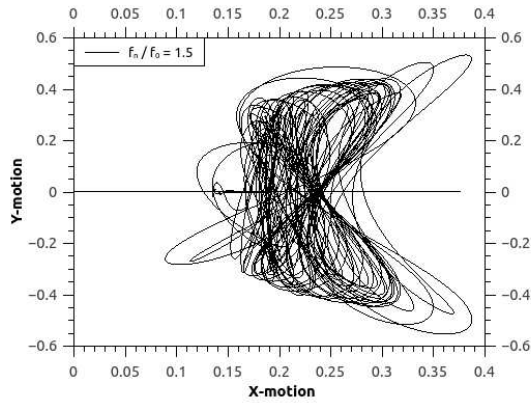
6.3. DISTINCT OSCILLATION CYLINDER GEOMETRIES FOR DIFFERENT MESH DIMENSIONS



(i) XY-motion plot of an elastic cylinder for $\frac{f_n}{f_0} = 1.3$ (j) Displacement and lift coefficient curves of an elastic cylinder for $\frac{f_n}{f_0} = 1.3$.



(k) XY-motion plot of an elastic cylinder for $\frac{f_n}{f_0} = 1.4$ (l) Displacement and lift coefficient curves of an elastic cylinder for $\frac{f_n}{f_0} = 1.4$.



(m) XY-motion plot of an elastic cylinder for $\frac{f_n}{f_0} = 1.5$ (n) Displacement and lift coefficient curves of an elastic cylinder for $\frac{f_n}{f_0} = 1.5$.

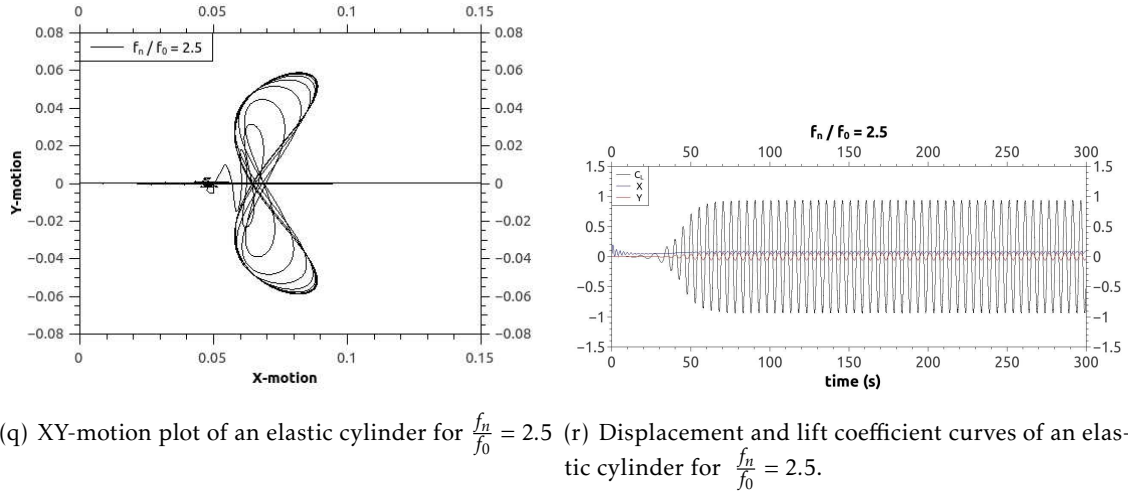
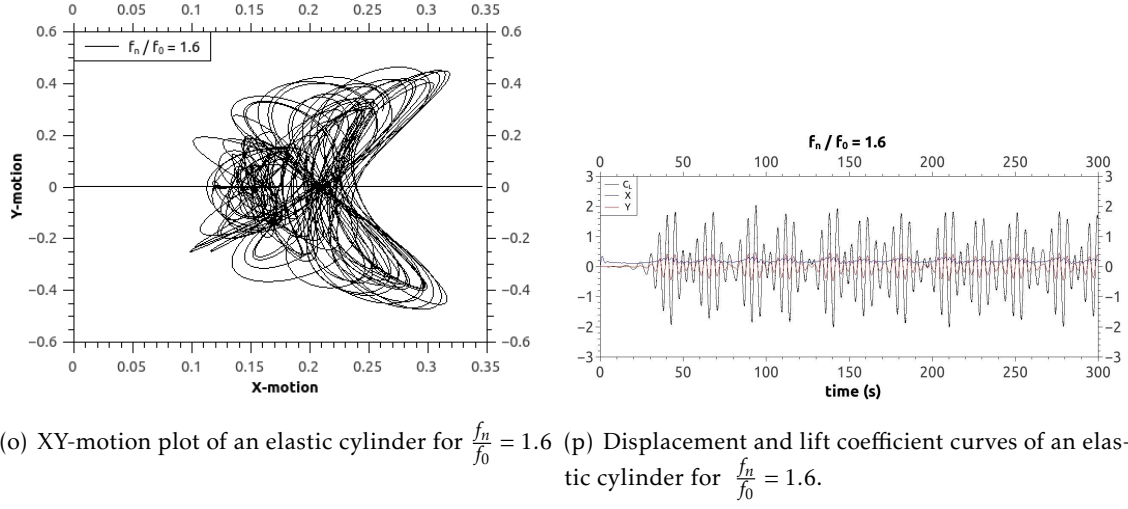


Figure 6.6: XY-motion plot of an elastic cylinder for a set of frequency ratios for the 20D mesh.

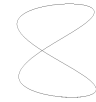
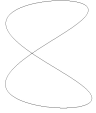







6.3.2 Mesh with 500D

Table 6.9 shows the in-line and the transversal cylinder oscillation amplitude relatively to flow direction and the x maximum initial cylinder displacement for the 500D mesh. In this table is also illustrated the cylinder 8-motion respective to the last cycle for each frequency ratio.

This section presents the responses given by the cylinder to a mesh with size 500D. In the table 6.10 are shown the 500D mesh characteristics. As previously described, the only changed parameter was the domain dimension to 500D and the respective number of elements in the radial direction, N_{rad} . The parameters corresponding to the size of the element along the cylinder wall, the number of elements in the cylinder wall and the progression value of the elements in the radial direction in the direction of the domain external border to the cylinder boundary, are unchanged when compared to the studies

6.3. DISTINCT OSCILLATION CYLINDER GEOMETRIES FOR DIFFERENT MESH DIMENSIONS

Table 6.9: Fundamental quantities and 8-motion last cycle of the 500D mesh.

$\frac{f_n}{f_0}$	$Y_{max,osc}$	$X_{max,osc}$	X_{max}	8-motion
0.5	0.6869	0.1212	2.1212	
0.9	0.7941	0.2181	1.2439	
1.0	0.7853	0.1948	1.0440	
1.1	0.8246	0.4777	0.9308	
1.3	0.7146	0.5299	0.6169	
1.4	0.6411	0.3539	0.4896	
1.5	0.5345	0.1487	0.3817	
1.6	0.4562	0.0824	0.3419	
2.5	0.0501	0.0250	0.1943	

for $8D$ and $20D$ mesh sizes.

Table 6.10: Geometric parameters of the $500D$ mesh.

Mesh	$\frac{e}{D}$	N_{rad}	N_{ang}	N_{cells}	r
Current study	0.0012	162	436	70632	1.06

As observed for the mesh $20D$, the variation of the domain size impacts greatly the obtained cylinder motion. In fact, there are significant differences in the responses given by the cylinder for the mesh with the size of $500D$ when compared to the results obtained for $8D$ and $20D$ meshes. Particularly, for the frequency ratio of $\frac{f_n}{f_0} = 0.5$ the cylinder response sketched in plot 6.7(a) has an eight form. For the previously study meshes with smaller domain size it was observed that the cylinder motion for this specific frequency ratio was almost only in the orthogonal direction to the movement of the flow, varying very little in the orthogonal direction, even after stabilizing.

The amplitude of the movement described by the cylinder for the frequency ratio of $\frac{f_n}{f_0} = 0.5$ varies between -0.7 and 0.7 orthogonally to the motion of the flow. For the meshes $8D$ and $20D$ these range of amplitudes were achieved from the frequency ratio of $\frac{f_n}{f_0} = 0.9$. Nevertheless, the cylinder geometric center of oscillation increased once again the distance between it and the referential origin being positioned roughly at 2.1 to the right of the origin of the referential.

Figure 6.7(c) shows the response of the cylinder for the frequency ratio of $\frac{f_n}{f_0} = 0.9$ with a mesh size of $500D$. Comparing with the cylinder response for the $20D$ mesh, the cylinder oscillation center is located almost at the same distance from the origin of the referential being at approximately $x = 1$. The amplitude in the parallel direction to the flow displacement varies between 0.85 and 1.1 , slightly higher than the one obtained for the $20D$ mesh. Regarding the orthogonal oscillation amplitude, it varies between -0.8 and 0.8 being, hence, slightly higher than the amplitude achieved for the $20D$ mesh.

For the frequency ratio of $\frac{f_n}{f_0} = 1.0$ the obtained cylinder response has several similarities with the results achieved for $8D$ and $20D$ meshes. Specifically, the geometric center of oscillation is situated at $x = 0.8$, the oscillation amplitude orthogonal to the flow ranges between -0.8 and 0.8 . The amplitude of the oscillation parallel to the flow displacement direction varies between 0.68 and 0.9 , being slightly higher and forming a movement with a broader form of an eight than the one observed for smaller domain sizes.

Figure 6.7(g) represents the cylinder response at the frequency rate of $\frac{f_n}{f_0} = 1.1$. The cylinder answer for the $500D$ size mesh is quite different from what was achieved for the $20D$ mesh. The initiation of the oscillatory motion occurs at $x = 0.75$ and the amplitude of the 8-motion parallel to the flow displacement varies between 0.67 and 0.84 . As a full eight movement is performed in each cycle, the geometric center moves closer to the reference origin until a peak of the lift coefficient at time $t = 105s$, fact that is observable in plot 6.7(h). The occurrence of this peak induces a complete change in the intersection

6.3. DISTINCT OSCILLATION CYLINDER GEOMETRIES FOR DIFFERENT MESH DIMENSIONS

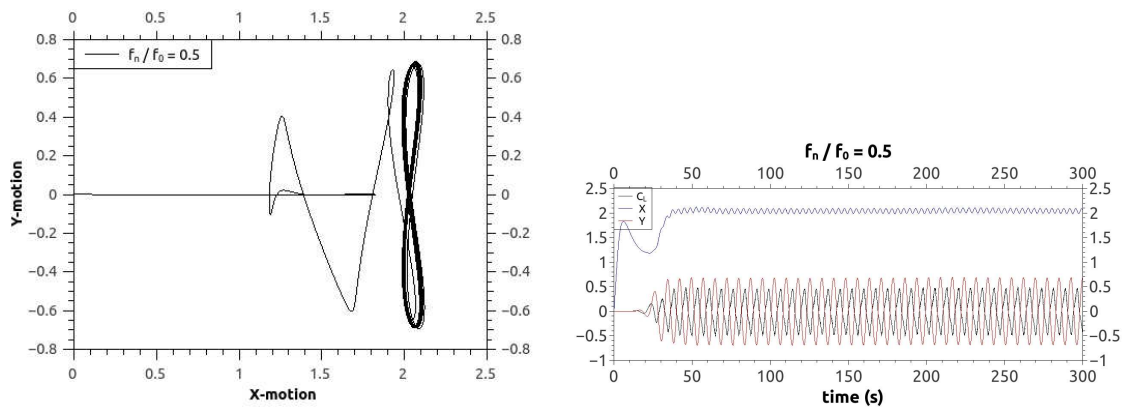
point between the cylinder motion curve and the x axis, shifting suddenly the geometric oscillation point nearest to the referential origin and changing the oscillation amplitude in the parallel direction to the flow motion between 0.37 and 0.8. It is with this oscillatory movement that the cylinder stabilizes for this frequency ratio at $t = 150s$, keeping the amplitude of the lift coefficient constant as well as the amplitude according to the y and x axis in the temporal graph.

Figure 6.7(i) shows the cylinder's response for the frequency ratio of $\frac{f_n}{f_0} = 1.3$. The obtained response is very similar to the one obtained for the 20D mesh. There are two overlapping frequencies and, hence, two types of overlapping movement as well. It is perceptible the cylinder 8-motion which ranges between 0.26 and 0.36 along the x axis and between -0.5 and 0.5 along the y axis, among the agglomerate of plot lines which translate the cylinder motion.

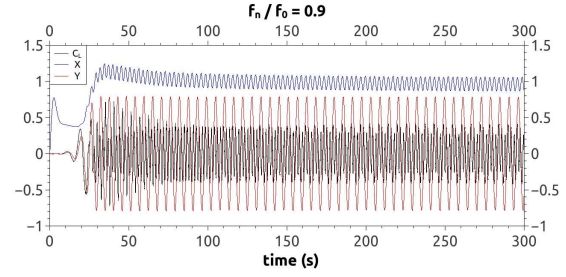
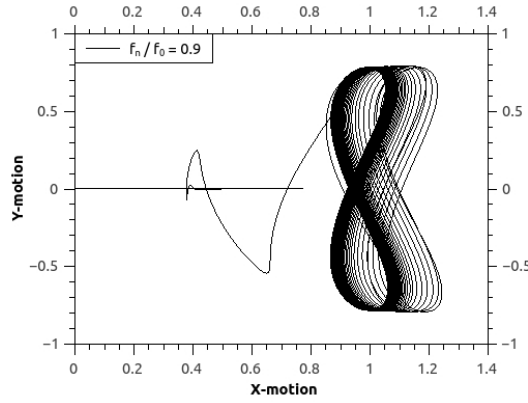
Just as for the previously described frequency ratio, the cylinder motion obtained for the frequency ratio $\frac{f_n}{f_0} = 1.4$ for the current mesh, shown in plot 6.7(k), is very similar to the results achieved for the 20D mesh.

For the frequency ratio of $\frac{f_n}{f_0} = 1.5$ and $\frac{f_n}{f_0} = 1.6$ there is a clear tendency for the cylinder to describe the movement in an eight shape, as can be seen by the dark areas in plots 6.7(m) and 6.7(o), respectively. This fact is visible for the frequency ratio of $\frac{f_n}{f_0} = 1.5$ after the oscillation stabilization at $t = 180s$. As for the frequency ratio $\frac{f_n}{f_0} = 1.6$ there is a clear tendency for the amplitude of the coefficients and motion values to tend towards the same oscillation maximum values.

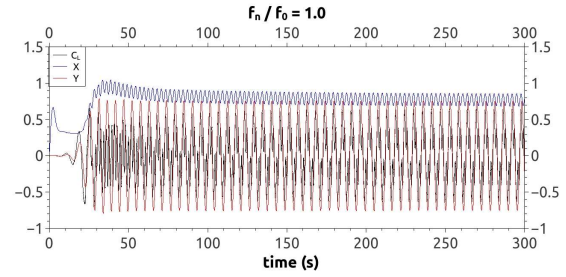
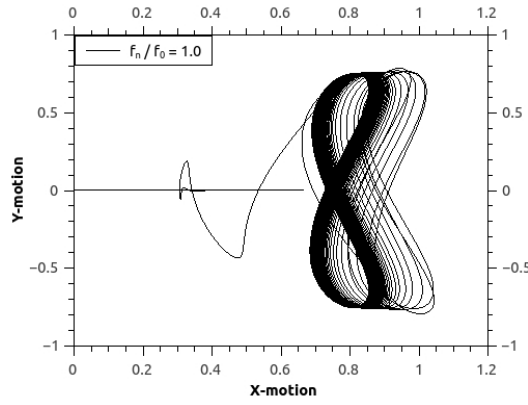
For the frequency ratio of $\frac{f_n}{f_0} = 2.5$, which is illustrated in figure 6.7(q), the amplitudes values according to the orthogonal and to the parallel direction of the flow motion as well as the position of the oscillation geometric center remain very similar to what was obtained for the 20D mesh. Once more, the difference lies in the movement geometry. For 500D it is verified that the upper and lower circular movements are not so inclined to the right side as the 20D ones, representing better the figure of an eight.



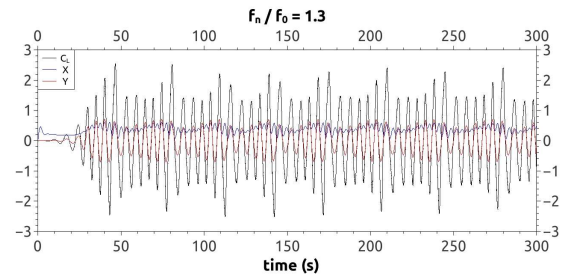
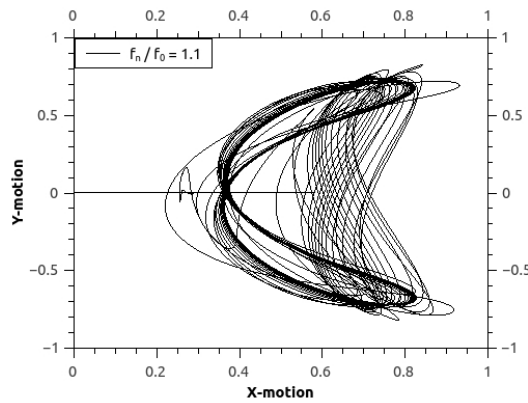
(a) XY-motion plot of an elastic cylinder for $\frac{f_n}{f_0} = 0.5$ (b) Displacement and lift coefficient curves of an elastic cylinder for $\frac{f_n}{f_0} = 0.5$.



(c) XY-motion plot of an elastic cylinder for $\frac{f_n}{f_0} = 0.9$ (d) Displacement and lift coefficient curves of an elastic cylinder for $\frac{f_n}{f_0} = 0.9$.

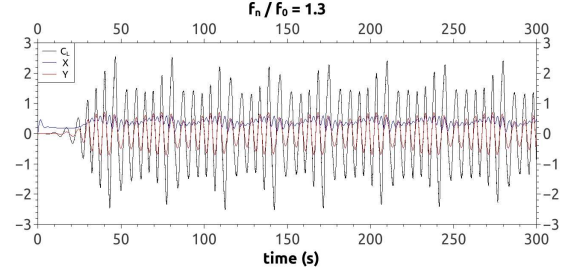
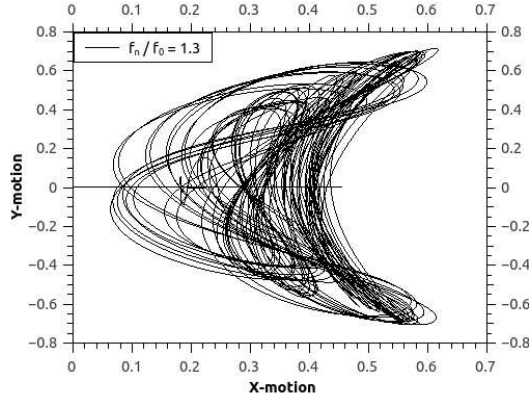


(e) XY-motion plot of an elastic cylinder for $\frac{f_n}{f_0} = 1.0$ (f) Displacement and lift coefficient curves of an elastic cylinder for $\frac{f_n}{f_0} = 1.0$.

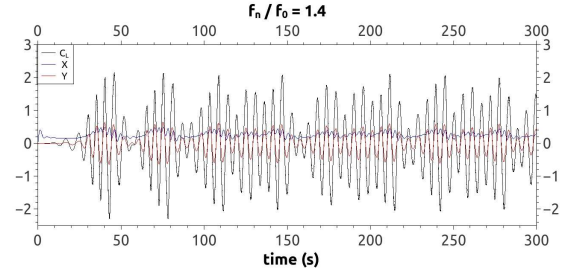
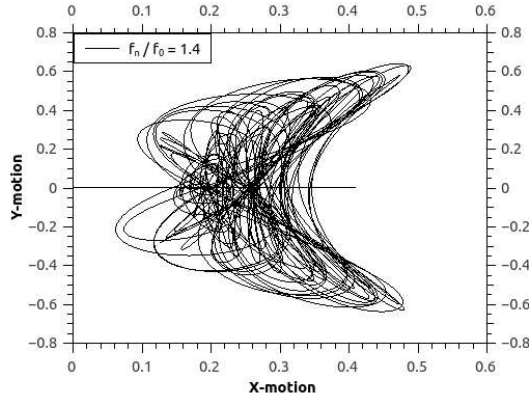


(g) XY-motion plot of an elastic cylinder for $\frac{f_n}{f_0} = 1.1$ (h) Displacement and lift coefficient curves of an elastic cylinder for $\frac{f_n}{f_0} = 1.1$.

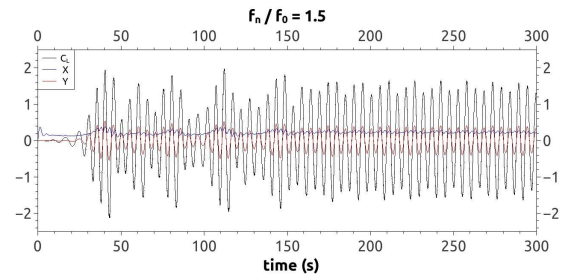
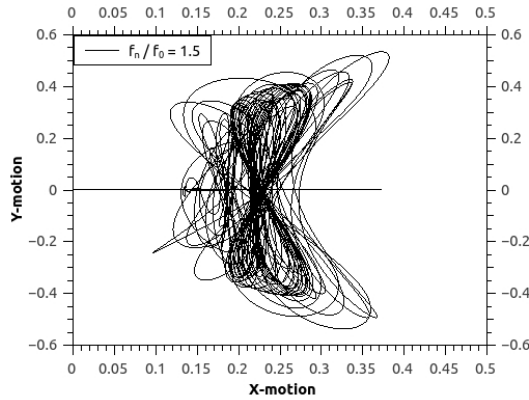
6.3. DISTINCT OSCILLATION CYLINDER GEOMETRIES FOR DIFFERENT MESH DIMENSIONS



(i) XY-motion plot of an elastic cylinder for $\frac{f_n}{f_0} = 1.3$ (j) Displacement and lift coefficient curves of an elastic cylinder for $\frac{f_n}{f_0} = 1.3$.



(k) XY-motion plot of an elastic cylinder for $\frac{f_n}{f_0} = 1.4$ (l) Displacement and lift coefficient curves of an elastic cylinder for $\frac{f_n}{f_0} = 1.4$.



(m) XY-motion plot of an elastic cylinder for $\frac{f_n}{f_0} = 1.5$ (n) Displacement and lift coefficient curves of an elastic cylinder for $\frac{f_n}{f_0} = 1.5$.

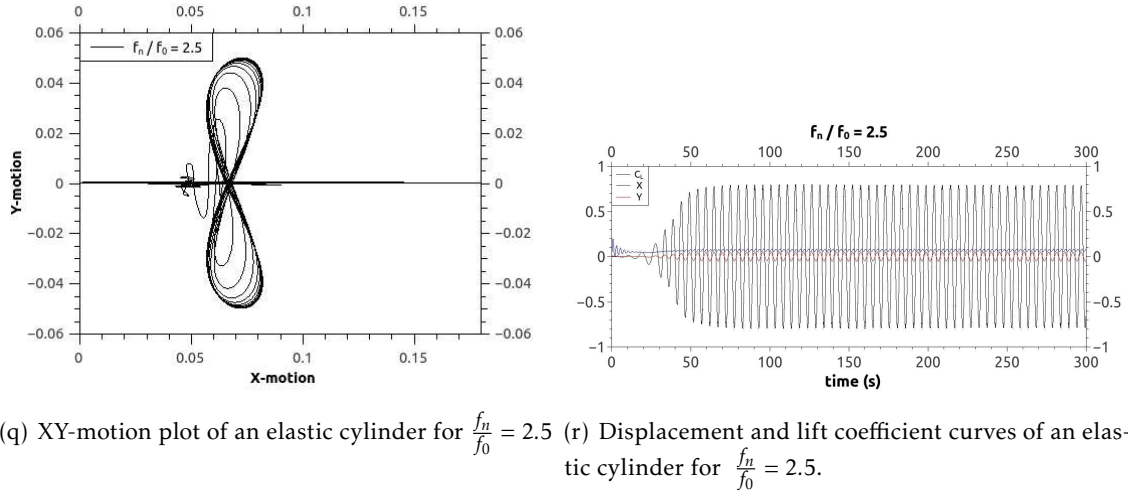
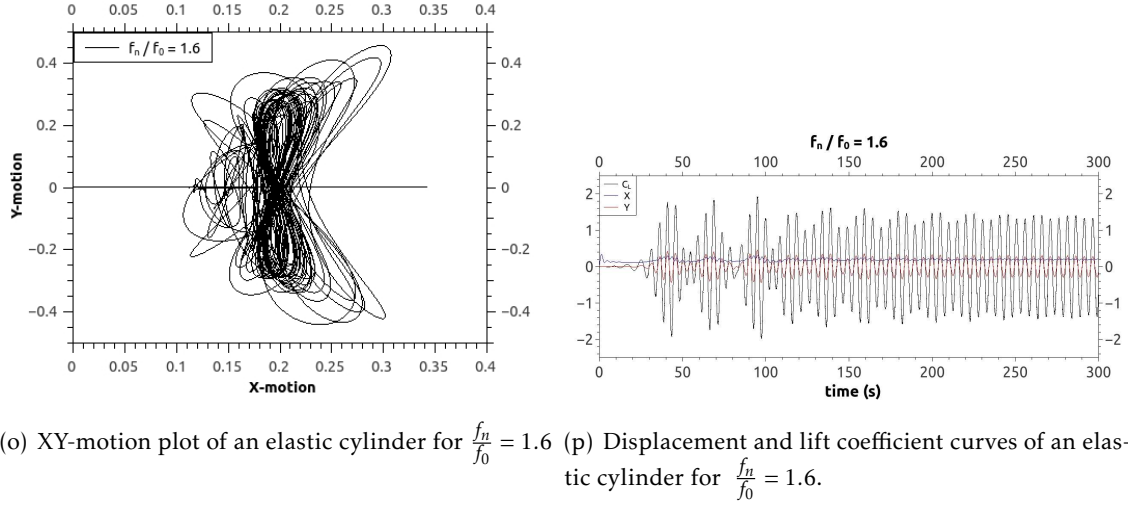


Figure 6.7: XY-motion plot of an elastic cylinder for a set of frequency ratios for the 500D mesh.



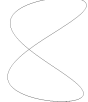






6.3.3 Mesh with 2500D

Table 6.11 shows the in-line and the transversal cylinder oscillation amplitude relatively to flow direction and the x maximum initial cylinder displacement for the 2500D mesh. In this table is also illustrated the cylinder 8-motion respective to the last cycle for each frequency ratio.

The current section presents the cylinder response using a 2500D mesh, which was previously used to study the fixed and the one DOF cylinder. The obtained results will be compared with the data achieved for the 8D, 20D and 500D meshes. Table 6.12 presents the 2500D mesh characteristics. This mesh corresponds to the mesh chosen to perform the analysis described in section 4.1 and in section 5.1. Furthermore, the mesh parameters which define the length of the element along the wall of the cylinder, the number of elements in the wall of the cylinder and the elements progression in the radial

6.3. DISTINCT OSCILLATION CYLINDER GEOMETRIES FOR DIFFERENT MESH DIMENSIONS

Table 6.11: Fundamental quantities and 8-motion last cycle of the 2500D mesh.

$\frac{f_n}{f_0}$	$Y_{max,osc}$	$X_{max,osc}$	X_{max}	8motion
0.5	0.7145	0.1283	2.2459	
0.9	0.8013	0.2162	1.2389	
1.0	0.7914	0.1997	1.0520	
1.1	0.8235	0.6888	0.9167	
1.3	0.7182	0.5260	0.6074	
1.4	0.6408	0.4180	0.4896	
1.5	0.5319	0.1132	0.3915	
1.6	0.4743	0.2282	0.3588	
2.5	0.0487	0.0251	0.2046	

direction towards the outside to the cylinder wall are equal to the defined for the prior $8D$, $20D$ and $500D$ meshes. Hence, the number of elements in the radial direction is for the 2500 mesh is 440 .

Table 6.12: Geometric parameters of the mesh $2500D$.

Mesh	$\frac{e}{D}$	N_{rad}	N_{ang}	N_{cells}	r
Current study	0.0012	189	436	82404	1.06

The meshes with the domain size of $500D$ and $2500D$ show the most similar results in the comparative study performed in the present section, with the cylinder response ranging very little between both these domain sizes.

The answer given by the cylinder for the frequency ratio of $\frac{f_n}{f_0} = 0.5$ for the $2500D$ mesh is nearly equal to the answer given by the cylinder for the same value of frequency ratio for the $500D$ mesh. The motion geometry is very similar and as well as the amplitudes variation in the orthogonal direction to the flow motion. It is only observable the slight change of the oscillation geometric center to the right, stabilizing at $x = 2.2$.

For the frequency ratios of $\frac{f_n}{f_0} = 0.9$ and $\frac{f_n}{f_0} = 1.0$ differences between the $500D$ and $2500D$ meshes are even smaller. Having the same oscillation motion geometry, the same value oscillation geometric center and the same amplitudes.

Concerning the $\frac{f_n}{f_0} = 1.1$ frequency ratio, the movement geometry of the cylinder response for the $2500D$ mesh is shown in plot 6.8(g) which, as referred for the previous frequency ratios, is very similar to the plot 6.7(g) obtained for the $500D$ mesh, keeping the same amplitude range. The main difference occurs at the lift coefficient maximum peak, which only occurs for the $2500D$ mesh for the time $t = 165s$. This means that the first 8-motion is extended for the current case. This fact is visible by comparing the plots for both $2500D$ and $500D$ meshes by which it is also possible to conclude that motion before the lift coefficient maximum peak is enhanced due to increase of the cylinder passing through that zone.

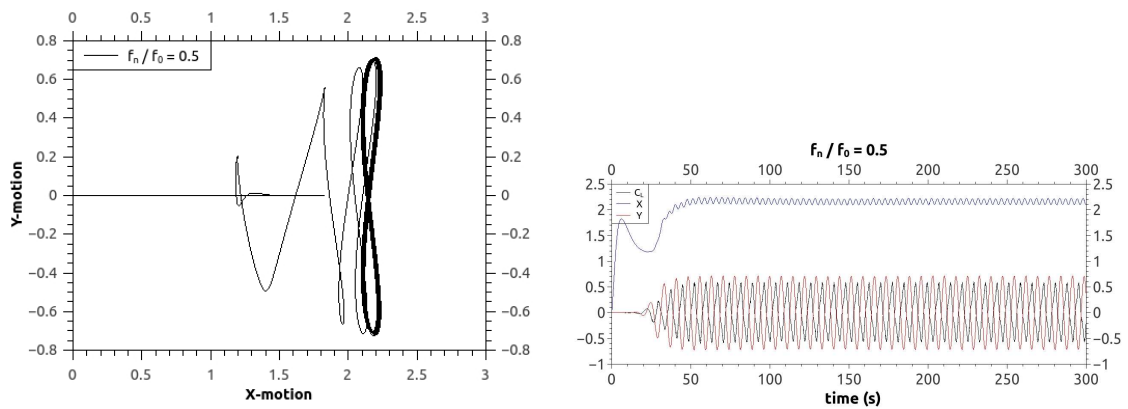
Figure 6.8(i) and 6.7(i) show the cylinder displacement for the frequency ratio $\frac{f_n}{f_0} = 1.3$ for the $2500D$ and $500D$ meshes, respectively. By the analysis of both figures it is possible to ascertain that the cylinder movement is very similar between both meshes. The same applies for the frequency ratio of $\frac{f_n}{f_0} = 1.4$, for which, as shown in figures 6.8(k) and 6.7(k), the cylinder response is also very similar between the $2500D$ and $500D$ meshes.

Regarding the frequency ratio of $\frac{f_n}{f_0} = 1.5$, by analysing plots 6.8(m) and 6.8(n) with comparing with the respective plots for the $500D$ mesh it is observable that the oscillatory motion stabilization occurs earlier for the $500D$ mesh than for the $2500D$ mesh. Consequently, it is possible to identify the cylinder movement path darkened in figure 6.8(n). The stabilization of the vortex shedding phenomenon and its parameters, such as the lift coefficient shown in figure 6.8(n) which influences the oscillatory motion of the cylinder, takes place from the time $t = 85s$.

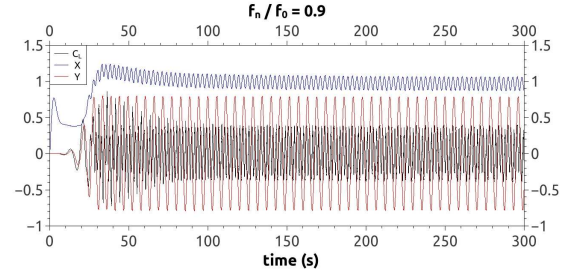
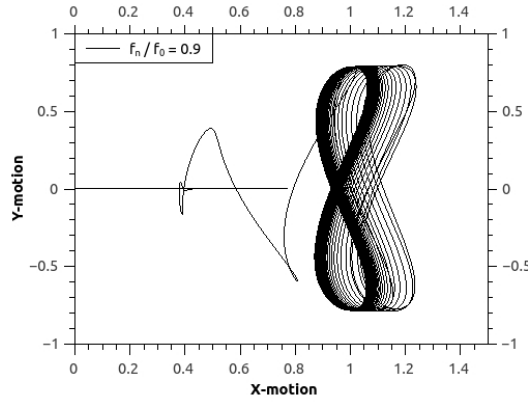
6.3. DISTINCT OSCILLATION CYLINDER GEOMETRIES FOR DIFFERENT MESH DIMENSIONS

The difference between the cylinder oscillatory motion for the frequency ratio of $\frac{f_n}{f_0} = 1.6$ between the 500D and the 2500D meshes lies in the parameters stabilization, namely, the stabilization of the lift coefficient and of the cylinder oscillation amplitudes in the x and y directions shown in fig 6.8(r) and 6.7(p). For the 500D mesh, the parameters stabilization tends towards a given range of oscillation in which each oscillation cycle of the cylinder always achieves the same value. Contrasting, for the 2500D mesh it is noticeable the tendency to keep the two overlapping frequencies present in the oscillation cycles, repeating the values cycle after cycle without having any tendency to soften the parameter values, such as the lift coefficient. This fact justifies why for the 500D mesh it is observable an oscillatory movement which describes a better eight shape, which is visible through the most darkened area due to the cylinder repeated passes through these areas. Whereas for the 2500D mesh the path of the cylinder undergoes various distinct movements and with different amplitudes forming the image shown in figure 6.8(q) agglomerated with various distinguished paths from each other.

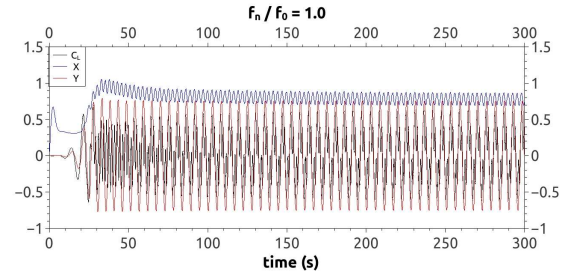
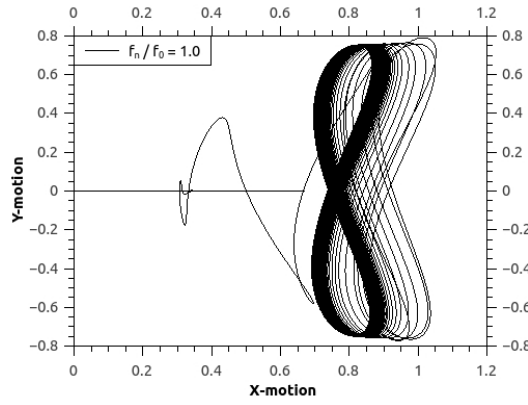
For the frequency ratio of $\frac{f_n}{f_0} = 2.5$ the response of the cylinder for the 2500D mesh is very similar when compared to the 500D mesh, with the same oscillatory motion geometry, the same amplitude and the same position of the oscillatory geometric center.



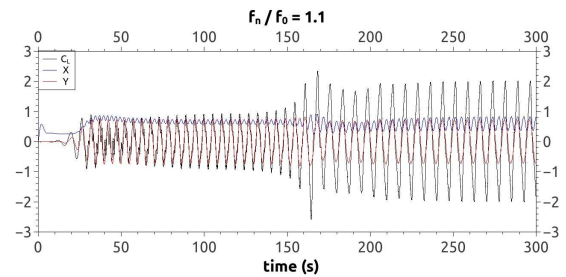
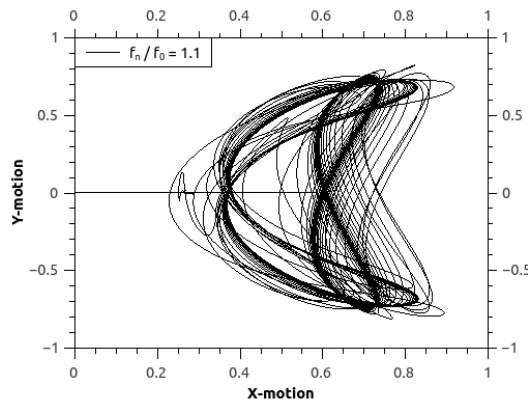
(a) XY-motion plot of an elastic cylinder for $\frac{f_n}{f_0} = 0.5$ (b) Displacement and lift coefficient curves of an elastic cylinder for $\frac{f_n}{f_0} = 0.5$.



(c) XY-motion plot of an elastic cylinder for $\frac{f_n}{f_0} = 0.9$ (d) Displacement and lift coefficient curves of an elastic cylinder for $\frac{f_n}{f_0} = 0.9$.

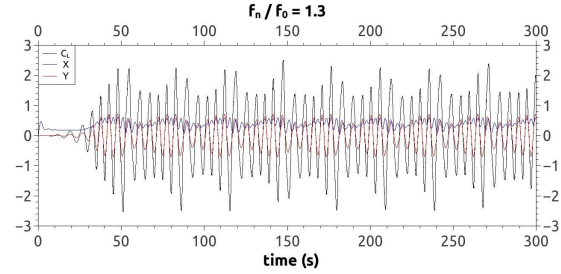
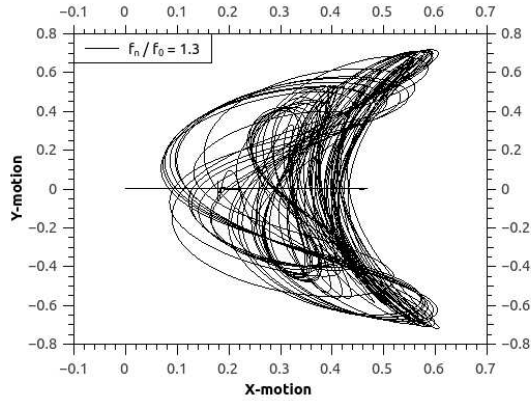


(e) XY-motion plot of an elastic cylinder for $\frac{f_n}{f_0} = 1.0$ (f) Displacement and lift coefficient curves of an elastic cylinder for $\frac{f_n}{f_0} = 1.0$.

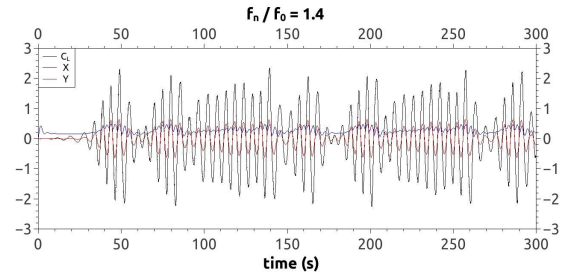
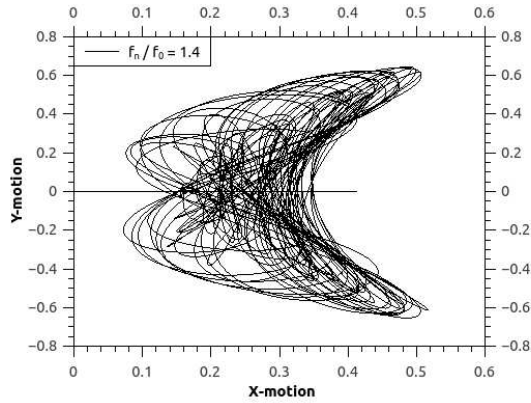


(g) XY-motion plot of an elastic cylinder for $\frac{f_n}{f_0} = 1.1$ (h) Displacement and lift coefficient curves of an elastic cylinder for $\frac{f_n}{f_0} = 1.1$.

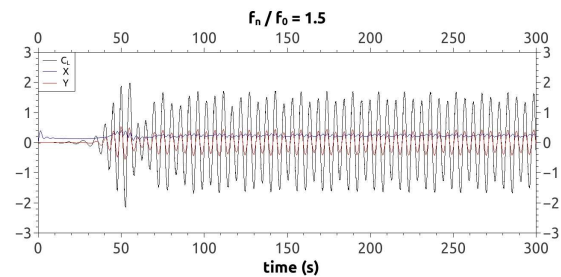
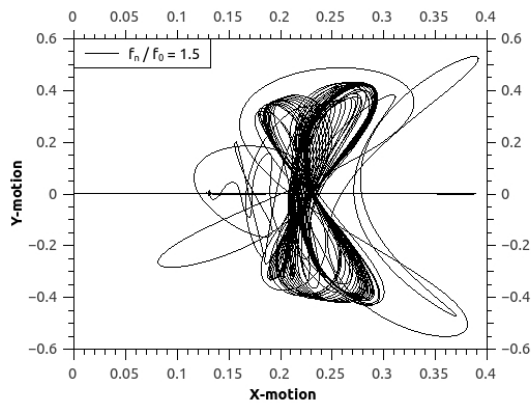
6.3. DISTINCT OSCILLATION CYLINDER GEOMETRIES FOR DIFFERENT MESH DIMENSIONS



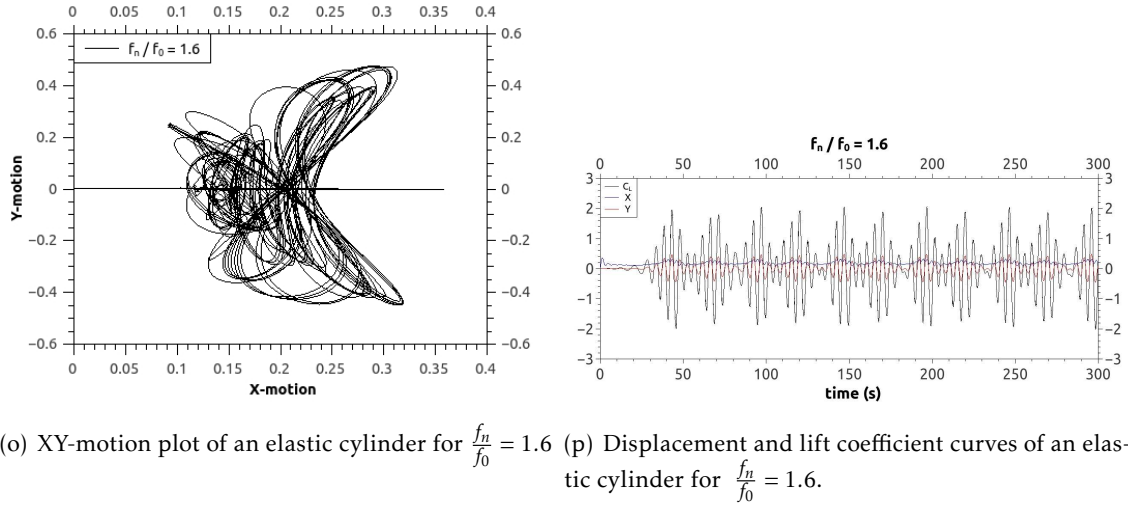
(i) XY-motion plot of an elastic cylinder for $\frac{f_n}{f_0} = 1.3$ (j) Displacement and lift coefficient curves of an elastic cylinder for $\frac{f_n}{f_0} = 1.3$.



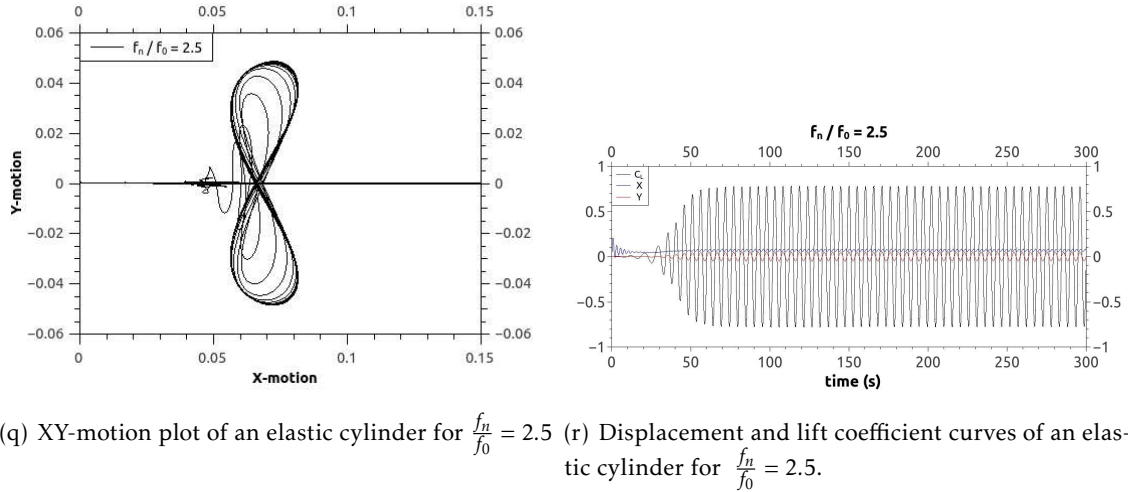
(k) XY-motion plot of an elastic cylinder for $\frac{f_n}{f_0} = 1.4$ (l) Displacement and lift coefficient curves of an elastic cylinder for $\frac{f_n}{f_0} = 1.4$.



(m) XY-motion plot of an elastic cylinder for $\frac{f_n}{f_0} = 1.5$ (n) Displacement and lift coefficient curves of an elastic cylinder for $\frac{f_n}{f_0} = 1.5$.



(o) XY-motion plot of an elastic cylinder for $\frac{f_n}{f_0} = 1.6$ (p) Displacement and lift coefficient curves of an elastic cylinder for $\frac{f_n}{f_0} = 1.6$.



(q) XY-motion plot of an elastic cylinder for $\frac{f_n}{f_0} = 2.5$ (r) Displacement and lift coefficient curves of an elastic cylinder for $\frac{f_n}{f_0} = 2.5$.

Figure 6.8: XY-motion plot of an elastic cylinder for a set of frequency ratios for the 2500D mesh.

6.3.4 Comparison of the cylinder displacement amplitude between the 8D, 20D, 500D and 2500D meshes

Figure 6.9 illustrates the cylinder transverse displacements for different mesh sizes for the elastic cylinder with two DOF for each frequency ratio studied in the current study. With the decrease of the frequency ratio the reduced velocity increases, given that these dimensions are inversely proportional. Similarly to what was referred in chapter 5, for low reduced velocity values the values of the transverse amplitude are very similar for the different mesh sizes. With the increase of the reduced velocity these values tend to be farther from each other, observing a clear approximation of the values between the 8D and the 20D meshes where the lock-in effect greatly influences the the cylinder response. Divergently, for the 500D and 2500D mesh the impact of the lock-in effect is negligible. From the frequency ratio of $\frac{f_n}{f_0} = 1.3$ until $\frac{f_n}{f_0} = 0.5$ it is evident the influence of the mesh

6.3. DISTINCT OSCILLATION CYLINDER GEOMETRIES FOR DIFFERENT MESH DIMENSIONS

size in the transverse amplitude obtained for an elastic cylinder with two DOF. Finally, it is possible to conclude that the cylinder displacement increases with the expansion of the mesh domain size for the sizes studied in this thesis.

Figure 6.10 shows the cylinder displacement along the x axis after the stabilization of the oscillatory motion. In this plot it is observed an order in the values with the several values of the studied mesh sizes. In fact, there is a consistent relation between the values order and the order of the mesh size. However, no trend is evident regarding the increasing of the reduced velocity or decreasing of the the frequency ratio as noted above.

In plot 6.11 are sketched the initial cylinder displacement along the x axis until the cylinder motion stabilizes and start to oscillate with a given frequency. For low reduced velocity, that is, for greater values of frequency ratio it is not visible the displacements achieved between the several mesh sizes. It is just from the frequency ratios of $\frac{f_n}{f_0} = 1.3$ until $\frac{f_n}{f_0} = 0.5$ that the employment of meshes with different sizes impacts the obtained results. Thereby, it is possible to conclude that the cylinder displacement increases which the increase of the mesh domain size used for the four mesh sizes studies in this thesis.

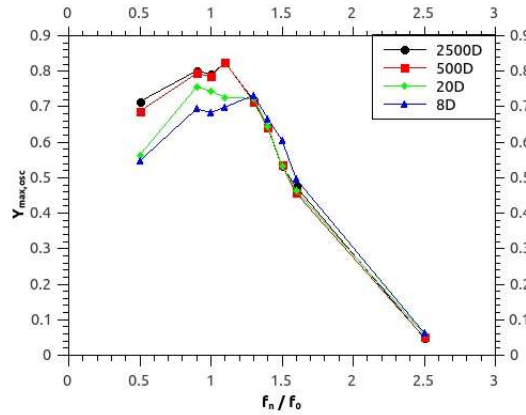


Figure 6.9: Y maximum cylinder displacement after the cylinder displacement stabilization for the 8D, 20D, 500D and 2500D meshes .

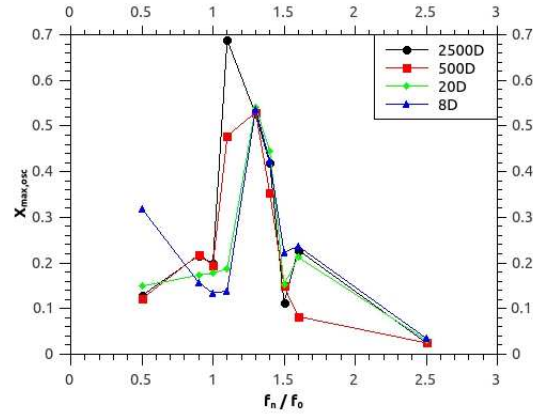


Figure 6.10: X maximum cylinder displacement after the cylinder displacement stabilization for the 8D, 20D, 500D and 2500D meshes .

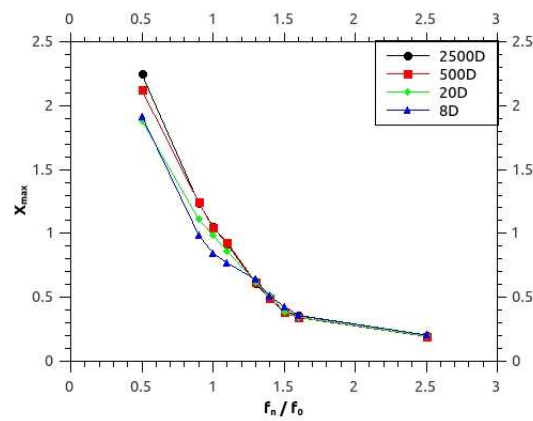


Figure 6.11: X maximum cylinder initial displacement between the 8D, 20D, 500D and 2500D meshes.

CONCLUSIONS

The main goal of this thesis is the validation of the OpenFOAM numerical code to solve the problem of a flow around a two DOF cylinder. The OpenFOAM software as an high potential in the CFD context, given that it is a free usable tool which provides its user the power and versatility to adapt and/or build his own case of study. In order to achieve this goal, and given that there are a scarce number of numerical studies about the flow around cylinders with two DOF, it were defined a set of steps to validate the used methodology and, hence, only afterwards perform the study for a flow around an elastic cylinder with two DOF, analysis described in chapter 6.

With the previous considerations in mind, this thesis begins by studying a flow around a fixed cylinder, which is presented in the chapter 4. In this chapter it was performed a mesh independence study, which examined the dependence of the simulation fundamental quantities, namely, number of Strouhal St , drag coefficient average $C_{D,mean}$, fluctuation of the drag coefficient $C_{D,rms}$ and fluctuation of the lift coefficient $C_{L,rms}$. It is based on these fundamental quantities that the study of a flow around a cylindrical section is done, since these values demonstrated good conditions for the captation of the phenomenon evolution. It was analysed how the fundamental quantities are influenced by the variation of the mesh refinement, study that is presented in section 4.1.1. The meshes analysed in this context had fundamental quantities values that are pretty reasonable allowing to conclude that this study started with a level of refinement which already has associated a good approximation of the reality. However, it is possible to observe a small improvement of the results as the level of refinement increases. Yet, once the chosen domain has a $2500D$ size in order to reduce the blockage effect, the mesh has a very large area and, for this reason, it was decided to proceed the study with the mesh which output valid results but required less computational power. To conclude the study for the fixed cylinder, in order to validate that the $2500D$ mesh did not impact negatively the achieved

results, it was analysed the influence of the simulation time-step in the obtained results. Subsequently, in section 4.1.3 it was performed a convergence analysis of the obtained results with the variation of the domain size. This analysis compares the results obtained for a $8D$, $20D$, $500D$ and $2500D$ and allows to conclude that the fundamental quantities tend to decrease with the increase of the domain size. With the intention of validate the comparative study with T. Li and Zhu (2009) for a two DOF cylinder described in chapter 6, it were evaluated in section 4.1.4 three different levels of mesh refinement for the mesh with size $8D$, which has the same size as the one used by T. Li and Zhu (2009). It is concluded, as expected, that the $8D$ mesh is fitted to study the interactions of a flow in a fixed cylinder. Moreover, the results for the comparative analysis made in section 4.2 shows a good coherence with the similar studies describe in the literature.

Chapter 5 describes the study which analyses a flow around a cylinder with one DOF orthogonal to the direction of the flow motion. The results obtained from this study were, then, compared with the ones described by Conde and Lopes (2015). It was studied the cylinder response for two distinct types of system: mass-spring and spring-mass-damper system, subject that was also studied by Conde and Lopes (2015). Congruently to what was concluded by Conde and Lopes (2015), both simulations demonstrate similar results with a consistency in the responses given by the cylinder. Nevertheless, the study performed in this thesis uses a $2500D$ mesh, which properties are describe in chapter 4, whereas Conde and Lopes (2015) used a $50D$ mesh, which has a great bias due to the proximity of the cylinder to the domain boundary which, consequently, induces the development of the simulation blockage effect. The occurrence of this phenomena for a $50D$ mesh is the main reason of the differences found between the study developed in this thesis and the results demonstrated by Conde and Lopes (2015). At an early stage, until roughly the reduced velocity of $U^* = 4$, the cylinder maximum oscillation, drag coefficient average and lift coefficient assume lower values for the current study than the ones achieved by Conde and Lopes (2015). This fact allows to conclude that that until $U^* = 4$ the increase of the cylinder oscillation amplitude is related with the size of the used mesh domain. This can be related with the fact that with the increment of the domain size the presence of the cylinder has lower impact in the fluid flow since the fluid is less "confinement". With this in mind, to greater meshes correspond lower flow velocities near the cylinder and, hence, a higher pressure field. This way, from the reduced velocity of $U^* = 4.5$ until $U^* = 6.5$ the cylinder oscillation amplitude continues to rise, until it reaches its maximum peak for $U^* = 6.5$, as it can be observed by figure 5.6(b). Furthermore, in figure 5.6(b) it is also possible to conclude that from the reduced velocity of $U^* = 4.5$ to $U^* = 7.5$ a particular behaviour in the cylinder oscillation which the $50D$ domain used by Conde and Lopes (2015) was not able to capture. From the reduced value of $U^* = 8$ it is visible for the study performed in this thesis with a $2500D$ domain the same behaviour observed from the reduced value of $U^* = 4$ for the analysis made by Conde and Lopes (2015).

In chapter 6 it was studied a flow around the cylinder with two DOF. This study was

based on the study developed by T. Li and Zhu (2009). This study uses a $8D$ mesh and, therefore, to allow the comparison between the results described by T. Li and Zhu (2009) and the ones obtained in the current thesis, the study for the two DOF proceeded with a mesh which size was $8D$ in an orthogonal direction to the fluid flow motion. The analysis developed by T. Li and Zhu (2009) focused on the frequency ratios of $\frac{f_n}{f_0} = 0.5$, $\frac{f_n}{f_0} = 0.9$, $\frac{f_n}{f_0} = 1.0$, $\frac{f_n}{f_0} = 1.1$, $\frac{f_n}{f_0} = 1.3$, $\frac{f_n}{f_0} = 1.4$, $\frac{f_n}{f_0} = 1.5$, $\frac{f_n}{f_0} = 1.6$ and $\frac{f_n}{f_0} = 2.5$. For each of these frequency values it were determined the parameters which characterize the simulation, such as the natural frequency, the reduced speed and the spring elasticity constant. By using the vortex shedding value in the frequency ratio equation it was extracted the parameters values used by T. Li and Zhu (2009). The results outputted from this analysis show a good agreement with the data described by T. Li and Zhu (2009), with similar amplitude ranges for each frequencies ratio and with similar oscillatory motion geometry. The major difference between both studies is the symmetry of the cylinder described motion, which shows a good symmetry in the current thesis contrasting with the asymmetric motion obtained by T. Li and Zhu (2009). This asymmetry referring to the responses given by the cylinder, was demonstrated in section 6.1.1 where the same asymmetry that T. Li and Zhu (2009) describes is achieved. This analysis sustains the conclusion that one possible cause of the motion asymmetry is related to the asymmetry of the mesh itself causing the asymmetry of the flow and its asymmetry in the cylinder response. Therefore, it highlights how important it is to ensure the symmetry of the mesh when simulating a symmetrical flow. To this end, it were presented some possibilities to ensure the symmetry of the mesh, especially the use of tools able to mirror the respective positions of all mesh elements according to a given symmetry axis. Subsequently, it was analysed how the refinement level of the $8D$ mesh impacts the obtained cylinder oscillatory motion. For that, it were developed three meshes with distinct refinement levels. From the evaluation of the results achieved with these three different meshes it is possible to identify some difference between them. Nevertheless, this study does not invalidate the mesh with the finer refinement which was used to perform the comparison study with the result described by T. Li and Zhu (2009). In fact, the mesh used by T. Li and Zhu (2009) has a lower refinement level than the one used in this thesis and, given that one of the goals was to mimic the results obtained by T. Li and Zhu (2009) it makes more sense to perform the analysis with the mesh with lower refinement level.

Lastly, it was evaluated the impact of the mesh size in the development of the blockage effect for a cylinder interacting with a flow with two DOF. For that it were used meshes with four different sizes: $8D$, $20D$, $500D$ and $2500D$. The results obtained for each one of the meshes were then compared. Similarly, to what was concluded for a cylinder with one DOF, the increase of the domain size has associated the increase of the cylinder oscillation amplitude. For low reduced velocity values, it is verified the approach between the values of the oscillation amplitude orthogonal to the flow displacement. However, as the reduced velocity values increase, i.e. as the frequency ratio lowers, the difference between

the amplitude of the cylinder oscillation motion regarding the orthogonal direction of the fluid displacement become increasingly pronounced. Nonetheless, this effect is only visible for the amplitudes regarding the direction orthogonal to the flow displacement, for the oscillation amplitudes towards to the parallel direction of the flow it is not perceptible any tendency.

7.1 Future Work

As a continuation of this study it would be interesting to analyse the cylinder problem with three DOF. This third degree of freedom should allow the cylinder rotation through the z axis and the respective momentum applied to the cylinder by the vortex shedding phenomena. Additionally, it would be interesting to evaluate how this third DOF would influence the answer given by the cylinder induced by the interaction with the flow displacement. This study is similar to the one performed to evaluate the cylinder displacement along the y axis for one and two DOF. Furthermore, this study will be a pioneer since there is no information in the literature about a similar study with three DOF until this date.

It would also be interesting to study for two DOF the answer given by the cylinder for the same values of reduced velocities studied for the cylinder with one DOF, in order to perform a comparative study between the responses given by the cylinder for both types of problem configuration.

As additional work, it would also be interesting to elongate the simulation time for the cylinder with two DOF, mainly for the cases in which it was detected the frequencies overlap. This would allow, for instance, to verify if eventually these cases stabilize somewhere in time, if the cylinder motion stabilizes so it describes an 8-motion or if the cases where several frequencies are superimposed the corresponding reduced velocities at which the movement described is maintained as it was shown in this thesis.

Lastly, in the same context, it would also be interesting to add the cylinder responses for the frequency ratios between 1.6 and 2.5, performing, this way, the connection between these two responses with the various responses that were already analysed in this thesis.

BIBLIOGRAPHY

- Inc ANSYS. Ansys-fluent. URL <http://www.ansys.com/Products/Fluids/ANSYS-Fluent>. Accessed: 2016-10-09.
- Autodesk. Autodesk cfd. URL <http://www.autodesk.com/products/cfd/overview>. Accessed: 2016-10-09.
- P. W. Bearman. Vortex shedding from oscillating bluff bodies. *Annual Review of Fluid Mechanics*, 16(1):195–222, 1984. doi: 10.1146/annurev.fl.16.010184.001211.
- K. Yusuf Billah and Robert H. Scanlan. Resonance, tacoma narrows bridge failure, and undergraduate physics textbooks. *American Journal of Physics*, 59(2):118–124, 1991. doi: <http://dx.doi.org/10.1119/1.16590>.
- R. D. Blevins. Flow-Induced Vibration. *Van Nostrand Reinhold Company Regional Offices, New York.*, 1977.
- R. M. C. So C. Y. Zhou and K. Lam. Vortex-induced vibrations of an elastic circular cylinder. *Journal of Fluids and Structures*, 13:165–189, 1999.
- C. Camichel and L. Escande. *Similitude hydrodynamique et technique des modèles réduits*. Ministere de l’air. Publications scientifiques et techniques. Blondel La Rougery, 1938.
- C. Camichel, P. Dupin, and M. Teissié-Solier. Sur l’application de la loi de similitude aux périodes de formation des tourbillons alternés de Bénard-Karman. *Acad. Sci. Comptes Rendus*, 185:1556–1559, 1927.
- OPEN CASCADE. Salome platform documentation. URL <http://docs.salome-platform.org>. Accessed: 2016-10-09.
- cd adapco. Star-ccm+. URL <http://mdx.plm.automation.siemens.com/star-ccm-plus>. Accessed: 2016-10-09.
- J. M. P. Conde and R. M. V. Lopes. Numerical study of the vortex-induced vibrations of an elastic circular cylinder with 1 degree of freedom using OpenFOAM. In *23rd ABCM International Congress of Mechanical Engineering*, 2015.
- M. Coutanceau and R. Bouard. Experimental determination of the main features of the viscous flow in the wake of a circular cylinder in uniform translation. Part 1. Steady flow. *Journal of Fluid Mechanics*, 79:231–256, 1977.

- E. Didier. Convergência assintótica das quantidades fundamentais na modelação numérica do escoamento em torno de um cilindro circular. *Revista Iberoamericana de Ingeniería Mecánica*, 16(1):87–99, 2012.
- enGits GmbH. engrid - open-source mesh generation. URL <http://engits.eu/en/engrid>. Accessed: 2016-10-09.
- J.H. Ferziger and M. Peric. *Computational Methods for Fluid Dynamics*. Springer Berlin Heidelberg, 2001. ISBN 9783540420743.
- Peter Freymuth. The vortex patterns of dynamic separation: A parametric and comparative study. *Progress in Aerospace Sciences*, 22(3):161 – 208, 1985. ISSN 0376-0421. doi: [http://dx.doi.org/10.1016/0376-0421\(85\)90005-3](http://dx.doi.org/10.1016/0376-0421(85)90005-3).
- J. H. Gerrard. The three-dimensional structure of the wake of a circular cylinder. *Journal of Fluid Mechanics*, 25(01):143, 1966. ISSN 0022-1120. doi: 10.1017/S0022112066000090.
- J. H. Gerrard. The wakes of cylindrical bluff bodies at low Reynolds number. *The Royal Society Publishing*, 288:351–382, 1978.
- Christophe Geuzaine and Jean-François Remacle. Gmsh: A 3-d finite element mesh generator with built-in pre- and post-processing facilities. *International Journal for Numerical Methods in Engineering*, 79(11):1309–1331, 2009. ISSN 1097-0207. doi: 10.1002/nme.2579.
- R. Govardhan and C. H. K. Williamson. Resonance forever: existence of a critical mass and an infinite regime of resonance in vortex-induced vibration. *Journal of Fluid Mechanics*, 473:147–166, 12 2002. doi: 10.1017/S0022112002002318.
- User Guide. Open V FOAM. (December), 2011.
- F. Homann. The effect of high viscosity on the flow around a circular cylinder and around a sphere. *National Advisory Committee For Aeronautics*, pages 1–31, 1936.
- N. Jauvtis and C. H K Williamson. Vortex-induced vibration of a cylinder with two degrees of freedom. *Journal of Fluids and Structures*, 17(7):1035–1042, 2003. ISSN 08899746. doi: 10.1016/S0889-9746(03)00051-3.
- A Khalak and C H K Williamson. Motions, forces and mode transitions in vortex-induced vibrations at low mass-damping. *Journal of Fluids and Structures*, 13(7-8):813–851, 1999.
- a. Khalak and Chk Williamson. Dynamics of a hydroelastic cylinder with very low mass and damping. *Journal of Fluids and Structures*, 10(5):455–472, 1996. ISSN 08899746. doi: 10.1006/jfls.1996.0031.

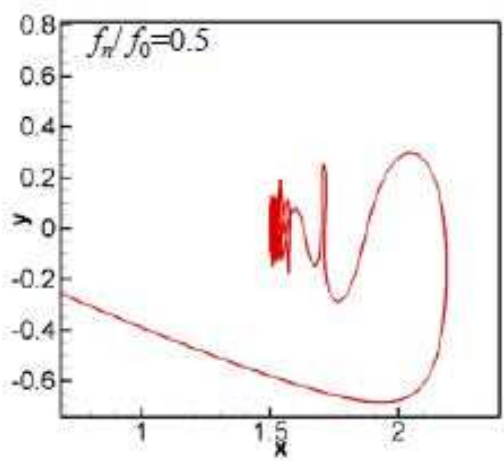
- L. S. G. Kovasznay. Hot-wire investigations of the wake behind cylinders at low Reynolds number. *Proceedings Royal Society*, 109:1–24, 1949.
- C. Mayes, H. Schlichting, E. Krause, H.J. Oertel, and K. Gersten. *Boundary-Layer Theory*. Physic and astronomy. Springer Berlin Heidelberg, 2003. ISBN 9783540662709.
- F. Moukalled, L. Mangani, and M. Darwish. *The Finite Volume Method in Computational Fluid Dynamics: An Advanced Introduction with OpenFOAM® and Matlab*. Fluid Mechanics and Its Applications. Springer International Publishing, 2015. ISBN 9783319168746.
- M. Nishioka and H. Sato. Mechanism of determination of the shedding frequency of vortices behind a cylinder at low reynolds numbers. *Journal of Fluid Mechanics*, 89: 49–60, 1978.
- H. Nisi and A. W. Porter. On eddies in air. *Philosophical Magazine*, 46:754–768, 1923.
- OpenFoam. Openfoam guide/the pimple algorithm in openfoam, a. URL https://openfoamwiki.net/index.php/OpenFOAM_guide/The_PIMPLE_algorithm_in_OpenFOAM. Accessed: 2016-10-09.
- OpenFoam. Openfoam guide/the piso algorithm in openfoam, b. URL https://openfoamwiki.net/index.php/OpenFOAM_guide/The_PISO_algorithm_in_OpenFOAM. Accessed: 2016-10-09.
- OpenFoam. Openfoam guide/the simple algorithm in openfoam, c. URL https://openfoamwiki.net/index.php/OpenFOAM_guide/The_SIMPLE_algorithm_in_OpenFOAM. Accessed: 2016-10-09.
- OpenFoam. *OpenFOAM. The Open Source CFD Toolbox. User Guide*. Free Software Foundation, Inc., 2009. Accessed: 2016-09-02.
- O Posdziech and R Grundmann. A systematic approach to the numerical calculation of fundamental quantities of the two-dimensional flow over a circular cylinder. *Journal of Fluids and Structures*, 23(3):479–499, 2007. ISSN 08899746. doi: 10.1016/j.jfluidstructs.2006.09.004.
- QtiPlot. Qtiplot: data analysis and scientific visualization, 2004. URL <http://www.qtiplot.com/>. Accessed: 2016-10-09.
- Singiresu S Rao and Yap Fook Fah. *Mechanical vibrations; 5th ed. in SI units*. Prentice Hall, Singapore, 2011.
- Roshko. On the drag and shedding frequency of two-dimensional bluff bodies. *NACA Technical Note 3169*, (July 1954):1–30, 1954a.

- A. Roshko. On the drag and shedding frequency of two-dimensional bluff bodies. *National Advisory Committee for Aeronautics*, 1954b.
- A. Roshko. On the development of turbulent wakes from vortex streets. *National Advisory Committee for Aeronautics*, 1954c. ISSN 1098-6596. doi: 10.1017/CBO9781107415324.004.
- T. Sarpkaya. Vortex-Induced Oscillations: A Selective Review. *Journal of Applied Mechanics*, 46:241–258, 1979.
- Joachim Schöberl, Johannes Gerstmayr, and Robert Gaisbauer. Netgen - automatic 3d tetrahedral mesh generator., May . Accessed: 2016-10-09.
- Vincenz Strouhal. Ueber eine besondere Art der Tonerregung. *J. Phys. Theor. Appl.*, 8(1): 36–38, 1878.
- SU2. Su2 - the open-source cfd code. URL <http://su2.stanford.edu/>. Accessed: 2016-10-09.
- W.H. Zhang T. Li, J.Y. Zhang and M.H. Zhu. Vortex-Induced-Vibration-Characteristics-of-an-Elastic-Circular-Cylinder. *World Academy of Science, Engineering and Technology*, 109:1–24, 2009.
- Sadatosh Taneda. Experimental Investigation of the Wakes behind Cylinders and Plates at Low Reynolds Numbers. *Journal of the physical society of Japan*, 11:302–307, 1956.
- A. Thom. The flow past circular cylinders at low speeds. *Proceedings of the Royal Society of London A: Mathematical, Physical and Engineering Sciences*, 141(845):651–669, 1933. ISSN 0950-1207. doi: 10.1098/rspa.1933.0146.
- D. J. Tritton. Experiments on the flow past a circular cylinder at low Reynolds numbers. *J. Fluid Mech.*, 6(1936):547–567, 1959. ISSN 0022-1120. doi: 10.1017/S0022112059000829.
- H.K. Versteeg and W. Malalasekera. *An Introduction to Computational Fluid Dynamics: The Finite Volume Method*. Pearson Education Limited, 2007. ISBN 9780131274983.
- H. G. Weller, G. Tabor, H. Jasak, and C. Fureby. A tensorial approach to computational continuum mechanics using object-oriented techniques. *Computers in Physics*, 12(6): 620–631, 1998.
- J.F. Wendt, J.D. Anderson, and Von Karman Institute for Fluid Dynamics. *Computational fluid dynamics: an introduction*. Von Karman Institute book. Springer, 1996. ISBN 9783540594710.
- C. M. White. The drag of cylinders in fluids at slow speeds. *Proceedings of the Royal Society of London A: Mathematical, Physical and Engineering Sciences*, 186(1007):472–479, 1946. ISSN 0080-4630. doi: 10.1098/rspa.1946.0059.

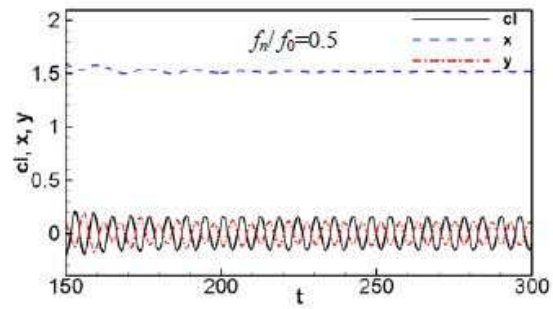
- C. Wieselsberger. New data on the law of hydro and aerodynamic resistance. *Physikalische Zeitschrift*, 22, 1921.
- C. H. K. Williamson. Sinusoidal flow relative to circular cylinders. *Journal of Fluid Mechanics*, 155:141–174, 06 1985. doi: 10.1017/S0022112085001756.
- C. H. K. Williamson. Defining a universal and continuous Strouhal-Reynolds number relationship for the laminar vortex shedding of a circular cylinder. *The Physics of Fluids*, 31(10):2742–2744, 1988. ISSN 0031-9171. doi: 10.1063/1.866978.
- C. H. K. Williamson. Oblique and parallel modes of vortex shedding in the wake of a circular cylinder at low Reynolds numbers. *Journal of Fluid Mechanics*, 206:579, 1989. ISSN 0022-1120. doi: 10.1017/S0022112089002429.
- C. H K Williamson and N. Jauvtis. A high-amplitude 2T mode of vortex-induced vibration for a light body in XY motion. *European Journal of Mechanics, B/Fluids*, 23(1):107–114, 2004. ISSN 09977546. doi: 10.1016/j.euromechflu.2003.09.008.
- C. H K Williamson and A. Roshko. Vortex formation in the wake of an oscillating cylinder. *Journal of Fluids and Structures*, 2(4):355–381, 1988. ISSN 10958622. doi: 10.1016/S0889-9746(88)90058-8.
- C.H.K. Williamson and R. Govardhan. Vortex-induced vibrations. *Annual Review of Fluid Mechanics*, 36(1):413–455, 2004.
- M. M. Zdravkovich. Flow induced oscillations of two interfering circular cylinders. *Journal of Sound and Vibration*, 101(4):511 – 521, 1985. ISSN 0022-460X.
- M. M. Zdravkovich. *A reflection on two modes of eddy shedding at $Re=180-300$* . Springer, 1992.
- M. M. Zdravkovich. *Flow Around Circular Cylinders*. Oxford Science publications, 1997. ISBN 0198563965.



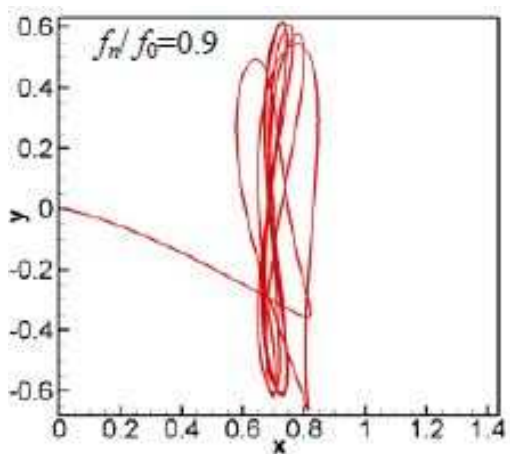
RESULTS OBTAINED BY T. LI AND ZHU (2009) FOR A CYLINDER WITH XY-MOTION



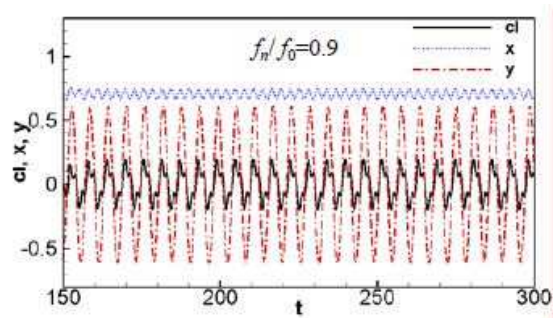
(a) XY-motion plot of an elastic cylinder for $\frac{f_n}{f_0} = 0.5$.



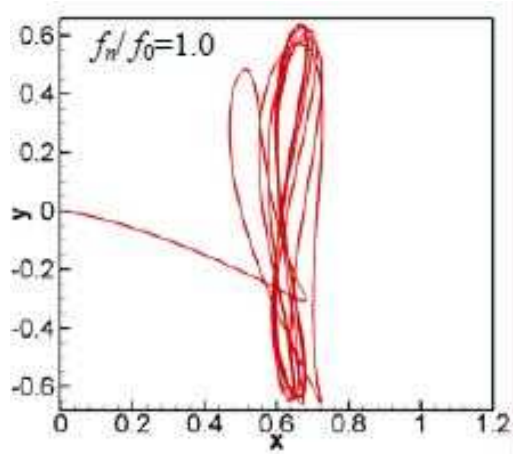
(b) Displacement and lift coefficient curves of an elastic cylinder for $\frac{f_n}{f_0} = 0.5$.



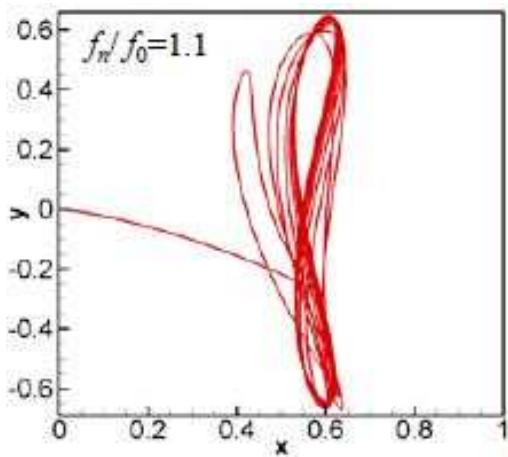
(c) XY-motion plot of an elastic cylinder for $\frac{f_n}{f_0} = 0.9$.



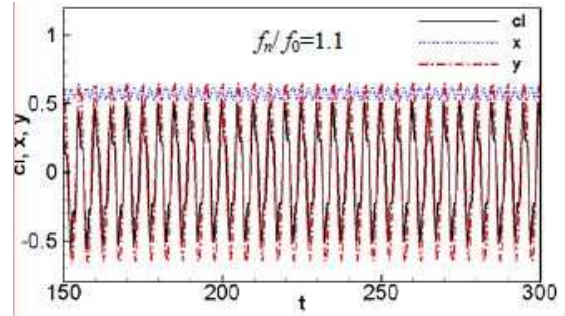
(d) Displacement and lift coefficient curves of an elastic cylinder for $\frac{f_n}{f_0} = 0.9$.



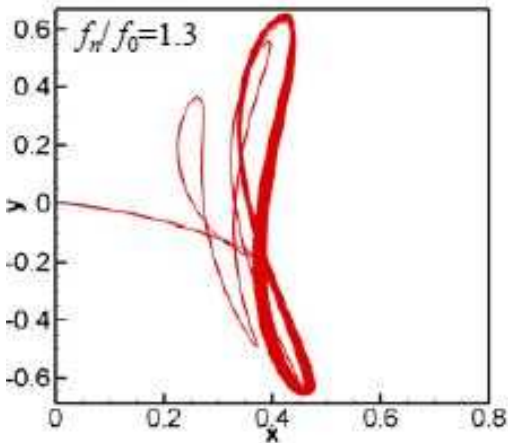
(e) XY-motion plot of an elastic cylinder for $\frac{f_n}{f_0} = 1.0$



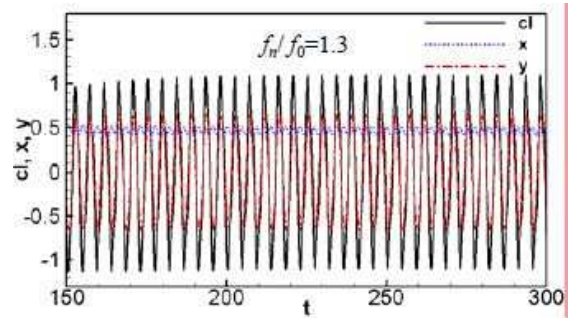
(f) XY-motion plot of an elastic cylinder for $\frac{f_n}{f_0} = 1.1$



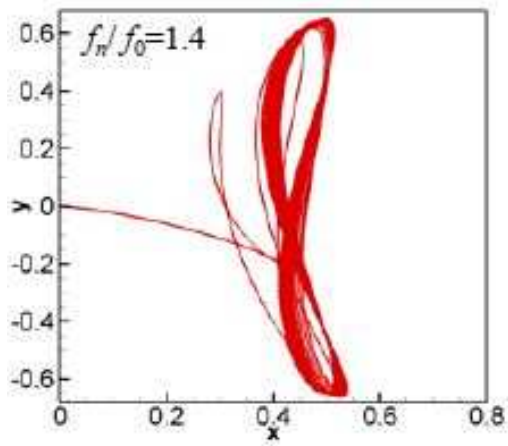
(g) Displacement and lift coefficient curves of an elastic cylinder for $\frac{f_n}{f_0} = 1.1$.



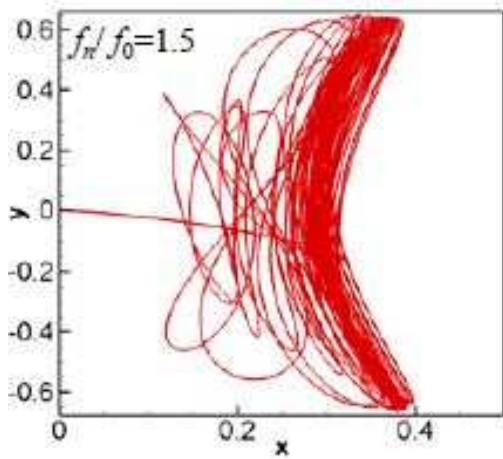
(h) XY-motion plot of an elastic cylinder for $\frac{f_n}{f_0} = 1.3$



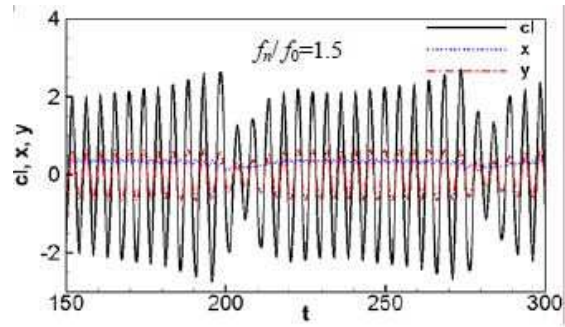
(i) Displacement and lift coefficient curves of an elastic cylinder for $\frac{f_n}{f_0} = 1.3$.



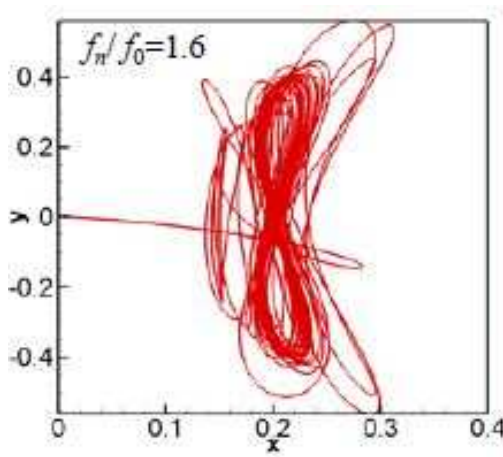
(j) XY-motion plot of an elastic cylinder for $\frac{f_n}{f_0} = 1.4$



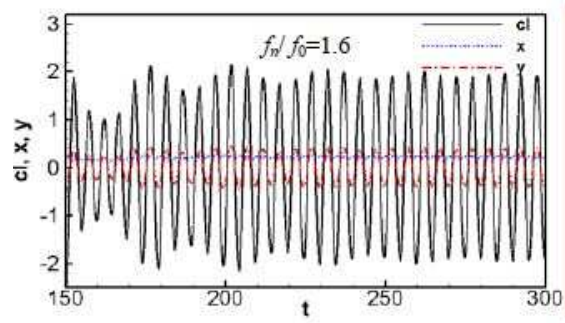
(k) XY-motion plot of an elastic cylinder for $\frac{f_n}{f_0} = 1.5$



(l) Displacement and lift coefficient curves of an elastic cylinder for $\frac{f_n}{f_0} = 1.5$.



(m) XY-motion plot of an elastic cylinder for $\frac{f_n}{f_0} = 1.6$



(n) Displacement and lift coefficient curves of an elastic cylinder for $\frac{f_n}{f_0} = 1.6$.

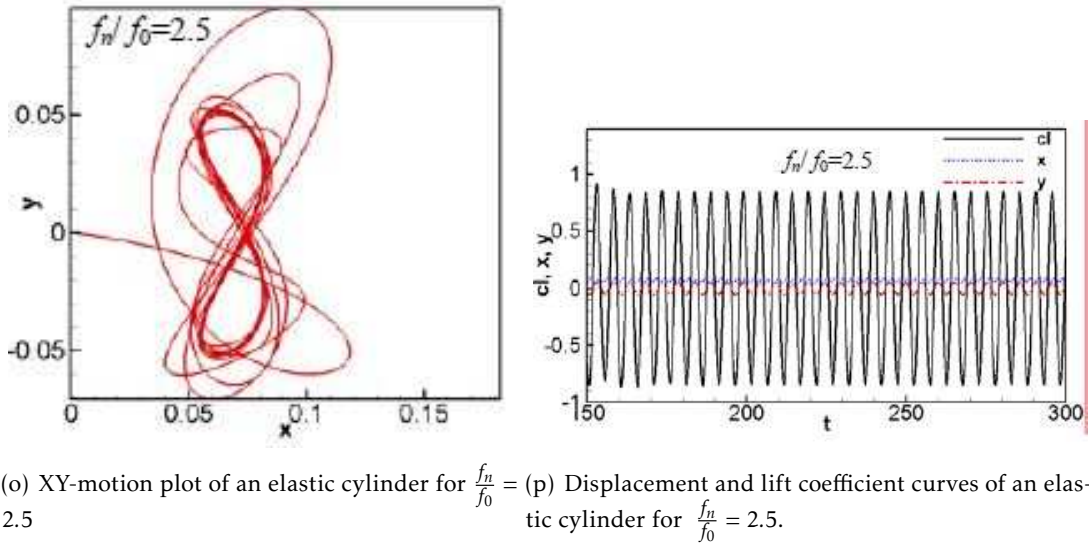


Figure A.1: Obtained results by T. Li and Zhu (2009) for XY-motion of an elastic cylinder for a set of frequency ratio and respective displacement and lift coefficient curves.